Imperial College London

Department of Physics

Investigating the structure of the near-Sun solar wind

Ronan Luke Laker

2023

Submitted for the degree of Doctor of Philosophy of Imperial College London and the Diploma of Imperial College London

I confirm that the research presented throughout this thesis has been completed by me. I have appropriately referenced any work and/or ideas from other sources.

The copyright of this thesis rests with the author.

Unless otherwise indicated, its contents are licensed under a Creative Commons Attribution-Non Commercial 4.0 International Licence (CC BY-NC). Under this licence, you may copy and redistribute the material in any medium or format. You may also create and distribute modified versions of the work. This is on the condition that: you credit the author and do not use it, or any derivative works, for a commercial purpose. When reusing or sharing this work, ensure you make the licence terms clear to others by naming the licence and linking to the licence text.

Where a work has been adapted, you should indicate that the work has been changed and describe those changes. Please seek permission from the copyright holder for uses of this work that are not included in this licence or permitted under UK Copyright Law.

Ronan Luke Laker, March 2023

Abstract

The recent launch of two flagship missions, Parker Solar Probe and Solar Orbiter, have ushered in an exciting new era for solar wind research. This thesis uses this novel data to study structures in the solar wind, with the aim of elucidating how the solar wind is heated and accelerated.

First, a newly formed constellation of spacecraft was used to study the structure and dynamics of the solar wind from different perspectives. This included the identification of small-scale ripples in the heliospheric current sheet, along with a study of a co-rotating interaction region in latitude.

Parker Solar Probe was then used to study small-scale switchbacks, which are folds in the magnetic field that dominate the near-Sun solar wind. Since switchbacks are seen throughout the solar wind, it is important to characterise their properties to test against theoretical predictions. In one of the first investigations of its kind, switchbacks were estimated to have a width of $\sim$50,000 km and an aspect ratio of the order of 10. It was also demonstrated that the magnetic field in switchbacks tended to deflect in certain directions, implying a systematic source closer to the Sun.

Finally, as Parker Solar Probe moved to only 13 $R_\odot$ from the Sun, a coherent pattern in the switchbacks was identified, which had a spatial scale comparable to bright points on the solar surface. It was also found that switchbacks were associated with consistent temperature enhancements. This feature, together with the newly identified systematic pattern in the switchback magnetic field, were used to propose a new switchback definition. This provides a more robust way to identify switchbacks, which does not rely solely on the absolute magnetic field angle. These observations were used to conclude that switchbacks represent the imprint of interchange reconnection on the solar wind.

Acknowledgements

I would like to take this opportunity to thank the people that have helped me get to this point. I can't possibly list every name here, but I appreciate everyone's support nonetheless.

I would first like to thank my supervisor, Tim, for his excellent guidance and support through two placements, a masters project and a PhD. Many an hour has been spent talking about everything and nothing, something that I will sorely miss. You have also made me feel part of two exciting space missions, and for that, I will always be grateful.

To my close collaborators: Stuart, Lorenzo, Lloyd, Julia and Tom, I thank you for your influence and help with my research. I would especially like to thank Stuart for his invitation and warm reception at Berkeley, as well as Tom for his much-needed assistance in picking out a Hawaiian shirt.

To the rest of the Space and Atmospheric group, I feel lucky to have spent the last three years here. Whether it was a trip to the pub, farmers market, or a muffin break, there has never been a quiet moment. I look forward to seeing where Ozzy the octopus will travel next.

Thanks to my parents and brother for the weekly phone calls and reminding me of the important things in life. A special mention to Mum, Dad, Aunt Mary and Liv, all of whom poured over every word in this thesis.

Finally, the greatest thanks must go to Liv, who has believed this was possible since we sat next to each other in the school science lab. Your love and support are what has made this thesis possible.

Contents

1 Introduction **14**

1.1 RTN coordinate system 16

2 Theory and measurements of the solar wind **17**

2.1 Plasma theory 18

2.1.1 Kinetic theory 19

2.1.2 Fluid description 21

2.2 The Sun 26

2.2.1 Solar cycle 28

2.2.2 Solar features 30

2.3 The solar wind theory 33

2.3.1 Parker solar wind solution 33

2.3.2 Interplanetary magnetic field 36

2.4 Solar wind observations 38

2.4.1 Velocity distribution functions 39

2.4.2 Alfvén waves in the solar wind 42

2.4.3 Types of solar wind 44

2.4.4 Heating and acceleration 46

2.4.5 T-V relationship 48

2.4.6 Large-scale structures 50

2.5 Instrumentation 55

2.5.1 Fluxgate magnetometers 55

2.5.2 Particle measurements . . . 57
2.6 Relevant missions . . . 60
2.6.1 Reference frames . . . 60
2.6.2 Parker Solar Probe . . . 61
2.6.3 Solar Orbiter . . . 66
2.6.4 Additional missions . . . 66

3 Multi-spacecraft study of the solar wind in latitude 69
3.1 Introduction . . . 69
3.2 Methodology . . . 70
3.2.1 Modelling the heliospheric current sheet . . . 73
3.2.2 Ballistic mapping . . . 75
3.2.3 Estimating magnetic polarity . . . 76
3.2.4 Determining sector boundaries . . . 78
3.2.5 Measuring the local orientation . . . 80
3.3 Results . . . 82
3.3.1 Global structure . . . 82
3.3.2 Local orientations of the sector boundaries . . . 89
3.3.3 Fine-scale structure . . . 91
3.3.4 Co-rotating interaction region in latitude . . . 93
3.3.5 Effect of transient structures on the heliospheric current sheet 97
3.4 Conclusions . . . 99

4 Properties of solar wind switchbacks 101
4.1 Switchback properties . . . 102
4.2 Theoretical models . . . 106
4.3 Identifying switchbacks . . . 109
4.3.1 Clock angle . . . 111
4.3.2 Arc-polarised deflections . . . 114
4.3.3 Estimating background magnetic field . . . 116

4.4 Size and shape of solar wind switchbacks . . . 118
4.4.1 Apparent duration . . . 118
4.4.2 Measuring switchback shape . . . 123
4.4.3 Results . . . 126
4.4.4 Discussion . . . 131
4.5 Preferential switchback deflection directions . . . 133
4.5.1 Switchback deflection distributions . . . 134
4.5.2 Discussion . . . 137
4.5.3 Linking time series to a physical shape . . . 143
4.6 Conclusions . . . 146

5 Systematic deflections in the near-Sun solar wind 148
5.1 Motivation . . . 149
5.1.1 Switchback definition . . . 149
5.1.2 Potential signatures of generation mechanisms . . . 150
5.2 Systematic deflections . . . 155
5.3 Scale of the deflections . . . 162
5.4 Temperature enhancements inside switchbacks . . . 166
5.4.1 Heating inside switchbacks . . . 171
5.4.2 Temperature inside a full reversal switchback . . . 175
5.5 T-V relationship on the large scale . . . 179
5.6 Solar wind types . . . 182
5.7 Conclusions . . . 187

6 Conclusions 190

A Papers 196

B Symbols 198

C Abbreviations 200

D Software **202**

E Data **203**

F Permissions **204**

List of Figures

1.1 Diagram of the RTN coordinate system 16

2.1 Diagram of Sweet-Parker reconnection 24
2.2 Diagram of Alfvénic fluctuations in the magnetic field and velocity . . 25
2.3 Images of the Sun at different wavelengths 27
2.4 Sunspot numbers over time showing the 11-year solar cycle 28
2.5 Evolution of magnetic flux during the solar cycle 30
2.6 Sketch of the coronal magnetic field 31
2.7 Different classes of solution for a hydrodynamic expanding gas 35
2.8 Parker spiral diagram 37
2.9 Solar wind speed and magnetic polarity in latitude 39
2.10 Example proton VDFs in the solar wind 40
2.11 Electron VDF diagram 42
2.12 Diagram showing how particle VDFs are rotated in the solar wind . . 43
2.13 Diagram of the heliospheric current sheet 50
2.14 Diagram of a typical co-rotating interaction region 53
2.15 Diagram of the shock formation at CIRs 54
2.16 Fluxgate magnetometer diagram 56
2.17 Faraday cup diagram 57
2.18 Electrostatic analyser diagram 59
2.19 Trajectories of the different spacecraft used in this thesis 63
2.20 Diagram showing the placement of the relevant instruments on PSP . 65
2.21 Simulated VDFs that will be seen by SPAN 68

3.1 Trajectories of the different spacecraft during Chapter 3 71
3.2 PFSS solution for a dipole magnetic field 75
3.3 Demonstration of ballistic mapping 77
3.4 Diagram of how magnetic polarity is classified 78
3.5 Examples of different sector boundary configurations 79
3.6 Polarity structure for CR2231 84
3.7 Polarity structure for CR2232 85
3.8 Polarity and speed maps for CR2231 87
3.9 Polarity and speed maps for CR2231 88
3.10 Comparison of local orientation of sector boundaries to a PFSS model 89
3.11 Closer look at a small warp in the HCS 91
3.12 Diagram of the draped magnetic field measured by Solar Orbiter . . . 93
3.13 Comparing the speed profile of STEREO-A and Wind when measuring the same CIR 95
3.14 Demonstration of how the speed profiles at STEREO-A and Wind could be explained by a fast solar wind stream at higher latitudes . . 96
3.15 Sector boundary with a flux rope as measured by PSP 97
3.16 Spacecraft configuration when measuring the same sector boundary . 98

4.1 Radial magnetic field measurements from the first PSP encounter in 2018. 102
4.2 Diagram of the different switchback generation mechanisms 107
4.3 Comparing switchback definitions 111
4.4 Clock angle diagram 112
4.5 Comparing clock angle definitions 113
4.6 Example of the arc-polarised behaviour of switchbacks 114
4.7 Superposed epoch analysis of switchback deflections across the encounters 116
4.8 Comparing Parker spiral estimate to the magnetic field in each encounter 117

4.9 Demonstrates how cutting shapes at different angles can affect the distance measured . . . 119
4.10 Switchback dimensions . . . 120
4.11 Diagram of distance measured by a spacecraft cutting through the switchbacks, as in equation 4.6 . . . 121
4.12 Ring of possible switchback speeds . . . 122
4.13 Diagram showing how the alignment between the switchbacks and velocity ring can affect how distance varies with clock angle . . . 124
4.14 Solar wind streams used for Section 4.4 . . . 125
4.15 Demonstration that the switchback velocities lie on a circle . . . 127
4.16 Duration of switchbacks as a function of deflection angle . . . 128
4.17 Final results of the fitting procedure to find the most consistent alignment direction . . . 129
4.18 Summary of switchbacks in E2 . . . 135
4.19 Summary of switchback deflection directions across the first eight encounters . . . 136
4.20 Diagram of interchange reconnection . . . 137
4.21 Summary of predictions for switchback deflections . . . 139
4.22 Diagram of magnetic funnels close to the Sun . . . 141
4.23 Demonstration of the S-shaped switchback shape . . . 145

5.1 Plumelet scenario from Kumar et al. (2022) . . . 151
5.2 Interchange reconnection simulation from Wyper et al. (2022) . . . 152
5.3 Asymmetric velocity profile created by interchange reconnection . . . 154
5.4 Example of anti-correlated deflections in B_T and B_N . . . 156
5.5 Comparing the current and proposed definition of switchbacks . . . 157
5.6 Example of correlated deflections in B_T and B_N . . . 158
5.7 Polar histogram of CA for the two example periods in E11 . . . 160
5.8 Example of a cluster of switchbacks . . . 161
5.9 Example power and cross-spectral density for a period in E10 . . . 163

5.10 Example power and cross-spectral density with respect to angular displacement for a period in E10 . . . 165
5.11 Example deflection with increased temperature . . . 167
5.12 VDFs from example deflection . . . 168
5.13 Example temperature enhancements for a patch of switchbacks . . . 169
5.14 Enhanced proton parallel patches from Woodham et al. (2021a) . . . 170
5.15 Temperature vs θ_{RB} for several encounters . . . 172
5.16 Diagram of the two heating scenarios . . . 174
5.17 Example of a full reversal switchback in E5 . . . 176
5.18 Comparing SPAN and SPC temperatures for a full reversal deflection 178
5.19 Smoothed speed and temperature for E11 . . . 180
5.20 T-V relationship for various encounters . . . 181
5.21 Comparison of T-V relationship with Helios results . . . 183
5.22 Transition from 'patchy' to 'quiet' solar wind . . . 184
5.23 Plasma properties of the patchy and quiet wind . . . 185
5.24 T-V relationship for the quiet regions . . . 186

List of Tables

3.1 List of measurements used in Chapter 3 72
3.2 List of events identified in Chapter 3 90

4.1 Table showing the results of Section 4.4 130
4.2 Summary of other switchback size estimates 132

5.1 Results of fitting the temperature model to switchbacks across the encounters 173

Chapter 1

Introduction

Out of the countless stars in the observable universe, the Sun is the only one that can be truly studied in detail. Since the start of the space age, many spacecraft have been sent to explore the Sun and the solar wind that escapes from its atmosphere. In addition to being an excellent laboratory to study fundamental plasma physics, the solar wind has long been known to affect conditions on Earth. Therefore, it is important to understand how the solar wind is formed and accelerated.

Small-scale dynamics and plasma properties measured by spacecraft can provide clues to the origin of the solar wind, although many of these smaller-scale features become washed out as the solar wind travels to Earth (at 1 AU). Therefore, spacecraft must be sent closer to the Sun, with the closest measurements coming from the Helios mission in the 1980s ($\sim$62 $R_\odot$, Schwenn and Marsch 1990). While this dataset vastly improved the understanding of the solar wind, instrumentation and remote sensing observations were limited. As a result, there are still many unanswered questions regarding the solar wind almost 40 years later. This knowledge gap provided the motivation to launch two new missions since 2018, Parker Solar Probe (PSP) and Solar Orbiter, which represent a new era for inner heliosphere science.

Parker Solar Probe, named after Eugene Parker[1], is the closest man-made object to ever orbit the Sun and is a 'mission to touch the Sun' (Fox et al. 2016). This will be achieved by completing 25 orbits, with seven Venus gravity assists slowly

[1]Who theorised the solar wind's existence as described in Section 2.3.2

lowering the perihelion distance to only 9.86 $R_\odot$. Therefore, PSP will explore an entirely new region of the heliosphere and hopefully identify structures and processes that cannot be measured at 1 AU ($\sim$215 $R_\odot$).

At the same time, Solar Orbiter will provide more detailed composition and remote sensing observations, allowing for a better connection to be made between the Sun and solar wind. While it does not travel as close to the Sun as PSP, it does include a wider range of instruments, including six remote sensing telescopes and four in situ detectors (Müller et al. 2020). This will hopefully allow Solar Orbiter to identify structures on the Sun that can later be directly measured by the spacecraft in the solar wind (Rouillard et al. 2020). Such observations could be crucial in uncovering how the solar wind is heated and accelerated.

In this thesis, the first data from these groundbreaking missions are used to explore the properties and dynamics of both small and large-scale structures in the solar wind. After outlining the relevant theory and literature, the different spacecraft are introduced at the end of Chapter 2. These spacecraft are then used to form a constellation in the inner heliosphere in Chapter 3, which provides unprecedented coverage of the solar wind. This also allows for the dynamics of several large-scale phenomena to be studied in detail, which would otherwise not be possible with only a single spacecraft.

The remainder of the thesis then focuses on magnetic switchbacks that are seen to dominate the PSP observations close to the Sun. These structures have become an active area of research, with many authors proposing ways in which they can be created. Therefore, to help uncover the true origin of switchbacks, Chapter 4 attempts to characterise the size and shape of switchbacks, as well as their tendency to deflect in certain directions. Chapter 5 then presents some novel switchback properties that became evident as PSP travelled to only 13 $R_\odot$ from the Sun. These could have major implications for the understanding of switchbacks, and may even represent the direct signature of a heating process at the Sun. Finally, the conclusions are presented in Chapter 6, together with suggestions for future studies.

1.1 RTN coordinate system

Throughout this thesis, the magnetic field and plasma measurements are made in the RTN coordinate system. In this system, $\vec{R}$ is defined to point from the Sun to the spacecraft, $\vec{T}$ is the cross product of $\vec{R}$ and the solar rotation axis with $\vec{N}$ completing the right-handed set. This is coordinate system is depicted in Fig. 1.1.

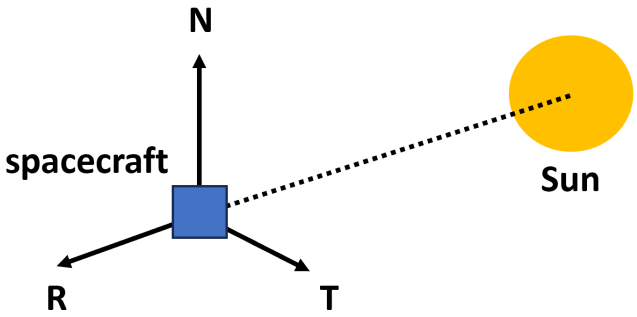


Figure 1.1: Diagram of the RTN coordinate system, which is defined with respect to the spacecraft.

The magnetic field can be referred to as angles away from $\vec{R}$, so that:

$$\phi_B = \tan^{-1}\left(\frac{B_T}{B_R}\right), \tag{1.1}$$

$$\theta_B = \tan^{-1}\left(\frac{B_N}{\sqrt{B_R^2 + B_T^2}}\right), \tag{1.2}$$

are the angles in and out of the R-T plane, respectively.

Chapter 2

Theory and measurements of the solar wind

The solar wind is a supersonic plasma expanding away from the Sun at speeds of the order of 500 km/s. While the Sun has been observed for centuries, the measurements and theory behind the solar wind are relatively recent. Early ideas regarding 'solar corpuscular radiation' emanating from the Sun were used to explain the link between solar activity and geomagnetic disturbances on Earth (Birkeland 1908; Chapman 1917). This idea was strengthened by Biermann's observations of anti-Sunward comet tails, which suggested that some sort of corpuscular radiation emanates from the Sun in all directions (Biermann 1951; Biermann 1957). To explain these results, Parker (1958b) proposed the theory of a hot gas expanding radially from the Sun, later coined the 'solar wind' (Parker 1958a). This idea was subsequently confirmed by spacecraft at the start of the space age (Gringauz et al. 1960; Neugebauer and Snyder 1966), which observed a continuous flow of charged particles from the Sun.

This chapter first outlines the theory of plasmas from both a kinetic and fluid approach, based on Verscharen et al. (2019) and Meyer-Vernet (2007). Some important features of the Sun are then described, followed by a summary of the solar wind literature. Finally, the relevant spacecraft, along with their instrumentation, are introduced.

2.1 Plasma theory

A plasma like the solar wind is a quasi-neutral ionised gas that exhibits collective motion through magnetic ($\vec{B}$) and electric ($\vec{E}$) fields (Kivelson and Russell 1995; Wilson et al. 2018). For simplicity, in this thesis, a plasma is treated as an equal concentration of positive charged ions (with charge $+e$ and mass m_i) and negatively charged electrons (with charge $-e$ and mass m_e). However, random perturbations can locally break the neutrality of the plasma, i.e. proton density, n_i, does not equal electron density, n_e. To estimate the scale at which this becomes important, consider adding another charged particle to the plasma. In response, the ions and electrons will rearrange in such a way as to screen this new charge, so that the plasma appears neutral on scales larger than the Debye length:

$$\lambda_D = \sqrt{\frac{\epsilon_0 k_B T}{n e^2}}, \tag{2.1}$$

using $n \approx n_e \approx n_i$ and equal electron and ion temperatures ($T_e \approx T_i$). For typical solar wind conditions near Earth ($T = 10^5\,\mathrm{K}$ and $n = 5\,\mathrm{cm}^{-3}$), this is equal to $\sim$10 m. Since a plasma is quasi-neutral, there should be many charged particles in a sphere of radius λ_D, leading to the plasma condition that $n\lambda_D^3 >> 1$, which holds in the solar wind.

The plasma frequency, ω_p, is another fundamental property that sets the scales of plasma dynamics. This arises from the electrons moving to restore neutrality in a plasma after a perturbation. Due to their inertia, the electrons will oscillate like a simple harmonic oscillator with a frequency:

$$\omega_p = \sqrt{\frac{n_e e^2}{m_e \epsilon_0}}. \tag{2.2}$$

Again, with the same typical values near Earth, this frequency will be around $2{\times}10^4\,\mathrm{Hz}$[1]. This quantity can be directly measured by space-based instruments, and is commonly used to estimate the electron density (referred to as the quasi-

[1] Using $f_p = \omega_p / 2\pi$

thermal noise).

Before describing the collective behaviour of the plasma, it is necessary to consider the motion of a single charged particle in response to $\vec{E}$ and $\vec{B}$ fields. A charged particle moving with a velocity, $\vec{v}$, and a charge, q, will experience the Lorentz force according to:

$$\vec{F} = q(\vec{E} + \vec{v} \times \vec{B}). \tag{2.3}$$

In the absence of a strong electric field, this force will be perpendicular to both the velocity and magnetic field, causing the particle, of mass m, to gyrate around the magnetic field at the gyrofrequency, or cyclotron frequency:

$$f_c = \frac{|q||\vec{B}|}{2\pi m}, \tag{2.4}$$

with a radius:

$$r_L = \frac{|\vec{v} \times \vec{B}|}{2\pi f_c}, \tag{2.5}$$

known as the Larmor radius (or gyroradius). For a typical magnetic field strength near Earth of $|\vec{B}| \approx 5\,\mathrm{nT}$, the proton cyclotron frequency will be equal to $\sim 8 \times 10^{-2}\,\mathrm{Hz}$. Combined with a constant velocity parallel to $\vec{B}$, the particles will move in a helical fashion about the magnetic field direction, with the ions (electrons) having a left-handed (right-handed) sense about the magnetic field.

While it is important to understand the motion of a single particle, the magnetic and electric fields in a plasma are dependent on the interaction between many charged particles. Therefore, it is not practical to define an equation of motion for each particle separately, based on interactions with all the other particles. Instead, two approaches are usually taken, either treating the plasma in a statistical way in the 'kinetic description', or as a macroscopic fluid in the 'fluid description'.

2.1.1 Kinetic theory

Instead of dealing with the forces on individual particles, the kinetic description tracks the evolution of the six-dimensional velocity distribution function.

The particle velocity distribution, $f_j(\vec{x}, \vec{v}, t)$ for a species j, can be defined so that the number of particles in a position ($\vec{x}$) and velocity ($\vec{v}$) phase space is given by:

$$N_j = \int f_j(\vec{x}, \vec{v}, t)\, d^3\vec{x}\, d^3\vec{v}, \tag{2.6}$$

at a time, t. The evolution of f_j is then governed by the Boltzmann equation:

$$\frac{\partial f_j}{\partial t} + \vec{v} \cdot \nabla f_j + \vec{a} \cdot \nabla_{\vec{v}} f_j = \left(\frac{\partial f_j}{\partial t}\right)_c, \tag{2.7}$$

where ∇ is the spatial derivative, $\nabla_{\vec{v}}$ is the velocity derivative, $\vec{a}$ is the acceleration and the term on the right-hand side describes the effect of particle collisions. This reduces to the Vlasov equation for the collisionless solar wind:

$$\frac{\partial f_j}{\partial t} + \vec{v} \cdot \frac{\partial f_j}{\partial \vec{x}} + \frac{q_j}{m_j}(\vec{E} + \vec{v} \times \vec{B}) \cdot \frac{\partial f_j}{\partial \vec{v}} = 0, \tag{2.8}$$

using the Lorentz force from equation 2.3 and ignoring gravity. Therefore, the Vlasov equation describes the continuity of f_j in the phase space.

This framework is completed by using Maxwell's equations to describe the behaviour of the electric and magnetic fields:

$$\nabla \cdot \vec{E} = \frac{\rho_c}{\epsilon_0} \tag{2.9}$$

$$\nabla \cdot \vec{B} = 0, \tag{2.10}$$

$$\nabla \times \vec{E} = -\frac{\partial \vec{B}}{\partial t}, \tag{2.11}$$

$$\nabla \times \vec{B} = \mu_0 \vec{J} + \epsilon_0 \mu_0 \frac{\partial \vec{E}}{\partial t}, \tag{2.12}$$

where the charge and current densities are given by:

$$\rho_c = \sum_j q_j \int f_j d^3\vec{v} \tag{2.13}$$

$$\vec{J} = \sum_j q_j \int \vec{v} f_j d^3\vec{v}. \tag{2.14}$$

2.1.2 Fluid description

While the kinetic description contains all information needed to capture microphysics of wave-particle interactions (Pokhotelov et al. 2013), it is easier to reduce these equations to track the evolution of bulk fluid parameters in the fluid description. This can be done by taking the 'moments' of f_j, which integrates over velocity space so that the macroscopic quantities only vary in space and time.

The first two moments give the number density and bulk velocity, $\vec{u}$:

$$n_j = \int f_j \, d^3\vec{v}, \tag{2.15}$$

$$\vec{u_j} = \frac{1}{n_j} \int \vec{v} \, f_j \, d^3\vec{v}. \tag{2.16}$$

In general, the nth moment will have a dependence on the $n + 1^{th}$ moment, creating an infinite number of equations without a solution. Therefore, some assumptions are needed to close these equations, with some examples being the isotropic and Chew-Goldberger-Low closures (Chew et al. 1956).

However, for this thesis, the most relevant description is single fluid magnetohydrodynamics (MHD). This ignores the different particle species, and instead considers the plasma as a conducting fluid where the bulk density, ρ, and velocity are given by:

$$\rho = \sum_j m_j n_j \tag{2.17}$$

$$\vec{u} = \frac{1}{\rho} \sum_j m_j n_j \vec{u_j}. \tag{2.18}$$

Taking the zeroth moment of the Vlasov equation (equation 2.8) gives the continuity equation:

$$\frac{\partial \rho}{\partial t} + \nabla \cdot (\rho \vec{u}) = 0, \tag{2.19}$$

which represents the fact that no mass is lost in the system. A similar procedure

can be applied to the first moment to give the momentum equation:

$$\rho\left(\frac{\partial}{\partial t}+\vec{u}\cdot\nabla\right)\vec{u}=-\nabla P+\vec{J}\times\vec{B}, \tag{2.20}$$

where P is the isotropic scalar pressure. The system is closed by assuming an equation of state, which is usually adiabatic:

$$\frac{d}{dt}\left(\frac{P}{\rho^{\gamma}}\right)=0, \tag{2.21}$$

where γ is the ratio of specific heats, with a value of 5/3 for a monatomic gas.

Using Ampère's law (equation 2.12) the momentum equation can be written as:

$$\rho\left(\frac{\partial}{\partial t}+\vec{u}\cdot\nabla\right)\vec{u}=-\nabla P-\nabla\left(\frac{B^2}{2\mu_0}\right)+\frac{1}{\mu_0}(\vec{B}\cdot\nabla)\vec{B}. \tag{2.22}$$

The right-hand side of this equation can be understood as the gradient of the thermal pressure ($-\nabla P$), the gradient of the magnetic pressure ($-\nabla\left(\frac{B^2}{2\mu_0}\right)$) and a term for the magnetic tension force ($\frac{1}{\mu_0}(\vec{B}\cdot\nabla)\vec{B}$). The ratio of the two pressure gradient terms is useful for describing the motion of the plasma, and is known as the plasma beta[2]:

$$\beta=\frac{P}{B^2/2\mu_0}=\frac{4\mu_0 n k_B T}{B^2} \tag{2.23}$$

If $\beta << 1$ then the magnetic pressure dominates, and the plasma is governed by the magnetic field. On the other hand, if $\beta >> 1$ then the thermal pressure is dominant and the plasma motion controls the movement of the magnetic field.

It can also be shown that the magnetic field evolves according to:

$$\frac{\partial\vec{B}}{\partial t}=\nabla\times(\vec{u}\times\vec{B})+\frac{1}{\mu_0\sigma}\nabla^2\vec{B}, \tag{2.24}$$

where σ is the conductivity. The right-hand side can be split into a convective ($\nabla\times(\vec{u}\times\vec{B})$) and diffusive ($\frac{1}{\mu_0\sigma}\nabla^2\vec{B}$) term. Therefore, further simplification to MHD

[2]Using the ideal gas law $P=2nk_BT$

can be made by assuming a perfectly conducting fluid with no magnetic diffusion (i.e. $\sigma \to \infty$ in equation 2.24), which is valid on scales much larger than the Debye length and proton gyro-radius, as well as time scales longer than $1/f_c$. Under these 'ideal MHD' conditions, the magnetic field lines are said to be 'frozen in' to the plasma, meaning that the magnetic field lines are dragged with the plasma as it moves. Such an idea allows for the existence of 'flux tubes', where particles will remain inside the same bundle of magnetic field lines as they expand out into solar wind. The frozen-in theorem is responsible for the large-scale shape of the solar wind's magnetic field, which is derived later in Section 2.3.2.

The lack of diffusion also implies that plasma from different flux tubes cannot mix in this description. However, in reality, as the magnetic field lines are forced together, the assumptions behind ideal MHD start to break down. For example, consider two opposing magnetic field lines being forced together by the motion of the plasma in Fig. 2.1. A current sheet will be formed between the opposing magnetic fields lines, which will continue to be compressed as the plasma streams move towards each other. When the length scale of the current sheet reaches the ion scale ($\sim r_L$, see equation 2.5), a region will be formed where magnetic diffusion becomes important. In this diffusion region, the magnetic topology is changed so that magnetic field lines can reconnect in a fundamental process known as 'magnetic reconnection'. Plasma is now allowed to flow into the diffusion region, and will be accelerated by the magnetic tension from highly bent field lines to form opposing reconnection exhausts.

Such a simplified description of magnetic reconnection is known to be too slow at mixing the plasma when compared to observations (Parker 1957; Petschek 1964; Biskamp 2000; Priest and Forbes 2007). More complex models have been developed (Priest and Forbes 1986; Malyshkin 2008), but for this thesis, magnetic reconnection only needs to be understood as an explosive mechanism that can reshape the magnetic topology while accelerating charged particles. Such a process is seen throughout the solar system (Kopp and Pneuman 1976; Sonnerup et al. 1981; Antiochos

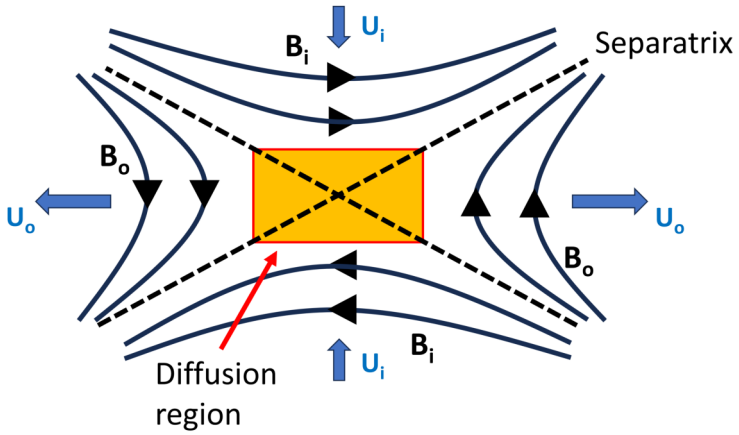


Figure 2.1: Diagram of Sweet-Parker magnetic reconnection (Parker 1957). Inward plasma velocity, $\vec{u_i}$, forces the magnetic field lines, $\vec{B_i}$, together. The topology of the magnetic field is allowed to change inside the diffusion region, which also creates a faster reconnection exhaust, $\vec{u_o}$.

et al. 1999; Gosling et al. 2005), and is responsible for several features observed on the Sun (Yokoyama and Shibata 1995; Torok et al. 2009; Karpen et al. 2017).

Much like a conventional fluid, the MHD approach allows for waves to propagate through the fluid. However, in a plasma, the magnetic pressure can now drive wave propagation as well as the thermal pressure. Wave solutions can be derived by linearising the ideal MHD equations, which examines the effect of applying small perturbations to a steady background. Applying this procedure to the MHD equations gives rise to three distinct wave modes: slow, fast and Alfvén waves.

The first two solutions are magneto-sonic waves, driven by both the thermal and magnetic pressure. However, it is the Alfvén mode (Alfvén 1942) that is the most relevant for this thesis, since these waves are seen throughout the solar wind (Belcher and Davis Jr. 1971). Unlike the magneto-sonic waves, Alfvén waves are incompressible, meaning there is no change in the plasma density or magnetic field strength. These waves are also non-dispersive, and are often compared to waves on a string, with magnetic tension providing the restoring force. With this analogy, and the magnetic tension from the final term of equation 2.22, the Alfvén speed is given by:

$$v_A = \frac{|\vec{B}|}{\sqrt{\mu_0 \rho}}. \tag{2.25}$$

One of the most defining signatures of Alfvén waves is the (anti-)correlation of the magnetic ($\delta\vec{B}$) and velocity fluctuations ($\delta\vec{u}$):

$$\frac{\delta\vec{B}}{|\vec{B}|} \propto \pm\frac{\delta\vec{u}}{v_A}. \tag{2.26}$$

When studying in situ data, it is common to say a fluctuation is 'Alfvénic' if equation 2.26 is met along with a constant $|\vec{B}|$ and density. Under these conditions, the magnetic field vectors will lie on a sphere centred at the origin with radius $|\vec{B}|$ (Matteini et al. 2014), and the velocity fluctuations will create a sphere with radius v_A, as demonstrated in Fig. 2.2.

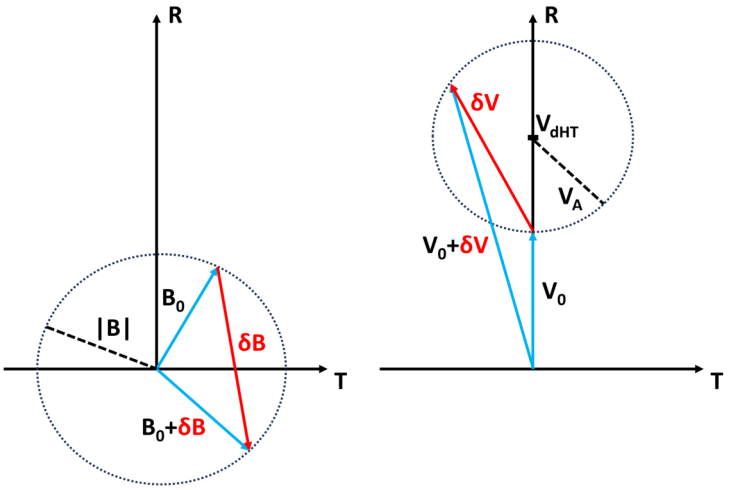


Figure 2.2: Diagram showing how the magnetic field and velocity vectors lie on the surface of a sphere (dashed circle in 2D) under Alfvénic fluctuations, $\delta\vec{B}$ and $\delta\vec{V}$. The sphere of magnetic field fluctuations is centred on the origin, but the velocity is at the deHoffmann-Teller velocity, V_{dHT}.

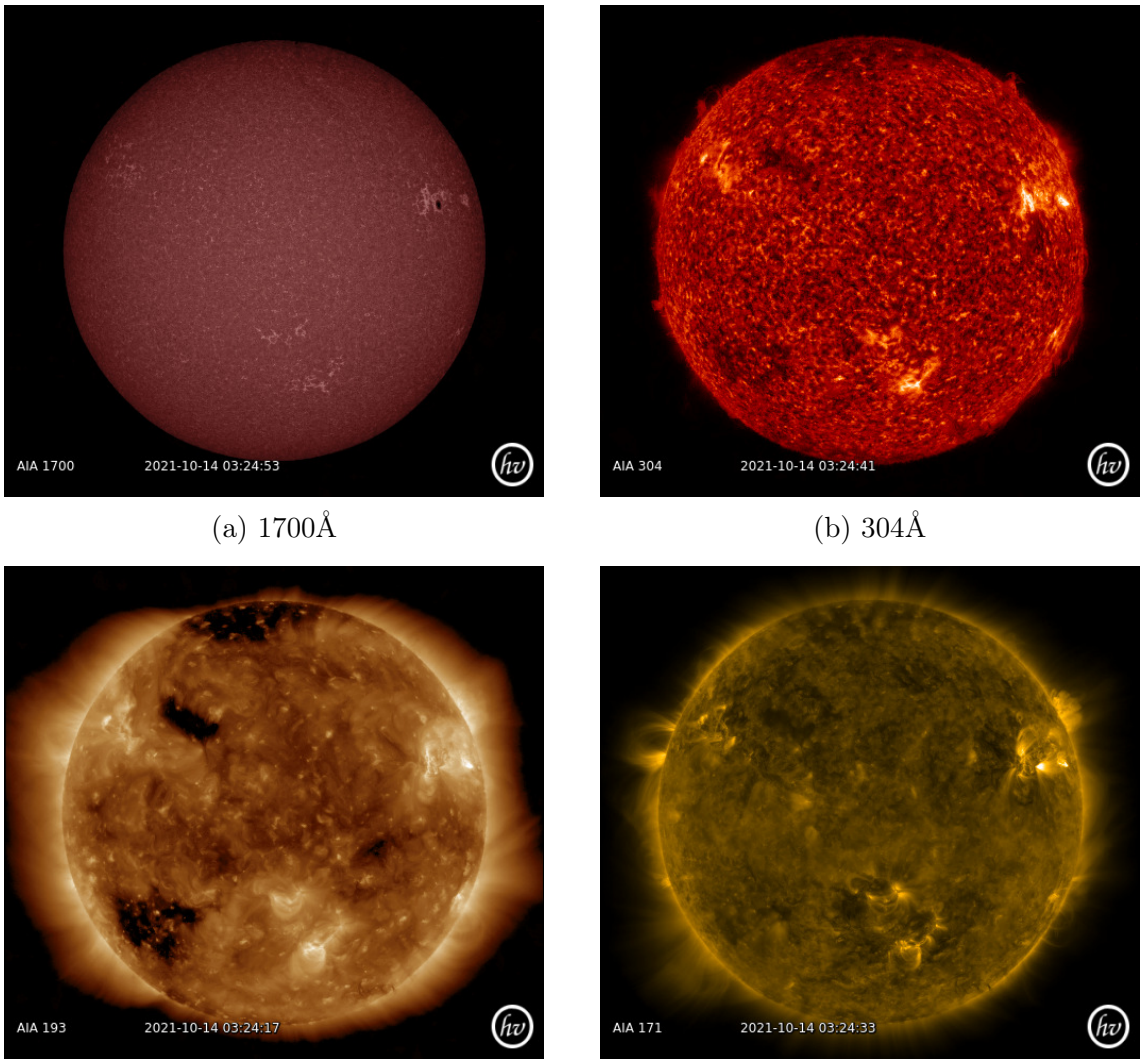
It has also been shown that these conditions represent an exact non-linear solution to the MHD equations (Barnes and Hollweg 1974; Hollweg 1974). This is true for any amplitude wave, so does not require the equations to be linearised as mentioned for other wave modes above. Such large-amplitude Alfvén waves are commonly observed in the solar wind, and are covered in more detail in Section 2.4.2.

2.2 The Sun

By astronomical standards, the Sun is an ordinary main sequence star, around halfway through its lifetime, with a radius ($R_\odot$) of ~695,000 km (Haberreiter et al. 2008). However, its proximity to Earth (1.5×10^8 km or 215 $R_\odot$) makes the Sun, and its surrounding environment, an excellent model star that can be studied in great detail through both remote sensing and in situ measurements. Despite appearing disconnected from the rest of the solar system, the Sun's influence reaches to all the planets, and can cause significant damage at Earth, known as space weather (Carrington 1859; Eastwood et al. 2017).

The Sun is the energy source for the solar system, where nuclear fusion in the core combines hydrogen (~90% of the Sun's mass) and helium (~10% mass) through several reactions, generating trace amounts of other elements (~0.1% mass). This process converts mass into energy, which is then transported from the core into the radiative zone via photons scattering through the almost opaque gas. As the temperature drops with distance from the core, the plasma will become unstable to convection around $3/4\,R_\odot$ in the convection zone (Christensen-Dalsgaard et al. 1991). Here, large convective cells transport the hotter plasma to the photosphere, where the temperature is sufficiently low (~5800 K) to allow visible light to escape. The bottom of the photosphere is often used to define the surface of the Sun, and has a distinct granulation pattern from the convection cells below the surface (Cloutman 1979; Roudier and Muller 1986), as shown in Fig. 2.3a. The inner structure of the Sun can be probed by observing resonant pressure modes, p-modes, that travel through the solar interior (Demarque and Guenther 1999). While there are many resonant modes in the Sun's spherical cavity, observations have long shown a characteristic '5-minute oscillation' on the Sun's surface (Leighton et al. 1962).

By observing different wavelengths of light, different layers of the Sun's atmosphere can be isolated by their temperature, as shown in Figs. 2.3a to 2.3d. Above the photosphere is the chromosphere, where the temperature steadily increases to ~8000 K before significantly heating to 10^6 K in the transition region up to around



(a) 1700Å (b) 304Å

(c) 193Å (d) 171Å

Figure 2.3: Images of the Sun at different wavelengths from the AIA instrument on the Solar Dynamics Observatory (Lemen et al. 2012), showing the different layers of the Sun's atmosphere. (a) The photosphere, with the dark spot on the right being a sunspot (Section 2.2.1). (b) The chromosphere. (c) The lower corona, with bright active regions and dark coronal holes (Section 2.2.2). (d) The upper corona, showing the coronal loops more clearly (Courtesy of NASA/SDO and the AIA team, sourced from Helioviewer.org).

7000 km from the surface. This leads to extreme temperatures in the Sun's outer layer (corona), the cause of which is still an open question in solar physics, commonly referred to as the 'coronal heating problem' (Klimchuk 2006). Most of the ions are completely ionised in the corona, except for some heavy elements (Fe and Ca) (Grotrian 1939; Edlén 1943), whose emission spectrum can be seen in the high energy EUV spectrum in Fig. 2.3c. The corona extends out into the solar system, creating a bubble in the interplanetary medium known as the heliosphere.

2.2.1 Solar cycle

Early observations of sunspots, dark patches on the Sun's surface, led to the idea that the Sun has an 11-year solar cycle (Schwabe 1844) with peaks and troughs in the sunspot numbers, Fig. 2.4, termed solar maximum and solar minimum, respectively.

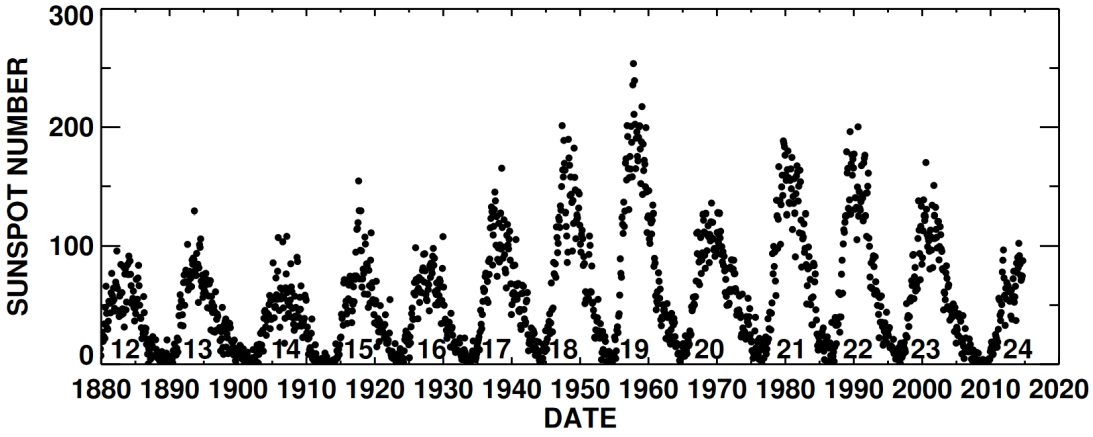


Figure 2.4: Sunspot numbers over time showing the 11-year solar cycle, with the number of the solar cycle shown underneath (reproduced from Hathaway 2015).

These sunspots are caused by the footpoints of magnetic field loops inhibiting the convective motion below the Sun's surface, creating a cooler and darker spot. The loop geometry also means that a pair of sunspot groups have opposite polarity, as observed by Hale and Nicholson (1925). The authors also noticed that the 'leading' group in sunspot pairs has the same polarity as the surrounding solar hemisphere, with the polarity flipping at the start of a new solar cycle (Hale and Nicholson 1925). These features are known as Hale's polarity laws and are key clues to the

inner workings of the Sun's magnetic field. In addition, Fig. 2.5 shows that sunspots appear closer to the equator as the cycle progresses (Carrington 1858). Therefore, these sunspot properties act as a test for any model that wishes to explain the generation of the Sun's magnetic field, known as the solar dynamo.

Babcock (1961) proposed one such model, in which the magnetic field starts as a simple dipole at solar minimum, with open magnetic field lines at the poles extending out the interplanetary space, and closed field lines near the equator.

Differential motion of the Sun's surface means that the poloidal field becomes wound up over time, as a consequence of the frozen-in theorem. This introduces an azimuthal component to the magnetic field, known as the ω effect, which matches the orientation of sunspot groups from Hale's polarity laws (Hale et al. 1919).

To explain the reversal of the Sun's magnetic field axis, consider the magnetic loops that create sunspots at their footpoints. As the magnetic field loops rise from the photosphere, the Coriolis force twists the loop in such a way that it introduces a poloidal field with the opposite sense of rotation to the surrounding solar hemisphere (the α effect). Over time, many of these poloidal fields will erode the ordered magnetic field at solar minimum, and create the disordered magnetic field seen at solar maximum. Eventually, a dipole magnetic field will be restored after $\sim$11 years, but with opposite rotation to the starting magnetic configuration, represented by the migration of polarity to the poles in Fig. 2.5. This process then happens once more to complete the 22-year solar cycle for the magnetic structure.

While there are more modern theories for the solar dynamo (Charbonneau 2010), for the purposes of this thesis, it is only important to note that the field will remain stable for several months at solar minimum (Thomas and Smith 1981; Riley et al. 2002). Chapter 3 investigates how this magnetic structure extends out into the solar wind, using measurements from several spacecraft simultaneously.

2.2.2 Solar features

Similar to the occurrence of sunspots, the solar cycle drastically changes the type of solar features seen on the Sun. There is a wide range of solar phenomena that continues to grow with the improvement of telescope resolution. However, only the relevant structures are covered here, while a comprehensive review can be found in Solanki et al. (2006).

As mentioned in Section 2.2, the solar surface is covered in a pattern of granulation, where individual granules are around 1 Mm wide and have a lifetime of $8 \rightarrow 15$ minutes (Roudier and Muller 1986; Nordlund et al. 2009). The granules themselves appear bright in remote sensing images, as they represent the hot material that has been convected upwards, whereas, the inter-granular lanes correspond to the cooler material returning to below the surface. Observations also show a larger pattern of granulation, known as supergranulation, that appears in the horizontal plasma flow and has a typical size of $\sim$30 Mm, with a lifetime of around $\sim$1.8 days (Rast 2003; Rieutord and Rincon 2010). A similar cell network also exists for the magnetic field near the photosphere, which seems to be connected to the supergranulation pattern

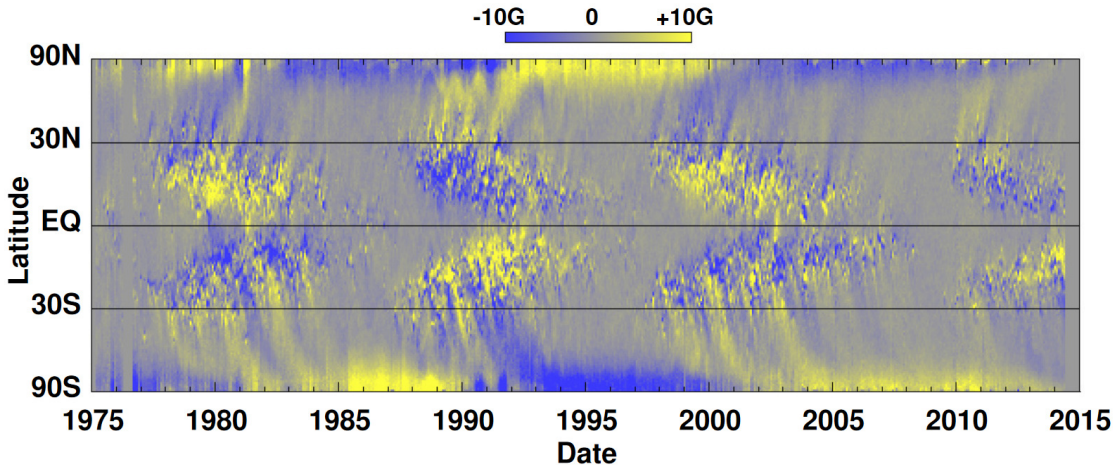


Figure 2.5: Line-of-sight magnetogram showing the radial magnetic field component on the Sun's surface over several solar cycles. Created by stacking slices of the magnetic field at the solar meridian. The colour scale indicates the strength and direction of the radial component, showing how the magnetic polarity flips every 11 years. The butterfly shape also demonstrates how sunspots are created closer to the equator as the solar cycle progresses (reproduced from Hathaway 2015).

(Leighton et al. 1962; Simon and Leighton 1964). This implies that the open magnetic field lines are grouped in the supergranular lanes, before expanding out to fill the available space above, as shown in Fig. 2.6.

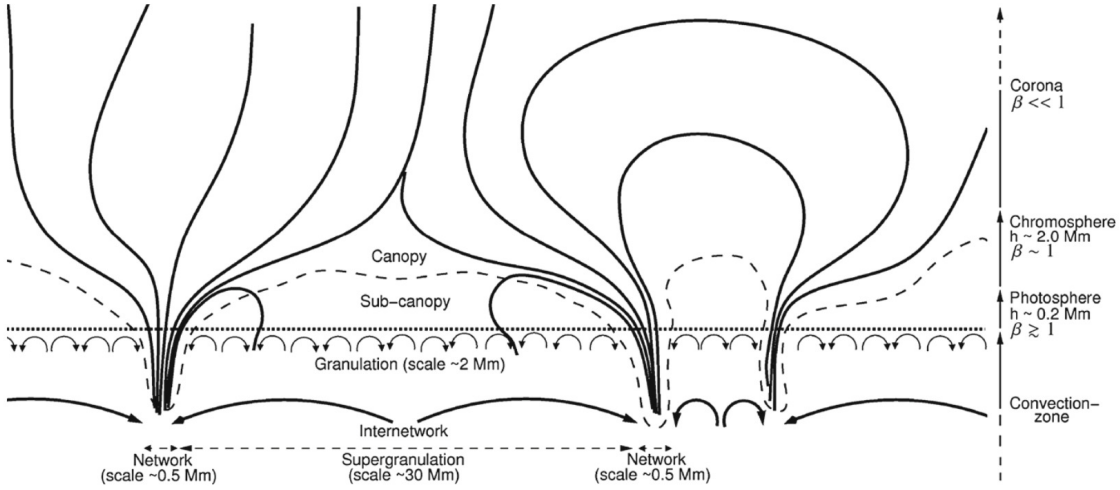


Figure 2.6: Sketch of the coronal magnetic field, showing that it is ordered into supergranules. The smaller granulation scale can be found on the solar surface (reproduced from Wiegelmann et al. 2014).

The Sun is also associated with many transient phenomena, such as coronal bright points (Dunn and Zirker 1973; Madjarska 2019). These appear all over the Sun's surface, with lifetimes ranging from 20 minutes to many hours (Alipour and Safari 2015). They are thought to represent small magnetic field loops connecting local areas of opposite magnetic polarity, and are often associated with convective motion at inter-granular lanes (Muller and Roudier 1992).

Bright points are often found at the base of coronal jets, which are bright collimated structures seen in extreme ultraviolet and x-ray images (Shibata et al. 1992; Raouafi et al. 2016). Such jets are typically $5{\times}10^3 \rightarrow 10^5$ km wide (Shimojo et al. 1996) and usually linked to small-scale reconnection events (Moore et al. 2010). Jets are observed to occur around 60 times per day (Savcheva et al. 2007), and can launch material into the corona (Raouafi et al. 2016). Some authors have suggested that jets can be used to explain the existence of certain structures in the solar wind (Neugebauer 2012). Finally, it has been proposed that the outflow from jets may be important for the heating and acceleration of the solar wind (Yu et al. 2014; Raouafi

et al. 2023b), as further explored in Section 2.4.4.

On a much larger scale, active regions are bright magnetic loops in the corona (see Fig. 2.3c), whose footpoints can appear as sunspots on the photosphere if the magnetic field is strong enough. Active regions are formed at mid-latitudes ($\pm 30°$ latitude) and, like the sunspots at their base, their occurrence is strongly tied to the solar cycle. The frozen-in flux theorem means that plasma on different magnetic loops cannot interact. Therefore, an equilibrium is established for each magnetic loop separately, with neighbouring magnetic loops having different temperatures, and hence brightness. This leads to a characteristic threaded structure in the active region, or indeed any coronal loop.

As their name suggests, active regions are associated with a wide range of solar activity (van Driel-Gesztelyi and Green 2015), such as coronal jets. On a larger scale, active regions are often the source of coronal mass ejections (CMEs), which are violent eruptions of plasma and magnetic field away from the Sun. These are rare during solar minimum, but become increasingly common at solar maximum, with around three per day (Webb and Howard 2012). CMEs typically contain cool, less dense material from deep within the corona, as well as having a twisted flux rope structure in the magnetic field. If directed at Earth, CMEs have the potential to cause damage to a range of technologies and power systems (Cannon 2013; Eastwood et al. 2017).

Another common feature found in the corona are coronal holes (see Cranmer 2009 for a review). These appear as large, dark regions in coronal images due to their lower temperature and density (see Fig. 2.3c). Such features are associated with open magnetic field lines only connected to the Sun at one end that extend out into the heliosphere (Wilcox 1968). During times of solar minimum, there will be a coronal hole at each of the magnetic poles, following the dipole-like magnetic field configuration. Coronal holes are stable structures which are often observed to persist for several solar rotations at solar minimum (Bohlin 1977). Equatorial coronal holes can also be found as the Sun moves towards solar maximum, but these

are typically smaller and have a shorter lifetime (Miralles et al. 2004).

When observed off limb, coronal holes appear to contain many ray-like structures, known as 'plumes' (Saito 1958; Poletto 2015). These structures are denser and cooler than their surroundings and can persist from hours to days (DeForest et al. 1997; DeForest et al. 2001). They can be seen up to $\sim 30\,R_{\odot}$ from the Sun's surface (DeForest et al. 1997), meaning they could be directly measured by Parker Solar Probe (see Section 2.6).

Observations of the coronal magnetic fields during an eclipse can also reveal the presence of large loops of closed magnetic field. These have an elongated 'stalk' that extends to many solar radii (Koutchmy and Livshits 1992), which has led to them being named helmet streamers. To separate the opposing magnetic polarities on each side of the helmet streamer, the heliospheric current sheet (HCS) is formed as a consequence of Ampère's law (see Section 2.4.6 for more detail). Since their footpoints are in opposite magnetic polarities, they often exist near the equator at solar minimum, which is often referred to as the streamer belt (Richardson and Paularena 1997). However, at solar maximum, these structures can appear at higher latitudes and are commonly associated with the transient release of plasma (Wang 2000; Rouillard et al. 2020). Pseudo-streamers are similar structures with a closed loop, but have footpoints of the same magnetic polarity (Wang et al. 2007), so are not associated with a current sheet.

2.3 The solar wind theory

2.3.1 Parker solar wind solution

The Sun is an extremely hot ball of plasma whose atmosphere cannot be held back by gravity. Therefore, the Sun emits the solar wind to balance with the surrounding low-pressure interstellar medium. Before the solar wind's existence was confirmed (Gringauz et al. 1960; Neugebauer and Snyder 1966), Parker (1958b) used a fluid model to show that a supersonic flow of solar wind could create a sufficiently low

pressure to balance with the interstellar medium, which is not possible with a hydrostatic solution.

Following Parker's original argument, in a time-stationary ($\frac{\partial}{\partial t} = 0$), spherically symmetrical fluid (only dependent on r) with no magnetic or electric fields ($\vec{J} \times \vec{B} = 0$), the continuity equation (2.19) becomes:

$$\nabla \cdot (\rho \vec{u}) = \frac{1}{r^2} \frac{d(r^2 \rho u)}{dr} = 0, \tag{2.27}$$

and the momentum conservation equation (2.20) is now:

$$\rho u \frac{du}{dr} = -\frac{dP}{dr} - \rho \frac{GM_\odot}{r^2}. \tag{2.28}$$

Assuming an isothermal gas, with temperature T, the ideal gas law becomes $P = 2nk_BT$ for an equal number density of electrons and ions (so $\rho \sim nm_i$). It follows that equation 2.28 can be re-written in a more useful form:

$$\frac{1}{u} \frac{du}{dr}(u^2 - c_s^2) = \frac{2}{r}(1 - \frac{r_c}{r}), \tag{2.29}$$

where the sound speed is:

$$c_s = \sqrt{\frac{2k_bT}{m_i}}, \tag{2.30}$$

and there exists a critical radius for which the right-hand side of the equation 2.3.1 vanishes:

$$r_c = \frac{GM_\odot m_i}{4k_bT}. \tag{2.31}$$

There are several classes of solution to this equation, as depicted in Fig. 2.7, which can be deduced by examining the behaviour of equation 2.29. The right-hand side of equation 2.29 changes sign as r passes through r_c, which can either be caused by a change in sign of:

- $\frac{du}{dr}$ at $r = r_c$ representing a minimum or maximum (solutions 2 and 3)

- $(u^2 - c_s^2)$ at $r = r_c$ so that the fluid is transonic[3] (solutions 1 and 4)

In the first scenario, there is a valid solution where the fluid speed increases up to a maximum at $r = r_c$, and then decreases so that $u \to 0$ for $r \to \infty$ (solution 3 in Fig. 2.7). This solution, known as the solar breeze, can be valid for other stars[4]. However, in the case of the Sun, this predicts a pressure at $r \to \infty$ that is too high to match with the interstellar medium.

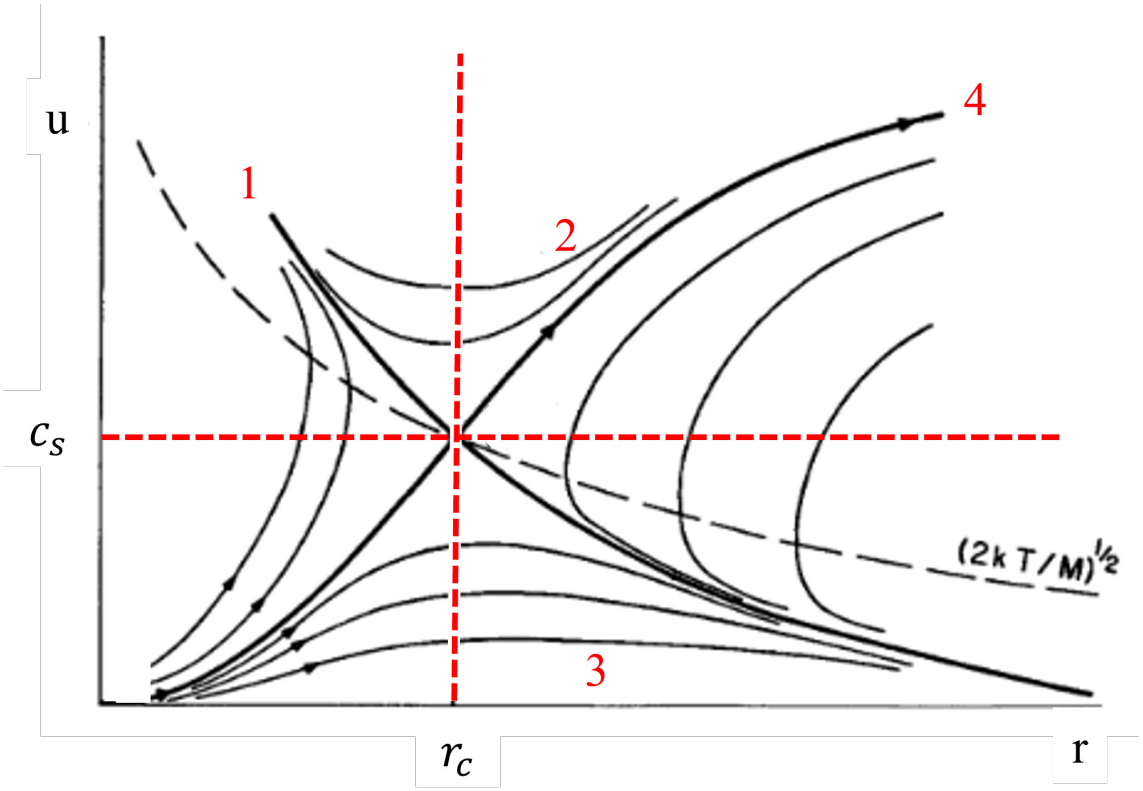


Figure 2.7: Different classes of solution to equation 2.29, where (4) is the solar wind solution. (1) is the other transonic solution, which is valid for accretion discs. The solar breeze solutions are in (3), which has maxima below c_s and there is another set of solutions with minima in (2) (adapted from Echim et al. 2010).

If instead the fluid is transonic, then there will be a solution with $\frac{du}{dr} > 0$ at all distances, leading to the fluid becoming supersonic at $r = r_c$. Unlike the solar breeze, this solution can create a sufficiently lower pressure as $r \to \infty$, and was used by Parker (1958b) to predict the existence of the solar wind.

In this last solution, the final speed of the wind is set by the temperature in the corona, and can generate solar wind speeds and mass flux of the correct order

[3]Has both subsonic and supersonic regions
[4]Either a cooler star or a higher pressure interstellar medium

of magnitude. However, this model, and other fluid models built upon it, struggle to explain the existence of faster solar wind speeds and high coronal temperatures (Parker 1965; Hansteen and Velli 2012). This is usually solved by the injection of energy from another source, such as from waves or magnetic reconnection (Fisk 2003; Cranmer et al. 2007; McComas et al. 2007).

Alternatively, there are other exospheric solar wind models that, unlike the fluid models, treat the protons and electrons separately. Doing so allows for an extra electric field to accelerate the wind, which can explain the slower solar wind speeds with no additional heating (Halekas et al. 2022). However, the energy source for faster solar wind still remains a mystery, as discussed further in Section 2.4.4.

2.3.2 Interplanetary magnetic field

Unlike the basic fluid model in the previous section, the solar wind has an interplanetary magnetic field that extends out from the complex magnetic structure in the corona (from Section 2.2.2). Since the solar wind can be described by ideal MHD, the frozen-in theorem causes the magnetic field to be dragged outwards by the radially expanding solar wind. This, coupled with the Sun's rotation, creates a spiral shape in the interplanetary magnetic field known as the 'Parker spiral' (Parker 1958b). Such a shape can be derived by considering two plasma parcels, released at different times, being connected by the same magnetic field line, giving the Parker spiral angle:

$$\tan(\phi_{ps}) = \frac{B_\phi}{B_R} = \frac{-r\Omega\cos(\Theta)}{V_{sw}}, \tag{2.32}$$

where r is the distance from the Sun, Ω is the solar rotation rate, Θ is the latitude and V_{sw} is the solar wind speed. For typical solar wind values at Earth ($V_{sw} = 400\,\mathrm{km/s}$, $r = 1\,\mathrm{AU}$, $\Omega = 14^\circ\,/\mathrm{day}$, $\Theta = 0^\circ$) the Parker spiral will be $\sim 45^\circ$, and almost 90° at Pluto's orbit ($\sim$40 AU). The typical Parker spiral shape for several solar wind speeds is shown in Fig. 2.8, and is measured directly by five separate spacecraft in Chapter 3.

Ensuring that the magnetic flux through a spherical surface is constant ($B_R \propto$

r^{-2}) gives a relationship for the magnetic field strength as a function of r:

$$|\vec{B}| = B_0 \left(\frac{r_0}{r}\right)^2 \sqrt{1 + \left(\frac{r\Omega \cos(\Theta)}{V_{sw}}\right)^2}. \tag{2.33}$$

The radial expansion of the solar wind also means that the density is expected to scale as:

$$n \propto \frac{1}{r^2}, \tag{2.34}$$

using a mass conservation argument. The scaling of these parameters will become clear when comparing solar wind measurements from 1 AU, $|\vec{B}| \sim 10\,\mathrm{nT}$ and $n \sim 5\,\mathrm{cm}^{-3}$, to those made much closer to the Sun, $|\vec{B}| \sim 1000\,\mathrm{nT}$ and $n \sim 600\,\mathrm{cm}^{-3}$ at $\sim 20\,R_\odot$ (Parker Solar Probe in Section 2.6.2).

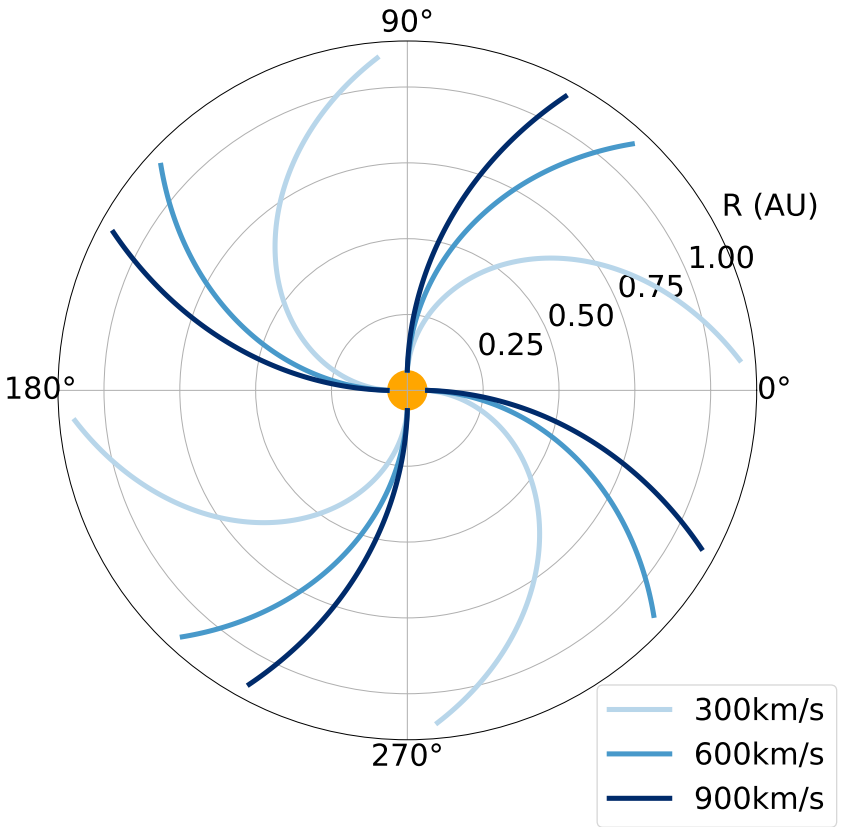


Figure 2.8: Demonstration of the theoretical Parker spiral shape for three different solar wind speeds in a top down view of the ecliptic plane ($\Theta = 0°$).

2.4 Solar wind observations

The solar wind has been measured by many spacecraft since the confirmation of its existence in the 1960s (Gringauz et al. 1960; Neugebauer and Snyder 1966). This section summarises the history of in situ solar wind measurements: from ∼0.3 AU with the twin Helios spacecraft (Kutzer 1977); above the poles with the Ulysses mission (McComas et al. 1998); and with the consistent observations from 1 AU with Wind (Ogilvie and Desch 1997). The basic solar wind properties and features are outlined, as well the many unanswered questions that provided the motivation for the new missions of Parker Solar Probe (Fox et al. 2016) and Solar Orbiter (Müller et al. 2013). The background and literature on a particular solar wind phenomenon known as 'switchbacks' are not covered until Chapter 4, as these are the direct focus of Chapters 4 and 5.

Historically, the solar wind has been viewed as having a two-part structure, with a steady 'fast solar wind' (>600 km/s) and a denser, more variable 'slow solar wind' (<400 km/s Schwenn 1983). The Ulysses spacecraft best demonstrated this dichotomy when orbiting above the solar poles at solar minimum, as can be seen in Fig. 2.9. Fast solar wind was observed to emanate from the poles, with the slower wind coming from low latitudes around the streamer belt. This matches the simple dipole-like structure of the Sun at solar minimum, where the magnetic field points away (red) or towards (blue) the Sun, termed the 'magnetic polarity'. The distinction of magnetic polarity is crucial when investigating the structure of the solar wind in Chapter 3, and this same colour scheme is used throughout the thesis. When Ulysses returned above the poles at solar maximum, a more disordered picture was seen (right of Fig. 2.9), where slow and fast wind could exist at any latitude with no clear hemispheres of magnetic polarity.

This basic idea of the solar wind structure is useful for visualisation purposes, but is now seen as a flawed way to classify the solar wind (Zhao et al. 2009; Stansby et al. 2019a). However, before a more detailed description of the large-scale structure in the solar wind, there first needs to be a discussion of the typical kinetic features.

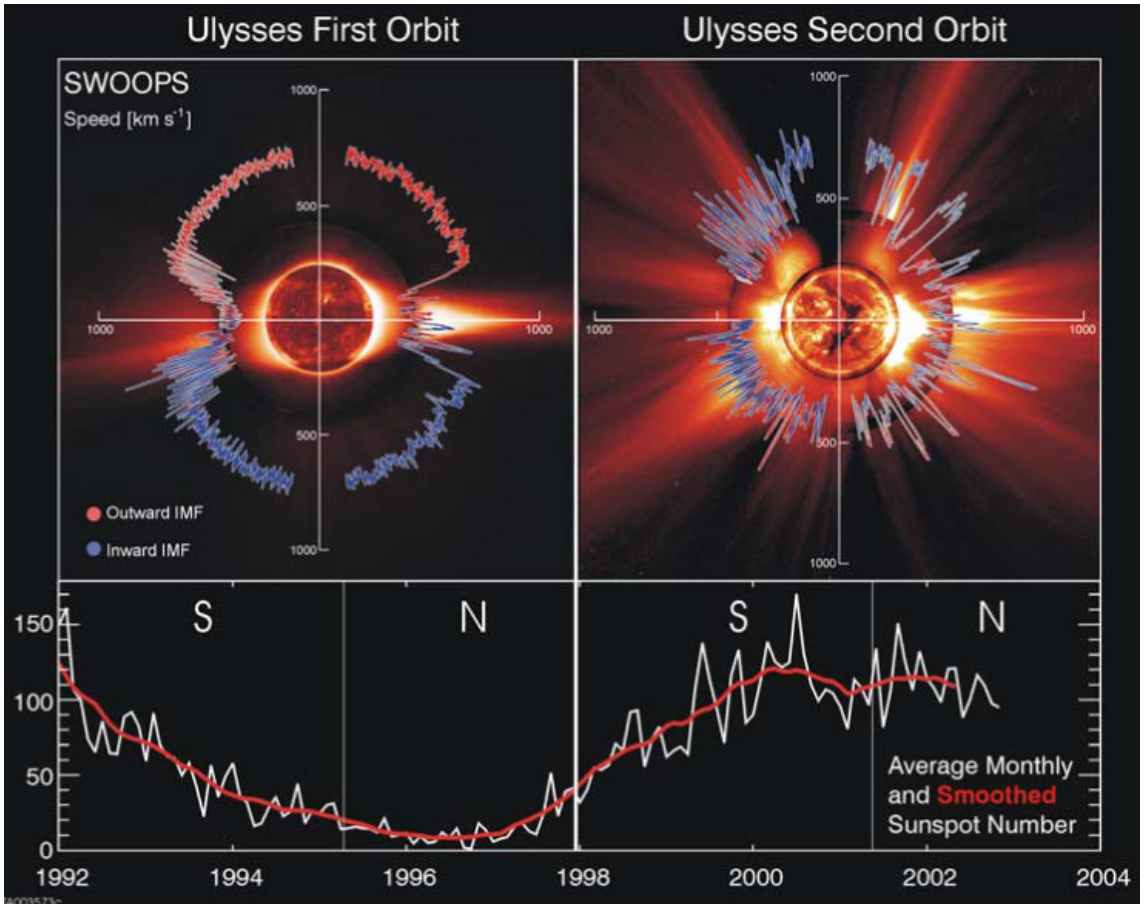


Figure 2.9: Ulysses' measurements of the solar wind structure in latitude at solar minimum (left) and maximum (right), as marked by the sunspot number in the lower panel. The Sun has a clear structure at solar minimum, with two distinct hemispheres and fast solar wind at high latitudes. In contrast, fast solar wind and either magnetic polarity can be found at any latitude at solar maximum (reproduced from McComas et al. 2003).

2.4.1 Velocity distribution functions

The solar wind mostly consists of protons and electrons travelling away from the Sun at a range of velocities, which are measured as a velocity distribution function (VDF) by a spacecraft in the solar wind. While the exact instrumentation is described in Section 2.5, an example of a proton VDF is shown in Fig. 2.10. The proton core is the largest population (centred on the origin), whose speed is commonly quoted as the speed of the solar wind. The proton beam is a smaller, faster population of protons that sits ahead of the core along the local magnetic field direction (dotted black line, Marsch 2012). This is usually around v_A faster than the proton core, which suggests a preferential acceleration of the proton beam along the magnetic

field. However, the cause of this observation, and the presence of the beam itself, are still open problems in the solar wind (Verscharen et al. 2019).

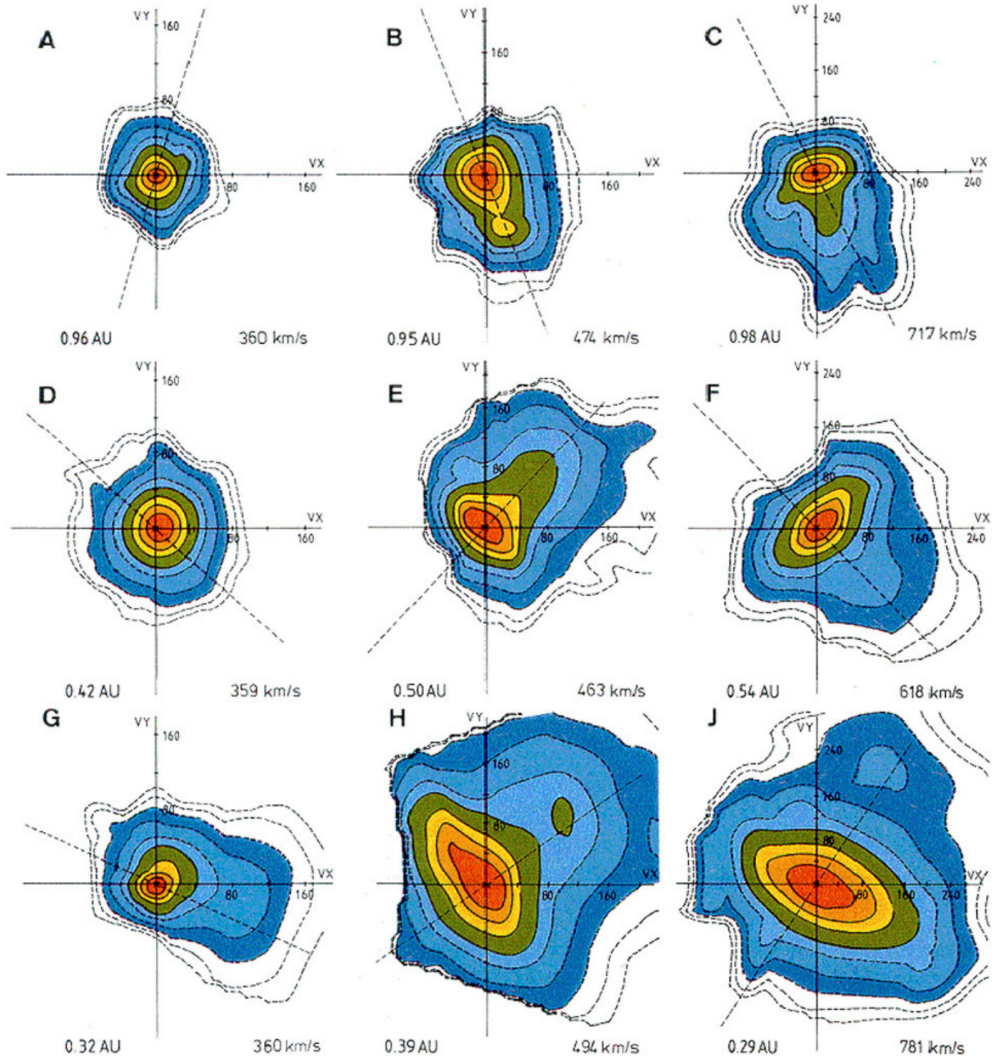


Figure 2.10: Example proton VDFs in the solar wind from the Helios mission. The proton core is the main population in red, with a secondary proton beam travelling faster along the magnetic field direction (dotted black line). Several panels show that the proton core is wider perpendicular to the magnetic field, so $T_\perp > T_\parallel$ (reproduced from Marsch 2012).

Similar to the proton beam, the alpha particle (He^{2+}) population is typically observed to drift ahead of the proton core by the local Alfvén speed (Yamauchi et al. 2004). Alpha particles make up around 5% of the solar wind by number density, although this abundance can vary over the solar cycle, as well as depending on the solar wind type (Kasper et al. 2007; Kasper et al. 2012).

The solar wind also has several minor ion populations (heavier than ^4He). These

trace ions do not contribute much to the dynamics of the solar wind, but can be used as a tracer of solar wind source region and acceleration processes. For example, charge state ratios, such as O^{7+}/O^{6+}, can be used to probe the temperature of the solar wind in the corona (Hundhausen et al. 1968). The charge states are set by collisions with electrons in the corona, which are then 'frozen in' to the plasma as the solar wind becomes collisionless (Owocki et al. 1983).

The lack of particle collisions also means that solar wind VDFs can exhibit some non-thermal features that deviate from the typical Maxwellian distribution. As well as the proton beam, the most relevant signature is the proton core 'temperature anisotropy', $T_\perp/T_\parallel$, which is typically > 1 in the solar wind close to the Sun ($<$1 AU, Marsch et al. 1982b). This, as seen in Fig. 2.10, makes the proton core appear elongated perpendicular to the magnetic field, suggesting that the proton core is preferentially heated in this direction. Such an effect is a prevalent feature of the solar wind and therefore must be explained by any proposed heating mechanism.

To describe the shape of solar wind VDFs, and derive macroscopic parameters, a bi-Maxwellian distribution is often used, motivated by the observed temperature anisotropy. This distribution is described by:

$$f_{Bimax}(v_\perp, v_\parallel) = \left(\frac{m}{2\pi k_B}\right)^{\frac{3}{2}} \frac{n}{T_\parallel^{\frac{1}{2}} T_\perp} \exp\left(-\frac{m}{2k_B}\left(\frac{(v_\perp - u_\perp)^2}{T_\perp} + \frac{(v_\parallel - u_\parallel)^2}{T_\parallel}\right)\right), \tag{2.35}$$

where the proton core has temperatures of $T_\perp$ and $T_\parallel$, and is centred on $\vec{u}$ (Baumjohann and Treumann 2022). Fitting such a distribution to a measured VDF can extract these bulk parameters, as outlined in the description of solar wind instrumentation in Section 2.5.

The electron VDFs also exhibit a number of non-thermal features, which are usually split into three components: core, halo and strahl as demonstrated in Fig. 2.11 (Feldman et al. 1975; Rosenbauer et al. 1977; Pilipp et al. 1987). The core is a Maxwellian distribution that contains ∼95% of the electrons, and is surrounded by the supra-thermal halo ($>$70 eV, Verscharen et al. 2019). In contrast, the strahl is

a focused population of electrons that travel anti-Sunward along the local magnetic field direction. Therefore, the direction of the electron strahl propagation with respect to the magnetic field can be used as a diagnostic tool for the magnetic topology in the solar wind (Owens et al. 2013). For example, the electron strahl will be focussed parallel to the magnetic field with an away polarity, and antiparallel to the magnetic field with a towards polarity. This behaviour can be used to confirm a change in magnetic polarity at a sector boundary, as done in Chapter 3.

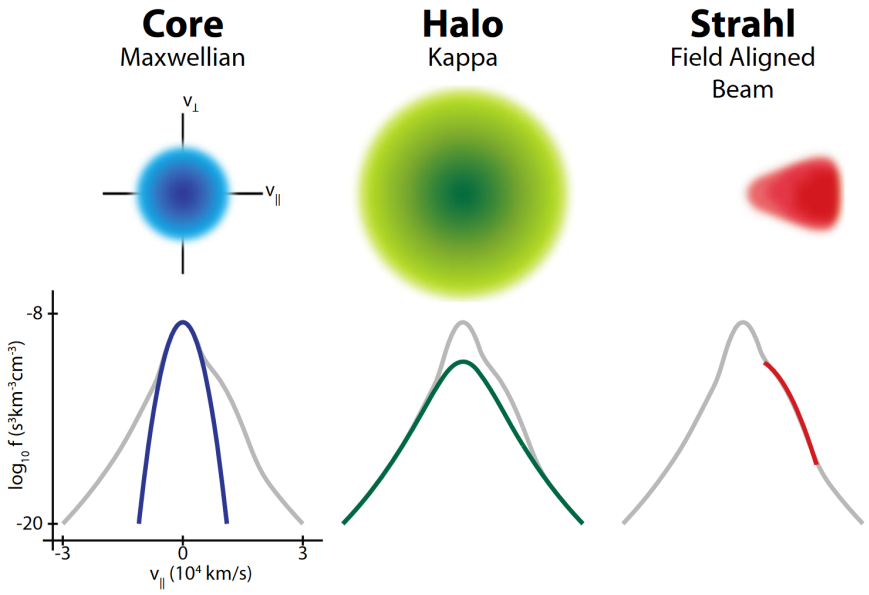


Figure 2.11: Diagram showing the velocity distribution functions of the different electron populations usually found in the solar wind (reproduced from Salem et al. 2021).

2.4.2 Alfvén waves in the solar wind

Alfvén waves are a common feature in the solar wind, that lead to large-amplitude fluctuations in both the velocity and magnetic field (Belcher and Davis Jr. 1971; Smith et al. 1995). As described earlier (Section 2.1.2), the incompressible nature of these fluctuations means that the ends of the magnetic and velocity vectors lie on the surface of a sphere.

It is well observed that these fluctuations will create one-sided increases in the solar wind speed when the magnetic field is deflected away from the background di-

rection (Matteini et al. 2014; Gosling et al. 2009). In velocity space, this corresponds to a rigid rotation of the protons about the wave frame velocity, which acts as a pivot (Matteini et al. 2015). The same principles apply to any particle population in the solar wind, although this can be in the opposite sense to the proton core if the drift speed is higher than the pivot velocity (Neugebauer and Goldstein 2013; McManus et al. 2022), as depicted in Fig. 2.12.

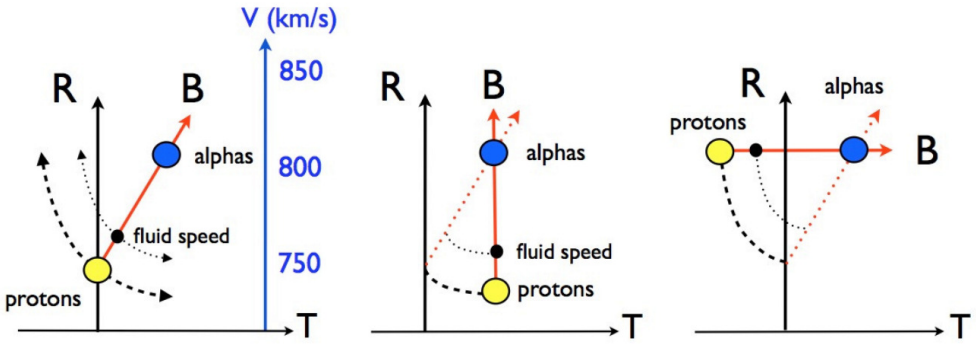


Figure 2.12: Diagram showing how particle VDFs are rotated by Alfvénic fluctuations in the solar wind. The middle panel shows a case where the magnetic field (red arrow) is radial, with alpha particles (blue) travelling at a local wave speed above the protons (yellow). In this example, the alphas sit at the pivot point, so do not change their speed (blue y-axis on the left panel). However, as the magnetic field moves away from radial, the protons are rotated above the pivot point leading to an increase in speed (reproduced from Matteini et al. 2015).

Since the alpha particles typically drift ahead of the proton core by $\sim v_A$, they will sit at the pivot velocity and thus not rotate with the fluctuations (Marsch et al. 1982a; Matteini et al. 2014). In the wave frame, the electric field created by the fluctuations will vanish, making this frame equivalent to the deHoffman-Teller frame, first introduced for analysis of MHD shocks (De Hoffmann and Teller 1950). This can be found in the solar wind by minimising the motional electric field ($\vec{E} = -\vec{u} \times \vec{B}$) over a period of time (Khrabrov and Sonnerup 1998).

For sufficiently large fluctuations, the radial magnetic field component will reverse in a switchback, as first observed by Helios (Horbury et al. 2018) and Ulysses (Balogh et al. 1999; Yamauchi et al. 2004; Neugebauer and Goldstein 2013). More recently, these structures have become an active area of research due to their dominance of the first Parker Solar Probe data (Bale et al. 2019; Kasper et al. 2019).

Since these structures are the subject of Chapters 4 and 5, a dedicated review is provided in Section 4.1.

2.4.3 Types of solar wind

It is well established that the fast solar wind originates from large coronal holes (Krieger et al. 1973; Nolte et al. 1976), whose stable structure is reflected in the steady outflow of solar wind. Besides the increased speed, fast solar wind is often characterised by an increased number of Alfvénic fluctuations (Belcher and Davis Jr. 1971; Tu and Marsch 1995) and by a low density compared with the slow solar wind. A lower rate of collisions also means that the fast wind exhibits more extreme non-thermal features, such as a high temperature anisotropy ($T_\perp/T_\parallel \sim 3$) and a significant proton beam (Marsch et al. 1982b; Schwenn and Marsch 1990).

Charge state ratios (such as $^{7+}\mathrm{O}/^{6+}\mathrm{O}$) are found to be anti-correlated with the solar wind speed (Geiss et al. 1995), suggesting that the fast solar wind originates from a lower electron temperature, and thus a lower height in the solar atmosphere (von Steiger et al. 1995). This agrees with the fact that the minor ion abundances in the fast wind match those found in the photosphere (Bochsler 2000; Gloeckler and Geiss 2007). Finally, there is also a well known anti-correlation between the speed of the fast wind and the magnetic expansion factor (Wang and Sheeley 1990).

In contrast, the slow solar wind is typically characterised by being much more variable and dense than the fast solar wind. This type of wind has long been associated with the streamer belt at low latitudes (see Fig. 2.9), and surrounds the HCS (Gosling et al. 1981; Richardson and Paularena 1997).

However, it is becoming clear that solar wind speed alone should not be used to classify the solar wind (Zhao et al. 2009). This is because there is a continuous distribution of proton speed in the solar wind, meaning there is no clear way to split the solar wind on the basis of speed. Furthermore, the speed and density of the solar wind can be altered during propagation. Instead, there are increasing efforts to classify the solar wind by its source region on the Sun. This can either be achieved

through back mapping the solar wind to a location on the Sun (Nolte et al. 1976; D'Amicis and Bruno 2015; Bale et al. 2019), or by using ion composition to infer a source region type (Zhao et al. 2009; Geiss et al. 1995).

Recently, it was found that the slow solar wind could be split into two separate populations: Alfvénic and non-Alfvénic slow solar wind (D'Amicis and Bruno 2015; Stansby et al. 2019a). The slow Alvénic wind shares many properties with the fast solar wind, such as high Alfvénicity and low charge state ratios, which suggests that it may be released from the Sun via the same mechanism (D'Amicis et al. 2018; Stansby et al. 2020a). This type of solar wind is found to originate from the edges of coronal holes (D'Amicis et al. 2021), where the increased magnetic expansion would explain the slower solar wind speed (Wang and Sheeley 1990).

Therefore, the non-Alfvénic wind would then correspond to what was traditionally known as the slow solar wind, whose origin is currently debated (see Abbo et al. 2016 for a comprehensive review). Many theories are based on observations that charge state ratios for the slow solar wind match the temperature of closed magnetic field loops on the Sun (von Steiger et al. 1995). The concept of 'interchange reconnection' between closed and open field lines on the photosphere (Fisk and Schwadron 2001; Fisk 2003) is often invoked as a way to release plasma from closed field lines into the solar wind (Titov et al. 2011; Antiochos et al. 2011).

There have also been suggestions that magnetic reconnection at the tips of helmet streamers could release the plasma 'blobs' that have been observed both in remote sensing data (Wang et al. 1998; Rouillard et al. 2010) and in situ (Viall et al. 2008; Viall and Vourlidas 2015; Sanchez-Diaz et al. 2019). These are often associated with flux rope like structures, which supports the idea that this type of magnetic reconnection is occurring (Réville et al. 2020). However, it has subsequently been shown that this mechanism can only account for ∼15% of the slow solar wind mass flux (Sanchez-Diaz et al. 2017).

Finally, active regions have also been put forward as a source for the slow solar wind (Neugebauer et al. 2002; Fu et al. 2017), whose contribution to the solar wind

may vary from ∼0% at solar minimum to ∼60% at solar maximum (Stansby et al. 2021).

2.4.4 Heating and acceleration

The basic solar wind theory, as first outlined by Parker (1958b) and summarised in Section 2.3, cannot reproduce the magnitude of the fast solar wind speeds or the observed proton temperatures near Earth (Durney 1972; Parker 1965). This, in combination with the fact that the corona is also observed to be several MK hotter than the chromosphere (Grotian 1939; Edlén 1943; Dunbar 2012), suggests there that is an additional heating mechanism, which remains a major open question in solar and heliophysics (McComas et al. 2007; Fox et al. 2016). The convective motion of the photosphere has long been regarded as a sufficient energy reserve for this heating (Klimchuk 2006), but it is not known how this energy is transported into the corona and solar wind.

Low-frequency MHD waves driven by the photospheric motion could heat the plasma, but due to the large gradients in density and temperature, neither the slow nor the fast MHD modes can reach the corona (McComas et al. 2007; Rosenthal et al. 2002; Parnell and De Moortel 2012). Alfvén waves do not have this problem, with their incompressible nature meaning they can travel large distances and carry energy into the corona. These waves are commonly observed in the solar atmosphere (Tomczyk et al. 2007), making them a strong candidate for coronal heating. However, these Alfvén waves cannot easily deposit energy into the plasma. To solve this problem, several non-linear effects have been proposed, such as phase mixing (Heyvaerts and Priest 1982) and resonant absorption (Ionson 1978). There are also suggestions that Alfvén waves in the corona could steepen into shocks or drive compressive fluctuations (Suzuki and Inutsuka 2005), which should be a measurable signal with Parker Solar Probe.

The non-thermal features of the solar wind can provide valuable information regarding the heating that occurs closer to the Sun. Therefore, any heating mechanism

should be able to reproduce the proton beam and large temperature anisotropies of the proton core, discussed in Section 2.4.1. Additional observations show that minor ions are preferentially heated close to the Sun ($<4\,R_\odot$ Kohl et al. 1998; Tracy et al. 2016; Kasper et al. 2017). Both of these effects can be explained by ion-cyclotron resonance, where left-handed waves are in resonance with the ion gyro-motion (Narita 2017). Several authors have proposed that high-frequency waves generated via magnetic reconnection in the chromosphere could be responsible for this type of heating (Axford and McKenzie 1992; Isenberg 2001; Isenberg 2004). However, the heating in this scenario would be confined to a region below the solar corona, whereas $T_\perp$ is observed to cool less rapidly than expected in the solar wind all the way to 1 AU (Hellinger et al. 2011; Perrone et al. 2019). Instead, lower frequency Alfvén waves may survive into the corona, where they would become resonant as the ion cyclotron frequency decreases with distance from the Sun (Tu and Marsch 2001; Hollweg 2008).

Another popular theory is that non-linear interactions of counter-propagating Alfvén waves (Coleman 1968; Velli 1993) could drive a turbulent cascade of energy to smaller scales, where the heat is then dissipated to the plasma (Matthaeus et al. 1999; Verdini and Velli 2007; Cranmer et al. 2007). Such Alfvénic turbulence is observed throughout the solar wind (see Bruno and Carbone 2013 for a review), and models based on this process can successfully reproduce fast solar wind streams (Cranmer 2010; Verdini et al. 2010). However, it is unclear whether the same mechanism can provide sufficient heating in the corona (Roberts 2010).

An alternative view is that magnetic reconnection between a network of open and closed field lines on the Sun's surface could provide the necessary heating for the corona and solar wind (Parnell and De Moortel 2012). Following observations of x-ray spikes (Lin et al. 1984), Parker (1988) suggested that small-scale 'nano-flares' could heat the corona, although estimates at the time could not match the heating observed in the corona. However, as seen in Section 2.2.2, reconnection events exist on a wide range of scales on the solar surface. These could either directly heat the

plasma via the reconnection exhausts, or launch waves into the corona that would dissipate the heat. There is mounting evidence that jet-like features could supply significant mass and energy to the solar wind (McIntosh et al. 2011; Tian et al. 2014; Raouafi et al. 2023b). Such jets have been observed to reach several solar radii in remote sensing observations (Wang et al. 1998), and have potentially been seen in the solar wind (Wang et al. 2006; Neugebauer 2012). Finally, interchange reconnection (Fisk et al. 1999; Fisk 2003) can allow for the release of energy built up in small-scale coronal loops that make up the Sun's magnetic carpet (Priest 1998; Parnell 2001). The acceleration of the solar wind would then depend on the mass flux and energy released at the base of the corona.

The source of heating and acceleration remains a highly debated topic. While many of the proposed heating mechanisms likely exist in the corona and solar wind, the individual contributions from each mechanism still need to be quantified. The key evidence will likely come from linking consistent heating signatures and structures in the solar wind to a source on the Sun. This provided the motivation to launch both Parker Solar Probe and Solar Orbiter, which aim to make the connection between the Sun and the solar wind (see Section 2.6).

2.4.5 T-V relationship

Observations in the solar wind have long shown a positive correlation between the proton temperature and speed, known as the T-V relationship, which could help understand how the solar wind is heated. When averaged over long time periods (several hours), it has been observed that the proton core temperature increases with the solar wind speed (Neugebauer and Snyder 1966; Burlaga and Ogilvie 1970). Early attempts to find an empirical relationship saw many different functional forms (quadratic, cubic, power law, linear) applied to the data, with no clear consensus (Lopez et al. 1986; Neugebauer et al. 2003). Elliott et al. (2012) provided a comprehensive investigation into the T-V relationship over several years, showing that a linear fit was a good match to the data, after removing the effect of interplanetary

CMEs (see Section 2.4.6). They also found that the T-V relationship varied with distance from the Sun, as interactions between different solar wind speeds led to compressions and rarefactions.

Matthaeus et al. (2006) attempted to explain the existence of the T-V relationship with a single fluid model. Under the assumption that speed did not vary with distance from the Sun, they showed that the solution to the MHD energy equation would only vary with the 'convective age' of the plasma parcel (r/V).

Another explanation was provided by Démoulin (2009) who, unlike Matthaeus et al. (2006), considered the acceleration of the solar wind (i.e. did not assume constant speed). They found that the T-V relationship was created by the acceleration of the solar wind closer to the Sun, where faster wind would be both heated and accelerated more, leading to an increase in both speed and temperature together (Démoulin 2009). Using an example heat flux, they derived a relationship that matched the observations well, although they did note that the T-V relationship would still hold for any heating mechanism close to the Sun. Finally, the lack of T-V relationship inside CMEs was used as evidence for the solar wind being heated by some other mechanism.

With the Helios spacecraft, both Horbury et al. (2018) and Perrone et al. (2019) showed that the T-V relationship held within a single stream, as well-being valid for large aggregations of data that had been used up until then. Perrone et al. (2019) also separated the proton temperature into its perpendicular and parallel components, with $T_\perp$ having a steeper gradient than $T_\parallel$.

It was also shown that the T-V relationship flattened as the distance from the Sun increased. Similarly to Matthaeus et al. (2006), Perrone et al. (2019) argued that slower wind would have more time to interact with any heating mechanism as it travelled to the same distance from the Sun. Therefore, when PSP is closer to the Sun, there should be a more pronounced T-V relationship, as investigated in Chapter 5.

2.4.6 Large-scale structures

As well as having signatures of heating, the solar wind also has several large scale features that can reveal information about the dynamics as the solar wind expands out into the heliosphere. The heliospheric current sheet (HCS) was briefly mentioned earlier as the boundary between the two opposite magnetic polarities of the interplanetary magnetic field.



Figure 2.13: Theoretical shape of the heliospheric current sheet in the heliosphere. The orbits of the planets are shown, with the Sun in the centre. The ripples in this current sheet are often described as a 'ballerina skirt', and are due to the Sun's rotation axis not being aligned to the magnetic axis (credit Heil 1980).

Early spacecraft measurements reported that the observed magnetic polarity in the ecliptic plane[5] would flip several times per solar rotation (Wilcox 1968), with a single polarity measured at higher latitudes (Rosenberg and Coleman 1969). This 'sector structure' of the solar wind eventually lead to the idea of a warped HCS, as depicted in Fig. 2.13. The change in polarity of the magnetic field at the equator means there is a current perpendicular to the Parker spiral shaped magnetic field.

[5]The plane in which the Earth orbits

This leads to a hyperbolic spiral shape for the current, which starts with a large azimuthal component and becomes nearly radial far from the Sun.

Due to the Sun's magnetic dipole axis not being aligned with the rotation axis, the HCS is warped and has been likened to a 'ballerina skirt' (Alfvén 1977). Therefore, even for a perfect dipole configuration, giving a flat HCS, a spacecraft would still measure a clear sector structure in the ecliptic plane.

At solar minimum, the HCS is confined to within $\pm 15°$ of the solar equator, which can increase to $\sim 90°$ as the Sun's magnetic field becomes more complex towards solar maximum (Hoeksema et al. 1983). The local inclination of the current sheet has been shown to be a good match to coronal models (Burton et al. 1994), and is something that is also investigated in Chapter 3.

Being the largest structure in the heliosphere, many solar wind properties can be organised by their distance from the HCS. In general, the density increases close to the HCS, while the speed and temperature decrease (Borrini et al. 1981; Gosling et al. 1981; Suess et al. 1993). The width of the current sheet is $\sim$10,000 km at 1 AU (Winterhalter et al. 1994; Liou and Wu 2021), which can take several hours to traverse with a spacecraft.

On crossing the HCS, the source region for the solar wind flips into the other magnetic hemisphere. Therefore, knowledge of the shape and location of the HCS is extremely important. For example, if a fast solar wind stream is detected far from the current sheet, then it almost certainly came from a polar coronal hole that can be located in coronal images.

Therefore, modelling the location of the HCS is important for both predicting the solar wind conditions at Earth, and finding the source region. This can be achieved by using white light images above the solar limb to track the position of the streamer belt, and in turn the HCS, as the Sun rotates (Rouillard et al. 2020). Alternatively, several numerical models are also used, with the most common being the Potential Field Source Surface (PFSS) model, which is described in Chapter 3.

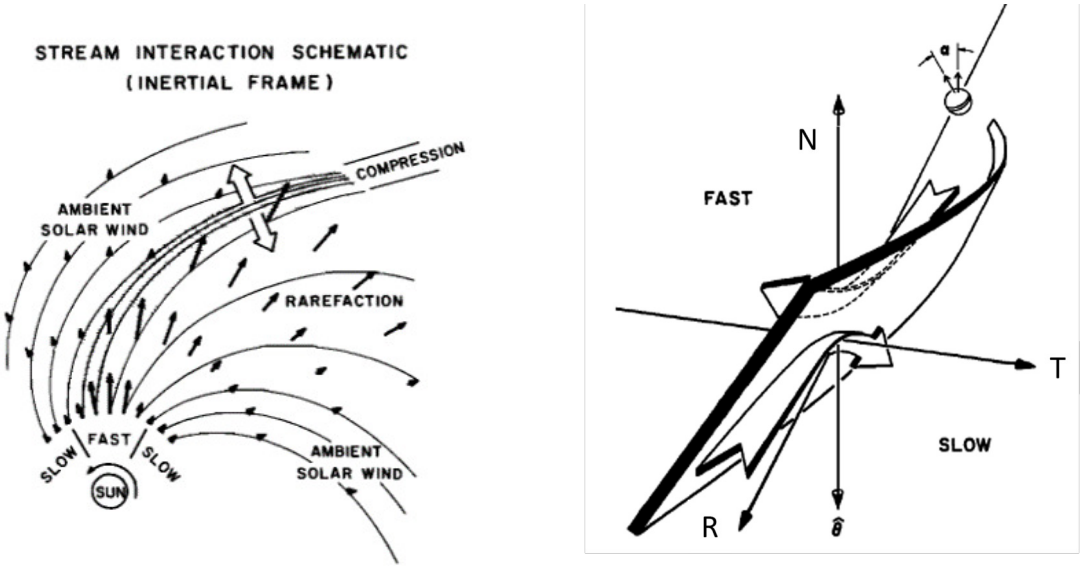
Since the HCS is usually limited to low latitudes, and is surrounded by slow

solar wind from the streamer belt, it can be described by a simple 'tilted dipole model' with a band of slow solar wind at the equator and fast wind elsewhere (Pizzo 1994a). As a result of the Sun's tilted rotation axis, or coronal structure, fast solar wind streams can co-exist with slower solar wind at the same latitude. As the solar wind expands into the heliosphere, the faster solar wind catches up with the slower stream ahead, leading to the formation of a stream interaction region (SIR). This can be described as a co-rotating interaction region (CIR) if the sources of the fast and slow solar wind are stable for successive solar rotations (Richardson 2018).

A compression region is formed at the stream interface, and a rarefaction region towards the trailing edge of the fast stream, as demonstrated in Fig. 2.14a. The compression region has enhanced proton density, $|\vec{B}|$ and temperature (Belcher and Davis Jr. 1971; Gosling et al. 1972), and develops into a forward shock farther from the Sun (usually $>$1 AU, Jian et al. 2006). Equally, the rarefaction region will steepen into a reverse shock, leading to a pair of shocks commonly being observed far from the Sun (Smith and Wolfe 1976; Hundhausen and Gosling 1976).

Due to the curved shape of the stream interface, CIRs exhibit a characteristic east-west deflection of the slow and fast wind, respectively (Siscoe et al. 1969). The tilt of the stream interface will also introduce a meridional flow deflection, as demonstrated in Fig. 2.14b, for a frame moving with the stream interface. In this example, the slow wind moves towards the interface where it is deflected down and right in the stream interface frame, whereas the faster wind is deflected in the opposite direction. The exact nature of this deflection is dependent on the tilt of the stream interface (Siscoe and Finley 1969).

The CIR orientation also has an effect on the forward and reverse shock propagations. In the standard diagram of the solar wind at solar minimum, pictured in Fig. 2.15, CIRs are formed whenever there is a significant warp in the HCS that brings the fast wind at higher latitudes into the same plane as the slow wind surrounding the HCS (Richardson and Paularena 1997; Richardson and Paularena 1997). Therefore, the tilt of the CIRs will follow that of the HCS warp, meaning that forward



(a) (b)

Figure 2.14: (a) shows a diagram of CIR formation in the ecliptic plane, which leads to a signature east-west deflection of the slow and fast wind, respectively. There will also be meridional flow deflections, as demonstrated in (b), that depend on the tilt of the CIR (adapted from Pizzo 1978 and Pizzo 1991).

shocks will be directed towards the equator and reverse shocks towards more extreme latitudes. Such a theoretical understanding has been confirmed by Ulysses, which exclusively observed reverse shocks from CIRs at latitudes $\geq 30°$ (Gosling et al. 1993; Gosling et al. 1993).

Since the HCS is embedded within the slow solar wind, it will eventually be enveloped by the CIR, significantly distorting its shape far from the Sun (Pizzo 1994b). Planar magnetic structures (PMSs, Nakagawa et al. 1989; Nakagawa et al. 1989) can be formed as a result of this compression, where magnetic field vectors are forced to lie in the same plane as the stream interface (Broiles et al. 2012; Broiles et al. 2012).

The compression regions of CIRs are known to drive space weather effects at Earth, which is a particularly common cause at solar minimum (Richardson et al. 2001). Therefore, it is important to be able to predict the occurrence of CIRs to warn of any potential disruption (Odstrcil 2003; Sunny et al. 2023).

However, the most important source of space weather effects are the in situ manifestations of CMEs, known as interplanetary CMEs (ICMEs, Kilpua et al.

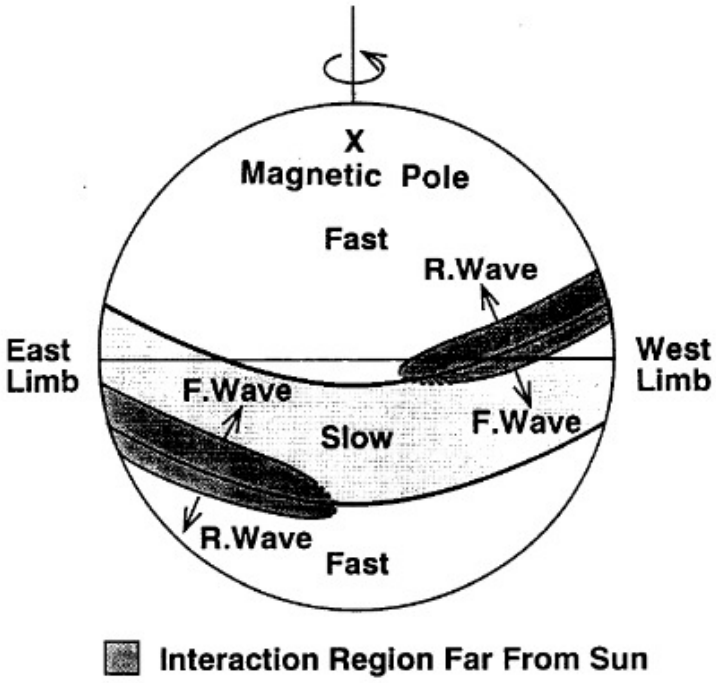


Figure 2.15: Diagram of the typical solar wind structure at solar minimum, with slow solar wind surrounding the HCS at low latitudes, and faster wind at higher latitudes. If there is a warp in the HCS, then CIRs can be formed, creating a forward wave towards the equator and a reverse wave away from the equator (reproduced from Gosling et al. 1993).

2017). As discussed earlier (Section 2.2.2) these are large eruptions of plasma which commonly have a flux rope structure to the magnetic field. When viewed by a spacecraft in situ, the flux rope is seen as a smooth rotation of the magnetic field with significantly enhanced $|\vec{B}|$ (Zurbuchen and Richardson 2006). It is also common to see bidirectional electron strahl signatures inside ICME flux ropes, indicating that the magnetic field is connected to the Sun at both ends.

These large eruptions of plasma are commonly launched at low latitudes, so are often associated with the HCS (Hundhausen 1993; Hundhausen 1993). When released from a helmet streamer, the 'legs' of the flux rope magnetic field have different magnetic polarity which, when observed in situ, can carry the change in polarity seen at the sector boundary (Crooker et al. 1998; Crooker et al. 1998). Therefore, this subset of CMEs, also referred to as streamer blowout CMEs (Nieves-Chinchilla et al. 2020; Nieves-Chinchilla et al. 2020), are thought to 'propagate as an occlusion' inside the HCS (Crooker and Intriligator 1996; Crooker and Intriligator

1996), rather than pushing the HCS aside (Forsyth et al. 1997; Forsyth et al. 1997). These ideas are used in Chapter 3 to uncover the magnetic topology of an ICME during a HCS crossing.

2.5 Instrumentation

While the previous sections have summarised relevant information regarding the Sun and the solar wind, it is still important to understand how many of the space-based measurements are made. This section covers the general working principles of three types of instrument, while mission specific details are provided in the next section.

2.5.1 Fluxgate magnetometers

The magnetic field is a fundamental part of the solar wind plasma, and is useful for providing a reference direction for other measurements, such as $T_\perp$ and $T_\parallel$. All the spacecraft providing data for this thesis have some kind of fluxgate magnetometer that can measure low-frequency magnetic fields ($<$10 Hz). These are light, reliable instruments that require low power and can survive the long time scales needed for space missions. Since a single fluxgate can only measure the magnetic field in one dimension, three of these devices are usually placed orthogonal to each other in order to measure the vector magnetic field.

A fluxgate magnetometer works by taking advantage of the hysteresis effect of a ferromagnetic core. Therefore, the magnetic field within the core depends not only on the field applied to it, but also on the history of its magnetisation. This means that there will be some critical value at which the core becomes saturated and cannot increase the generated magnetic field any further.

A diagram of the basic design is shown in Fig. 2.16, where a ferromagnetic core is wrapped in a 'drive' and 'sense' coil. A triangular shaped waveform is driven as a current through the drive coil, making the core repeatedly go into and out of saturation. When no external field is applied, the core spends equal time in positive

and negative saturation. However, with an external field (either direction along the arrow in Fig. 2.16) the core will spend longer in positive, rather than negative, saturation. This results in the induced field having a truncated triangular waveform, with an asymmetric shape (Verscharen et al. 2019).

The sense coil, via Faraday's law (equation 2.11), then measures an irregular square wave voltage, where the timing and phase of the signal is related to the magnitude and direction of the external field (Ness 1970). The precision of these instruments is much lower than the magnetic field they are measuring, e.g. the Solar Orbiter magnetometer can measure a typical magnetic field of tens of nT with a precision $< 10\,\mathrm{pT}$ (Horbury et al. 2020a).

There is an alternative design, the search coil magnetometer, that uses Faraday's law to directly measure the high-frequency changes in the magnetic field. However, these high-frequency measurements were not relevant for this thesis.

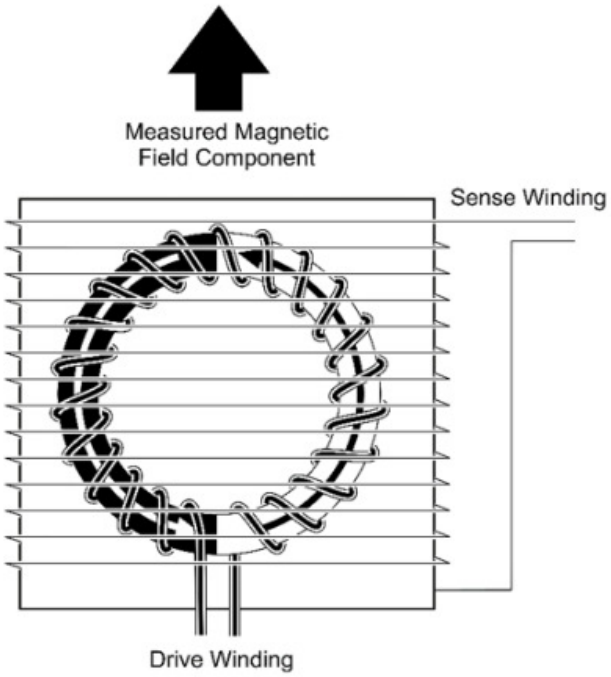


Figure 2.16: Fluxgate magnetometer diagram, where a sense coil is wound around the drive coil. This set-up can measure magnetic fields in either direction along the arrow shown (reproduced from Miles et al. 2017).

2.5.2 Particle measurements

In addition to the magnetic field, knowledge of the plasma conditions (n_p, $T_\perp$, $T_\parallel$ and v) is crucial for many in situ studies. However, these properties cannot be measured directly. Instead, space-based instruments measure the distribution of particle energies in different directions, from which macroscopic plasma properties are derived. There are two common ways to measure these particle distributions, either with a Faraday cup or an electrostatic analyser (ESA).

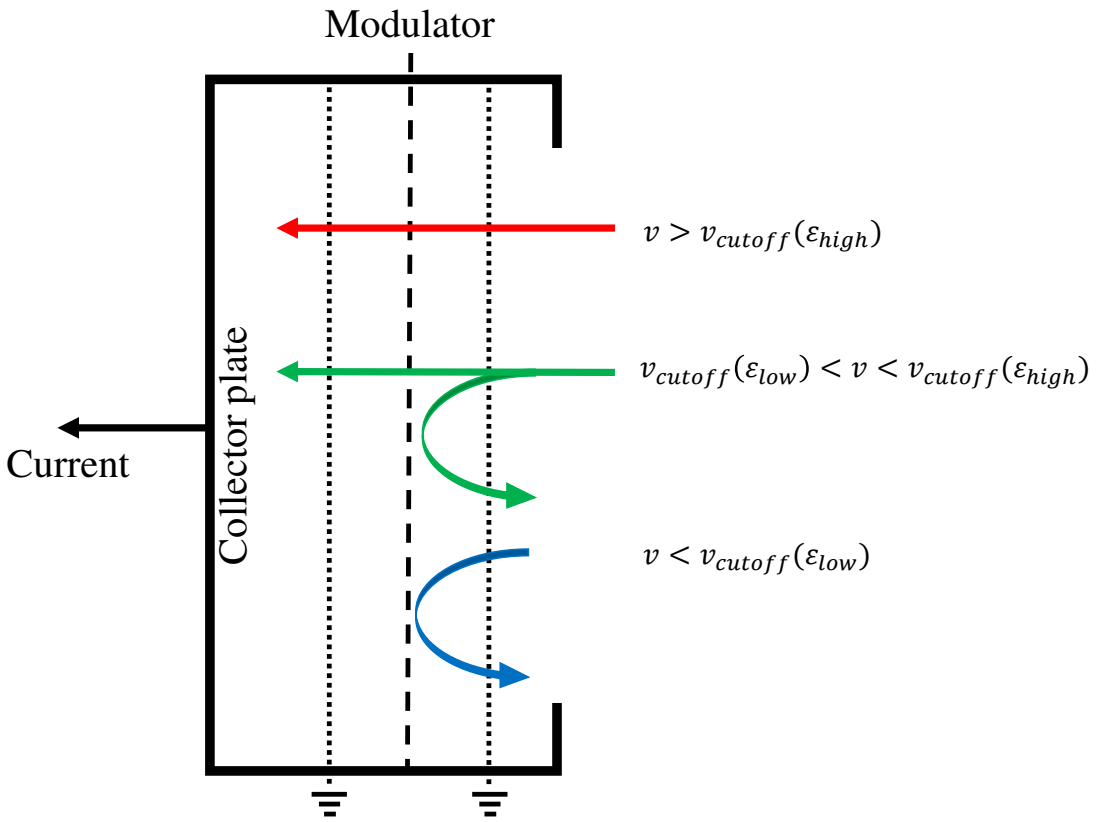


Figure 2.17: Diagram of a Faraday cup, where a collector plate sits behind two grounded and one modulated grid with voltage, ε. Particles with $v > v_{\mathrm{cutoff}}(\varepsilon_{\mathrm{high}})$ (red) will always make it to the plate, and those with $v < v_{\mathrm{cutoff}}(\varepsilon_{\mathrm{low}})$ will always be deflected (blue). The signal measured by the instrument comes from the modulation of the intermediate particle population (green). These particles are deflected away when the voltage is at $\varepsilon_{\mathrm{high}}$, but allowed through for $\varepsilon_{\mathrm{low}}$.

The Faraday cup is a simple instrument that has been extensively used since the first solar wind observations (Gringauz et al. 1960; Neugebauer and Snyder 1966). A basic outline for this type of instrument is shown in Fig 2.17, where a collector

plate sits behind a series of metal grids. This plate measures a current from the inflowing charged particles of the solar wind. In order to obtain a particle energy distribution, there must be some way to allow only a range of particle energies to reach the collector plate. This is achieved by applying a voltage, ε, to the middle grid and grounding the other two grids. Therefore, only particles with a velocity greater than the cut-off:

$$v_{\text{cutoff}}(\varepsilon) = \sqrt{\frac{2q_j\varepsilon}{m_j}}, \tag{2.36}$$

can reach the detector.

A range of particle energies can then be selected by modulating the voltage between:

$$\varepsilon_{\text{low}} = \varepsilon_0 - \frac{\Delta\varepsilon}{2}, \tag{2.37}$$

$$\varepsilon_{\text{high}} = \varepsilon_0 + \frac{\Delta\varepsilon}{2}, \tag{2.38}$$

where ε_0 is the centre voltage and $\Delta\varepsilon$ is the width of the voltage window.

If a particle has a velocity greater than $v_{\text{cutoff}}(\varepsilon_{\text{high}})$ then it will always reach the collector plate, whereas those below $v_{\text{cutoff}}(\varepsilon_{\text{low}})$ will never be collected. Particles with a velocity between $v_{\text{cutoff}}(\varepsilon_{\text{low}})$ and $v_{\text{cutoff}}(\varepsilon_{\text{high}})$ will only generate a current in the collector plate when the voltage is low. Therefore, the modulation of the current is used to measure the influx of charged particles in the correct energy window, while ignoring the constant signal from the rest of the particles.

The full energy distribution of the particles can be measured by sweeping the energy window across the desired range. It is important to note that the width and location of the energy windows is only dependent on the voltage created in the metal grid. Therefore, the resolution and range of the instrument can be updated in flight.

Such an instrument cannot directly distinguish between different particle species. However, the individual particle velocity distributions are shifted by the mass-to-charge ratio of the ion, according to equation 2.36. Therefore, if this velocity shift is large enough, the different particle populations can be separated, which is usually

done for the proton core and alphas.

A Faraday cup has a restricted field of view (FOV) of around 100° (Verscharen et al. 2019). Therefore, several methods are used to provide a greater FOV, as discussed for each specific mission.

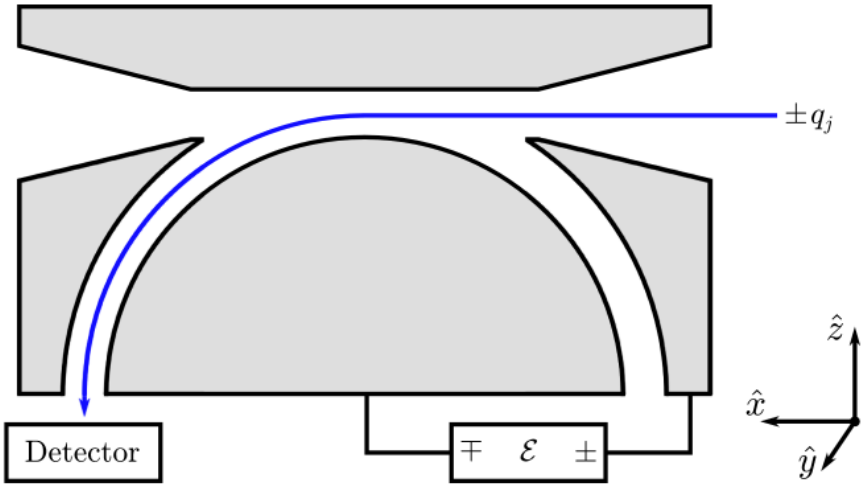


Figure 2.18: Basic diagram of an electrostatic analyser. Particle trajectories (blue line) are bent by the voltage applied between the two curved plates. If the energy-to-charge ratio is within a certain range, the particle will reach the detector at the bottom. By applying different voltages across the plates, a range of particle energy can be sampled (reproduced from Verscharen et al. 2019).

In comparison, an ESA can look in both azimuth and elevation, directly building up a 3D particle distribution. While the design of ESAs varies per mission, Fig. 2.18 demonstrates the basic working principle. In this 'top hat' design, a detector sits below a set of curved plates that are charged to create a voltage, V, between them. For a particle to reach the detector, it must have the right energy-to-charge ratio to not hit the plates.

By varying the voltage between the plates, different energy-to-charge ratios can be selected from the solar wind. There is some spread in the energy-to-charge ratios allowed per ε, which is set by the width of the curved gap that the particles must pass through. Therefore, unlike a Faraday cup, the width of energies allowed into the detector cannot be changed in flight (Verscharen et al. 2019).

Similar to a Faraday cup, this design cannot directly distinguish between different particle species, with the distributions potentially being separated when shifted by

their mass-to-charge ratio. However, by adding an extra time of flight measurement, there can be an independent measurement of the particle speed, which can allow for the mass-per-charge ratio to be estimated.

After measuring the particle velocity distributions, the macroscopic quantities can be extracted by taking 'moments' of the distribution (Paschmann et al. 1998). This is similar to taking the moments of the Vlasov equation in Section 2.1.2, and are usually provided as a data product by the instrument team. It is important to note that these moments will include contributions from the proton beam, if present, which will inflate the speed and density estimates of the proton core.

Therefore, it is often preferable to fit a bi-Maxwellian distribution (equation 2.35) only to the proton core, which can provide a more accurate estimation of the proton core properties. This also allows for $T_\perp$ and $T_\parallel$ to be measured as the width of the distribution, which cannot be done with moments. Again, these fits are commonly provided by the instrument team, but can also be performed separately to target the proton beam and alpha populations (Stansby et al. 2018; Woodham et al. 2021a).

2.6 Relevant missions

As mentioned earlier, there are still many open questions in the study of the Sun and the solar wind, which provided the motivation for two new missions: Parker Solar Probe (Fox et al. 2016) and Solar Orbiter (Müller et al. 2013). These flagship missions are complemented by several other spacecraft that will help map the global structure of the solar wind in Chapter 3. Before summarising the specifics of each mission, it is important to define the reference frames used to describe the spacecraft measurements and trajectories.

2.6.1 Reference frames

There are several useful reference frames for spacecraft orbiting the Sun. There are many different inertial frames, one being ECLIPJ2000 which has its $\vec{x}$ and $\vec{y}$

coordinates in the ecliptic plane. However, for the purposes of this thesis, a more useful frame is one that rotates with the surface of the Sun, referred to as the 'Carrington frame'. This is based on the Heliographic coordinates first used by Carrington (1853) to track the location of sunspots on the Sun's surface. Each point on the solar surface is given a longitude, Φ, and latitude, Θ, which can be extended out into the heliosphere with a distance to the Sun parameter, r (Ulrich and Boyden 2006).

This frame rotates at a rate of 14.18° per day, as defined by the International Astronomical Union (Archinal et al. 2011). For an observer on Earth, the longitude observed will decrease from 360° $\rightarrow$ 0° before a new 'Carrington rotation' starts. The first of these started on November 9th 1953 (Thompson 2006) and are useful for naming the solar rotations.

All spacecraft in the inner heliosphere, except for PSP, orbit more slowly than the solar rotation, meaning they move towards lower Φ over time. However, within each PSP orbit, there will be two points of co-rotation when PSP's orbit matches the solar rotation: one inbound and outbound. At these times, PSP will move very slowly in Φ and effectively sample solar wind from the same source region over a longer period ($\sim$ several hours). In between the co-rotation points, PSP will super co-rotate by outpacing the Sun's rotation, creating a loop in the orbit when viewed in the Carrington frame. This also means that PSP will sample the same Φ at different r over the same orbit. This has never been possible with a spacecraft before, and can be extremely useful for studying how a solar wind stream evolves with distance from the Sun.

2.6.2 Parker Solar Probe

After launching in August 2018, the first data from PSP was returned in December 2018 from $\sim$35 $R_{\odot}$ (Bale et al. 2019), and PSP has currently completed 15 orbits, reaching 13 $R_{\odot}$ at the time of writing and depicted in Fig. 2.19. For mission operations, the data is usually taken within 53 $R_{\odot}$ (Kasper et al. 2016) and then

downloaded from the spacecraft when it is farther from the Sun. Therefore, the PSP data is often organised by the encounter number. For example, encounter 1 will be referred to as E1 in this thesis.

PSP's unique trajectory comes with the compromise that instruments must be protected by a large heat shield that faces the Sun at all times. This limits the number and type of instrument that can be carried, which includes four sets of instrument suites:

- Electromagnetic Fields Investigation (FIELDS, Bale et al. 2016) for measuring the magnetic and electric fields with both fluxgate and a search coil magnetometer, as well as five voltage probes
- Solar Wind Electrons Alphas and Protons Investigation (SWEAP, Kasper et al. 2016) with a Faraday cup and ESA to measure the protons and alphas, plus two additional ESAs for the electrons
- Integrated Science Investigation of the Sun, Energetic Particle Instruments (IS⊙IS, McComas et al. 2016) to measure the energetic particles (>20keV)
- Wide-field Imager for Solar Probe Plus (WISPR, Vourlidas et al. 2016) to image the solar wind leaving the Sun

Therefore, there are no compositional instruments or solar telescopes on this mission. Only the FIELDS and SWEAP instrument suites are relevant in this thesis, for the magnetic field and basic plasma parameters.

The FIELDS instruments are built on the heritage of previous space missions, such as STEREO-A and Wind. Like many other spacecraft, the magnetometers are placed on a boom to avoid any contamination from the spacecraft electronics. The fluxgate magnetometers can operate at 256 samples/NYseconds[6], although the highest resolution needed in this thesis was the 4 samples/cycle ($\sim$ 4.58 samples/second) data product.

[6]The instrument is based on the 150kHz power supply. So to have 2^{17} clock cycles per NYsecond, this is defined as $2^{17}/150,000 = 0.873813...$ seconds (Bale et al. 2016)

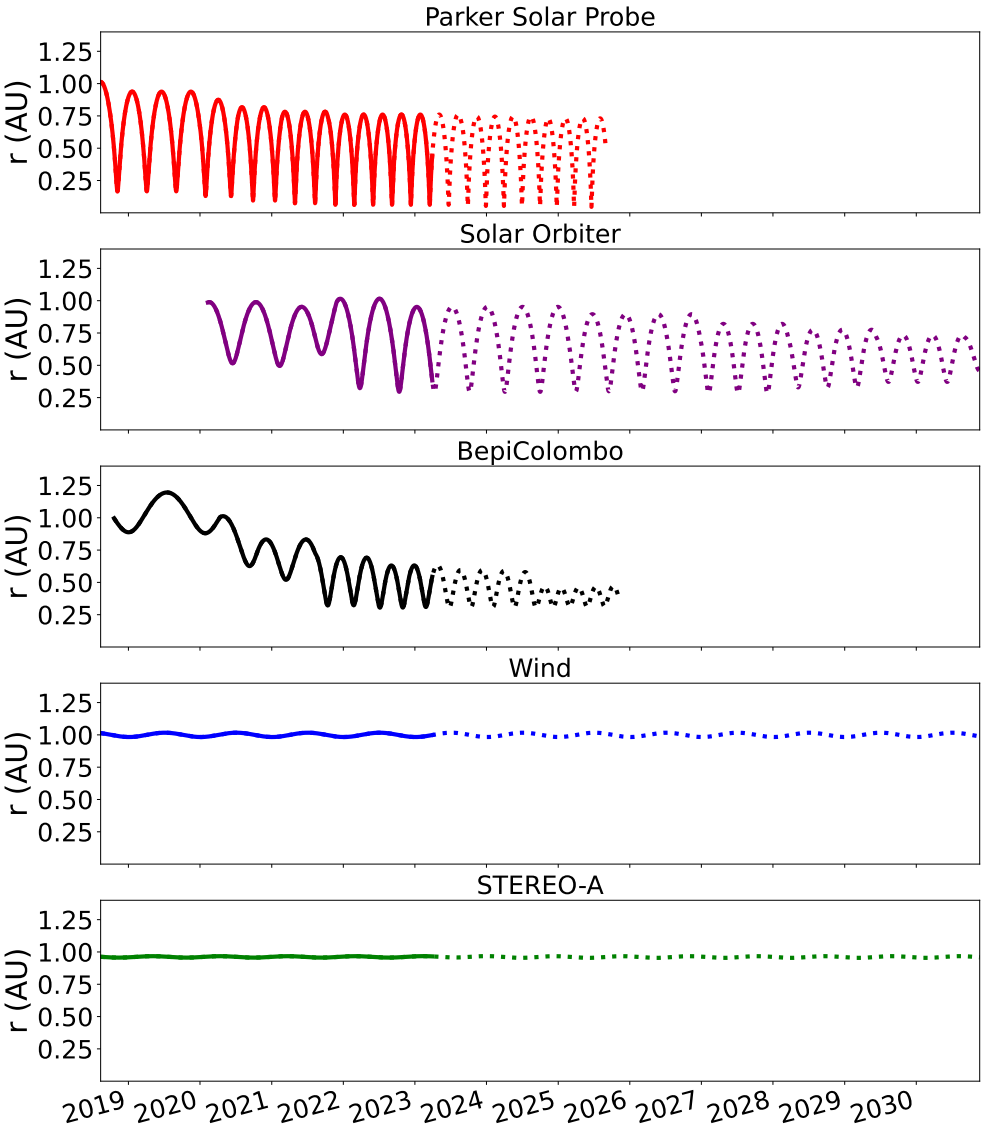


Figure 2.19: Trajectories for the missions used in this thesis. Dashed lines show the projected orbits, and the solid lines show what the spacecraft have already completed at the time of writing.

Unlike many spacecraft designs, the SWEAP instrument suite has both a Faraday cup and a set of ESAs, which are known as the Solar Probe Cup (SPC) and Solar Probe ANalyzers (SPAN), respectively. There is one ESA for the protons, alphas and electrons (split into SPAN-Ai and SPAN-Ae) and another dedicated ESA for the electrons (SPAN-B), as shown in Fig. 2.20. Since the electron data is used rarely in this thesis, SPAN-Ai is simply referred to as SPAN. SPAN also includes time of flight measurements, so can fully separate the alpha particles from the proton measurements.

The placement of SPAN on the ram side of the spacecraft means that its FOV is cut off by the heat shield. If the spacecraft were not moving, then the solar wind would travel radially into the heat shield and be outside the SPAN FOV. However, as the spacecraft moves closer to the Sun, there is a large orbital speed component in the $+\vec{T}$ direction ($\sim$90 km/s for E1), meaning that the solar wind is angled towards the ram side in the spacecraft frame. A demonstration of this effect is shown in Fig. 2.21, where only a portion of the full VDF can be seen by SPAN. As the PSP mission progresses, more of the proton distribution will become visible in the SPAN FOV, increasing the accuracy of the measurements. It is important to note that the particle VDFs can be rotated by Alfvén waves in the solar wind, as discussed in Section 2.4.2. This can either deflect the proton core into (with $-V_T$) or out of (with $+V_T$) the FOV, which was crucial for determining the temperature inside switchbacks in Chapter 5.

The SPAN instrument team provides moments in the data files, although these can be misleading when a large portion of the VDF is not present. Instead, for a better estimation of the proton core parameters, fits are used according to the method of Woodham et al. (2021a). These data are provided every $\sim$4 seconds, although the actual measurements are completed within 0.437 seconds. This short integration time is important as it helps reduce any blurring as the VDF rotates in response to the Alfvén waves in the solar wind. The fitting procedure is not attempted if the variance in the magnetic field is above 10°.

To complement the SPAN measurements, PSP also has SPC that points directly at the Sun, whose 60° FOV (blue line in Fig. 2.21) can cover a region SPAN cannot see. To survive the high temperatures (>1000°C, Kasper et al. 2016), this instrument is made from refractory metals (including tungsten and molybdenum) in a sapphire housing (Case et al. 2020).

As mentioned earlier, the basic Faraday cup design can only measure the energy of the particles, not their direction. To provide some information about the flow angle of the solar wind, SPC has four collector plates that equally cut the circu-

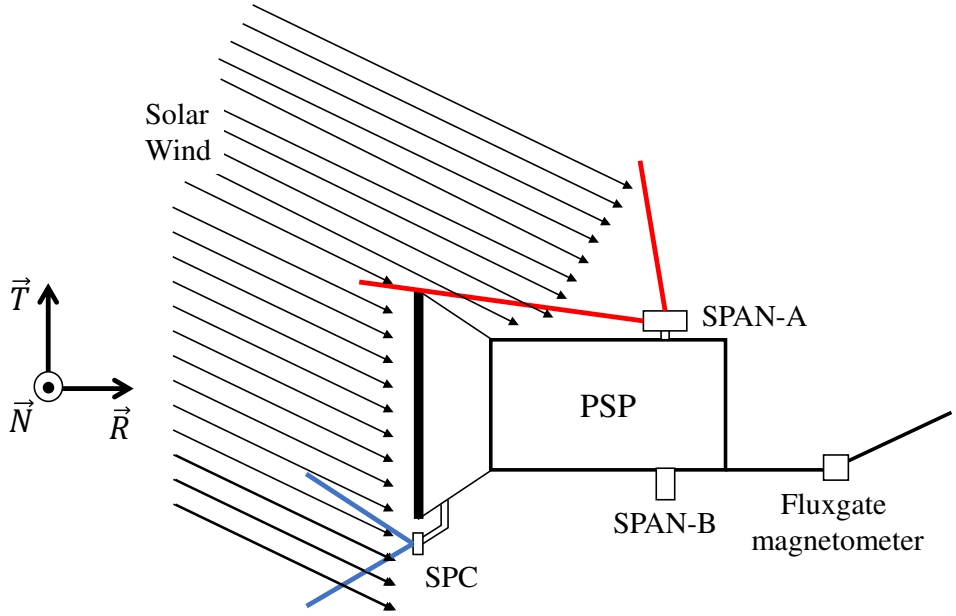


Figure 2.20: Diagram showing the placement of the relevant instruments on PSP. A radially flowing solar wind will appear at an angle in the spacecraft frame, and will appear more in the SPAN-A FOV (red). SPC can then look directly at the radial solar wind, with its FOV being shown in blue. The fluxgate magnetometer sits on a boom to avoid any interference from the spacecraft electronics.

lar collector plate. The flow angle is then estimated from the differential currents between the plates.

The Faraday cup design also means that SPC can only measure a radial cut through the full 3D VDF that SPAN can measure. Therefore, SPC can only measure a radial proton core temperature, $T_{p,R}$, according to:

$$T_R = T_\perp \sin^2(\theta_{RB}) + T_\parallel \cos^2(\theta_{RB}), \tag{2.39}$$

with a magnetic field θ_{RB} away from $\vec{R}$. This is an important caveat to the SPC data, and care should be taken when discussing the temperature results from this instrument.

2.6.3 Solar Orbiter

Since launching in February 2020, Solar Orbiter has completed five orbits, reaching a perihelion of ∼0.28 AU. Further on in its mission, Solar Orbiter will use a Venus gravity assist to climb out of the ecliptic plane, eventually reaching ∼33° latitude in 2030. Here, it will image the Sun's poles for the first time, potentially helping to reveal the source of the fast solar wind. The magnetic field is provided at 8 Hz by a fluxgate magnetometer (MAG, Horbury et al. 2020a) and the plasma moments are supplied by the Proton Alpha Sensor (PAS, Owen et al. 2020) based on the ESA design.

So, after waiting since the Helios spacecraft in the 1980s, there are now two modern missions orbiting in the inner heliosphere. Each mission will reveal new information about the Sun and the solar wind as they travel to a currently unexplored part of the solar system. The co-existence of these missions also allows for research opportunities that would not be possible with a single spacecraft (Velli et al. 2020). For example, an individual plasma parcel can be tracked as it expands into the heliosphere, potentially revealing how structures and heating process evolve with distance from the Sun. This concept of multi-spacecraft measurements is central to Chapter 3, with a total of five spacecraft being used.

2.6.4 Additional missions

Alongside the two flagship missions discussed above, BepiColombo[7] was launched in October 2018 and aims to understand the magnetospheric dynamics of Mercury. In order to orbit Mercury in 2025, and build up a large set of observations, BepiColombo has to make several gravity assists. Fortunately for the heliophysics community, the fluxgate magnetometer aboard the Mercury Planetary Orbiter (MPO) can take measurements of the solar wind during this cruise phase (Glassmeier et al. 2010). As shown in Fig. 2.19, BepiColombo orbited between 0.5 → 1 AU, providing

[7]Named after Giuseppe 'Bepi' Colombo who suggested that gravity assist could be used for Mariner 10 mission to fly past Mercury (ESA 2023a)

observations at an intermediate distance between the inner heliosphere missions of PSP and Solar Orbiter, and those spacecraft at 1 AU.

One such spacecraft at 1 AU is Wind, which has been providing solar wind measurements at the L1 Lagrange point since 2004 (NASA 2023). Wind is a spin stabilised spacecraft that can provide magnetic field data through the Magnetic Field Investigation (MFI, Lepping et al. 1995); plasma from its Solar Wind Experiment (SWE, Ogilvie et al. 1995) and electron properties from the 3DP instrument (an ESA, Lin et al. 1995b). These are especially important for space weather mitigation, as real-time data from Wind can give a ∼45 minute warning of any potentially hazardous solar wind conditions (Owens et al. 2008).

Finally, there is STEREO-A which was orbiting at a lower Carrington longitude than Earth at ∼1 AU. This originally had a twin satellite, STEREO-B, and aimed to provide stereoscopic images of the Sun to better understand the structure on the Sun. Unfortunately, STEREO-B lost contact in 2014, but STEREO-A is still extremely useful for CME observations. STEREO-A represents another observation point at 1 AU to complement those from Wind just ahead of Earth. Again, a fluxgate magnetometer (IMPACT) and an ESA (PLASTIC) provide the magnetic field and proton measurements, respectively.

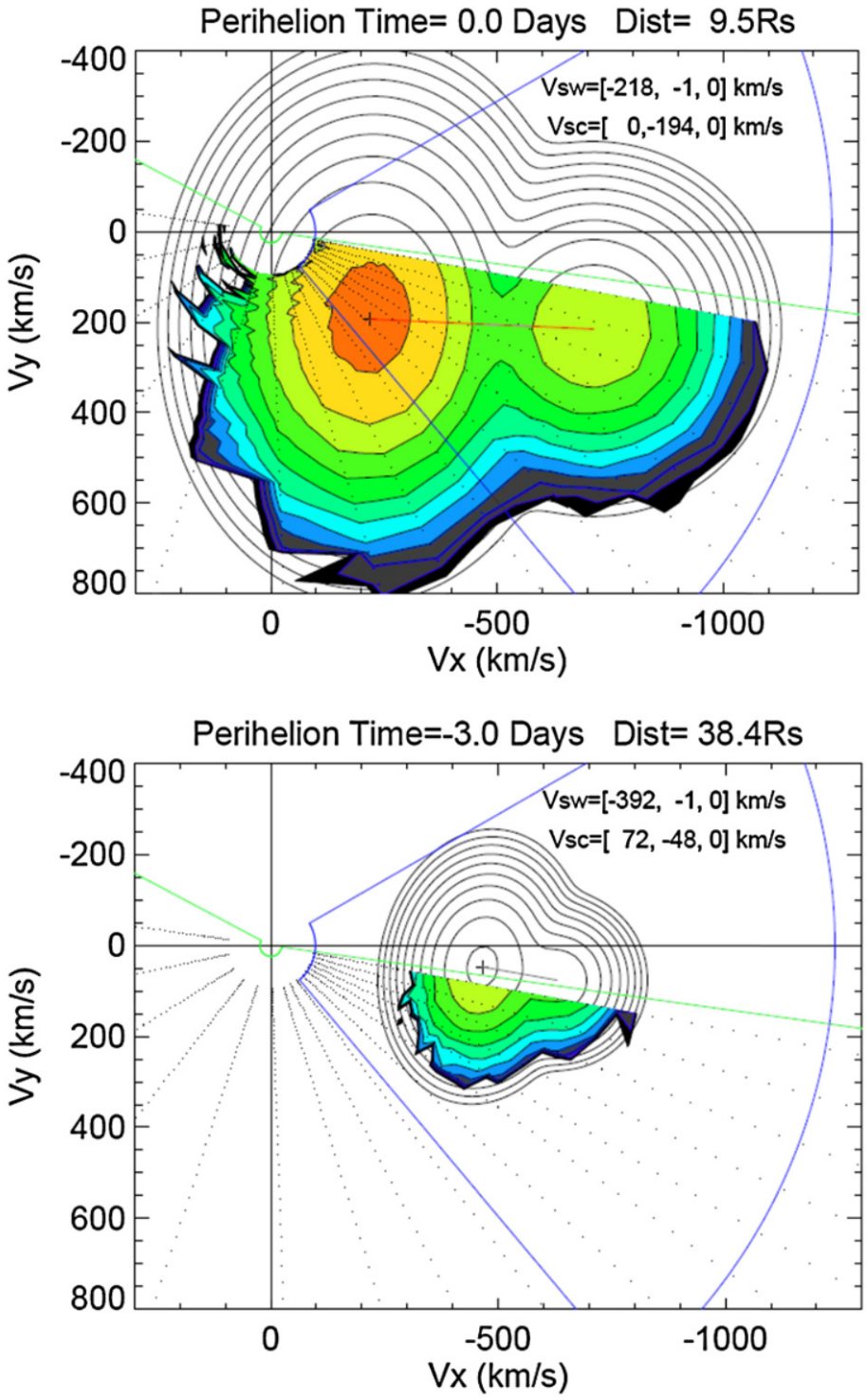


Figure 2.21: Simulations of what SPAN is expected to see at 9.5 $R_\odot$ (top) and 38.4 $R_\odot$ (bottom). SPAN's FOV is limited by the heat shield, so cannot see the full distribution in the lower panel. This will become less of an issue as PSP travels closer to the Sun in the upper panel. For times when SPAN cannot see enough of the VDF, SPC will provide the plasma parameters instead, whose FOV is shown by the blue line (reproduced from Kasper et al. 2016).

Chapter 3

Multi-spacecraft study of the solar wind in latitude

3.1 Introduction

The launches of Parker Solar Probe (PSP, Fox et al. 2016) in August 2018, and Solar Orbiter (Müller et al. 2013) in February 2020, have ushered in a new era of inner heliosphere research. This has generated a wealth of data for a region last studied by the Helios spacecraft in the 1980s (Schwenn and Marsch 1990). Along with BepiColombo, on a cruise phase to Mercury (Benkhoff et al. 2010), STEREO-A (Kaiser et al. 2008) and the spacecraft ahead of Earth (e.g. Wind, Ogilvie and Desch 1997), there is now a constellation of spacecraft in the inner heliosphere. This set of spacecraft can go beyond the usual limits of single point measurements and allow for the coordinated study of the global structure of the heliosphere, with each spacecraft helping to untangle the spatial and temporal variations in the solar wind.

Each mission has a specific trajectory to fulfil its own mission objectives: PSP eventually orbiting only 9.86 $R_\odot$ from the Sun; Solar Orbiter travelling to higher latitudes; BepiColombo on the way to Mercury; STEREO-A to the side of Earth and Wind at the L1 Lagrange point. By targeting different spacecraft alignments, researchers are provided with the opportunity to answer specific science questions.

For example, numerous studies have used radially aligned spacecraft for the study of solar wind evolution of turbulence (Telloni et al. 2021b) and large-scale structures (Allen et al. 2021).

In this chapter, a different approach is taken, with an investigation into how the solar wind varied in latitude. The Ulysses mission has already demonstrated the 3D nature of the solar wind by orbiting above the poles, with a very well-defined structure at solar minimum (McComas et al. 2003). However, this chapter focusses more on the fine-scale structure which, for the first time, can be measured with five separate spacecraft spanning $\pm 10°$ latitude. After showing how the global structure of the solar wind was stable across the rotations in Section 3.3.1, several case studies are undertaken into structures in the solar wind from Sections 3.3.3 to 3.3.5. It is demonstrated that this newly formed spacecraft constellation can allow for the solar wind to be studied from new perspectives. This represents work undertaken in Laker et al. (2021a).

3.2 Methodology

The launch of Solar Orbiter, in February 2020, completed the formation of the spacecraft constellation that was used in this chapter, as summarised in Fig. 3.1. After launch, Solar Orbiter began to approach the Sun on the way to its first perihelion on June 15th 2020. To make use of this new collection of spacecraft as soon as possible, a period between May and July 2020 was chosen for this study, giving two full Carrington rotations, CR2231 and CR2232 (Thompson 2006). Earlier than this, Solar Orbiter was in the early mission phase, where instruments were still being switched on and calibrated.

Ideally, to study the large-scale structure of the solar wind, measurements of magnetic field and plasma parameters are essential, along with the useful diagnostic tool of electron strahl PADs (see Section 3.2.4). However, given the early stage of the Solar Orbiter mission, only magnetic field data was present throughout our period of interest, with a few days of plasma data from PAS being taken specially

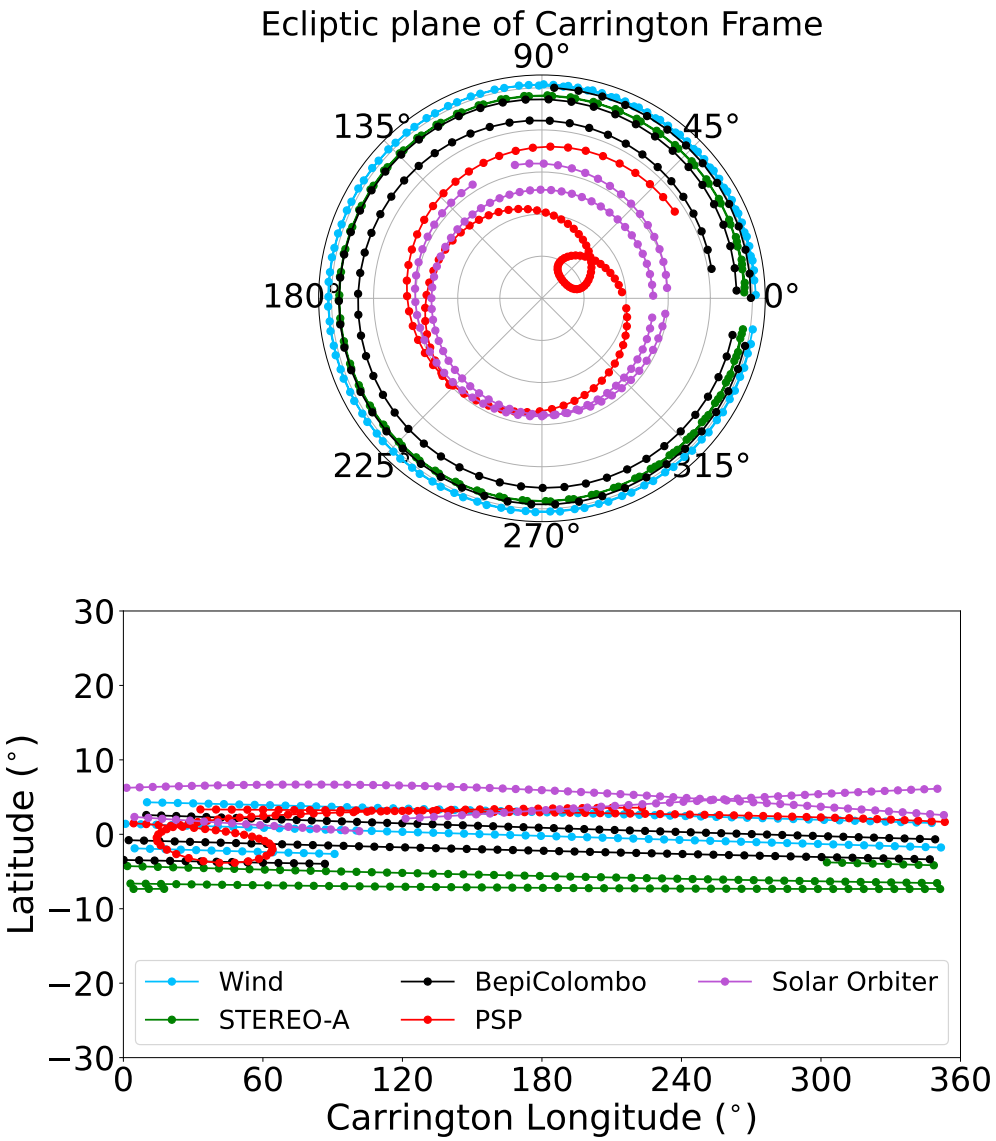


Figure 3.1: Trajectories of the different spacecraft for the time period of this study, May to July 2020, in the ecliptic plane of the Carrington frame (upper) and Carrington coordinates when mapped back to the Sun (lower). Each spacecraft moves towards lower longitudes in the Carrington frame, except for PSP (red) that can super-corotate. The spacecraft constellation covers ±10° latitude.

for the predicted encounter with comet ATLAS (see Section 3.3.3, Jones et al. 2020). A full list of the data used in this study can be found in Table 3.1.

In contrast, by early 2020, PSP was entering its fifth perihelion, providing full measurements from 0.13 AU to 0.5 AU, where the specially designed instruments stop measuring at further distances from the Sun.

Spacecraft	Instrument	Type	Reference
PSP	FIELDS	Mag	Bale et al. (2016)
PSP	SPC	Plasma	Kasper et al. (2016), Case et al. (2020)
PSP	SPAN-e	e^- PAD	Kasper et al. (2016), Whittlesey et al. (2020)
Solar Orbiter	MAG	Mag	Horbury et al. (2020a)
Solar Orbiter	PAS	Plasma	Owen et al. (2020)
BepiColombo	MAG	Mag	Glassmeier et al. (2010) Heyner et al. (2020)
STEREO-A	IMPACT	Mag	Acuña et al. (2008)
STEREO-A	PLASTIC	Plasma	Galvin et al. (2008)
Wind	MFI	Mag	Lepping et al. (1995)
Wind	SWE	Plasma	Ogilvie et al. (1995)
Wind	3DP	e^- PAD	Lin et al. (1995a)

Table 3.1: Comprehensive list of the different measurements used in this study. All spacecraft had magnetic field (Mag) data available, although only Wind and PSP had bulk plasma parameters and electron pitch angle distributions (reproduced with permission from Astronomy & Astrophysics, ©ESO Laker et al. 2021b).

While both Solar Orbiter and PSP are dedicated solar wind missions, BepiColombo is a planetary mission on a cruise to orbit Mercury in 2025. Due to the challenge of entering into this orbit, BepiColombo will complete several planetary gravity assists (first proposed by Guiseppe 'Bepi' Colombo for Mariner 10 ESA 2023b). During the period of interest, BepiColombo had just completed an Earth flyby on April 10th 2020, meaning it was ahead of Earth and moving from 0.99 AU to 0.85 AU from the Sun. Fortunately for this study, and several others (Davies et al. 2021; Alberti et al. 2022), the magnetometer aboard the Mercury Planetary Orbiter (MPO, Glassmeier et al. 2010) was operating at 16 vectors/s, and recorded near-continuous data.

In addition to the Wind spacecraft at the L1 Lagrange point, data from STEREO-A was also used, which was orbiting at a lower Carrington longitude than Earth at ∼1 AU. This meant that STEREO-A observed any co-rotating structures ∼6 days before Earth, based on a solar rotation of $\Omega = 14.18°/\text{day}$ (Archinal et al. 2011). In general, each spacecraft measured the same mapped longitude within a few days of each other (except for PSP, which has a unique orbit in Fig. 3.1). Therefore, to study the global structure of the solar wind, it was assumed that the solar wind

sources were time-stationary on the scale of a few days. Given that both CR2231 and CR2232 were in a period of low solar activity (Nandy 2021), this was reasonable, since the HCS has been shown to be stable over several solar rotations at solar minimum (Thomas and Smith 1981; Riley et al. 2002).

3.2.1 Modelling the heliospheric current sheet

One method for establishing the shape of the HCS is by tracking the streamer belt in white light images, which represents light scattered via Thomson scattering from solar electrons (Vourlidas and Howard 2006). After observing the limbs of the Sun for half a solar rotation, the location of the streamer belt, and in turn HCS, can be mapped out (Rouillard et al. 2020). While this can give accurate results, the need to measure over half a solar rotation (∼14 days) means it is rarely used in favour of numerical models.

Several such models exist, each aiming to extend an inner boundary condition at the Sun and model the magnetic field out into the corona until the field becomes radial. Typically, this inner boundary condition is the line-of-sight magnetic field at the photosphere (magnetogram), taken by telescopes on Earth observing the splitting of the Ni I 6768Å line via the Zeeman effect (Norton et al. 2006; Liu et al. 2012; Hill 2018).

While many solar corona models can successfully capture the coronal structure by solving the full MHD equations, (see Section 2.1.2) they are computationally expensive (Mikić et al. 1999). Fortunately, there is another widely adopted model, the Potential Field Source Surface (PFSS), that requires far less computing power (Altschuler and Newkirk 1969; Schatten et al. 1969). This model assumes a current free corona, meaning Ampère's law becomes:

$$\nabla \times \vec{B} = \mu_0 \vec{J} = 0 \tag{3.1}$$

and the magnetic field, as the model name suggests, can be described as the gradient

of a scalar potential:

$$\vec{B} = -\nabla\Psi, \tag{3.2}$$

where Ψ is the magnetic scalar potential. Along with a divergent free magnetic field ($\nabla \cdot \vec{B} = 0$), Ψ then satisfies Laplace's equation:

$$\nabla^2\Psi = 0, \tag{3.3}$$

where solutions in spherical coordinates are well known (Mackay and Yeates 2012). Therefore, the PFSS model can integrate from the inner boundary condition up to the 'source surface'; a user controlled input defining the distance at which the magnetic field becomes radial. Fig. 3.2 shows the PFSS solution for a dipole magnetic field, where a flat HCS (black line) separates the two hemispheres of opposing magnetic polarity, and the magnetic field lines (right panel) become radial at the source surface (black dotted line).

Of course, this assumed lack of current is not true of many structures seen on the Sun, e.g. active regions. Yet this assumption is often reasonable on a global scale at solar minimum, and the PFSS model has been shown to compare well with more sophisticated MHD models (Riley et al. 2006), and measurements at 1 AU (Jian et al. 2015).

Therefore, in this chapter, the PFSS model was used as a reference for the HCS shape and location, which has been adapted for *Python* in *pfsspy* (Yeates 2018; Stansby et al. 2020b). This model has become the most widely adopted for tracing the origin of the solar wind, and underpins the popular connectivity tool from IRAP[1].

The PFSS model uses magnetograms as the input, which were provided by ground-based observatories in the Global Oscillation Network Group (GONG) (Harvey et al. 1996; Hill 2018). Since these were only ground-based measurements, only half of the Sun could be viewed at any one time, making some parts of the map up to 27 days out of date. To address this issue, magnetograms from the Air Force

[1]http://connect-tool.irap.omp.eu/

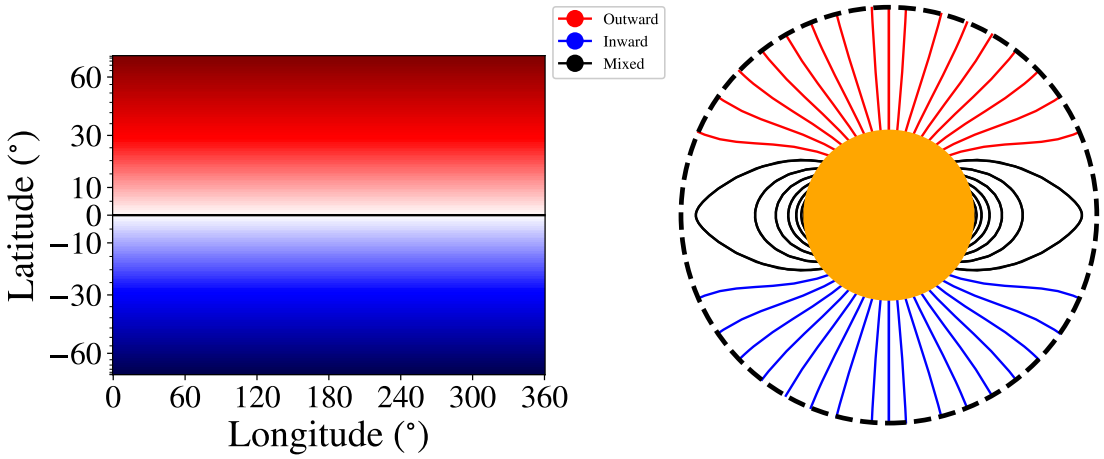


Figure 3.2: PFSS solution for a dipole magnetic field. On the left panel, a flat HCS (black line) separates the outwards (red) and towards (blue) polarities of the magnetic field. Magnetic field lines are shown on the right, which become radial at the source surface (dotted black line).

Data Assimilative Photospheric Flux Transport (ADAPT) model, that attempt to model the far side of the Sun (Hickmann et al. 2015), were used. An average of the 12 model runs given in a single ADAPT file was used. This provided more consistent results compared to the original GONG magnetograms, which can change significantly when the observations scan over part of an active region. The only user input is the source surface height, which is usually taken as $2.5\,R_{\odot}$ to match observations (Hoeksema et al. 1983), but can vary from 2-3 $R_{\odot}$ (Arden et al. 2014; Badman et al. 2020; Panasenco et al. 2020). Following recent modelling work with PSP data, a value of $R_{SS} = 2\,R_{\odot}$ was used for both Carrington rotations (Nikolić 2019; Badman et al. 2020).

3.2.2 Ballistic mapping

While time was assumed not to be relevant, it is still important to note that the data is taken in four dimensions: time, longitude, latitude and distance from the Sun. Therefore, in order to plot a map of longitude against latitude, the effect of chang-

ing distance from the Sun had to be removed. This was achieved by 'ballistically mapping' each spacecraft onto the source surface, so that they could be compared to each other, as well as to the PFSS model. As demonstrated in Fig. 3.3, the solar wind measurements at a location, specified by r_{SC}, Φ_{SC} and Θ_{SC}, were then propagated back to the source surface, R_{SS}, using:

$$\Phi_{SS} = \Phi_{SC} + \frac{\Omega(r_{SC} - R_{SS})}{V_{sw}}, \tag{3.4}$$

with a constant radial solar wind speed, V_{sw}. Since only a radial speed was assumed, there was no change in latitude when mapping to the source surface. For each spacecraft, V_{sw} was estimated by taking the average of the bulk proton speed in a 6-hour window. Since BepiColombo was orbiting near Earth, and lacked plasma measurements, the radial speed measured by Wind was used as a proxy, as they were separated by only $\sim$0.1 AU and $<5°$ longitude.

The same could not be done for Solar Orbiter, which was around 0.5 AU. In this case, a constant speed of 350 km/s was used, based on the typical speed seen by Wind over the two solar rotations of interest. Given a speed deviation of 50 km/s with Solar Orbiter at 0.5 AU, there would be a 5° shift in mapped longitude, which should be noted throughout this chapter. Added to this uncertainty in V_{sw} was the fact that ballistic mapping does not account for interactions between solar wind parcels, which can only be achieved with more sophisticated MHD models (Odstrcil 2003; Poedts and Pomoell 2017). Even with the lack of interactions, ballistic mapping has long been shown to provide accurate results for solar wind studies (Nolte et al. 1976; Riley and Lionello 2011; Badman et al. 2020), making it appropriate for this chapter.

3.2.3 Estimating magnetic polarity

In order to establish the sector structure of the solar wind, the magnetic polarity was estimated for a 6-hour window in each of the spacecraft. After trialling various time windows, this 6-hour period was chosen to reveal the large-scale structure while

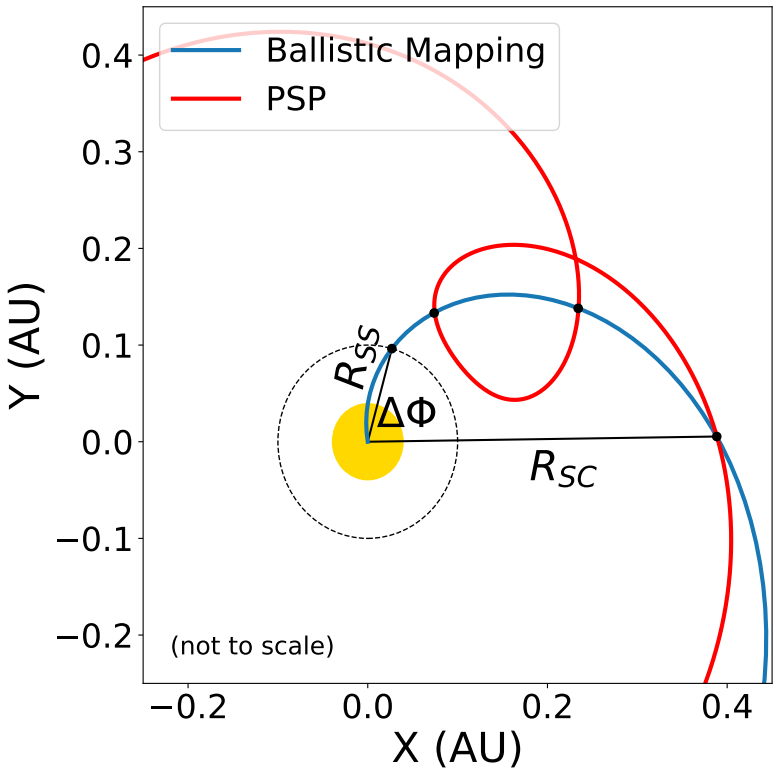


Figure 3.3: Demonstration of ballistic mapping, where a measurement at r_{SC}, Φ_{SC} is mapped along the Parker spiral (blue) to the source surface, R_{SS}. The resulting change in angle, $\Delta\Phi$, is equal to $\Phi_{SC} - \Phi_{SS}$. PSP's unique orbit meant that several points along the orbit (red) could map back to the same longitude on the Sun.

not dwelling on smaller-scale structures not relevant to this thesis. Under normal solar wind conditions, the interplanetary magnetic field will follow the Parker spiral (equation 2.32), either pointing towards ($\phi_{ps,T}$) or away ($\phi_{ps,A}$) from the Sun:

$$\phi_{ps,A} = \phi_{ps,T} + 180 = \tan^{-1}\left(\frac{-r_{SC}\Omega\cos(\Theta_{SC})}{V_{sw}}\right). \tag{3.5}$$

In the RTN coordinate system, $\phi_{ps,A}$ is $\sim 315°$ for a 300 km/s solar wind at 1 AU, meaning that the sign of the R component could not be used to assess the magnetic polarity. Instead, as in Fig. 3.4, outwards polarity (positive polarity) was assigned if the magnetic field angle in the R-T plane, ϕ_B, was within $\phi_{ps,A} - 45 < \phi_B < \phi_{ps,A} + 45$ and towards polarity (negative polarity) for $\phi_{ps,T} - 45 < \phi_B < \phi_{ps,T} + 45$. If ϕ_B lay outside these ranges, then the polarity was described as 'mixed'.

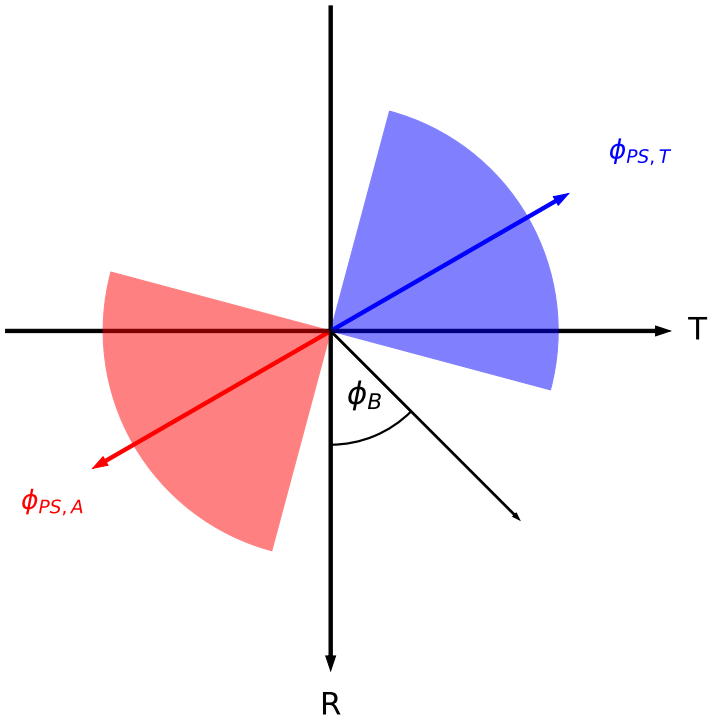


Figure 3.4: Diagram showing how the magnetic polarity was defined. The magnetic field makes an angle ϕ_B in the R-T plane. If within $\pm 45°$ of $\phi_{ps,A}$ or $\phi_{ps,T}$ then it was assigned as outwards and towards polarity, respectively. Otherwise, the polarity is assigned as mixed.

3.2.4 Determining sector boundaries

Transient events near sector boundaries can make the magnetic field signatures more complex than a simple flip in magnetic field direction. When a CME is released from a helmet streamer, the 'legs' of the flux rope magnetic field have different magnetic polarity which, when observed in situ, can carry the change in polarity seen at the sector boundary (Crooker et al. 1998).

As well as large impulsive CMEs, remote sensing observations have long shown the release of 'periodic density structures' (PDS) from the tips of helmet streamers, separated by smaller-scale flux ropes (Wang et al. 1998). These are often present within the in situ data surrounding sector boundaries, but do not carry the polarity change as the larger ICMEs can (Sanchez-Diaz et al. 2019). This repeated and continuous ejection of plasma material has led to the suggestion that it could constitute ~15% of the slow solar wind surrounding the HCS (Sanchez-Diaz et al. 2017).

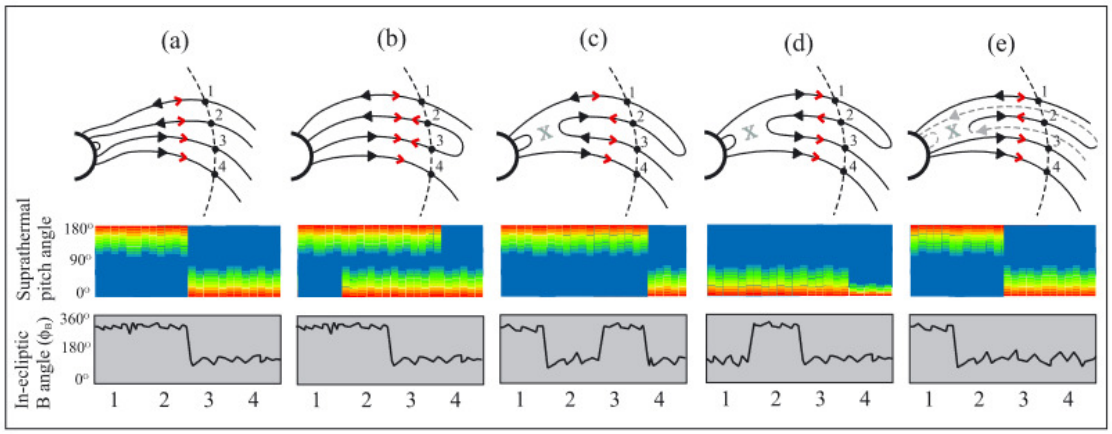


Figure 3.5: Several magnetic configurations at sector boundaries, along with their representation in the electron strahl PAD and magnetic field data seen by the spacecraft. The direction of the magnetic field is shown by the black arrows and the electron strahl direction by the red arrows. An 'X' depicts the location of magnetic reconnection, and out-of-plane magnetic field lines are shown in dashed grey lines (reproduced from Owens et al. 2013).

The magnetic field alone cannot be used to determine the presence of a sector boundary, with the electron strahl PADs being the most effective diagnostic. As outlined in Section 2.4.1, this electron population originates in the solar corona and is directed along the magnetic field (Feldman et al. 1975; Pilipp et al. 1987). For a typical open field line, the electron strahl will travel parallel to an outward polarity field line (0° pitch angle) and antiparallel to a toward polarity magnetic field (180°).

Therefore, at a sector boundary, there should be a reversal in the strahl pitch angle in conjunction with a change of magnetic field direction. However, as outlined by Owens et al. (2013), the sector boundary can present a number of different magnetic and strahl configurations, each indicating a different magnetic topology, as demonstrated in Fig. 3.5. This means that the electron strahl PAD is an extremely important diagnostic tool and is used throughout this chapter to confirm a change in magnetic polarity.

For those spacecraft without such a data product (see Table 3.1), a change of polarity was confirmed with a change of sign in the cross helicity:

$$\sigma_c = 2\frac{\left\langle \vec{v}\cdot\vec{b} \right\rangle}{\left\langle |\vec{v}|^2 + |\vec{b}|^2 \right\rangle}, \tag{3.6}$$

where $\vec{v} = \vec{v_p} - \vec{v_{p0}}$ is the proton velocity fluctuations in the wave frame, $\vec{v_{p0}}$ is the local Alfvén wave phase velocity and $\vec{b} = v_A(\vec{B}/|\vec{B}|)$ (Stansby et al. 2020a). The $\langle\rangle$ symbols indicate that average values were taken over 30-minute intervals following the method of Bruno and Carbone (2013) and Stansby et al. (2019a). This parameter is a proxy for the Alfvénicity and the sign of σ_c indicates the direction of Alfvén wave propagation with respect to the magnetic field, where negative (positive) values correspond to outward (towards) polarity[2]. Since Alfvén waves predominantly travel away from the Sun, σ_c can be used as a proxy for magnetic polarity.

3.2.5 Measuring the local orientation

After identifying and confirming sector boundaries in each spacecraft, the local orientation of the interface was assessed. This was achieved using Minimum Variance Analysis (MVA, Paschmann et al. 1998), which finds the plane with the least variance in the magnetic field. As the spacecraft moves through the HCS, there will be a change in magnetic field direction. Due to the divergence theorem ($\nabla \cdot \vec{B} = 0$), the normal magnetic field component will remain unchanged across a thin interface, such as a current sheet. Therefore, the plane containing the least amount of variance across the boundary will also represent the current sheet normal. The same technique can also be applied to planar magnetic structures (PMSs, Nakagawa et al. 1989), where the magnetic field vectors are forced to lie in a plane due to some compression.

Formally, the variance of a set of K magnetic field vectors, $\vec{B}^{(m)}$, can be written as:

$$\sigma^2 = \frac{1}{K}\sum_{k=1}^{K}\left|\left(\vec{B}^{(k)} - \left\langle\vec{B}\right\rangle\right)\cdot\hat{n}\right|^2, \tag{3.7}$$

where:

$$\left\langle\vec{B}\right\rangle = \frac{1}{K}\sum_{k=1}^{K}\vec{B}^{(k)} \tag{3.8}$$

[2]A value of 0 could indicate lack of Alfvén waves, or equal amounts of counter-propagating waves.

and $\hat{n}$ is the normal direction subject to the constraint that $|\hat{n}|^2 = 1$. To minimise the variance, σ^2, subject to this constraint, Lagrange multipliers can be used:

$$\nabla\sigma^2 = \lambda\nabla\left(|\hat{n}|^2 - 1\right). \tag{3.9}$$

By evaluating this expression, it can be re-written as:

$$\sum_{\nu=1}^{3} M^B_{\mu\nu} n_\nu = \lambda n_\mu, \tag{3.10}$$

where $\nu, \mu = x, y, z$ are the Cartesian components and the magnetic variance matrix is:

$$M^B_{\mu\nu} = \langle B_\mu B_\nu \rangle - \langle B_\mu \rangle \langle B_\nu \rangle \tag{3.11}$$

Finally, it can be seen that equation 3.10 follows the standard eigenvector equation $\mathbf{A}\vec{x} = \lambda\vec{x}$. Consequently, the eigenvectors of the magnetic variance matrix, $M^B_{\mu\nu}$, correspond to the maximum, intermediate and minimum variance directions, when the eigenvalues are sorted in descending order ($\lambda_1 \geq \lambda_2 \geq \lambda_3$). MVA will always produce a set of eigenvectors, but to ensure they represent a significantly low variance direction, it was ensured that $\frac{\lambda_2}{\lambda_3} \geq 5$ (Jones and Balogh 2000; Kilpua et al. 2017).

Following the method of Palmerio et al. (2016), an algorithm that searched for the longest period where $\frac{\lambda_2}{\lambda_3} \geq 5$ by moving a window by 10-minute steps over the boundary was used. The width of the window was increased until it was the same size as the region of interest. Such a procedure was also used to find the orientation of PMSs inside the ICME sheath regions (compressed region ahead of the flux rope). Table 3.2 shows the events used in this thesis, which will be referred to by their unique identifier, e.g. SO_2005XO. The word before the underscore denotes the spacecraft, followed by the two-digit year and month and two random characters for uniqueness.

3.3 Results

3.3.1 Global structure

As discussed in the previous section, the global structure of the solar wind can be mapped by plotting the magnetic polarity at each spacecraft. This procedure was carried out over 6-hour periods for each of the spacecraft, as shown in Fig. 3.6 and 3.7, for CR2231 and CR2232, respectively. The polar plots at the top of each diagram represent a top-down look on the ecliptic plane in the Carrington frame, where the spacecraft constellation consists of three spacecraft at ∼1 AU (Wind, STEREO-A and BepiColombo) and two spacecraft closer to the Sun (Solar Orbiter at ∼0.5 AU, PSP between 0.13 AU and 0.5 AU). To make the connection between spacecraft clearer from the polar perspective, Parker spiral magnetic field lines are plotted along with their associated polarity, from the Wind spacecraft. Therefore, for a consistent magnetic structure, the magnetic polarity at each spacecraft should match the polarity of the Parker spiral field line at that position. This was found to be true for the majority of solar wind observations across the two rotations, where there were periods of persistent outward (red) and towards (blue) polarity consistent across both solar rotations, as expected for the HCS at solar minimum (Hoeksema et al. 1983).

While there was good agreement in magnetic polarity between the different spacecraft, there were some notable periods when the polarity did not match. For example, STEREO-A at 1 AU in O4 (CR2232, Fig. 3.7) measured a consistent towards polarity, seemingly disagreeing with all the other spacecraft. However, this can be reconciled when looking at the distribution of magnetic polarity in latitude, as shown in the lower panels of Figs. 3.6 and 3.7. By removing the radial dependence, using the ballistic mapping technique in Section 3.2.2, the spacecraft can all be compared at the source surface. For this example, it is clear that STEREO-A was at a much lower latitude than the other spacecraft, meaning it measured towards polarity on the other side of the HCS. It is important to note that the mapped longitude in

the lower panels is always higher than the Carrington longitude in the polar plots, according to equation 3.4.

By comparing the magnetic polarity of different spacecraft over the two rotations, it is clear that only a few degrees of latitude can drastically change the solar wind conditions experienced. This corroborates previous findings (Schwenn 1990; Owens et al. 2020b), and means that latitude should always be considered when comparing solar wind at different spacecraft.

While a similar mapping technique has been applied previously to spacecraft data (Schwenn et al. 1978), this chapter had unprecedented detail covering $\pm 10^{\circ}$ latitude, which allowed for the global structure of the solar wind to be resolved using only in situ measurements (Figs. 3.6 and 3.7). The same could be said of the speed structure in Figs. 3.8 and 3.9, which showed several persistent high-speed streams and CIRs (grey highlights). These, and several transient events (Table 3.2), were associated with an increase in field magnitude strength (represented by an increased scatter point area), and will be investigated later in this chapter.

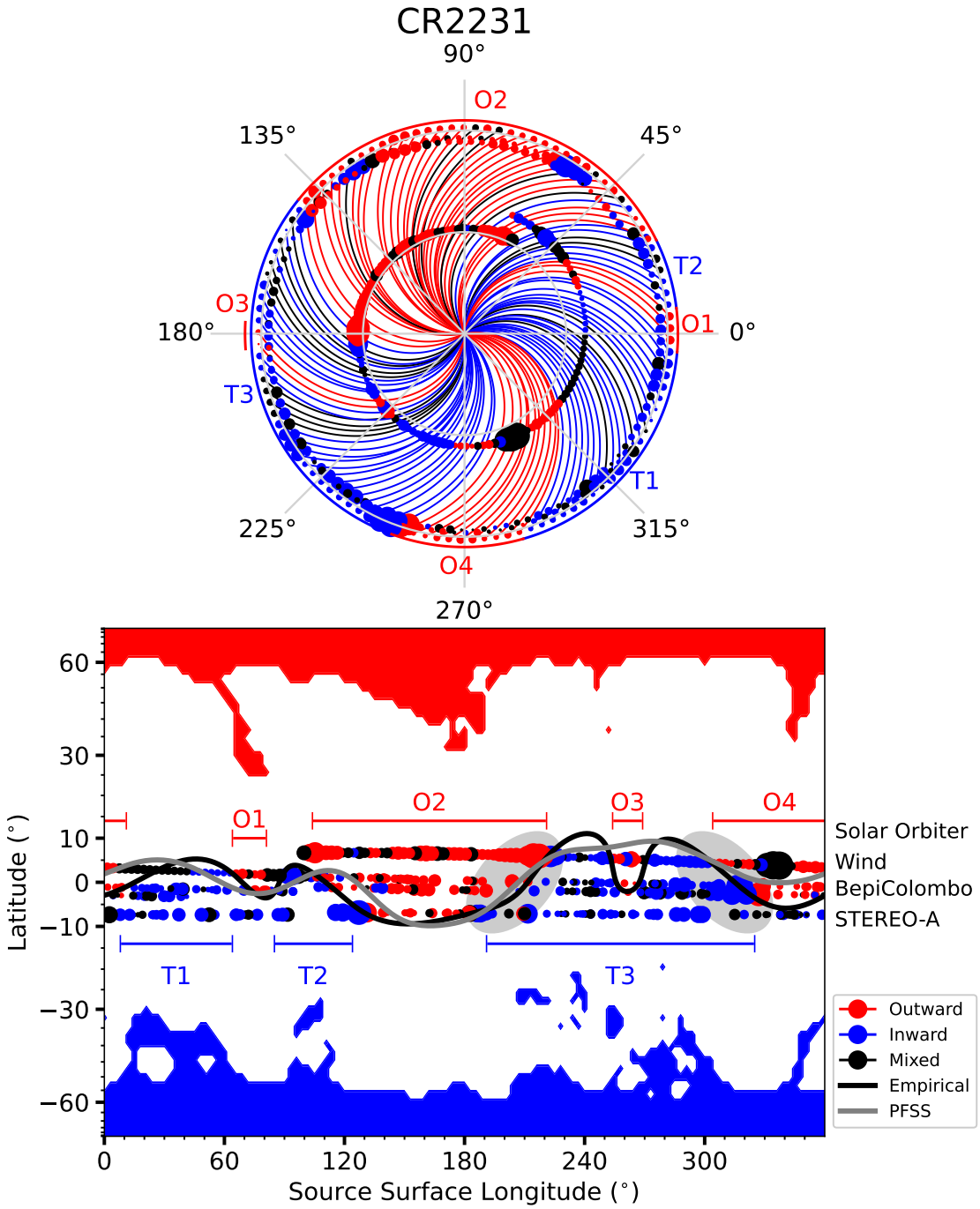


Figure 3.6: Polarity structure for the CR2231 rotation as mapped by the in situ measurements from the different spacecraft used in this thesis. The colour of the scatter points represents the average magnetic polarity in a 6-hour window, with the area being proportional to $|\vec{B}|^2$ to highlight any compressions. A clear sector structure can be seen, with three towards and four outwards sectors. Drawing a line through the changes in polarity gives the 'empirical' HCS (black line), which compared well with the PFSS model (grey line). CIRs are highlighted by the grey ellipses, which were identified using the velocity and density measurements in Fig. 3.8.

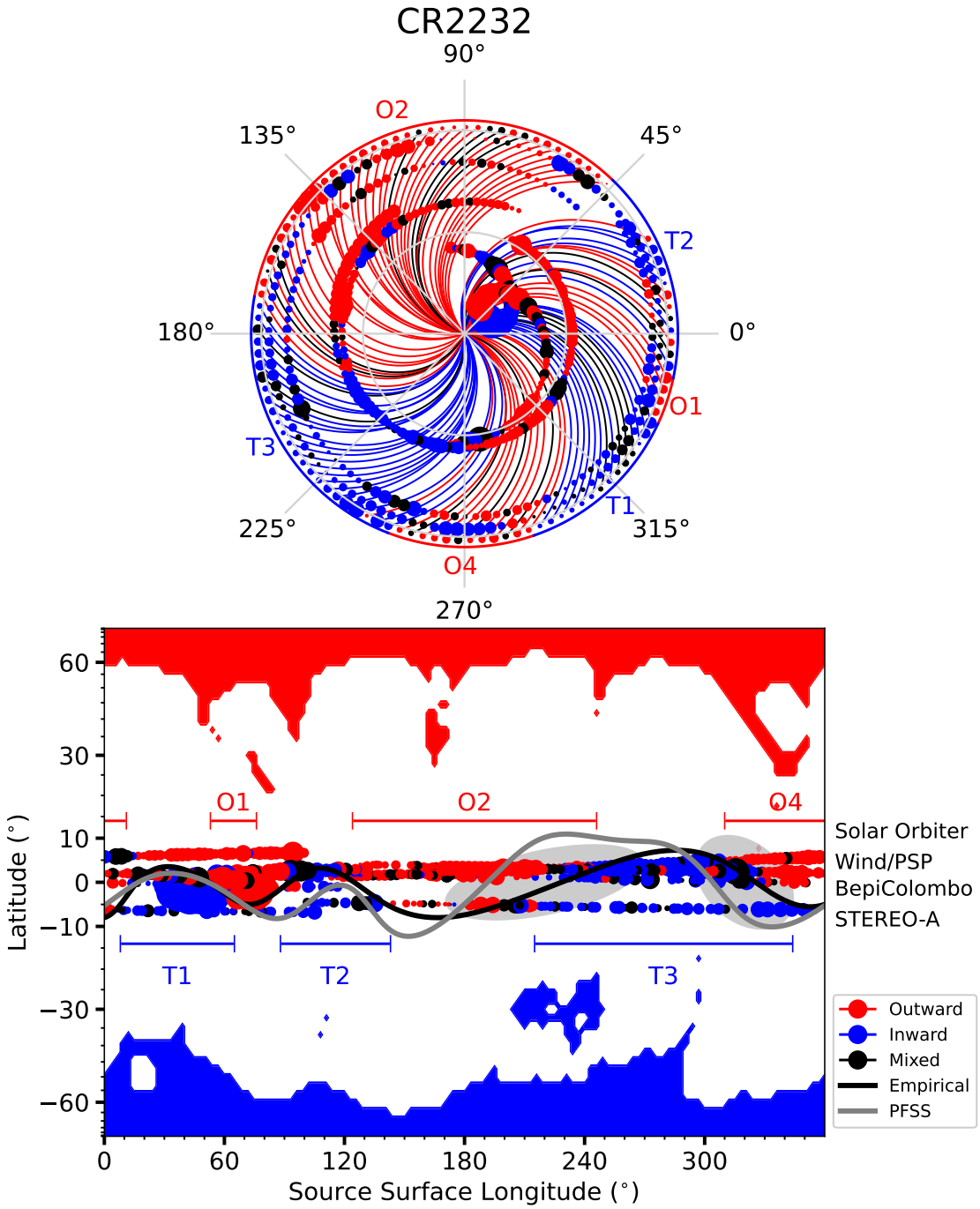


Figure 3.7: Polarity structure for the CR2232 rotation, in the same form as Fig. 3.7. From the outside inwards on the polar plot, the spacecraft are: Wind, STEREO-A, BepiColombo, Solar Orbiter and PSP. Again, there was a clear polarity sector structure, which matched the previous rotation well except for the lack of O3. The empirical HCS had a lower latitudinal extent than the PFSS model in this case. CIRs are highlighted by the grey ellipses, which were identified using the velocity and density measurements in Fig. 3.9. Due to PSP co-rotating with the Sun, it overlapped both Carrington rotations, but was best aligned with other spacecraft for CR2232.

Tracing the boundaries between these magnetic sectors, and confirming with the electron strahl PADs (not shown), the shape of the HCS can be mapped, which is referred to here as the 'empirical HCS' (solid black line). Comparing with the results from a PFSS model[3] (grey line), Figs. 3.6 and 3.7 demonstrate good agreement on the overall morphology of the HCS, e.g. O2 had good agreement for both rotations. Although the general shape was correct, there were clear discrepancies between the PFSS model and empirical HCS for some magnetic sectors, e.g. O4 in CR2231 (Fig. 3.6).

These stark differences between model and spacecraft are obvious when plotted in longitude vs latitude. Typically, such coronal models are validated by flying a virtual spacecraft through the simulation and comparing the result to the in situ time series. By comparing the magnetic polarity of Solar Orbiter and STEREO-A in CR2231 (Fig. 3.6), it is clear that such a method of validation is inherently flawed, as even small changes in latitude can lead to a different magnetic polarity between two spacecraft. It is therefore recommended that solar wind models are compared in both longitude and latitude, converting spacecraft data into the simulation domain, rather than converting 3D simulation data into a time series. If the latter is still preferred, then modellers should introduce some uncertainty in the virtual spacecraft latitude, which would help capture some of the variation in this dimension.

In summary, the results above show that the new constellation of spacecraft can be used to provide enhanced mapping of the solar wind structure. While the PFSS model captured the general shape of the HCS, the in situ measurements represented a more true representation of the solar wind. Since the HCS was flat over the two solar rotations, small changes in latitude led to a significant change in the solar wind conditions, which may prove important for future space weather predictions.

[3]Using magnetograms from 2020-06-01 for CR2231 and 2020-07-01 for CR2232

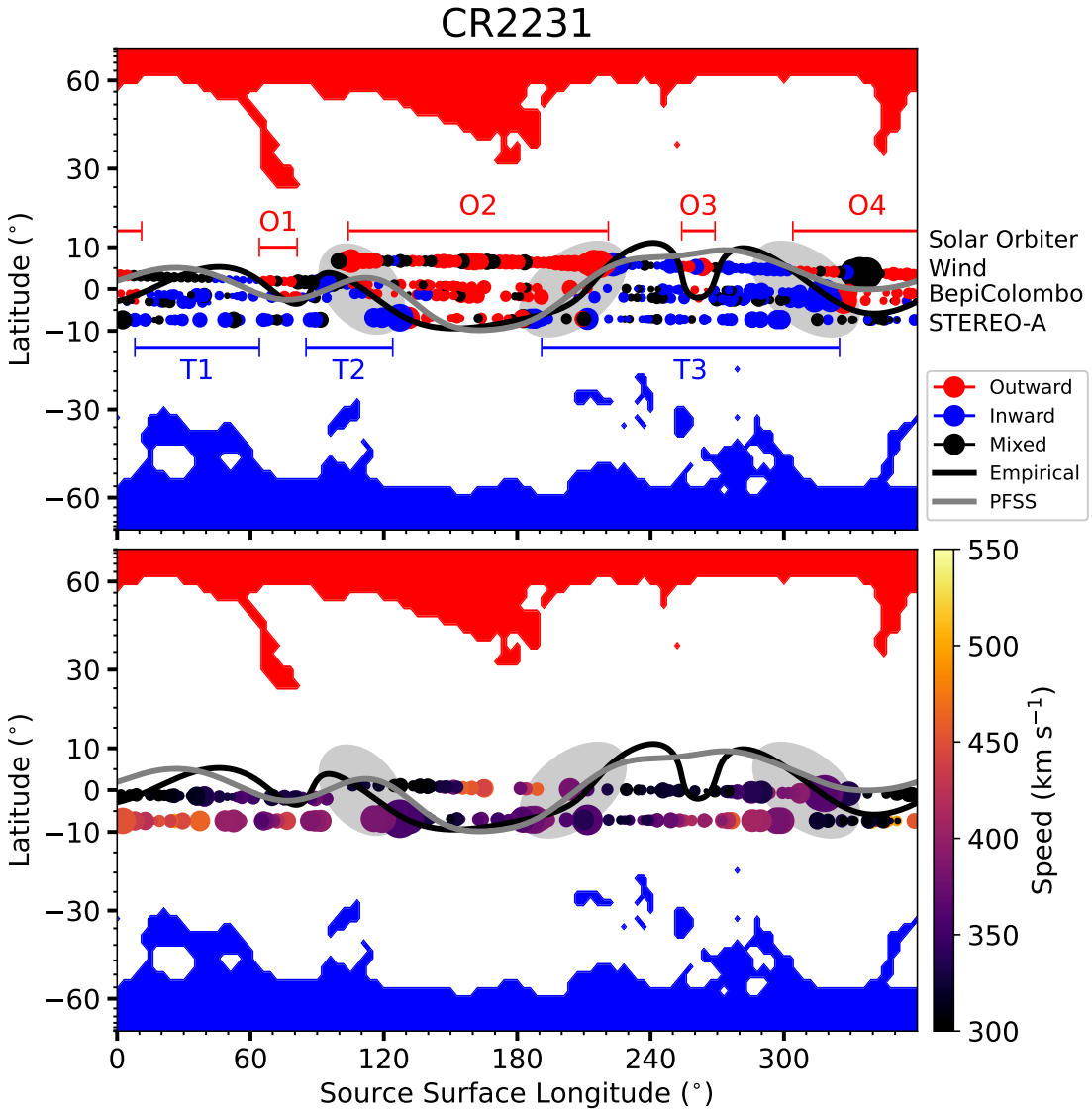


Figure 3.8: Polarity and speed profiles for the CR2231 rotation, where only Wind and STEREO-A measured the full plasma parameters. Several CIRs are highlighted (grey ellipses) which are characterised by their increased $|\vec{B}|$ (dot area $\propto |\vec{B}|^2$) and speed increase (colour scale). Fig. 3.14 looks at the CIR $\sim$200° in more detail.

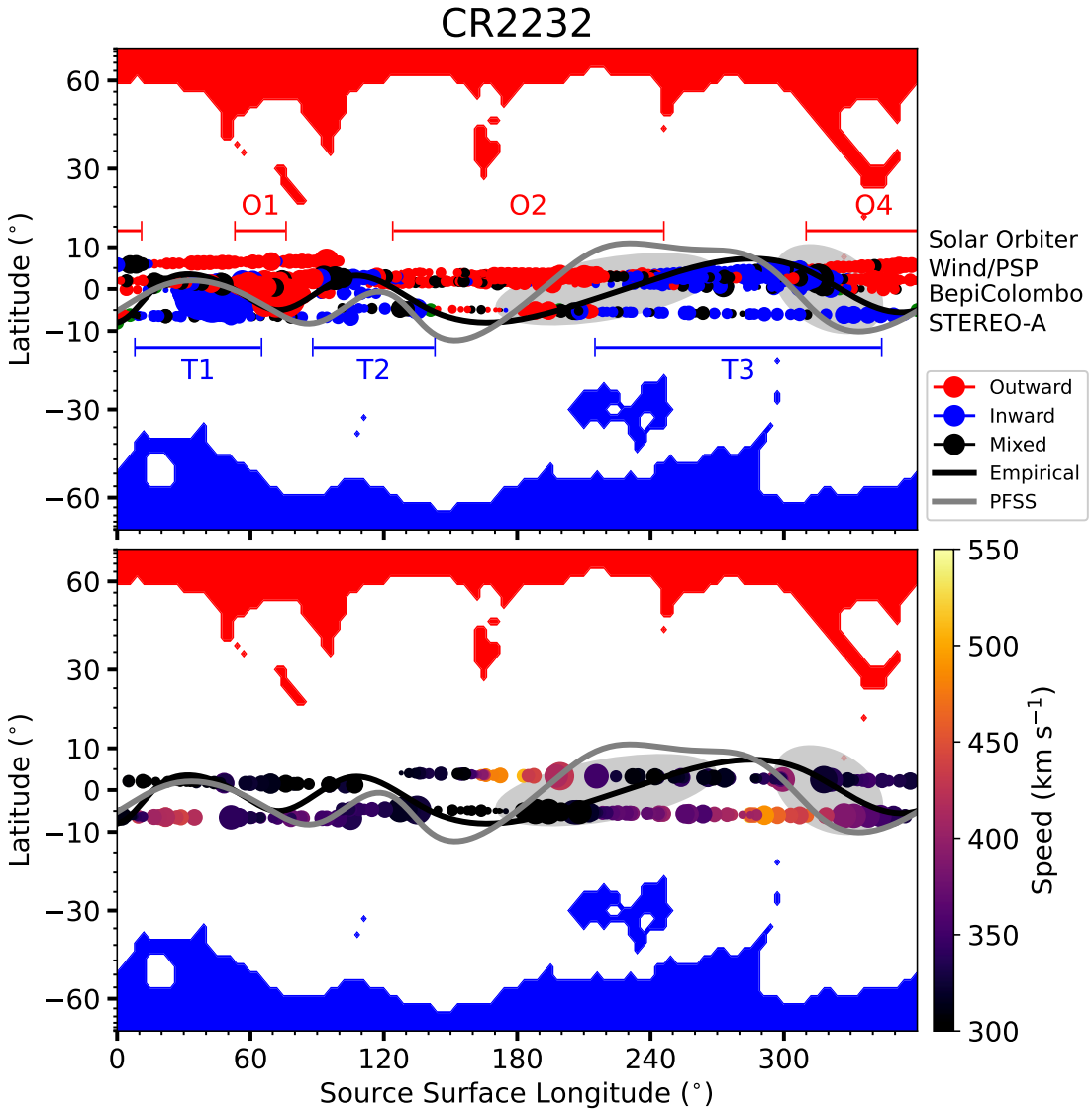


Figure 3.9: Polarity and speed profiles for the CR2231 rotation, with CIRs highlighted in the grey ellipses. Although PSP did measure speed close to the Sun, this is much lower than at 1 AU and is not included here. The two CIRs ∼200° and ∼300° are still visible from the previous rotation.

3.3.2 Local orientations of the sector boundaries

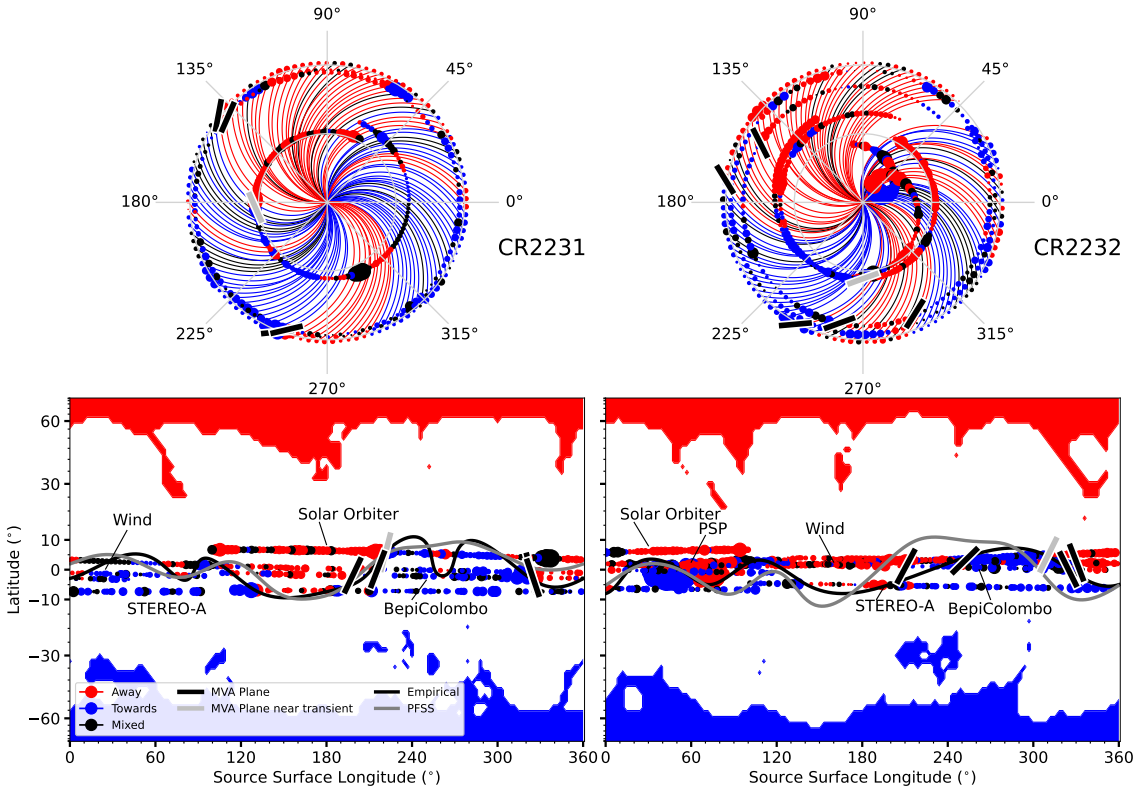


Figure 3.10: Local orientations of sector boundaries, as measured by MVA (Section 3.2.5). In general, these orientations were as expected from the empirical HCS and PFSS model, but were much steeper. Those times with a transient event nearby are coloured grey. This may have influenced the orientation, as investigated in Section 3.3.5 (reproduced with permission from Astronomy & Astrophysics, ©ESO Laker et al. 2021a).

The study also included an investigation into how well the PFSS model compared to the local orientation of the sector boundaries, as measured by MVA (Section 3.2.5). As Fig. 3.10 demonstrates, there was good agreement in the ecliptic plane, with the local orientations (thick lines) matching the expected Parker spiral. The same was true for the local inclination of the HCS, in the lower panels, when compared to the PFSS model, except in those cases where a transient event was seen in proximity to the sector boundary (coloured grey). While this agrees with previous results at solar maximum (Klein and Burlaga 1980; Burton et al. 1994; Peng et al. 2017), the local inclinations were much steeper than expected from a flat current sheet seen in both the empirical and PFSS model. This was most likely

caused by the presence of stream interactions, which compressed and warped the HCS, an effect that is known to be significant far from the Sun ($\geq$2 AU Pizzo 1994b; Riley et al. 2002). Ideally the steepening with distance from the Sun would have been measured, but in this study the sector boundaries closer to the Sun were all associated with transient events (Table 3.2), so would not provide reliable results. To confirm this hypothesis, future studies should evaluate more sector boundaries over a greater period of time.

Event	Date	Type	Φ (°)	Θ (°)	r (AU)	Φ_{SS} (°)	MVA Start End	MVA (ϕ, θ) (°, °)	λ_2/λ_3
SO_2005XN	29/05/2020 00:00	ICME	290	3.9	0.56	330	-	-	
BC_2005OW	29/05/2020 15:30	HCS CIR	252	-2.7	0.97	325	29/05/2020 08:20 30.05/2020 08:20	(31, 23)	18
Wind_2005AW	30/05/2020 04:18	HCS CIR	250	-0.9	1.01	320	29/05/2020 15:51 30/05/2020 15:51	(27,18)	13
BC_2006LP	06/06/2020 18:30	HCS CIR	140	-1.9	0.95	198	07/06/2020 01:50 07/06/2020 13:50	(17,-31)	5.2
Wind_2006HR	07/06/2020 12:00	HCS CIR	140	0.1	1.01	216	07/06/2020 03:48 08/06/2020 03:48	(28, -26)	5.9
SO_2006ZS	07/06/2020 18:00	HCS CIR ICMEs	184	5.9	0.53	220	07/06/2020 16:10 08/06/2020 16:10	(20, -18)	11
BC_2006YZ	22/06/2020 21:00	HCS	295	-0.2	0.9	375	22/06/2020 14:30 23/06/2020 02:30	(31, -16)	10.5
BC_2006YU	25/06/2020 14:00	HCS CIR	260	0.1	0.89	325	25/06/2020 10:00 25/06/2020 22:00	(33, 32)	17.5
PSP_2006XO	26/06/2020 00:00	ICME	280	2.4	0.52	316	-	-	
Wind_2006JJ	26/06/2020 13:00	HCS CIR	241	2.4	1.02	330	26/06/2020 13:00 27/06/2020 13:00	(34, 26)	10.2
SO_2007KG	02/07/2020 04:00	HCS	270	5	0.56	310	01/07/2020 22:00 02/07/2020 10:00	(20, -32)	6.1
Wind_2007BU	02/07/2020 11:00	HCS CIR	170	3	1.02	250	02/07/2020 14:05 03/07/2020 02:05	(41, -52)	7.2
BC_2007JH	03/07/2020 23:00	HCS CIR	150	1.1	0.86	210	03/07/2020 17:50 03/07/2020 23:50	(57, -34)	6

Table 3.2: List of events used in this thesis. The string before the underscore denotes the spacecraft that made the measurement; the digits represent the two-digit year and month, with the final two random characters differentiating the events within each month. MVA was used to determine the orientation of the boundary and was left blank for ICMEs.

3.3.3 Fine-scale structure

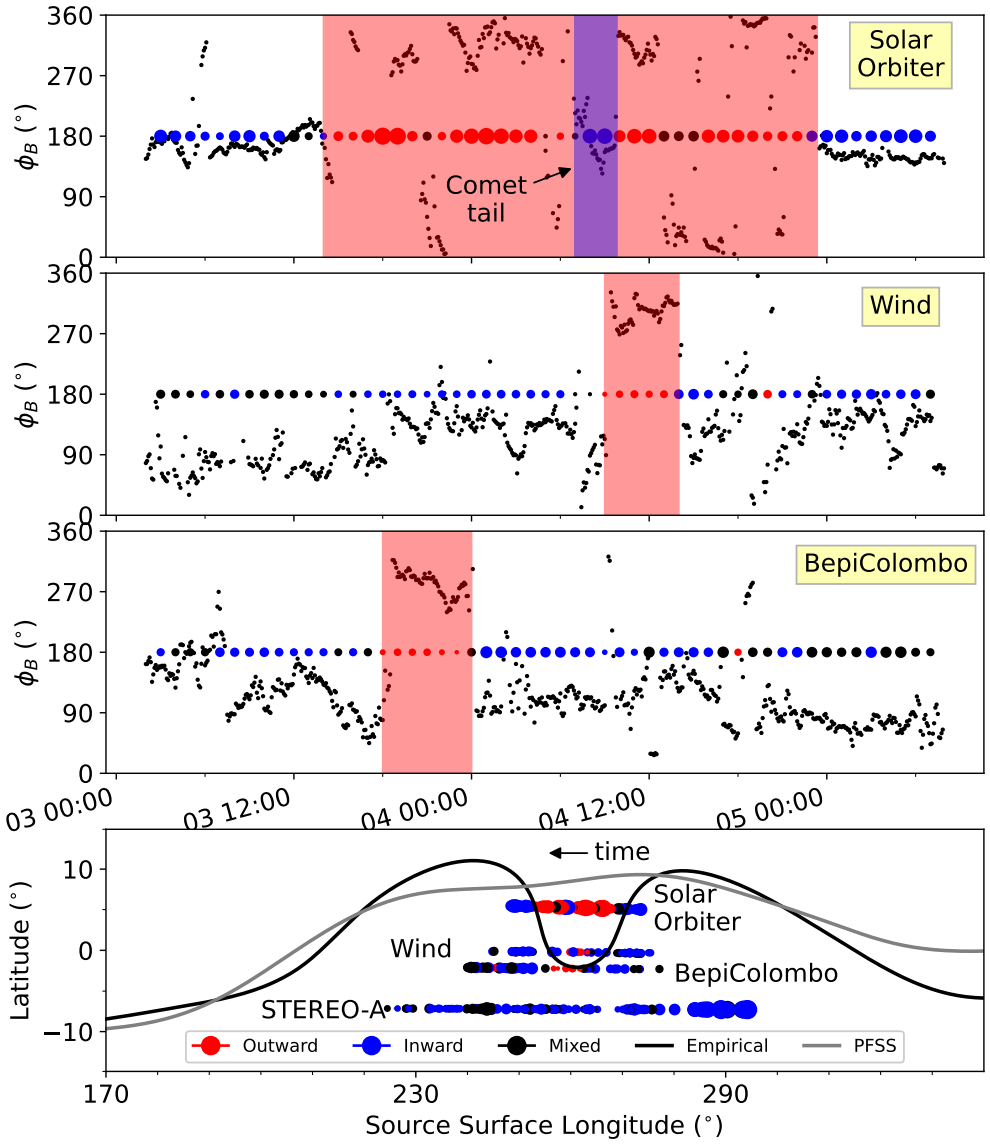


Figure 3.11: A more detailed look at the fine-scale warp in the HCS, which can be seen as O3 in CR2231 (Fig. 3.6). The lower panel shows the data on a longitude against latitude map, with the same data plotted against time in the panels above. Note that the spacecraft move towards lower longitudes over time in the bottom panel. ϕ_B is the angle of the magnetic field in the R-T plane, which was used to classify the polarity of the magnetic field as defined in Fig. 3.4. The top panel shows that Solar Orbiter, at the highest latitude, measured a long outwards polarity (red), with a small towards polarity structure inside (blue). Two hours later, BepiColombo measured the same outwards sector, followed by Wind ∼12 hours later.

The spread in spacecraft latitude can also provide contextual information, allowing for the identification of structures that would otherwise not be possible with

a single spacecraft. Fig. 3.11 shows a more detailed look at O3 in CR2231 (Fig. 3.6), which was observed by Solar Orbiter, Wind and BepiColombo from 5.4° to −2.3° latitude. This short inversion of magnetic polarity lasted ∼15° longitude in Solar Orbiter, but only ∼5° in BepiColombo and Wind, suggesting that this was a rounded dip in the HCS towards lower latitudes as depicted by the empirical HCS line.

The leading HCS crossing was first observed by Solar Orbiter at 16:00 on June 3rd 2020 at 0.5 AU, and was subsequently seen by BepiColombo 2 hours later at 0.97 AU, and Wind a further 13 hours later. For the longitude separation between BepiColombo and Wind, a co-rotating structure would be expected to appear ∼12 hours later. This, and the timing between Solar Orbiter and BepiColombo, led to the conclusion that this structure was indeed a fine-scale ripple in the HCS, similar to those proposed by Villante et al. (1979) and Gosling et al. (1993). An advantage of the study presented here is that the spread in latitude allowed the shape of the ripple to be directly measured as 15° in longitude at its widest. Since STEREO-A, at −7° latitude, did not observe a change in magnetic polarity, the lowest latitude extent of the ripple was between −2.3° and −7° latitude. This was likely to be closer to −2.3°, as STEREO-A (at −7° latitude) measured a slowly declining solar wind speed consistent with the trailing edge of a HSS, rather than the streamer belt wind that usually surrounds the HCS.

During this time, Solar Orbiter was predicted to encounter the tail of comet ATLAS (Jones et al. 2020). The classification of an outward polarity region was crucial for the context of Solar Orbiter measurements, which did not have plasma or electron data available. Although this period (O2) was classified as being outwards polarity, the Solar Orbiter measurements showed another field reversal that was not part of the BepiColombo or Wind data. Such a feature, combined with the presence of exotic wave activity not normally found in the solar wind, helped Matteini et al. (2021) to conclude that this period was associated with the tail of comet ATLAS. Those authors explored this idea in more detail, further reconstructing the draping

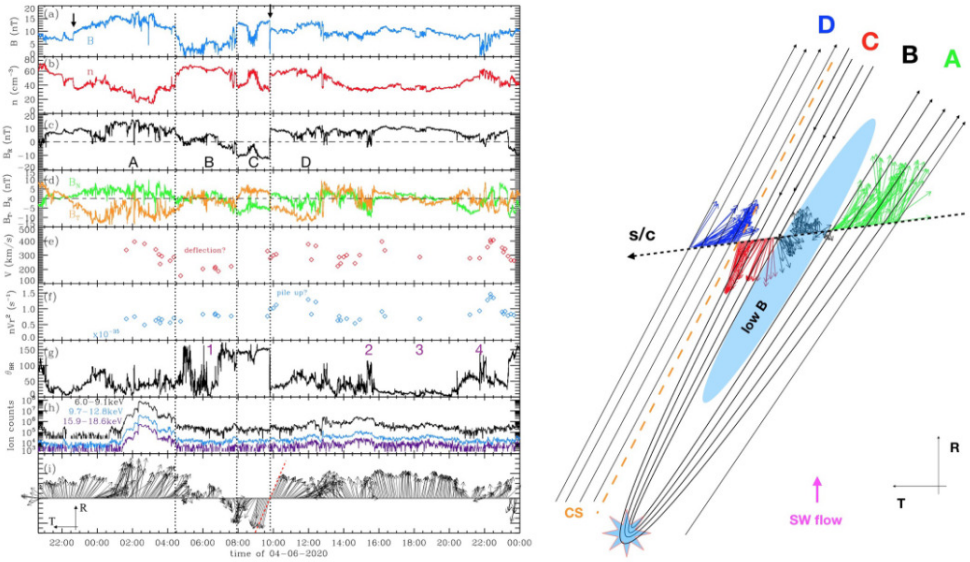


Figure 3.12: Left panel shows Solar Orbiter data from June 4th 2023, which has been interpreted as draping from a comet tail by Matteini et al. (2021) in the right diagram. This same period of data represents the change in magnetic field direction (labelled comet tail) in Fig. 3.11 (reproduced from Matteini et al. 2021).

of the magnetic field around the comet (see Fig. 3.12), as well as investigating the unusual wave activity.

As a result, by combining the data from different spacecraft, solar wind could be measured at a higher resolution than in the PFSS model, which helped provide context for each spacecraft. This was especially valuable for the early stage of the Solar Orbiter mission, where the classification of a comet tail would not have been possible with only magnetic field data from one spacecraft.

3.3.4 Co-rotating interaction region in latitude

The spread in spacecraft latitude also allowed for detailed study of a CIR around 200° mapped longitude in CR2231 (Fig. 3.8), as measured by Wind, STEREO-A, BepiColombo and Solar Orbiter. Until now, the majority of CIR studies have relied on a large catalogue of events built up over several solar rotations, with any insights being based on statistical averages. However, the current collection of spacecraft in the inner heliosphere now enables the investigation of individual CIRs from new perspectives, which can lead to a better understanding of their complex dynamics.

The spacecraft measurements in Fig. 3.10 show that the longitude of the sector boundary decreased with decreasing latitude, visually marking the tilt of the CIR, which was further confirmed by the local orientation of the stream interfaces (Wind_2006HR, BC_2006LP). This tilt, and the outward polarity of the HSS in Wind, meant that the HSS originated from the northern hemisphere, most likely the northern polar coronal hole. Although Solar Orbiter did not have plasma measurements, there was a clear increase in the large-amplitude Alfvén waves, normally associated with fast solar wind streams (Belcher and Davis Jr. 1971).

Solar Orbiter also observed a very complex magnetic structure as a result of the combination of a HCS crossing, CIR and two CMEs (SO_2006ZS). The multi spacecraft measurements of this event helped uncover the structure of this event, which contributed to a more detailed study by Telloni et al. (2021a). For the purposes of this thesis, it is only important to note that this occurred for Solar Orbiter at 18:00 on June 7th 2020, at 0.5 AU, after all the other spacecraft. Therefore, these CMEs were not considered in the other spacecraft for this particular event, with the focus being on the CIR and HCS crossing.

While being able to visually map the CIR tilt is a new capability in the inner heliosphere, perhaps the most interesting feature can be seen by comparing the measurements from Wind and STEREO-A in Fig. 3.13, at 1° and −7° latitude, respectively. Wind (black line) saw typical CIR signatures, with a gradient in the speed accompanied by a compression (n_p and $|\vec{B}|$ both increase) along with a characteristic east-west deflection in velocity (fifth panel). The electron strahl PAD in the lower panels confirm that this was also a sector boundary. Interestingly, STEREO-A observed similar increases in n_p and $|\vec{B}|$, but only a 30 km/s increase in speed, far below the 165 km/s increase seen by Wind. This leads to the conclusion that STEREO-A, at −7° latitude, measured the compression of the CIR, without measuring the fast stream that caused it.

This can be explained by considering the tilt of the CIR, outlined in Fig. 3.14, which introduced a southern component to the forward propagating compression,

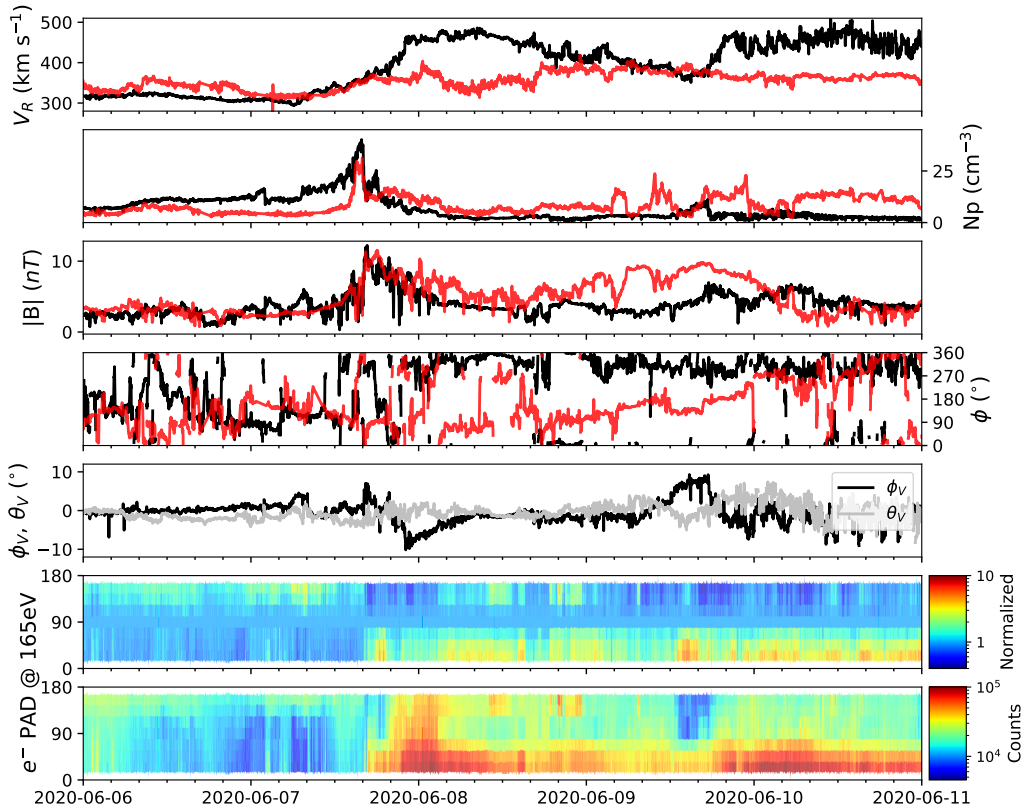


Figure 3.13: CIR observed around ∼200° in CR2231, between T3 and O2, as measured by Wind (1°, black) and STEREO-A (−7°, red). Wind saw two fast streams, along with increases in n_p and $|\vec{B}|$ and the signature east-west deflection (fifth panel). The electron strahl PAD are shown in the lower panels, confirming that this was also a sector boundary. STEREO-A did not measure the same gradient in speed, only a 30 km/s increase, yet still observed similar increases in n_p and $|\vec{B}|$ (reproduced with permission from Astronomy & Astrophysics, ©ESO Laker et al. 2021a).

making it travel to lower latitudes. By 1 AU, the compression region had extended low enough in latitude that STEREO-A could travel through without seeing the fast stream above. This is the same principle that dictates the evolution of the forward and reverse shocks (which are steepened versions of the compression and rarefaction regions) farther from the Sun, which leads to only reverse shocks being seen at high latitudes ≥30° (Gosling et al. 1993).

Similar compressions, without an obvious cause, have been observed previously with Voyager (Burlaga 1983), but, without other accompanying spacecraft, those authors were only able to speculate on the cause of these events. Whereas, in Fig. 3.14, the CIR was studied from multiple positions, giving a clearer picture of the evolving dynamics.

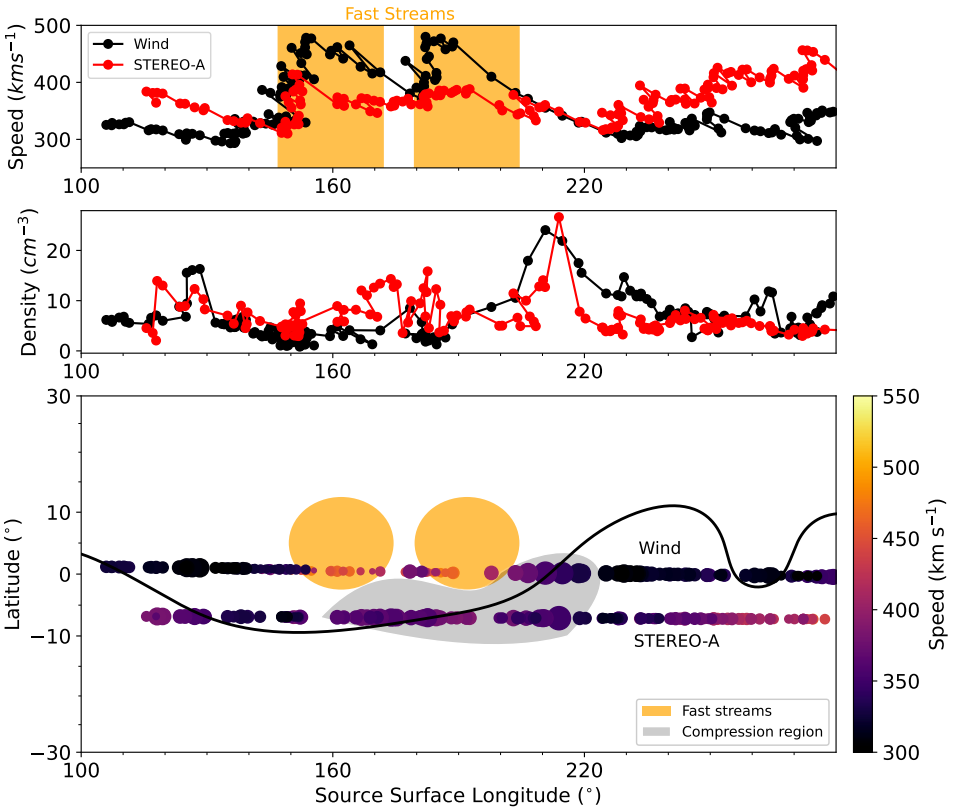


Figure 3.14: A more detailed look at the CIR at ∼200° longitude from Fig. 3.8. The time series of solar wind speed and density is plotted in the top panels, which are also the colour and area of the scatter points in the map in the lower panel. Wind measures the two HSS, shown as yellow ellipses, which created a compression region that extended to lower latitudes and was then seen by STEREO-A.

While this is an elegant demonstration of the 3D structure of a CIR, it could also be important for space weather predictions, which are commonly caused by CIRs at solar minimum (Richardson et al. 2001). For example, if a spacecraft measures a CIR that will rotate around to Earth, it may be possible to calculate the separation in latitude that would change the conditions seen by Earth. Such knowledge could help reduce the number of false positives (Owens et al. 2020a), which is an important step in the planning of future space weather missions at L5 Lagrange point (Kraft et al. 2017).

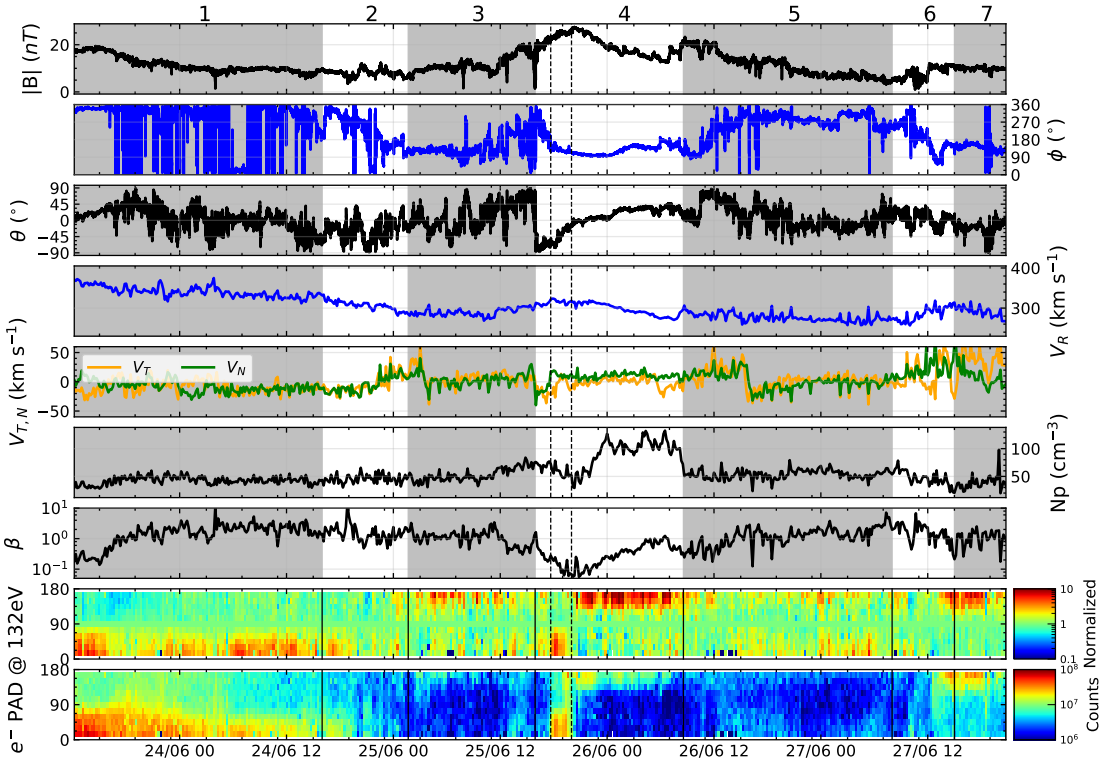


Figure 3.15: Time series of a sector boundary observed by PSP, with ambient solar wind conditions seen in regions 1 and 7, and the transient event (PSP_2006XO) appearing in region 4. This was classified as an ICME due to the decreasing radial speed, reduction in V_R, and smooth magnetic field rotation. The penultimate panel shows the electron strahl PAD, normalised to its value at 90°. The lower panel shows a lack of bidirectional electrons in region 4 meaning that this ICME was only connected to the Sun at one end (reproduced with permission from Astronomy & Astrophysics, ©ESO Laker et al. 2021a).

3.3.5 Effect of transient structures on the heliospheric current sheet

In addition to the co-rotating structures described above, several transient events were observed in association with sector boundaries. In this section, several observations of the same sector boundary are used to assess the effect of transients on the HCS.

PSP observed a flux rope structure at a sector boundary around 0.5 AU and 280° longitude (PSP_2006XO), as shown in Fig. 3.16. While an apparently similar event was observed at the same location by Solar Orbiter on the previous solar rotation (SO_2005XN), this was not a co-rotating structure. The absence of this event in other spacecraft, as well as a low plasma β and a smoothly decreasing radial speed,

were indicative of an ICME (Zurbuchen and Richardson 2006; Richardson and Cane 2010). Looking in more detail at Fig. 3.15, a flux rope structure can be seen (region 4), which sits between the change in magnetic sector (regions 1 and 7), as inferred from the electron strahl direction in the bottom two panels. The lack of bidirectional electron strahl in the flux rope suggests that this represents an open ICME, with only one 'leg' connected to the Sun, which is a common signature for flux ropes inside sector boundaries (Crooker et al. 2004). In summary, it is clear that this sector boundary had a transient ICME event at 0.5 AU on June 26th 2020.

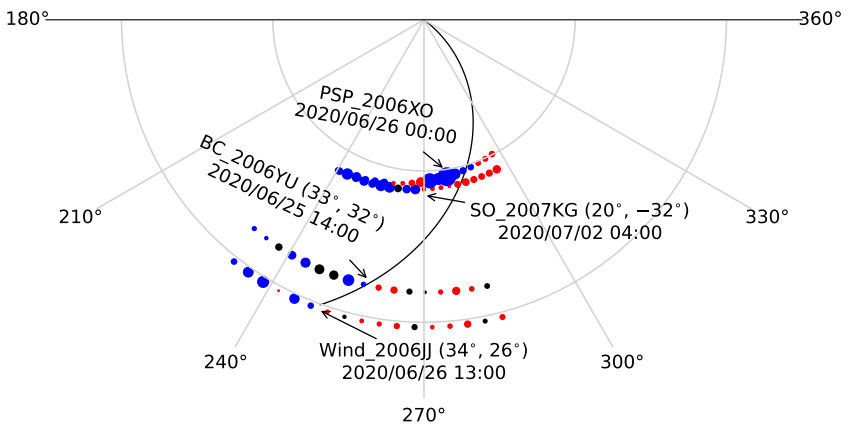


Figure 3.16: Spacecraft configuration in the ecliptic plane of the Carrington frame, similar to Fig. 3.7. PSP observed a transient structure, PSP_2006XO, at a sector boundary. Wind and BepiColombo observed the same boundary at a similar time, seeing the same orientation. A few days later, Solar Orbiter measured the sector boundary with a flipped orientation, suggesting that the transient event at PSP influenced the HCS.

The same sector boundary was also observed by Wind and BepiColombo at a similar time at ∼1 AU, which represents an earlier configuration of the same source region. The timings and location of the measurements are depicted in Fig. 3.16, along with the measured orientations from MVA. Wind observed a small increase in $|\vec{B}|$ and n_p, suggesting a weak CIR (Wind_2006JJ). Using MVA, the orientation of

the sector boundary was found to be (34°ϕ, 26°θ) and (33°ϕ, 32°θ) in Wind_2006JJ and BC_2006YU, respectively.

In contrast, Solar Orbiter crossed the same sector boundary at the same location as PSP but ∼5 days later, with an orientation of (20°ϕ, −32°θ) in SO_2007KG. Therefore, at Solar Orbiter, the HCS had the opposite inclination when compared to the other spacecraft and the PFSS model. Combined with the ICME at PSP, this suggests that the change in boundary orientation was in fact due to the HCS reforming after the passage of the transient event. While it is well known that the HCS can reform after a CME, the timescale of this is still debated (Blanco et al. 2011; Zhao and Hoeksema 1996). If the Solar Orbiter measurements do represent a reforming HCS, then this puts a lower limit of ∼5 days. This is consistent with the timescales found using numerical models (3-5 days, Temmer et al. 2017; Desai et al. 2020).

Due to the lack of plasma measurements at Solar Orbiter this claim remains speculative, although, it does serve to demonstrate that data from multiple spacecraft can be pieced together to better understand the effects of transient events in the solar wind.

3.4 Conclusions

This chapter explored how the newly formed spacecraft constellation can be used to provide new insights regarding the inner heliosphere. Despite the absence of plasma data from several spacecraft, the global structure of the HCS was successfully mapped using only in situ measurements. Specifically, it was shown that the:

- Sector structure could be resolved with five separate spacecraft spanning ±10° latitude
- HCS was especially flat in the study period, meaning that small changes in latitude could drastically affect the solar wind conditions experienced by a spacecraft

- In situ data could be used to validate the PFSS model, as well as resolving finer scale structure than the model

This final point has implications for the testing of any solar wind model. Instead of converting simulation data into a time series and comparing to in situ measurements, it was demonstrated that the new constellation of spacecraft can now map polarity/speed in both longitude and latitude, facilitating direct comparison to simulation data. This capability could be used to validate simulations more effectively in the future.

There was also a demonstration of how the data from several spacecraft could be combined to create a clear picture of the large-scale dynamics, which would not have been possible otherwise. Significant findings included:

- Observing a fine-scale ripple in the HCS ($\sim$15° longitude, $\sim$5° latitude)
- Classifying a period within this ripple as being related to Comet ATLAS, see Matteini et al. (2021)
- Determining how a CIR varied in latitude, including an observation of a compression region without an accompanying fast stream
- Observing a sector boundary before, during and after an ICME, finding evidence of HCS distortion lasting $\sim$5 days

Therefore, by using other spacecraft, researchers can now be more confident about the context of a solar wind measurement, which opens up new research opportunities, e.g. measuring the bottom of a CIR or skimming the HCS.

Finally, it is important to note that these spacecraft were not specifically designed to collaborate, but, combining their measurements creates a multi-spacecraft mission in the solar wind. The results presented in this chapter summarise the fortuitous alignments of spacecraft in a two-month period. Given the evolution of each mission over time – PSP to closer distances; BepiColombo to Mercury; Solar Orbiter to higher latitudes – there will be plenty of new research opportunities in the future.

Chapter 4

Properties of solar wind switchbacks

Switchbacks are large deflections in the magnetic field that have become a highly active area of research due to the early PSP measurements (Bale et al. 2019; Kasper et al. 2019). These structures had been seen by previous spacecraft (Horbury et al. 2018; Balogh et al. 1999), but it was the dominance of the PSP data, see Fig. 4.1, which led to speculation that they could be an important driver of the solar wind. This chapter characterises several key switchback properties, with the aim of determining their origin. Since PSP has returned new data roughly every three months, the understanding of switchbacks has continued to evolve over time. Therefore, in this chapter, context is given for the state of switchback research where appropriate.

Section 4.1 first describes many of the known switchback properties, while Section 4.2 discusses the different ways in which they could be generated. The method of switchback identification is outlined in Section 4.3. The average size and shape of switchbacks is then investigated in Section 4.4, which also explains the link between switchback duration and deflection direction. This research represents work carried out in Laker et al. (2021b), using data from the first two PSP encounters (November 2018-April 2019).

In subsequent encounters, switchbacks remained an important research topic. Based on the early PSP measurements, some authors have argued that switchbacks tended to deflect towards the $+\vec{T}$ direction (Schwadron and McComas 2021), or at least have a preferred deflection direction (Fisk and Kasper 2020). Evidence

for such deflections, or lack of, would help distinguish between several switchback generation methods. Section 4.5 addresses these claims, and presents an analysis of the switchback deflection directions across the first eight PSP encounters (November 2018-May 2021), which was carried out in Laker et al. (2022).

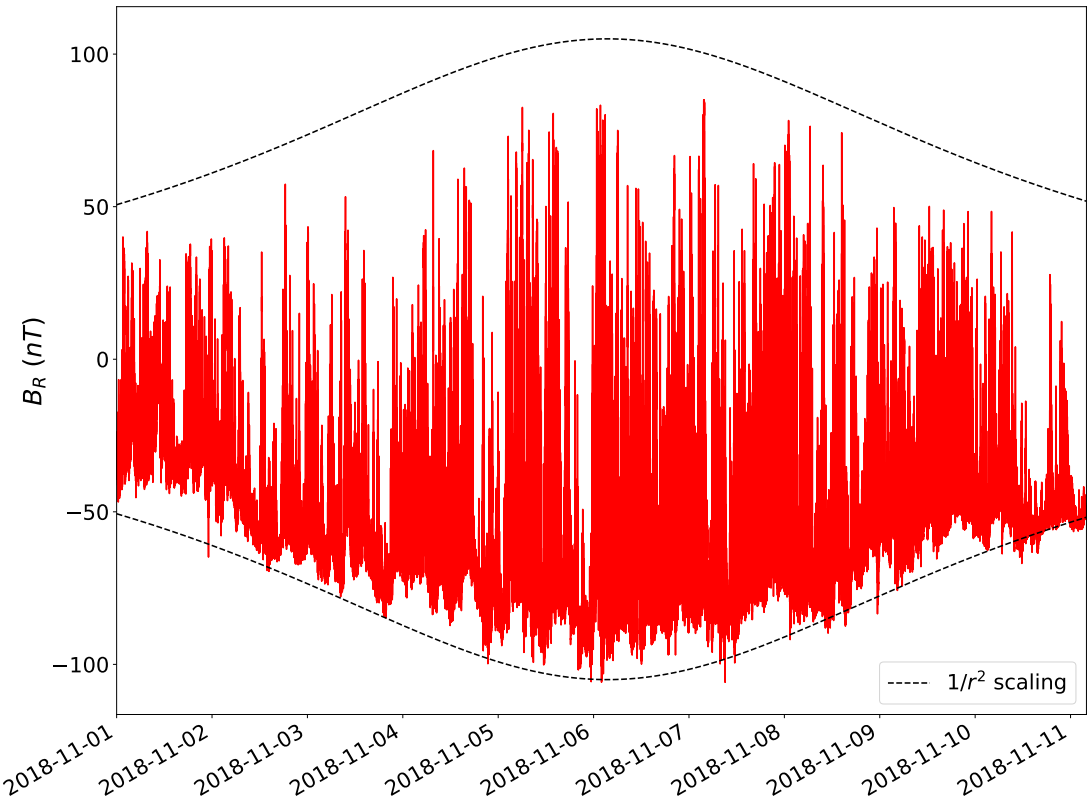


Figure 4.1: Radial magnetic field measurements from the first PSP encounter in 2018. Expected $1/r^2$ scaling is shown in black, with switchbacks being large magnetic field deflections, leading to almost full reversals in B_R.

4.1 Switchback properties

In their most basic description, switchbacks are just magnetic field deflections away from some background direction. However, they also have some other key characteristics that will be described in this section, which can help provide clues to their origin.

One of the most defining features of switchbacks is that they are Alfvénic fluc-

tuations, leading to the associated velocity fluctuations appearing as spikes in the solar wind speed profile (Gosling et al. 2009; Matteini et al. 2014). As discussed in Section 2.4.2, the magnetic field and velocity fluctuations should be confined to a sphere of constant radius of $|\vec{B}|$ and v_A, respectively. Such behaviour has been confirmed for switchbacks in the PSP data (Woolley et al. 2020), leading to a maximum speed increase of $2v_A$ for a full magnetic field reversal (180°).

The magnetic field inside switchbacks is not seen to rotate past 180°, and even appears to be 'arc polarised' (Tsurutani et al. 1994; Bruno et al. 2004; Horbury et al. 2020b). Therefore, for a typical switchback the magnetic field will deflect along the arc of a sphere, and then return along the same arc. The direction in which the magnetic field deflects away from the background is an important property for the investigations in this chapter, and is described by a 'clock angle' in Section 4.3.1.

The Alfvénic nature of switchbacks also means that the ion populations will rotate with the magnetic field, which has been observed for both the alpha (Yamauchi et al. 2004) and proton beam populations (Neugebauer and Goldstein 2013). This demonstrates that switchbacks are folds in the magnetic field, rather than being local reversals in magnetic field polarity. Such a property has also been confirmed with the electron strahl population (see Section 2.4.1), which maintained a constant direction to the magnetic field (Kahler et al. 1996). The same conclusion was reached by Balogh et al. (1999) after studying the direction of Alfvén wave propagation inside switchbacks, which has since been repeated for the PSP measurements (McManus et al. 2020).

When measured by a spacecraft, the duration of a switchback is often used as a proxy for their physical size. However, as will be discussed in Section 4.4, there is a non-trivial relationship between the physical size and duration when measured by a single spacecraft. This is a major point that is reiterated throughout this chapter. For now, it is only important to note that there is no typical duration for a switchback, with values ranging from seconds to several hours (Dudok de Wit et al. 2020). Interestingly, there have been reports of switchback 'clusters' where several

longer duration switchbacks are seen to deflect in the same direction (Horbury et al. 2020b). This implies that there is some systematic effect, which will be explored further in Section 4.4.2.

On a larger scale, switchbacks are commonly observed to occur in 'patches' separated by 'quiet periods' with little activity (Horbury et al. 2020b). Similar 'microstream' structures have been seen previously in Ulysses above the Sun's poles (Neugebauer et al. 1995), where there was also modulation in the switchback occurrence over time. Several authors have noted that the spatial scales of these patches are well-matched to supergranules or coronal plumes at the Sun (Bale et al. 2021; Fargette et al. 2021; Thieme et al. 1990; Neugebauer and Sterling 2021). Switchback patches also have modulations in alpha particle abundance, further linking patches to structures closer to the Sun (Bale et al. 2021).

PSP has consistently shown that switchbacks are prevalent for all types of solar wind close to the Sun (Rouillard et al. 2020). Therefore, it is natural to ask whether switchbacks may play an important role in the heating and acceleration of the solar wind. One way to investigate this is to determine whether the plasma parameters are the same inside and outside individual switchbacks.

Using the SPC instrument, Woolley et al. (2020) showed that the parallel proton core temperature ($T_{p,\parallel}$) was similar inside and outside switchbacks. However, Woodham et al. (2021a) demonstrated that there were enhancements in $T_{\parallel}$ over groups of switchbacks for a small period in E2 using the SPAN instrument. The authors concluded that switchbacks may be embedded in a larger structure, whose heating may relate to a generation mechanism on the Sun. However, it is unclear how these newer observations reconcile with those from Woolley et al. (2020).

As discussed in Section 2.6.2, SPC can only measure a radial temperature, which is a 1D cut through the distribution that changes with the magnetic field orientation (see equation 2.39). Therefore, only the parallel temperatures inside ($\theta_{RB} = 180°$) and outside ($\theta_{RB} = 0°$) switchbacks could be compared. In contrast, both temperatures could be measured by SPAN, but the observations from Woodham et al.

(2021a) only covered deflections up to 60°. So the exact behaviour of the temperature within switchbacks has yet to be determined, which could be an important clue for the mechanism of switchback formation. Accordingly, Chapter 5 will attempt to address this ambiguity with the latest PSP data.

Aside from potentially distinct plasma signatures, switchbacks also seem to have well-defined boundaries. Many of the switchback edges were associated with an abrupt change in magnetic field direction, classed as rotational discontinuities (RDs, Larosa et al. 2021; Akhavan-Tafti et al. 2021). These sharp boundaries typically have:

- A dip in $|\vec{B}|$
- Increased proton density
- Enhanced wave activity of both MHD (Farrell et al. 2020; Mozer et al. 2020) and whistler waves (Agapitov et al. 2020)

Several authors have shown that the wave activity associated with switchbacks decreases with increasing distance from the Sun (Farrell et al. 2021; Akhavan-Tafti et al. 2021). This observation, combined with reports of magnetic reconnection at several switchback boundaries (Froment et al. 2021; Akhavan-Tafti et al. 2021), suggests that the switchback boundaries degrade and evolve as the solar wind expands.

Despite these findings, it is still not clear how the numerous switchbacks at PSP contribute to the more evolved state of the solar wind by 1 AU. Consequently, it is important to study how the occurrence of switchbacks varies with distance from the Sun, which can also help determine whether switchbacks are created on the Sun, or in situ. If switchbacks are indeed generated on the Sun, then there should be a decaying number of switchbacks with distance. On the other hand, an increasing, or stable, switchback occurrence rate would suggest that there is an in situ driver of switchbacks, that replenishes their numbers as the solar wind propagates. Analysis by Mozer et al. (2021) suggested that the rate of switchbacks per hour was constant with distance from the Sun, leading those authors to rule out

any in situ generation methods. It is interesting to note, however, that Macneil et al. (2020) used a greater range of distances with Helios to show that the switchback rate actually increased. Furthermore, Tenerani et al. (2021) found that the rate of switchbacks with duration >10 seconds increased with distance, while the rate of switchbacks with duration <10 seconds decreased. This could suggest that the switchback generation mechanism is more efficient at larger scales, though it should be noted that there was large variance in occurrence rate in all these studies.

Therefore, along with the temperature behaviour inside switchbacks, there is still some debate regarding their occurrence rate. There has not yet been any conclusive evidence regarding the generation of switchbacks, with the different theories being outlined in the next section.

4.2 Theoretical models

After the prevalence of switchbacks in the early PSP results, many authors proposed mechanisms for their formation, which are summarised in Fig. 4.2. This section outlines how each of these methods can create a switchback, with later sections discussing how the results from this thesis agree, or disagree, with any of the generation mechanisms.

While there are several competing theories, the main debate is whether switchbacks are created on the Sun by some transient event, or are generated in situ as the solar wind expands out into the heliosphere. Models that require transient events at the Sun usually invoke some sort of magnetic reconnection, with interchange connection between closed and open field lines being proposed by Fisk and Kasper (2020). The theory of interchange reconnection was first based on the observations that coronal holes seemed to rotate rigidly in the corona (Wang et al. 1996), dragging open magnetic field lines over the closed field loops on the photosphere and initiating reconnection (Fisk et al. 1999). This process has already been suggested as a potential driver of the solar wind (Section 2.4.4), but Fisk and Kasper (2020) then argued that this could also create a kink in the magnetic field that could grow

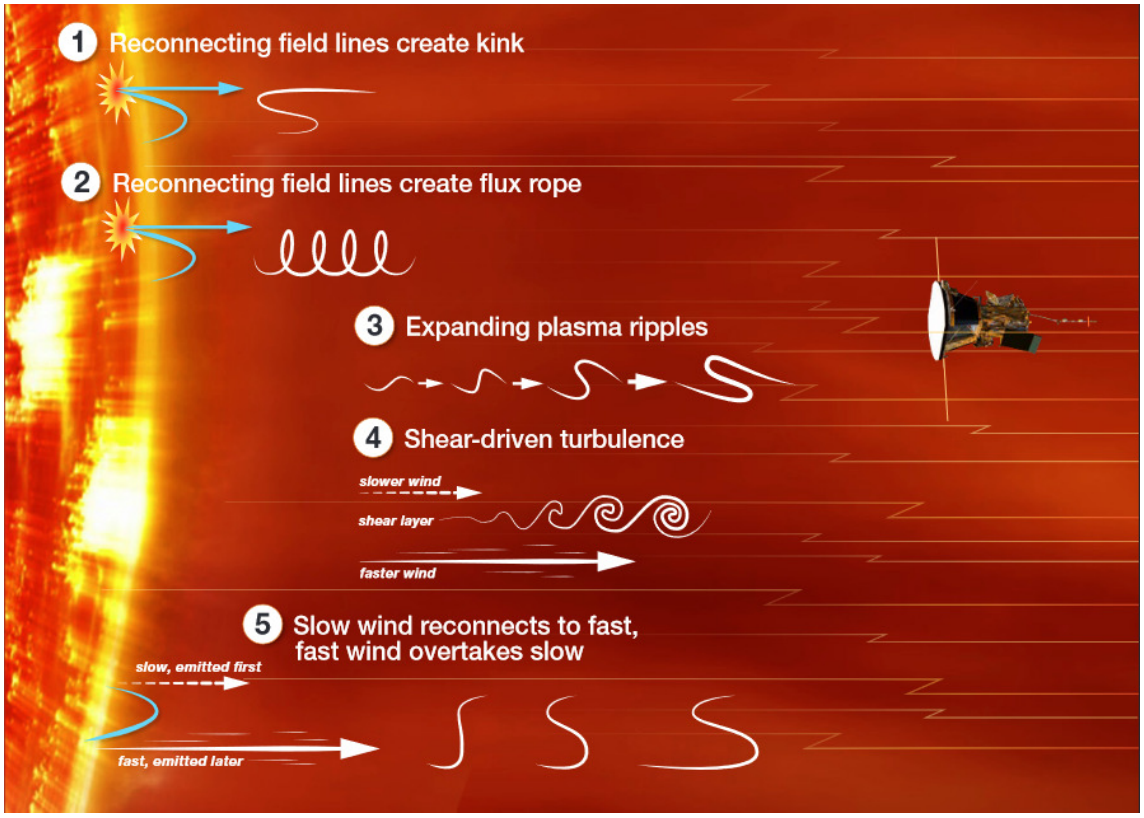


Figure 4.2: Diagram of the different switchback generation mechanisms:
(1) kinks in the magnetic field from interchange reconnection (Fisk and Kasper 2020; Zank et al. 2020; Liang et al. 2021).
(2) launching of flux ropes from interchange reconnection (Drake et al. 2021).
(3) expanding waves and turbulence (Squire et al. 2020; Shoda et al. 2021; Mallet et al. 2021).
(4) shear driven turbulence (Ruffolo et al. 2020).
(5) super-Parker spiral (Schwadron and McComas 2021).
(credit to NASA et al. 2021).

and be observed as a switchback by PSP.

However, it is unclear if such a kink in the magnetic field could survive out to PSP distances. Simulations of Alfvénic fluctuations, with constant $|\vec{B}|$, have shown that such kinks could survive in a calm background without any large density gradients (Tenerani et al. 2020). This disagrees with the work of several other authors, indicating that the magnetic field kink would unwrap as it propagated in the simulated corona (Landi et al. 2005; Magyar et al. 2021). Therefore, this remains a major open question for those theories that rely on the launching of waves from the lower corona.

Interchange reconnection is also invoked in the work of Zank et al. (2020), where

the initial magnetic field bend is supported by the generation of complex structures moving at the fast magnetosonic speed. A subsequent study by Liang et al. (2021) showed that such a scenario could explain around half of the observed switchbacks at PSP. It was also noted that interchange reconnection would naturally create switchbacks clustered in time (Zank et al. 2020), matching the observations (Dudok de Wit et al. 2020; Horbury et al. 2020b). However, this scenario relies on the fact that the switchbacks are compressive and, although there is some evidence for this (Larosa et al. 2021), it is not the case in general.

Instead of releasing an Alfvénic wave, Drake et al. (2021) proposed that interchange reconnection could launch a flux rope into the solar wind. Using 2.5D simulations, they demonstrated that such a structure would be arc polarised with constant $|\vec{B}|$, consistent with the switchbacks in the solar wind (Bruno et al. 2004; Horbury et al. 2020b). Unlike the kinks in the magnetic field, flux ropes are expected to be stable enough to survive the journey to PSP. However, these simulations struggle to create Alfvénic fluctuations, which is one of the defining features of switchbacks.

Sterling and Moore (2020) also suggested that reconnection can form a propagating wave that could be seen as a switchback. In this case, the reconnection would be associated with a coronal jet, which are seen to occur with a rate of 60 /day in the polar coronal holes (Savcheva et al. 2007). However, this occurrence rate is much lower than that for switchbacks in the solar wind (Mozer et al. 2020; Tenerani et al. 2021). Furthermore, switchbacks are observed in all solar wind types (Rouillard et al. 2020), not just the fast solar wind that is commonly linked to coronal jets.

Alternatively, switchbacks may be generated in the solar wind, thereby removing the need to survive in the complex environment of the corona. Ruffolo et al. (2020) argued that switchbacks could be created by the Kelvin-Helmholtz instability acting to drive turbulence at the boundaries of velocity shears. For this to work, the switchbacks must be generated near the Alfvén critical zone[1], where the magnetic field becomes weak enough to allow the plasma to drive the dynamics (i.e. when

[1]Where solar wind speed $= v_A$

$\beta > 1$). Therefore, a key testable prediction of this model is that switchbacks should stop being generated below the Alfvén critical zone, which will be explored by PSP in later encounters (Chhiber et al. 2018; Kasper et al. 2021).

Another form of stream interaction is the super-Parker spiral concept from Schwadron and McComas (2021). Here, the footpoint of a magnetic field line would move from a slow to fast source, thus creating a speed difference that would create a kink in the magnetic field. The authors argued that this could also explain observations of a $+V_T$ flow from Kasper et al. (2019). However, such a mechanism would not necessarily create an Alfvénic fluctuation.

Finally, several studies have suggested that switchbacks could be the result of small fluctuations growing as the solar wind expands. Expanding box simulations have demonstrated that this scenario can create realistic switchbacks with high Alfvénicity and constant $|\vec{B}|$ (Squire et al. 2020; Johnston et al. 2022). It has further been shown that a solar wind model based on this idea could also create realistic solar wind speeds at PSP (Shoda et al. 2021). However, neither of these simulations could generate enough switchbacks to match the in situ observations.

In summary, all the mechanisms described above can create a fold in the magnetic field. The question is whether any of them can produce signatures consistent with the observed switchbacks in the solar wind. To find the answer, more switchback properties need to be compared against testable predictions from these theories. Accordingly, Section 4.4 will attempt to find the shape and size of switchbacks, with Section 4.5 describing the tendency to deflect in certain directions.

4.3 Identifying switchbacks

Before investigating switchback properties, it is important to describe how they were identified in the data. Due to the large number of switchbacks in each encounter, it was unrealistic to identify them by eye. From early PSP observations, switchbacks were tentatively defined as deflections in the magnetic field, with the B_R component being the easiest to use to visually identify switchbacks, as in Fig. 4.1. Despite

their name, the magnetic field within a switchback does not necessarily have to 'switch back' and reverse direction ($B_R < 0$). Switchbacks only have to sufficiently deflect away from some nominal magnetic field direction, which was taken as the Parker spiral direction in this thesis, and will be discussed further in Section 4.3.3. Switchbacks can then be defined as deflections more than some threshold away from the background. However, it is important to note that the distribution of observed switchback deflections was continuous (Dudok de Wit et al. 2020), meaning that there was no obvious threshold to define a switchback. Many authors have defined switchbacks as being deflections greater than either 45°, 60° or 90°.

Fig. 4.3 shows the results of applying a 30° threshold to the deflection angle, with the switchbacks classified shown in red. While this can capture large deflections well, it inevitably leads to cases where the deflection angle hovers near the threshold, and many smaller switchbacks are mistakenly classified. Since, the duration of switchbacks is an important quantity to measure (see Section 4.4), a single threshold, like the upper panel of Fig. 4.3, would create many erroneous shorter switchbacks, skewing the results. To avoid this problem, a second threshold was introduced at 45°. Switchbacks were then defined as the time over which there were $\geq$30° deflections, when that period also included at least a 45° deflection, as shown in the lower panel of Fig. 4.3. This double threshold helped find sufficiently large deflections, while still sampling the true edges of the switchback and giving an accurate estimate of their duration, which was not provided by the single threshold at 45° in the middle panel of Fig. 4.3.

After applying the higher threshold, any switchback candidates separated by less than 2 seconds were merged together, which avoided splitting switchbacks in two. The lower threshold was then applied on the same data, where only cases with an accompanying 45° deflection were retained. Several combinations of high and low thresholds were trialled, with 30° and 45° providing the best results when visually inspected.

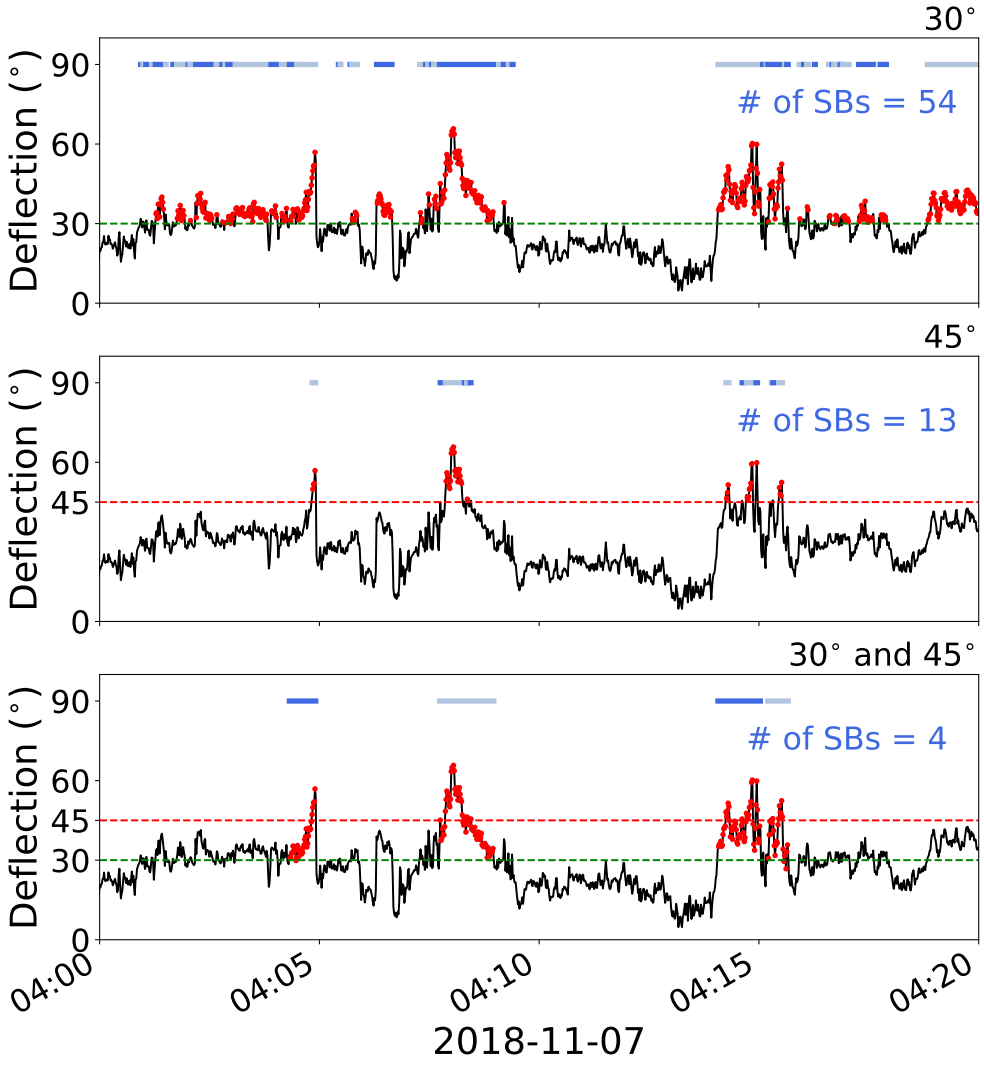


Figure 4.3: The top panel shows a single threshold at 30° applied to the magnetic deflection angle from the Parker spiral, which produces many erroneous 'switchbacks' (alternating blue lines). The middle panel shows that a higher threshold of 45° can reduce the number of switchbacks, but this only samples a small portion of each switchback. Finally, the lower panel shows the double threshold technique, which captures the larger deflections and produces a better estimate of switchback duration.

4.3.1 Clock angle

While all switchbacks are deflections away from the background magnetic field, they could deflect in any direction. To quantify this, a clock angle (CA) was defined, ranging from 0° to 360°. This is equivalent to placing a clock face perpendicular to the Parker spiral direction, where the clock angle describes the deflection direction in the rotated T-N plane. In order to be consistent, the reference Parker spiral

direction was forced to point away from the Sun, so that the clock angles can be compared regardless of magnetic polarity. As demonstrated in Fig. 4.4, 0° points towards $+\vec{N}$, 90° towards $+\vec{T}$, 180° towards $-\vec{N}$ and 270° to $-\vec{T}$.

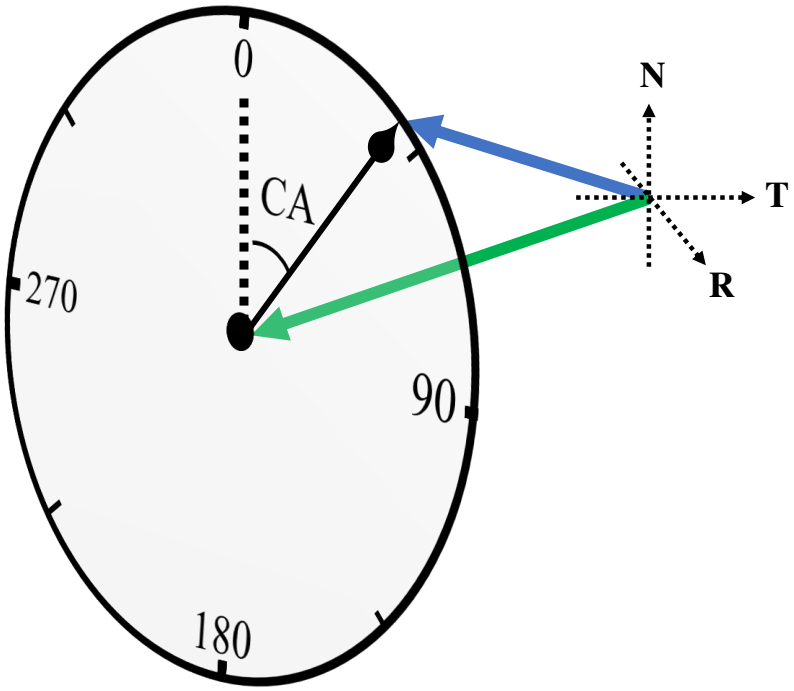


Figure 4.4: To quantify the direction of switchback deflection (blue), a clock face is placed normal to the local Parker spiral direction (green). The deflection can therefore be described by the angle on the clock face, where 0° points towards $+\vec{N}$, 90° towards $+\vec{T}$, 180° towards $-\vec{N}$ and 270° to $-\vec{T}$.

The advantage of using a clock angle is that it can describe the switchback deflection direction with a single value. However, the clock angle is a quantity that can be calculated for each magnetic field vector, so there are several ways to define a single clock angle per switchback. In Section 4.4, the average of each magnetic field component over the switchback duration was taken before applying:

$$CA\left(\langle B\rangle\right) = \tan^{-1}\left(\frac{\langle B'_T\rangle}{\langle B_N\rangle}\right), \tag{4.1}$$

where B'_T is the component perpendicular to the Parker spiral in the R-T plane.

A similar strategy would be to average the individual clock angles within a

switchback. Since the clock angle wraps around 360°, one must take the average of the T and N components, rather than an average of the clock angle itself:

$$\langle CA \rangle = \tan^{-1}\left(\frac{\langle CA_T \rangle}{\langle CA_N \rangle}\right) \tag{4.2}$$

More explicitly, the average clock angle of 315° and 45° would be 0°, rather than 180°.

This method was adopted in Section 4.5, where the clock angle was averaged when the deflection angle was within ±10° of 90°, or the maximum deflection angle if this was not reached. This approach helped avoid potential problems at the edges of switchbacks, where they may have been improperly classified.

The choice of clock angle should not affect the results in this chapter, as the different definitions gave consistent values across all encounters, as shown in Fig. 4.5.

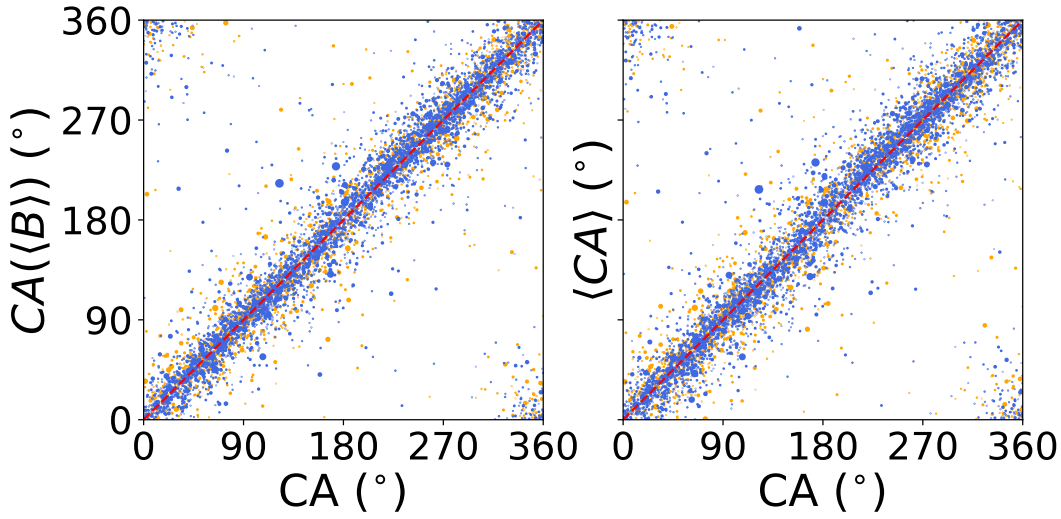


Figure 4.5: Comparison of the clock angle definition (CA) used in Section 4.5 (black) with the $CA\,(\langle B \rangle)$ used in Section 4.4 (orange). There is little difference between the definitions used, and even an alternative definition of $\langle CA \rangle$. Scatter point size is proportional to duration of the switchbacks.

4.3.2 Arc-polarised deflections

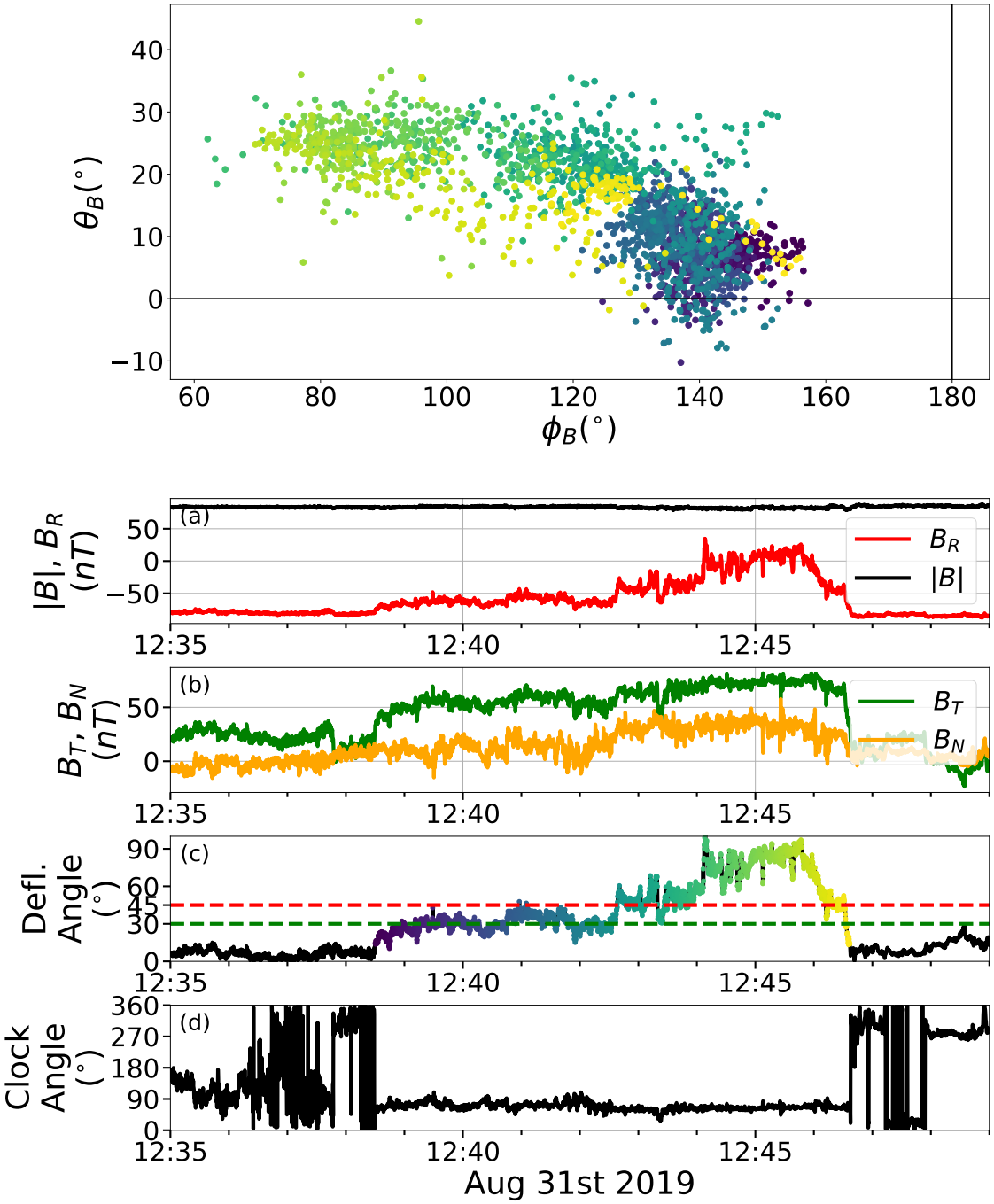


Figure 4.6: Example of a switchback exhibiting arc-polarised behaviour. That is, the magnetic field deflects along the arc of a sphere, and then returns along the same path. The top panel shows the magnetic field angles, where the colour represents time through the switchback, which is also plotted in the penultimate panel. This behaviour can also be seen in the fact that clock angle (lower panel) does not change with deflection angle (adapted from Laker et al. 2022).

To study the switchback deflections, it would be preferable to define the deflection

direction with a single clock angle. However, this would only be possible if the magnetic field were arc polarised within a switchback, i.e. the magnetic field deflects along the arc of a sphere with a radius of $|\vec{B}|$. Several studies have already stated that switchbacks are arc polarised (Bruno et al. 2004; Matteini et al. 2014; Horbury et al. 2020b), but before proceeding to study the deflection directions in the new PSP data, this property must be verified.

Fig. 4.6 shows an example of an arc-polarised switchback, where the clock angle inside the switchback was constant with respect to deflection angle. This can also be seen in the hodogram (top panel), where the colour gradient shows that the magnetic field inside this switchback deflects along an arc, and then, crucially, returns along the same arc. This motion of the magnetic field vector can be likened to a windscreen wiper, as seen for the example in Fig. 4.6. In terms of physical geometry, such behaviour would be consistent with an S-shaped switchback, as depicted in the appendix to Kasper et al. (2019).

To assess this behaviour across all encounters, a superposed epoch analysis was performed (Samson and Yeung 1986). For each switchback, the time through a switchback was normalised between $0 \rightarrow 1$, in the left panels of Fig. 4.7. The lower panels show the result of this technique for the variation in $|\vec{B}|$. While there was some variability in $|\vec{B}|$ at larger deflection angles, this distribution was still centred on 1, confirming the incompressible nature of switchbacks found by other authors (Krasnoselskikh et al. 2020; Larosa et al. 2021).

The upper panels of Fig. 4.7 demonstrate that there was little difference between the individual clock angles of each vector and the defined clock angle for that switchback (outlined in Section 4.3.1). The upper right panel shows that clock angle was better constrained around a deflection angle of 90°, which comes from the definition of clock angle from the previous section. While there was some spread in individual clock angles, this was well within 45°, so the switchbacks across the encounters can be classified as arc polarised.

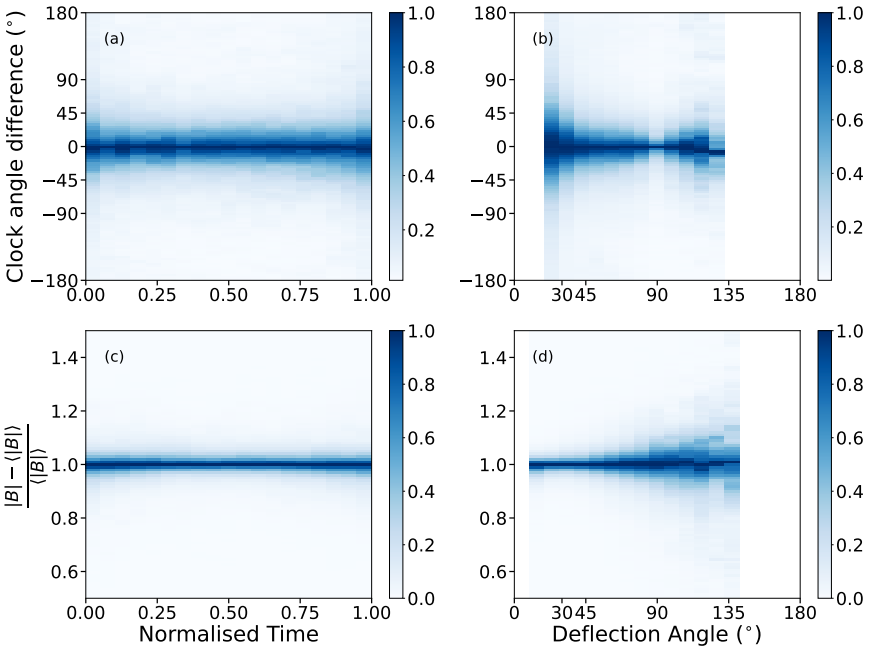


Figure 4.7: Superposed epoch analysis of switchback deflections, showing they were arc polarised across the encounters. After scaling each switchback in time, they are added to a 2D histogram, with each column normalised independently. The consistency of clock angle in both deflection angle and time (upper panels) shows that switchbacks are arc polarised. The lower panels show that $|\vec{B}|$ was constant, so the magnetic field lies on a sphere (adapted from Laker et al. 2022).

4.3.3 Estimating background magnetic field

The estimation of background magnetic field direction was crucial for identifying switchbacks and defining their clock angle. One might try and find an average magnetic field direction across some interval. Although the influence of switchbacks could be removed from the B_R component by using a mode average (Bale et al. 2019), the same could not be done for the other components.

Better results were obtained by considering all the magnetic field components as one, where the magnetic field vectors were binned in 3D, and the background direction was taken as the bin with the maximum count. However, this method was not reliable enough over all encounters, and required a large time window to build up a sufficiently dense distribution.

Consequently, throughout this chapter, the local Parker spiral was taken as the background direction, since it is a physical property of the interplanetary magnetic

field whose value is not influenced by the presence of the switchbacks. The Parker spiral was calculated with equation 2.32, where the spacecraft position was estimated using the SPICE toolkit (Acton 1996; Acton et al. 2018), which was imported into `Python` in `Spiceypy` (Annex et al. 2021). The effect of switchbacks on the radial solar wind speed must be removed when estimating V_{sw}. For Section 4.4, this was achieved by taking a 12-hour mode average of V_R. While this provided good results for the first two encounters, it produced large step changes in V_R in later encounters. Therefore, in Section 4.5 a low-pass Butterworth filter (of order 2, Butterworth et al. 1930) was used with a cut-off at 3 hours. This filter removed the contributions of the switchbacks and left a smoothly varying background estimation for V_{sw}. While Fig. 4.8 shows that ϕ_{ps} slightly underestimated ϕ_B in the first eight encounters, this should not significantly affect the identification of switchbacks.

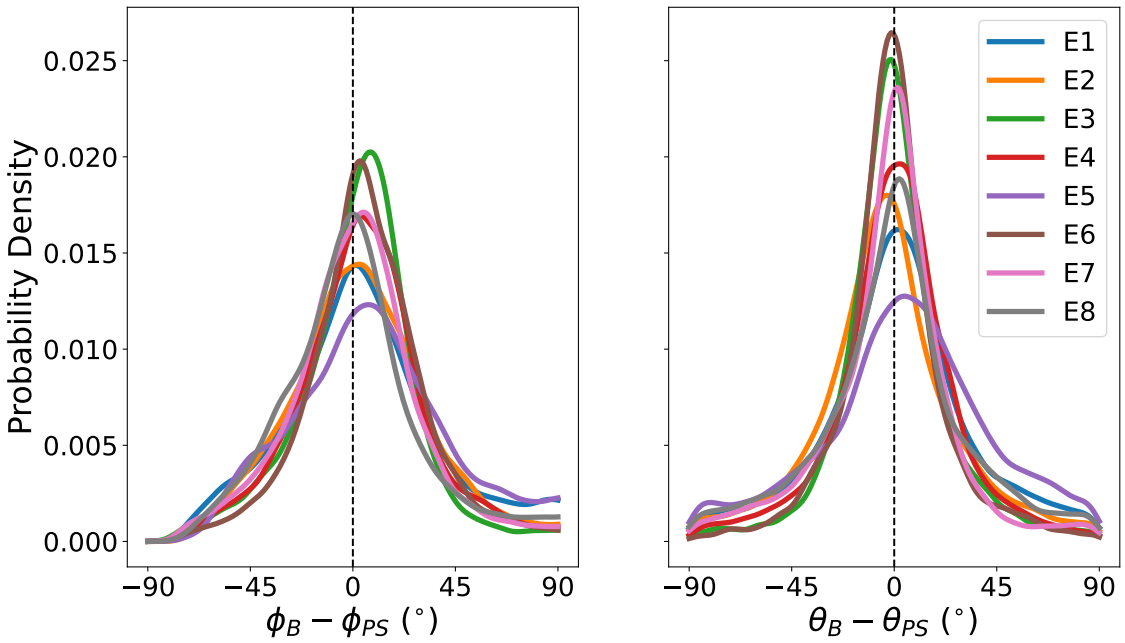


Figure 4.8: The difference between the magnetic field ϕ_B and θ_B angle with the expected Parker spiral. The peaks of all encounters are within ±7° of the expected Parker spiral direction, so should not affect the identification of switchbacks.

4.4 Size and shape of solar wind switchbacks

After the strong presence of switchbacks in the first two PSP encounters, many theories were put forward to explain their origin and nature (see Section 4.2). In order to distinguish between the suggested mechanisms, i.e. whether switchbacks are created on the Sun or in the solar wind, it would be helpful to have estimates of their size and shape. Using two streams from the first PSP encounter, Horbury et al. (2020b) provided the first evidence for their true physical shape as being long and thin. In this section, similar principles are extended to 16 solar wind streams across the first two encounters, which represented all the data available at the time the research in Laker et al. (2021b) was carried out.

4.4.1 Apparent duration

In order to investigate the 3D shape of solar wind switchbacks, it would be preferable to image them from multiple directions. Such a technique has previously been applied to CMEs (De Koning et al. 2009; Liewer et al. 2009), but is not suitable for switchbacks as they are largely incompressible and would not appear in images. An average switchback shape can still be probed using only single spacecraft measurements, by comparing the apparent duration in the time series to the direction at which the spacecraft cut through the structure. By sampling a wide range of cutting directions, a statistically average shape can be determined.

For example, when cutting through the centre of a circle, the distance measured along the spacecraft trajectory will be the same regardless of the direction of travel through the structure. However, as demonstrated in Fig. 4.9, there will a range of distances measured when cutting through an ellipse, which can be used to infer the 2D shape. Of course, any spacecraft cut away from the shape's centre will also be shorter. Combined with the fact that switchbacks will likely vary in shape and size, any study of their size must be statistical in nature.

Horbury et al. (2020b) observed that the longest duration switchbacks tended to deflect towards $+\vec{T}$ (90° clock angle) for a period in E1. In order to explain

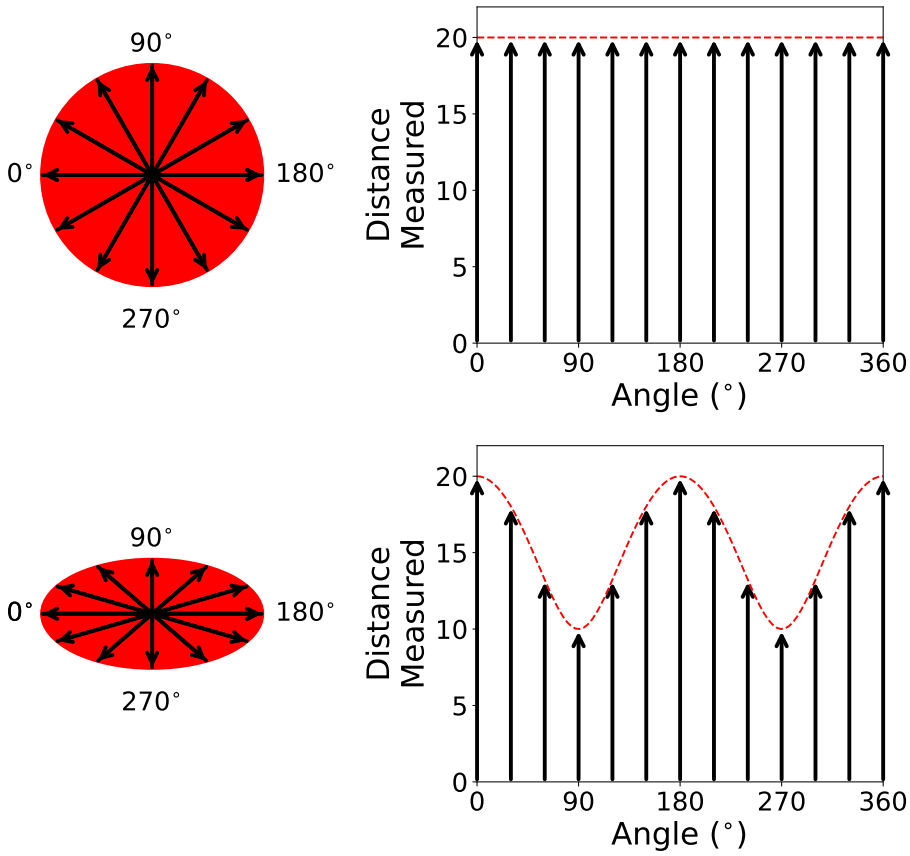


Figure 4.9: Demonstration of how cutting angle, between 0° and 360°, can affect the distance measured. For a circle (top), cutting angle has no effect, whereas, for an ellipse (bottom), or other asymmetric shape, the distance measured will be a maximum along the longest axis.

this correlation, the authors proposed that the switchback deflection direction will influence the way a spacecraft will cut through the structure, and hence affect the duration observed.

Given that switchbacks are Alfvénic, any deflection in the magnetic field will also result in a velocity deflection. Specifically, the relative velocity of the plasma with respect to the spacecraft can be written as:

$$V_{rel} = \langle V_{SB} \rangle - V_{SC}, \tag{4.3}$$

where $\langle V_{SB} \rangle$ is the average velocity inside the switchback, and V_{SC} is the spacecraft velocity. The largest tangential velocity deflection will be equal to the local Alfvén

speed, which was around 100 km/s at around 35 $R_\odot$. PSP had a large tangential velocity ~90 km/s, which was comparable to the switchback deflections.

Therefore, with knowledge of V_{rel}, the direction in which PSP cuts through the structure can be estimated. Following Horbury et al. (2020b), cylindrical symmetry was assumed, meaning that the direction could be specified by a single cutting angle:

$$\sin(\alpha_C) = \frac{\sqrt{V_{rel,T}^2 + V_{rel,N}^2}}{|\, V_{rel}\,|}, \tag{4.4}$$

for a radially aligned structure. As Fig. 4.10 shows, switchbacks were modelled as being cylindrical with width, W, and length, L, which could also be described by the angle of hypotenuse:

$$\alpha_H = \tan^{-1}\left(\frac{W}{L}\right). \tag{4.5}$$

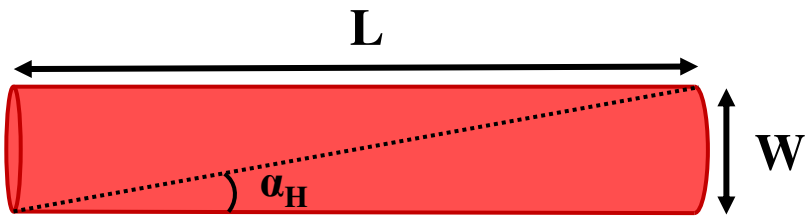


Figure 4.10: Model of switchback shape in this study, with length, L, and width, W. In Section 4.4.2, the angle α_H will be used to describe the aspect ratio.

For such a shape, when cutting through the structure at an angle α_C, the distance measured by the spacecraft should follow:

$$D(\alpha_C, V_{rel}) = t \times |V_{rel}| = \begin{cases} \frac{W}{sin(\alpha_C)} & \text{if } \alpha_C \geq \alpha_H \\ \frac{W}{\tan(\alpha_H)\cos(\alpha_C)} & \text{if } \alpha_C < \alpha_H \end{cases} \tag{4.6}$$

which is also displayed in Fig. 4.11.

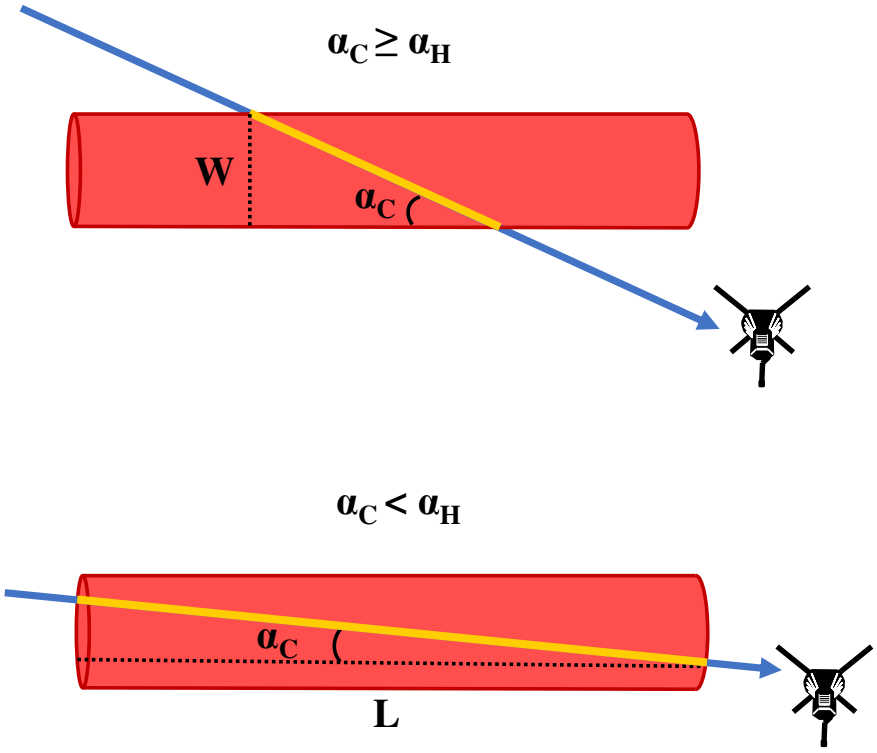


Figure 4.11: The distance measured (orange) by a spacecraft cutting through the switchback structure from Fig. 4.10. As described in equation 4.6, when cutting through the side ($\alpha_C \geq \alpha_H$) the distance is given by $W/\sin\alpha_C$. For a case when cutting down the length of the structure ($\alpha_C < \alpha_H$), the distance is given by $L/\cos\alpha_C$.

Ideally, a range of all possible angles will be measured, allowing for the reconstruction of the switchback shape. However, the Alfvénic nature of switchbacks means that the velocity deflection, and hence cutting angles, are subject to some physical constraints. Alfvénic fluctuations lie on the surface of a sphere, centred at the origin, with radius $|\vec{B}|$ for the magnetic field. The corresponding velocity fluctuations also lie on a sphere with radius v_A, which is centred on the local deHoffman-Teller velocity. This velocity represents the frame in which the fluctuations are stationary. Since switchbacks are deflections away from the background direction, and full reversals are rare (Woolley et al. 2020), there is only a band of possible velocity deflections in a patch of switchbacks (where the local Alfvén speed

is roughly constant). After rotating the coordinate system to the centre of this band, represented by a V', the band of velocity deflections will appear as a ring, as shown in Fig. 4.12.

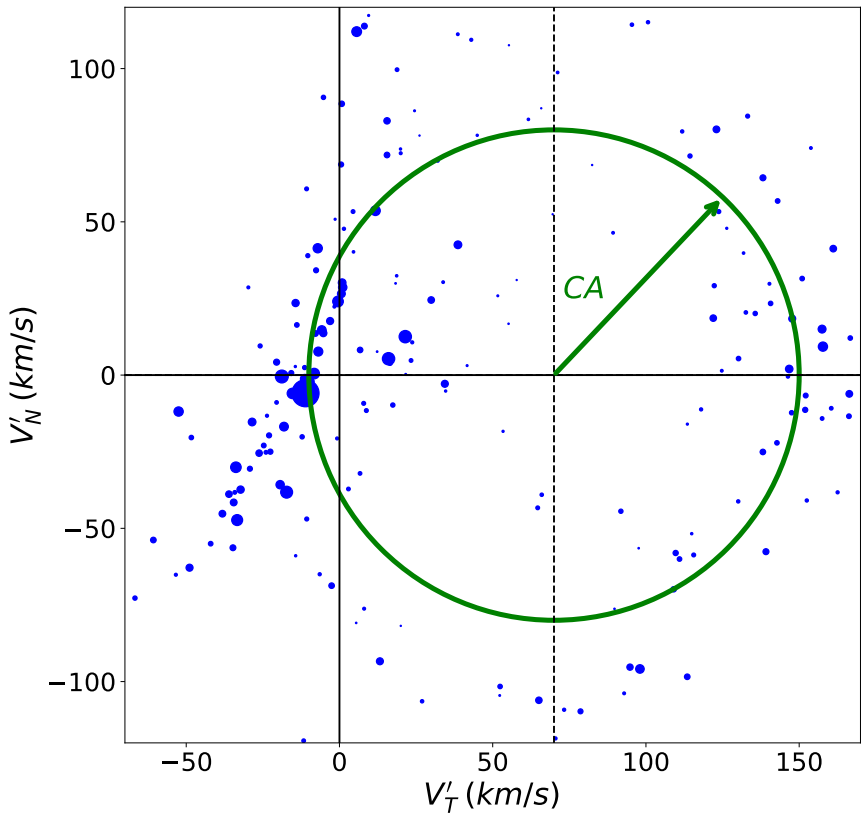


Figure 4.12: The rotated velocity, V', of each switchback for region E2S3 makes a ring of speeds, which can be described by the clock angle of the switchbacks (reproduced with permission from Astronomy & Astrophysics, ©ESO Laker et al. 2021b).

Therefore, the clock angle can be used to describe the range of possible cutting angles, with $V_{rel,T}$ following a sine, and $V_{rel,N}$ a cosine as a function of clock angle. Fig. 4.13a shows the respective geometry when the switchbacks (red cylinder) are aligned to the centre of the velocity ring (blue circle viewed from the side). This is just a 2D slice, but can be rotated about $\vec{R}$ with the assumed cylindrical symmetry. In this case, the cutting angle can then be written as:

$$\sin(\alpha_C) = \frac{\sqrt{k(\sin^2(CA) + \cos^2(CA))}}{\mid V_{rel} \mid} = \text{constant}, \tag{4.7}$$

leading to a constant α_C.

However, if the switchbacks and velocity ring are not aligned, and are offset by an angle Φ_A, then Fig 4.13b will apply. After rotating so the alignment vector points along $\vec{R}$, giving $V'_{rel,T}$ and $V'_{rel,N}$, there will be an offset in the $V'_{rel,T}$ component. This produces an asymmetry in the cutting angle, and therefore D, as a function of clock angle, through:

$$\sin(\alpha_C) = \frac{\sqrt{{V'_{rel,T}}^2(CA) + {V'_{rel,N}}^2(CA)}}{\mid V_{rel} \mid}, \tag{4.8}$$

In this specific case, a deflection of 270° clock angle will create a smaller cutting angle (orange line), due to the switchback deflection cancelling out the tangential spacecraft velocity. This idea can be extended out of the plane, by taking the average switchback alignment as $\vec{A}$. Therefore, different combinations of velocity rings and alignment directions will create specific distributions of duration with clock angle.

4.4.2 Measuring switchback shape

By using the observed distribution of switchback duration with clock angle, an attempt was made to estimate the average switchback dimensions, W and α_H. Only duration and V_{rel} were observed quantities, with the link between clock angle and duration being dependent on the average alignment direction. Therefore, for each solar wind stream, the alignment direction that was most consistent with observed duration distribution was searched for.

A total of 16 solar wind streams were selected from the first two PSP encounters. During the first encounter, the spacecraft was connected to an overexpanded equatorial coronal hole from October 29th and November 13th 2018, and then a larger coronal hole from 14th to 23rd November (Bale et al. 2019; Badman et al. 2020). Based on the switchback patch structure in the magnetic field and velocity, 10 streams were selected from the first encounter, as outlined in Fig. 4.14 and Table 4.1.

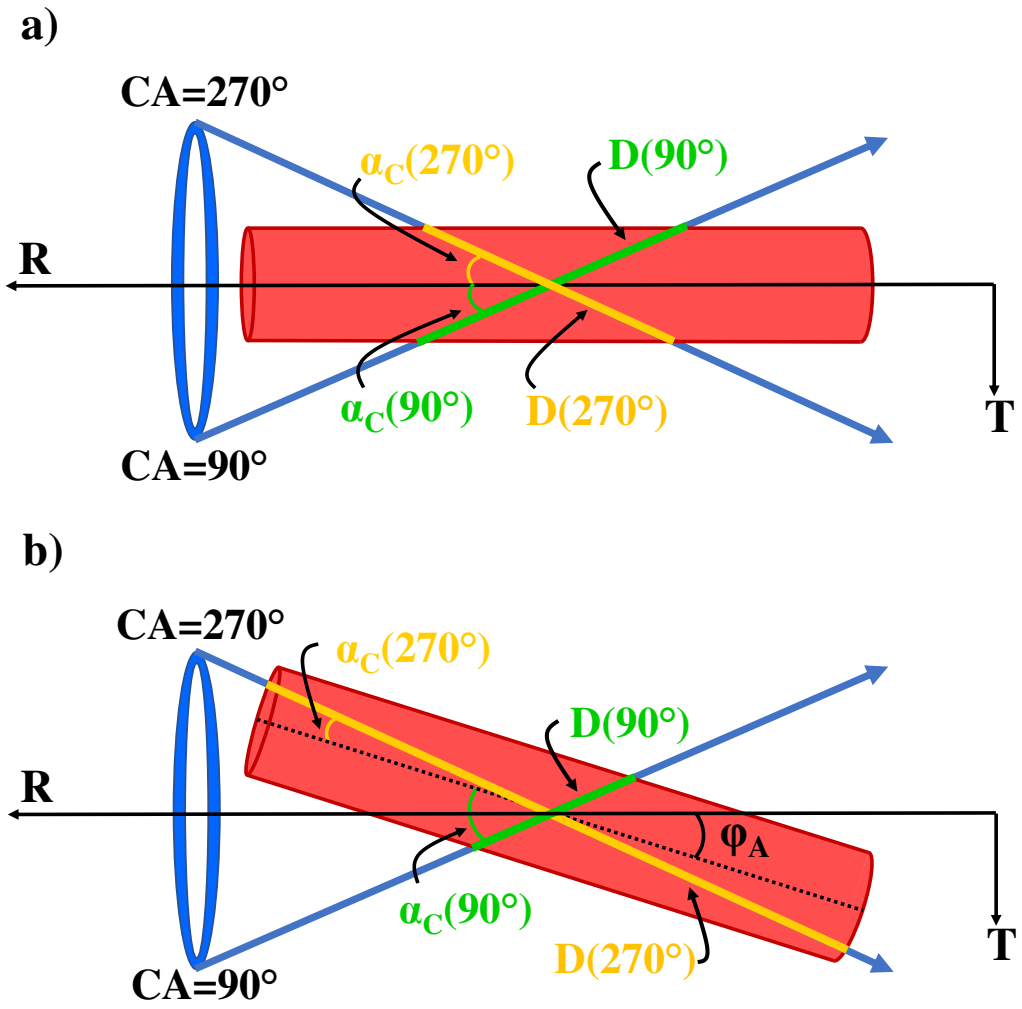


Figure 4.13: Diagram showing the spacecraft cuts in the R-T plane, so the ring of velocities from Fig. 4.12 (blue ellipse) are reduced to two cuts at 90° and 270°. As in Fig. 4.11 the spacecraft cuts along the blue arrows, measuring a distance, which is green when clock angle is 90° and orange for 270°. For case (a), when the structure is aligned with the ring of velocities, the distance measured will be constant with clock angle (equation 4.7). However, if they are not aligned, as in case (b), then the cut at 270° will measure a larger distance (equation 4.8)(reproduced with permission from Astronomy & Astrophysics, ©ESO Laker et al. 2021b).

While the source of solar wind in the second encounter was less well-defined, Rouillard et al. (2020) classified periods in this encounter related to the streamer belt. Therefore, of the six streams used here, there was a mix of solar wind type, all containing large numbers of switchbacks.

Switchbacks were first identified with the method from Section 4.3 using magnetic field data from the FIELDS instrument suite, and plasma data from SPC. The values of V_{rel} were calculated using a mean average of the switchback velocity and the

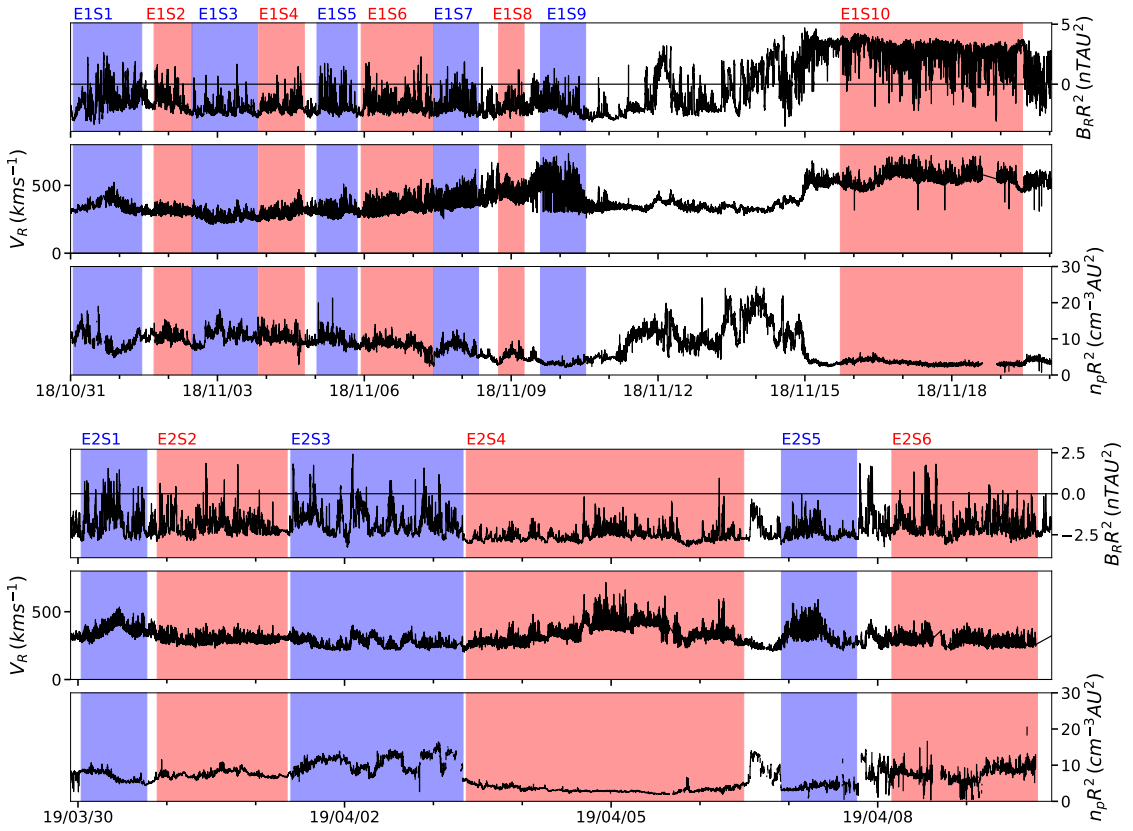


Figure 4.14: Solar wind streams, in E1 and E2, used in this study along with their identification numbers. All streams in E1, except for E1S10, are from the same equatorial coronal hole (Bale et al. 2019; Badman et al. 2020). The time between E1S9 and E1S10 was ignored, as this was a HCS crossing (Szabo et al. 2020). E2 streams were chosen according to the Rouillard et al. (2020) classification of non/streamer belt wind. B_R and n_p are both scaled by distance squared, to normalise their first order variation, keeping switchback amplitude roughly constant with distance (reproduced with permission from Astronomy & Astrophysics, ©ESO Laker et al. 2021b).

spacecraft velocity according to equation 4.3. For each stream, $\vec{A}$ was varied to find the direction that created a distribution between duration and α_C that was most consistent with long, thin structures. Choosing a value of $\vec{A}$ created a distribution between D and α_C, which was then fitted with equation 4.6, with W and α_H as free parameters to the least squares fit. Specifically, the directions of $\vec{A}$ were tested in 1° steps between ±20° in both the R-T plane, with Φ_A, and T-N plane, with Θ_A. For each choice of $\vec{A}$, the switchbacks were binned into 2° bins of α_C, with a minimum of 10 switchbacks per bin.

As discussed in Section 4.4.1, this equation only applies to cuts through the

centre of the structure. To meet these criteria, the top 10% of durations from each bin were used in the fitting, as this most likely represented the cut through the centre, rather than a case where the spacecraft clipped the edge of the structure. Constraints of $W > 0\,\text{km}$ and $0° < \alpha_H < 90°$ were used, and a minimum of five bins were needed to perform the fit.

The R^2 value was used to assess the goodness of fit, which was used as a proxy for how consistent D and α_C were with long, thin structures. For each stream, the combination of $\vec{A}$, W and α_H with the highest R^2 was used as the final result.

4.4.3 Results

Taking stream E1S6 as a first example, in Fig 4.15, the distribution of duration with clock angle is clearly skewed to have longer switchbacks around 90°, as previously observed by Horbury et al. (2020b). Such a link can be explained when taking the alignment direction as $(\phi_A = -6°, \theta_A = 3°)$, giving the relationships in the lower two panels that match expectation of long, thin structures from equation 4.6. Fitting this equation to the red points (the top 10% of durations per 2° bin) in the lower panel gave a value of $W = 55,000\,\text{km}$ with an aspect ratio of 15, and an R^2 of 0.87 indicating a good fit.

So, for the individual streams in Fig. 4.16, the theory set out in Section 4.4.1 can explain the observed link between switchback duration and deflection direction. However, as Table 4.1 shows, this only produced successful results for six out of the 16 streams tested across the first two encounters. This lack of success was due to an insufficient number of switchbacks or to a weak relationship between duration and clock angle.

There are two explanations for the lack of correlation between clock angle and duration. The first explanation is that, as demonstrated in equation 4.7, the alignment direction was along the centre of the velocity ring for that stream, leading to a constant cutting angle as a function of clock angle. Alternatively, the lack of correlation can also be explained by arguing that no such relationship existed in these

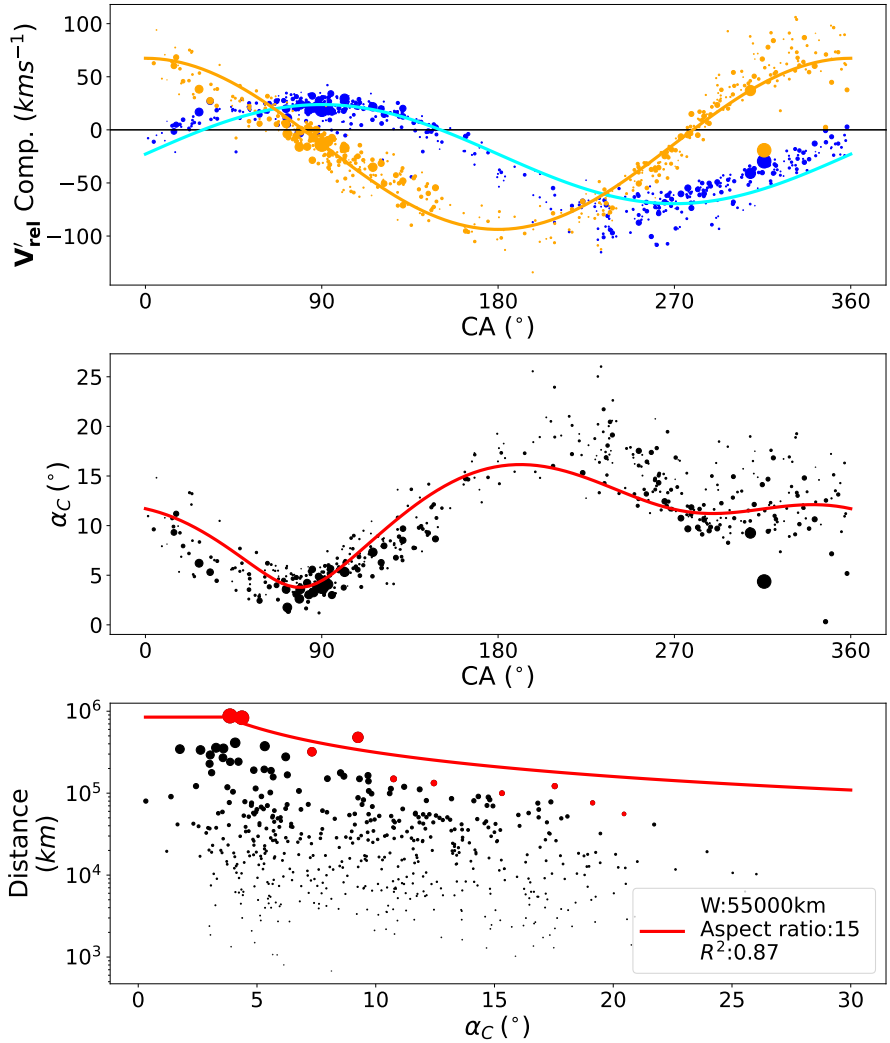


Figure 4.15: The upper panel shows the V'_{rel} components for the E1S6 stream, which lie on a circle like that in Fig. 4.12. Each scatter point represents a switchback, with the area being proportional to the duration. After using an alignment direction of $(\phi_A = -6°, \theta_A = 3°)$, the cutting angle, α_C, is shown as a function of clock angle in the middle panel. Finally, the lower panel shows how the distance measured per switchback varies with α_C, which has been fitted for the red points with equation 4.6.

streams. Unfortunately, these scenarios cannot be distinguished with only single point measurements, so such streams are not included in the final results.

Across the two encounters, Table 4.1 shows that the average switchback width varied from 20,000 km to 94,000 km, with a mean value of 56,000 km, similar to the estimated width of 10^4 km from Horbury et al. (2020b). However, this study had the added benefit of finding the best alignment direction, rather than setting it to the radial, or average flow direction. Although the width seemed to increase with

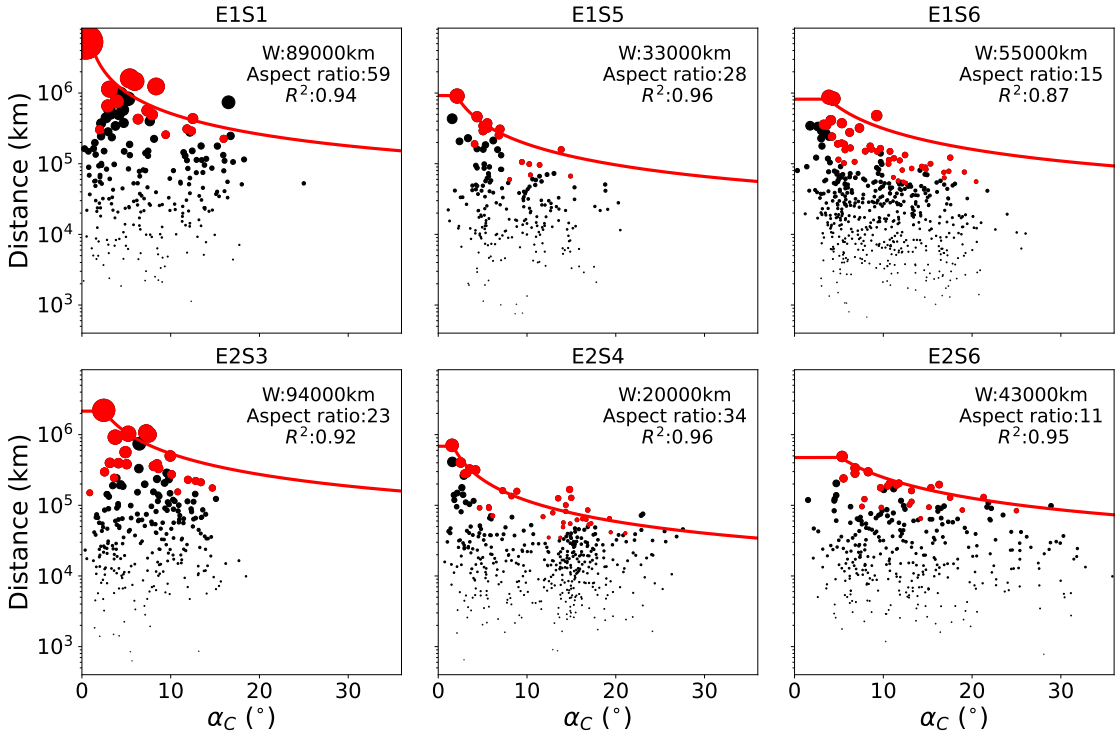


Figure 4.16: Duration of switchbacks as a function of α_C for the six streams with results, similar to the lower panel of Fig. 4.15. The red line represents the fitting of equation 4.6 to the red points, as described in Section. 4.4.2. The results for each stream are shown in the legend.

distance from the Sun, there was not a large enough spread in distance to estimate an expansion rate.

The aspect ratio ranged from 11 to 59, with a mean of 28. However, as it was impossible to be sure that the spacecraft measured the full length of a switchback, these aspect ratios are just lower limits. Therefore, the average switchback size can be summarised as having an aspect ratio of the order of 10, with a width ∼50,000 km. Combining these results gives a switchback length around 500,000 km, on the order of a Solar radius.

For the six successfully fitted streams in Table 4.1, the tested alignment directions are shown along with their accompanying R^2 value in Fig. 4.17. The tight grouping of R^2 in each stream suggests that there was a unique $\vec{A}$ that could create the observed distribution of duration with clock angle. All streams displayed an alignment direction away from the radial direction, towards the Parker spiral in the green highlighted regions, with little Θ dependence. There was no correlation

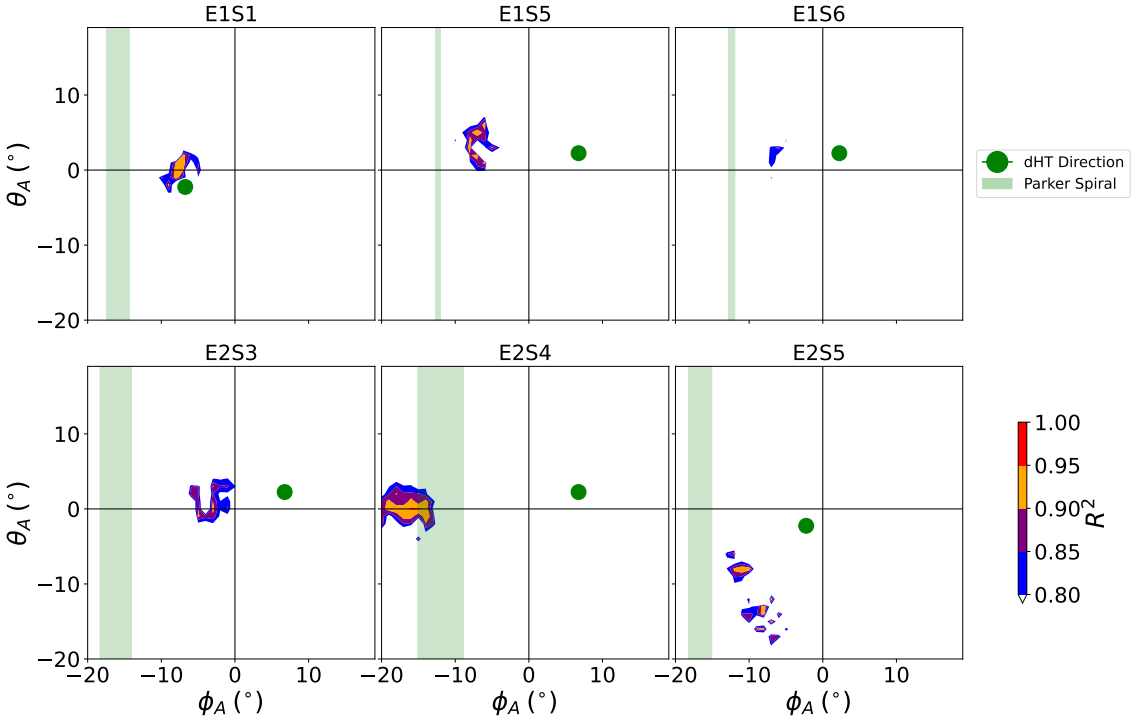


Figure 4.17: R^2 value for the tested alignment directions, in the R-T plane (Φ_A) and T-N plane (Θ_A), for the six successfully fitted streams (Table 4.1). Higher R^2 values signify an alignment direction which is more consistent with long, thin structures using equation 4.6. All streams show an alignment direction away from the radial, black cross-hairs, and the deHoffman-Teller direction with little change in Θ_A. Switchback alignment direction is towards the local Parker spiral, whose range is highlighted in green, using a 12-hour mode average of velocity (reproduced with permission from Astronomy & Astrophysics, ©ESO Laker et al. 2021b).

between the alignment direction and the deHoffman-Teller direction (green dot) in the stream. Therefore, the switchback alignment directions were not related to the $+\vec{T}$ flow deflection of the solar wind reported by Kasper et al. (2019) in the first two encounters.

In summary, if the assumptions in Section 4.4.1 are applicable, then switchbacks are long, thin structures with a width of 50,000 km and an aspect ratio of the order of 10, which are aligned towards the Parker spiral at $\sim$40 $R_\odot$.

ID	Start	End	# of switchbacks	Source	r (AU)	Φ_A (°)	Θ_A (°)	R^2	W (km)	Aspect Ratio
E1S1	31/10/2018 01:20	01/11/2018 10:53	239	CH	0.24	-8	0	0.94	89000	59
E1S2	01/11/2018 16:56	02/11/2018 11:28	114	CH	0.22	Not enough switchbacks				
E1S3	02/11/2018 11:35	03/11/2018 19:37	245	CH	0.2	No clear pattern in duration				
E1S4	03/11/2018 20:13	04/11/2018 18:35	283	CH	0.18	No clear pattern in duration				
E1S5	05/11/2018 00:48	05/11/2018 20:30	223	CH	0.17	-7	2	0.96	33000	28
E1S6	05/11/2018 22:28	07/11/2018 09:30	510	CH	0.17	-6	3	0.87	55000	15
E1S7	07/11/2018 09:54	08/11/2018 08:00	375	CH	0.18	No clear pattern in duration				
E1S8	08/11/2018 17:50	09/11/2018 06:19	178	CH	0.19	Not enough switchbacks				
E1S9	09/11/2018 14:23	10/11/2018 12:30	330	CH	0.21	No clear pattern in duration				
E1S10	15/11/2018 17:23	19/11/2018 10:39	1054	CH	0.38	No clear pattern in duration				
E2S1	30/03/2019 00:52	30/03/2019 18:36	214	NA	0.25	Not enough switchbacks				
E2S2	30/03/2019 21:24	01/04/2019 08:30	295	NA	0.22	No clear pattern in duration				
E2S3	01/04/2019 09:30	03/04/2019 08:00	285	Inside	0.19	-3	0	0.92	94000	23
E2S4	03/04/2019 08:52	06/04/2019 11:49	435	Outside	0.17	-15	0	0.96	20000	34
E2S5	06/04/2019 22:00	07/04/2019 18:19	198	Outside	0.19	Not enough switchbacks				
E2S6	08/04/2019 03:50	09/04/2019 19:09	396	Inside	0.21	-7	-15	0.95	43000	11

Table 4.1: Results from the 16 solar wind streams across the first two PSP encounters. Source location was either a coronal hole (CH) or inside/outside the streamer belt according to Rouillard et al. (2020). For several of the streams, there were no significant results, due either to a lack of switchbacks or lack of pattern in duration vs clock angle (reproduced with permission from Astronomy & Astrophysics, ©ESO Laker et al. 2021b).

4.4.4 Discussion

The consistency of switchback dimensions and alignment directions across the streams suggests that the theory set out in Section 4.4.1 can explain the observed link between duration and deflection direction.

Such an idea has implications for interpreting the influence of switchbacks on the background solar wind. Since this thesis provides evidence that switchback duration is related to how the spacecraft cut through the structure, duration alone cannot be used as a proxy for switchback size, nor contribution to the solar wind. In other words, it cannot be inferred that since a switchback is longer in time, it must be physically larger and thus make up a larger part of the solar wind. To assess the contribution of switchbacks to the solar wind, a metric that is unrelated to the duration, such as the Poynting flux (Woolley et al. 2020; Mozer et al. 2020) or magnetic curvature (Bandyopadhyay et al. 2021), must be used.

This also means that spacecraft data will be inherently biased towards the longest duration, not necessarily the largest, switchbacks. Therefore, a mean average solar wind velocity will be biased towards the longest switchbacks, which will point in the direction that minimises the cutting angle, rather than true background solar wind direction. A background solar wind velocity can still be calculated with a method that removes the switchback's contribution, such as the mode average (Bale et al. 2019) or the methods discussed in Section 4.3.3.

The size estimates from other studies are shown in Table 4.2. In this thesis, and in Horbury et al. (2020b), large statistics were used to estimate the average switchback width as $\sim 5 \times 10^4$ km. Krasnoselskikh et al. (2020) instead analysed several case studies of switchbacks, noting the presence of currents at their edges. They argued that these currents existed on the switchback surface, which was also assumed to be cylindrical. Applying careful analysis to the flow deflections around the chosen switchbacks, they found widths of 7,000 km and 50,000 km for a 'compressive' and Alfvénic switchback, respectively.

Another study, by Larosa et al. (2021), applied MVA to the switchback bound-

aries. An average normal direction to the switchback edges was estimated, and then used to project the spacecraft velocity perpendicular to the switchback structure. After multiplying by the relative speed, they found switchback widths vary from ∼1000 km to a solar radius (695,000 km), with a mode value around 10^4 km.

Study	Encounter	Transverse Scale (km)	Aspect ratio
Laker et al. (2021b)	1, 2	50,000 km	∼10
Horbury et al. (2020b)	1	10^4 km	-
Krasnoselskikh et al. (2020)	1	7000 km for compressive 50,000 km for Alfvénic	-
Larosa et al. (2021)	1	10^3 km - 10^5 km	-
Bandyopadhyay et al. (2021)	1-5	<16,000 km[2]	-

Table 4.2: Summary of the current estimates of switchback size. These range from 1000 km to 10^5 km, although all studies agree that switchback width is around 10^4 km

Finally, a novel approach was taken by Bandyopadhyay et al. (2021), who studied the behaviour of energetic particles (80-200 MeV) during switchback periods. They observed that in 86% of cases, energetic protons were not affected by the switchback, and continued to stream anti-Sunward. This then suggests that the curvature of the magnetic field inside switchbacks must be less than the local proton gyro-radius, ∼4000 km. A typical S-shaped structure has two bends in the magnetic field, making the width of the switchback roughly equal to four radii of curvature (<16,000 km). Interestingly, there were still 14% of switchbacks in their study that did affect the energetic particles, suggesting their magnetic curvature was greater than the proton gyro-radius, and thus represented physically larger switchbacks. Therefore, energetic particles could be an important size diagnostic for switchbacks in the future.

In summary, the results from several methodologies in Table 4.2 suggest that switchbacks are around 10^4 km in width. However, most of this research was performed on the early PSP encounters, so it is unclear how switchback size varies with distance, information which could be used to deduce the generation mechanism.

As well as physically changing in size, the switchbacks could appear differently in the later PSP encounters, which will eventually come within 9 $R_\odot$ of the solar surface. This can be predicted using the theory from Section 4.4.1.

[2]Assuming an S-shaped structure

Firstly, as noted earlier, only six streams out of 16 produced good results, with many streams having an insufficient range of deflection directions. During the first three encounters, PSP's orbit meant that it tracked slowly in longitude. This allowed many switchbacks to be measured per patch, providing large enough statistics to measure their size. In future encounters, an increased orbital speed could mean that insufficient switchbacks are measured per stream to apply the methodology from Section 4.4.2.

Nevertheless, predictions can still be made for how switchbacks will appear in these later encounters. If, as Fig. 4.17 suggests, switchbacks are aligned close to the Parker spiral, then they will become more radially aligned closer to the Sun. Combined with a larger transverse spacecraft speed, this means that PSP will cut switchbacks at larger angles to their longest axis. As a consequence, there will be fewer longer switchbacks, and a less pronounced relationship between duration and clock angle.

However, the true link between switchback duration and deflection will be a complex interplay between: spacecraft velocity; Alfvén speed; alignment direction; and the unknown evolution of switchback size and shape. These predictions will be revisited in Section 4.5.3 using more up-to-date PSP measurements.

4.5 Preferential switchback deflection directions

Based on the basic switchback properties described in the first two PSP encounters, several authors outlined their ideas for how switchbacks may be generated, as described in Section 4.2. One particularly interesting property was the switchback deflection direction, which was observed to have a preference towards $+\vec{T}$ in the first encounter (Horbury et al. 2020b; Dudok de Wit et al. 2020). Schwadron and McComas (2021), along with Fisk and Kasper (2020), argued that this observation could naturally be explained by their super-Parker spiral and interchange reconnection ideas, respectively. As those authors point out, any preferential switchback direction is more difficult to reconcile with the expanding wave set of generation

methods (e.g. Squire et al. 2020), where switchbacks are created from evolution of small, randomly distributed fluctuations closer to the Sun. Therefore, evidence, or lack thereof, for preferential switchback deflection directions could help differentiate between switchback origin theories, and move a step closer to understanding their link to the solar wind.

Crucially, much of the evidence for this switchback property was based on the data from the first PSP encounter, when the spacecraft was connected to a small equatorial coronal hole for a long period. These conditions are not representative of the typical near-Sun solar wind, which may have biased the current understanding of switchbacks. Given that PSP had completed a further six encounters by the time of this research in Laker et al. (2022), it is imperative that switchback deflections be revisited.

Therefore, in this section, the deflection directions of switchbacks are examined for the first eight PSP encounters, which reached only $16\,R_{\odot}$ from the Sun. This may represent a more pristine solar wind, that has not evolved as significantly as in the first encounter at $35\,R_{\odot}$, potentially making any pattern in the magnetic field clearer.

4.5.1 Switchback deflection distributions

As the PSP mission progressed, it became clear that each solar encounter had its own unique characteristics based on the source location of the solar wind. Accordingly, in this study, each encounter was treated separately, rather than trying to aggregate all the switchbacks across the encounters. A summary of E2 is shown in Fig. 4.18, where the proton speed indicates that both slow and fast wind were sampled. The lower panel of Fig. 4.18 displays the clock angle of every switchback in E2, demonstrating that switchbacks can deflect in any direction. This finding holds across all encounters studied, as well as the presence of switchback 'clustering', where several successive switchbacks are orientated in the same direction (Horbury et al. 2020b). However, when considering the distribution of clock angle across the encounter, the histogram

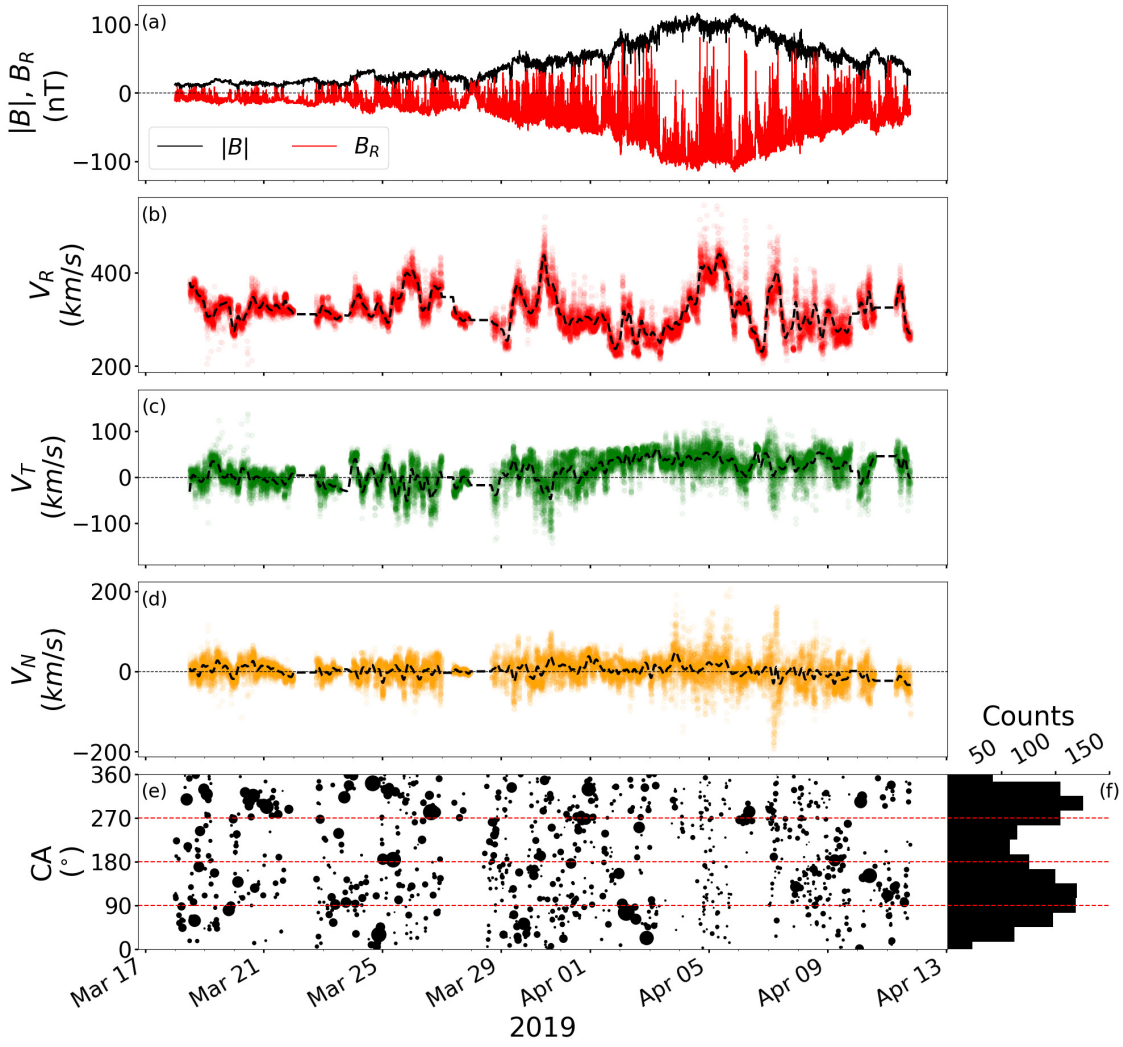


Figure 4.18: Summary of plasma conditions (a-d) and switchbacks (e-f) in E2. Panel (e) shows that switchbacks can deflect in any clock angle, with scatter size being proportional to duration, similar to Horbury et al. (2020b) and Section 4.4. However, the histogram in panel (f) suggests that switchbacks tend to deflect in either ∼100° and ∼300°.

in panel (f), there were two preferred directions, ∼100° and ∼300°.

Wrapping this histogram onto polar axes, in Fig. 4.19, made for easier comparison to the clock angle definition from Section 4.3.1. Here, bins of 30° were used, starting at 15°, meaning that there was a bin centred on 0°/360°. For this particular bin, the final result was taken as the sum of the two half bins spanning 345° → 360° and 0° → 15°. Due to the Alfvénic nature of switchbacks, the relationship between magnetic and velocity deflections depends on the magnetic polarity, which is plotted as blue for negative and red for positive polarity.

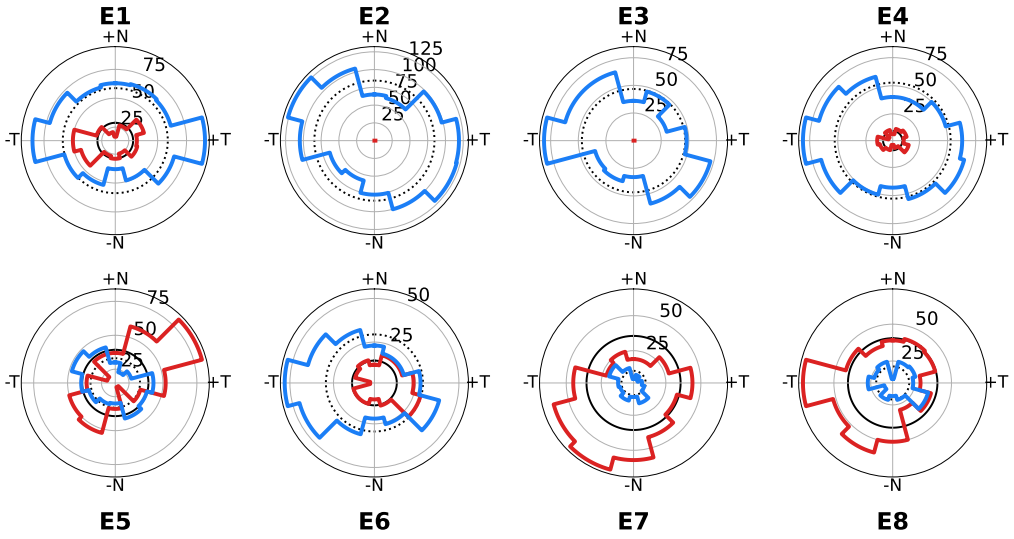


Figure 4.19: Distribution of switchback magnetic clock angles across the first eight encounters, split into negative (blue) and positive (red) polarity. None of the distributions followed a uniform distribution, as represented by the dashed (negative) and solid (positive) circles. This demonstrates that switchback deflections are not isotropic, with a preference in the tangential direction, 90° and 270° (reproduced from Laker et al. 2022).

Applying this procedure to all the encounters produced Fig. 4.19, which summarises the magnetic switchback deflections. Each distribution of clock angles was tested against a null hypothesis of a uniform distribution. This was taken as the number of switchbacks in that population divided by the number of bins, which is represented by the dashed (negative) and solid (positive) circles in Fig. 4.19. Using a Chi-square test with a 1% confidence level, it was concluded that the switchback deflections did not follow a uniform distribution. Although there was variation among the encounters, there was an apparent preference for tangential, rather than normal, deflections. In terms of clock angle, this is represented as a maximum in the distribution around 90° and 270°, rather than 0° or 180°.

Interestingly, for negative polarities these preferential directions were not purely tangential but had an offset axis of symmetry along ∼135° and ∼315°, best demonstrated in E2. In contrast, the positive polarities appeared to have an axis of symmetry along ∼45° and ∼225°, e.g. E5 and E7. This is equivalent to mirroring the negative polarity preferential directions about 180°. This cannot be explained by simply comparing their velocity, rather than magnetic field, which would require a

rotation of 180° in clock angle for the observed positive polarity[3].

4.5.2 Discussion

After the first two PSP encounters, several mechanisms for switchback creation were proposed, many of which cited the switchback's deflection directions as potential evidence. This study has re-evaluated the deflection property across the first eight PSP encounters, where it was observed that switchbacks could deflect in any direction, but had a tendency for this to be in the tangential, rather than normal, plane. Therefore, in this section, these proposed switchback generation mechanisms are re-visited in light of this new evidence.

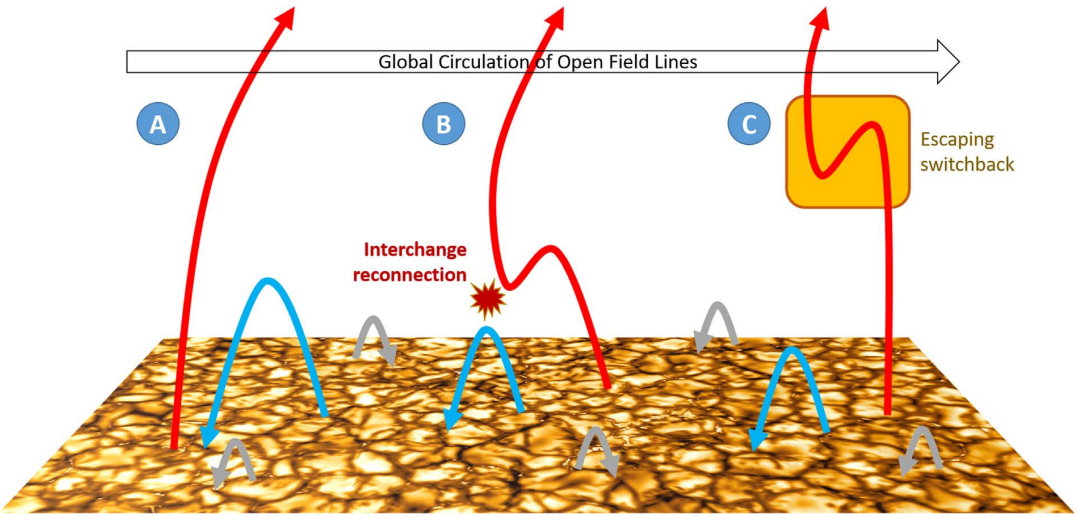


Figure 4.20: Diagram of interchange reconnection from Fisk and Kasper (2020). Open field lines (red) are dragged across closed loops (blue) by the differential rotation of the corona and photosphere. This initiates interchange reconnection at point B, where an S-shaped kink is launched into the solar wind (reproduced from Fisk and Kasper 2020).

As noted by Fisk and Kasper (2020), interchange reconnection can naturally explain both the tangential deflections and clustering behaviour of switchbacks. In this mechanism, open magnetic field lines are dragged over closed loops on the Sun's

[3]When the magnetic field has positive polarity, the velocity fluctuations will have opposite sign to the magnetic field deflections, meaning that the distributions of magnetic clock angle should be rotated by 180°

surface, initiating interchange reconnection and launching an S-shaped kink into the solar wind, as depicted in Fig. 4.20. Since the open field lines in coronal holes are observed to rotate quasi-rigidly with the corona, they are travelling faster than the closed loops on the surface. Even though the orientation of closed loops may be random, it is thought that this differential rotation rate could impart a preference for tangential deflections on the switchbacks.

While this matches the observations from the previous section, Fisk and Kasper (2020) argue that the kink in the magnetic field will be orientated such that the velocity deflection points towards the $+\vec{T}$ flow seen by Kasper et al. (2019). This would require a magnetic deflection in the $+\vec{T}$ (90°) direction for negative polarity, and $-\vec{T}$ (270°) for positive polarity. For clarity, the predictions from each method are converted in Fig. 4.21 to match the format of the results in this thesis. While such predictions match the positive polarity distribution from E7 and E8, the deflection angles across the encounters do not show a preference for a single direction, i.e., observations show $\pm\vec{T}$ rather than just $+\vec{T}$.

Interestingly, from arguments regarding the transport of open magnetic flux, there should be some component of magnetic shear in the normal direction, with the northern (positive) hemisphere transporting flux downwards and the southern (negative) hemisphere transporting flux upwards (Fisk 1996). A similar effect in the normal directions was observed in some encounters, where the two magnetic polarities had opposite normal components, i.e. in Fig. 4.19 the negative polarities had maxima at 135° and 315° and positive polarities at 45° and 225°. Therefore, it is promising that interchange reconnection could provide a normal component to explain the offset axes of symmetry from Fig. 4.19, although there is not an exact match between the observations and predictions from the transport of flux argument.

Finally, in this theory, switchback clustering can be explained if the source of interchange reconnection remains stable enough for several switchbacks to be launched with the same orientation (Zank et al. 2020). In this scenario, the specific orienta-

tion of a cluster of switchbacks would then be related to the magnetic configuration at the source location.

The super-Parker spiral theory from Schwadron and McComas (2021) also relates back to the source location of switchbacks to explain a preferential deflection direction towards $+\vec{T}$. Here, the magnetic field footpoint moves from slow to fast solar wind, which evolves into a kink farther from the Sun. Therefore, in order to create a kink, rather than a more radial magnetic field, the velocity deflection should always be in the same direction as the solar rotation, as summarised in Fig. 4.21.

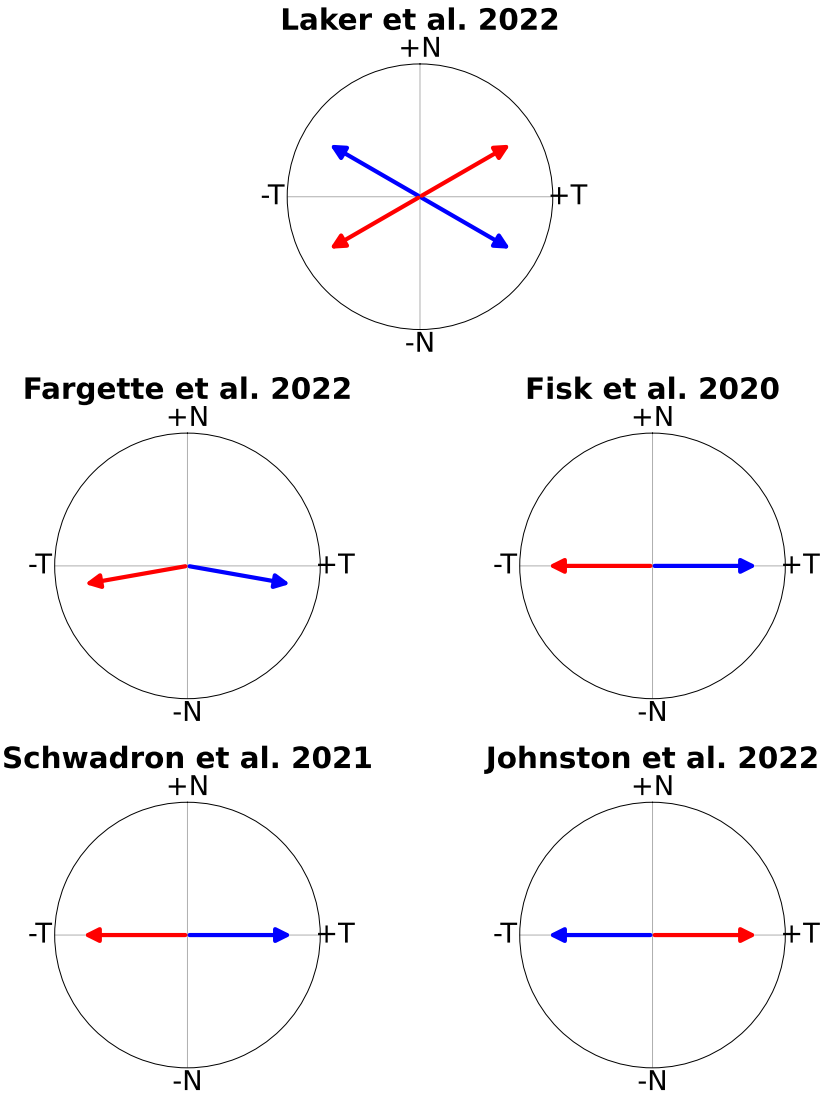


Figure 4.21: Summary of predictions for switchback deflections, adapted to follow the format of Fig. 4.19. Red indicates a background magnetic field with a positive polarity, and blue for negative polarity.

Again, like the predictions of Fisk and Kasper (2020) this was only seen in a few select cases, and is not the general rule across all the encounters.

Contrary to the evidence cited in Schwadron and McComas (2021), the switchbacks in E1 do not only deflect towards $+\vec{T}$, but have a preference for either $\pm\vec{T}$. Therefore, the result from Horbury et al. (2020b) was most likely a cluster of switchbacks, rather than a global pattern in the switchback deflections. However, it should be noted that Horbury et al. (2020b) argued that a connection between deflection direction and duration could be linked to the angle at which the spacecraft cut through a switchback. This, and other potential causes of the clustering, are discussed in the next section.

Perhaps the most compelling argument against the super-Parker idea is that switchbacks are Alfvénic, meaning that the maximum velocity deflection occurs at the maximum magnetic field deflection – i.e. a full reversal in the field direction. However, in this proposed mechanism, the maximum velocity will exist when the field is at 90°. So, while this mechanism may be responsible for large scale magnetic field deflections, on the order of CIRs, it is not likely to be the primary cause of the smaller scale switchbacks.

Another class of switchback generation theories are based on the expansion of random fluctuations in the nascent solar wind, rather than requiring some solar source (Squire et al. 2020; Mallet et al. 2021; Shoda et al. 2021). As noted by Fisk and Kasper (2020), without a systematic magnetic configuration, it seems difficult to reconcile the clustering behaviour and preference for tangential deflections. Following the results of this section, both Squire et al. (2022b) and Johnston et al. (2022) investigated the potential effect of the Parker spiral on the distribution of switchbacks, having only used simulations with a radial field previously. They found that this did in fact introduce a preferential deflection direction towards the radial direction from the Parker spiral. This, as demonstrated in Fig. 4.21, corresponds to $-\vec{T}$ (270° clock angle) for negative polarity and $+\vec{T}$ (90° clock angle) for positive polarity.

While this does not fully match the results from the previous section, it still suggests that offset magnetic field geometries can influence the evolution of switchbacks. Therefore, even without a consistent magnetic field orientation on the Sun, switchbacks generated from random fluctuations can still develop a preference for a particular direction.

Other than the Parker spiral, recent results in Bale et al. (2021) and Fargette et al. (2021) suggest that 'magnetic funnels' can provide a systematic magnetic shear that may influence the switchbacks. As seen in Fig. 4.22, these may relate to the super-granular network on the Sun, and can provide a magnetic shear in the tangential direction capable of influencing the switchback evolution.

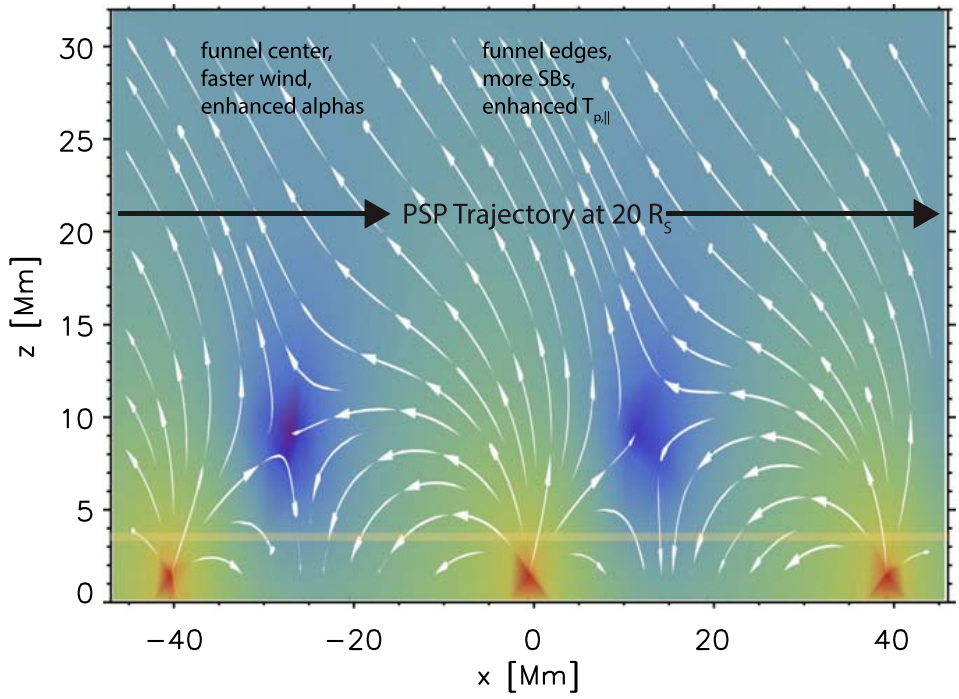


Figure 4.22: Figure from Bale et al. (2021) showing their proposed magnetic field geometry at the Sun (white vectors). Colour scale indicates the magnetic field strength with faster wind coming from the centre of magnetic funnels. Such a magnetic shear could influence the deflections of switchbacks (reproduced from Bale et al. 2021).

In terms of other observations, a similar study to that in this thesis was carried out on the first nine encounters by Fargette et al. (2022). They took a more probabilistic approach, and considered the full distribution of magnetic field directions

in the encounter, instead of trying to isolate individual switchbacks as done in this thesis. As noted by Fargette et al. (2022), their method cannot determine whether more switchbacks were deflecting in a certain direction, or if there was a greater contribution from longer switchbacks. Nevertheless, this provides a contrasting method to study the switchback deflections.

Fargette et al. (2022) also observed that switchbacks could deflect in any direction, but had a preference for 'clockwise [velocity] deflections'. As seen in Fig. 4.21, when converted to magnetic field deflections, this suggests a preference for tangential deflections. However, the authors only observed a preference towards clockwise velocity (see Fig. 4.21), rather than the $\pm\vec{T}$ result reported in this section. As well as confirming the presence of switchback clustering, they also found a slight bias towards negative B_N, similar to the offset symmetry axis from Fig. 4.19.

Therefore, the observations from Fargette et al. (2022) seem to better match the predictions from interchange reconnection (Fisk and Kasper 2020), with the authors making similar arguments regarding the differential rotation rate of the corona and photosphere. The same clockwise preference was also found by Meng et al. (2022) in the first two encounters, although they only used ∼100 switchbacks per encounter, rather than the several thousand found in this thesis (Table. 4.1).

So, while the exact distribution of switchback deflections is debated, it is clear that there is a tendency for deflections in the tangential plane. This study found that although there was a tangential preference, it was in both $\pm\vec{T}$, rather than the single $+\vec{T}$ direction observed by Fargette et al. (2022) and predicted by interchange reconnection (Fisk and Kasper 2020). While these results, and the clustering behaviour, can both be naturally explained by interchange reconnection, recent studies from Johnston et al. (2022) and Squire et al. (2022b) suggest that in-situ mechanisms cannot yet be ruled out.

4.5.3 Linking time series to a physical shape

The most common interpretation of the switchback clustering is that there are genuinely several larger switchbacks deflecting in the same direction. This may be as a result of consistent magnetic orientation closer to the Sun, or the influence of the Parker spiral. However, given that these claims are based on data from a single spacecraft, there are other ways to produce this effect in the time series.

With the current definition based on magnetic field deflection, the internal structure of a switchback is related to the definition itself. Therefore, it is possible that a cluster of 'switchbacks' could be the sub-structure of some larger phenomenon that has been misclassified. So, in order for switchback research to progress, a consistent definition should be established that does not rely fully on the magnetic structure.

One such definition could come from the parallel proton core temperature, which was observed to be enhanced in periods around 30 minutes long by Woodham et al. (2021a). Although this was only seen in a small period of E2, it suggests that there could be some larger structure that contains several deflections in the magnetic field, which have been classified as switchbacks to date.

Another potential definition could come from establishing the leading and trailing boundaries of the switchback. This could either be through looking for dips in $|\vec{B}|$ (Farrell et al. 2020); enhanced wave activity (Agapitov et al. 2020; Mozer et al. 2020; Larosa et al. 2021); or the presence of currents (Krasnoselskikh et al. 2020). A switchback could then be defined as the period between a pair of edges, allowing for the internal magnetic structure to be separate from the switchback definition.

Finally, the magnetic curvature inside a switchback could be probed by observing the propagation of the energy protons (Bandyopadhyay et al. 2021). In that study, the authors stated that energetic protons were not affected by switchbacks in 86% of cases. They then concluded that most switchbacks exhibited this behaviour, so the switchback size could be constrained to $<$16,000 km. However, those 14% of switchbacks that did affect energetic protons could be classified as having larger magnetic curvature, and therefore be physically larger. Such a subset of switchbacks

would be crucial for helping determine the link between switchback duration and size.

As outlined in Section 4.4 and Horbury et al. (2020b), the duration measured by the spacecraft could be related to the way in which it cut through the switchback. Therefore, a cluster of switchbacks would be created if there was a deflection direction that produced a longer duration in the time series. This would mean that such switchbacks would only appear longer, but would still have the same physical size as those switchbacks with a less favourable cutting angle. Using the method from Bandyopadhyay et al. (2021), the behaviour of energetic particles could be studied in a cluster of switchbacks to determine if they did indeed have a larger physical structure.

Based on arguments made in Section 4.4.4, it was expected that there would be a lessened dependence of duration on deflection direction in later encounters. However, this was not reflected in the observations in this more recent study. In searching for a way to reconcile these new observations with the framework of long, thin switchbacks, the link between physical shape and what is portrayed in the time series was explored further.

A typical representation of a switchback is often an S-shaped kink in the magnetic field, as depicted in Fig. 4.23 (Kasper et al. 2019; Macneil et al. 2020). Since the full context of the magnetic field and plasma is present in a simulation, the switchback is often defined by the shaded region. However, when dealing with time series data from PSP, a switchback is usually defined as a magnetic deflection over some threshold, e.g. 15°. Applying such a threshold to the diagram in Fig. 4.23 gives a thinner, off axis shape (red) when compared to the simulation (grey) classification.

This is reminiscent of the 'long, thin' structures with an alignment direction towards the Parker spiral, which was concluded to be the shape of the switchbacks in Section 4.4. So, while this earlier work may still be valid, it may not have measured the full switchback shape as would be defined in a simulation or diagram, where the full context is available.

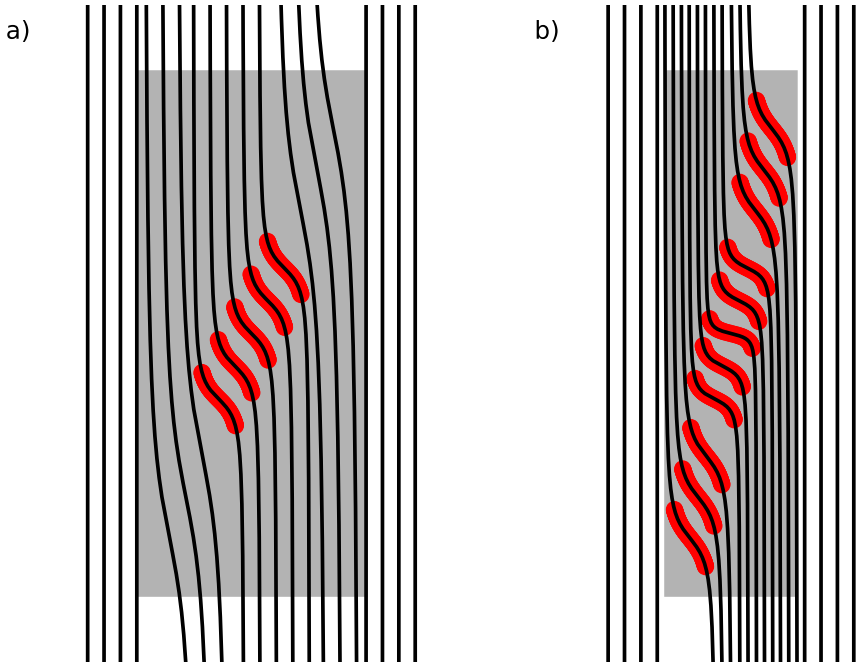


Figure 4.23: Demonstration of the difference between the time series definition (red) and the simulation perspective (grey rectangle). A threshold of 15° deflection angle is used, which creates a longer, thinner structure angled away from the background direction. As the magnetic curvature increases in b), this effect is more pronounced. These lines are for demonstration purposes only, and do not obey Maxwell's equations.

An important aspect of the demonstration in Fig. 4.23 is that this 'time series' shape will depend on the magnetic curvature inside the switchback. For example, a tighter S-shape, as in Fig. 4.23b, will result in a longer structure more aligned to the background magnetic field. Such an effect, combined with the unclear evolution of switchbacks with distance, means that there are now too many unknown variables to apply the method from Section 4.4.1 across the encounters. Even so, this work is still important for relating how the data presented in the time series actually corresponds to the true shape and size of switchbacks. Such a problem may be solved with a future multi-spacecraft mission, where the added spacecraft can provide context not possible with PSP alone.

4.6 Conclusions

This chapter has investigated the deflection characteristics of switchbacks, which was performed in two separate studies, Laker et al. (2021b) and Laker et al. (2022).

In the first study (Section 4.4), the link between switchback deflection direction and duration was investigated, with the aim to estimate the average switchback dimensions. Following Horbury et al. (2020b), switchbacks were assumed to be long and thin, with cylindrical symmetry. This made it possible to search for the alignment direction that could best describe the observed dependence between switchback duration and clock angle. For six streams in encounters 1 and 2, from $35\,R_{\odot}$ to $50\,R_{\odot}$, switchbacks were found to have consistent sizes with an average of $\sim$50,000 km and an aspect ratio of the order of 10. This provides a useful scale size to compare to switchback simulations or theories of their generation.

While the assumptions regarding switchback dimensions can never be proven with a single spacecraft, the consistent sizes and alignment directions suggest that the framework set out in this chapter could explain the link between duration and clock angle. The average switchback alignment direction was found to be towards the Parker spiral direction and not related to the background solar wind flow, which rules out a link to the $+\vec{T}$ flow deflection reported in Kasper et al. (2019). However, this would still be consistent with Alfvénic pulses travelling along the field, such as those suggested by Sterling and Moore (2020). There was still some variation in alignment directions across the streams, perhaps implying that alignment direction may be linked to the unique magnetic configuration closer to the Sun, such as the patches suggested by Bale et al. (2021) and Fargette et al. (2021).

If switchback duration is indeed linked to the direction at which a spacecraft cuts through a structure, then there needs to be another method for determining physical switchback size. This may come from studying the behaviour of energetic protons, which are directly affected by the magnetic curvature inside the switchbacks. An ability to detect the physical boundary of the switchback would also be useful, and may be possible by finding dips in $|\vec{B}|$ or enhanced wave activity (Farrell et al. 2020;

Mozer et al. 2020; Akhavan-Tafti et al. 2021).

In the latter study (Section 4.5), the distribution of switchback deflection angles was investigated over the first eight encounters in an attempt to distinguish between different generation mechanisms. This was motivated by claims that switchbacks should preferentially deflect in certain directions in some switchback theories.

By estimating the clock angle for each switchback, it was found that switchbacks did not deflect equally in all directions. Instead, switchbacks preferentially deflected in either 135° → 315° clock angle for inwards magnetic polarity, or 45° → 225° clock angle for outwards magnetic polarity. This did not fully match the prediction that switchbacks would have a single preferential direction (Fisk and Kasper 2020; Schwadron and McComas 2021), but it still demonstrated that there was a systematic effect in the switchback deflections.

It was originally thought that such a characteristic could not be explained by those theories based on the expansion of random fluctuations (Squire et al. 2020; Shoda et al. 2021; Mallet et al. 2021). However, motivated by these results, Johnston et al. (2022) demonstrated that the Parker spiral can influence switchbacks and create an asymmetric deflection distribution. It was also noted that a consistent magnetic configuration closer to the Sun, such as magnetic funnels (Bale et al. 2021), could create the same effect. So even though this chapter represents another step towards describing switchbacks and their properties, there is still ambiguity regarding the source of switchbacks.

Finally, there was a discussion of the limitations of single spacecraft measurements when trying to study the internal switchback structure. It was concluded that a better switchback definition is needed to make progress in switchback research, which will be addressed in the next chapter.

Chapter 5

Systematic deflections in the near-Sun solar wind

The previous chapter described the switchback size, shape and preferential deflection directions, which improved the understanding of switchbacks during PSP's first four years of operation (see Raouafi et al. 2023a for a review). However, with PSP travelling to only 13 $R_\odot$ from the Sun, this chapter now aims to find more direct signatures of heating and switchback generation in the nascent solar wind.

The relevant switchback theories, along with their testable predictions, are first outlined in Section 5.1. A new systematic pattern of magnetic field deflections will be introduced in Section 5.2, challenging the current understanding of switchbacks. The scale of these deflections is investigated in Section 5.3, with a focus on how these structures could relate to features found on the Sun. In addition to recognising a consistent pattern in the magnetic field, Section 5.4 demonstrates that switchbacks were associated with temperature enhancements close to the Sun. Finally, the larger-scale temperature behaviour and properties of two different solar wind types are discussed during Sections 5.5 and 5.6, which could ultimately help uncover the origin and role of magnetic switchbacks in the solar wind.

5.1 Motivation

5.1.1 Switchback definition

In the most basic definition, switchbacks are Alfvénic, arc-polarised deflections away from the magnetic field. Many of the additional switchback properties were deduced by averaging over large numbers of switchbacks in the early encounters, which were identified with a threshold in the magnetic field angle (e.g. $>45°$). While this was a quick, easy way to identify switchbacks over an entire encounter, it has influenced the way in which switchbacks are considered. For example, with this definition, any suitably large deflection in the magnetic field is classified as a distinct switchback. However, deflections could equally be part of some larger structure. These two scenarios are indistinguishable using a switchback definition based solely on the absolute magnetic field angle. Therefore, to improve the understanding of switchbacks and their internal structure, a new definition must be found.

This would be straightforward if there were a distinct difference in the plasma properties inside and outside the switchbacks. However, recent studies have presented conflicting reports on the temperature change seen inside switchbacks. On one hand, Woolley et al. (2020) used SPC to show that $T_{p,\parallel}$ was the same inside ($\theta_{RB} = 180°$) and outside ($0°$) switchbacks. Subsequently, with fits to the SPAN VDFs, Woodham et al. (2021a) showed that $T_{p,\parallel}$ was enhanced over groups of switchbacks. While this suggested different plasma conditions, it was unclear how switchbacks were related to the larger-scale structure of $T_{p,\parallel}$.

Furthermore, due to the limitations of SPAN in the early PSP encounters, Woodham et al. (2021a) could not determine the behaviour of the temperature past $\theta_{RB} = 90°$. Therefore, it is still not known whether the results from these two instruments are compatible with one another, i.e. whether the proton core temperature returns to background levels at $180°$, as SPC suggests.

Fortunately, with the higher orbital speed of PSP in E11, the proton core will become more visible in SPAN's FOV. This, combined with the fact that solar wind

structures should be more pristine closer to the Sun, means that it should be possible to fully characterise the behaviour of $T_{p,\perp}$ and $T_{p,\parallel}$ with magnetic field angle up to $\theta_{RB} = 180°$.

In summary, to create a more robust switchback definition, this chapter aims to answer the following questions:

1. Is there a consistent plasma signature inside switchbacks?

2. How do the larger-scale enhancements in $T_{p,\parallel}$ from Woodham et al. (2021a) relate to switchbacks?

3. What is the behaviour of the proton core temperature inside switchbacks with $\theta_{RB} > 90°$?

4. Can plasma properties be used to help define a switchback?

5.1.2 Potential signatures of generation mechanisms

Many of the switchback theories proposed in Section 4.2 were based on the properties described in the first few PSP encounters. Since then, new evidence has been reported, which has formed the basis for several new switchback generation mechanisms. These will be outlined in this section, with a focus on the signatures that could be measured now that PSP has travelled to only 13 $R_\odot$ from the Sun.

To explain the existence of both switchbacks, and their larger-scale modulation in patches, Kumar et al. (2022) have suggested that coronal plumes could be the source, as shown in Fig. 5.1. These stable column-like structures have long been observed inside coronal holes (see Section 2.2.2). Recent studies have shown that they contain significant sub-structure and dynamics, with the existence of numerous reconnection driven jets at the base, termed 'plumelets' (Raouafi and Stenborg 2014; Uritsky et al. 2021; Kumar et al. 2022). While there is some debate, these features seem to be the manifestation of the small-scale 'jetlets' at the base of the plumes (Raouafi et al. 2008; Kumar et al. 2019). Observations suggest that they are caused

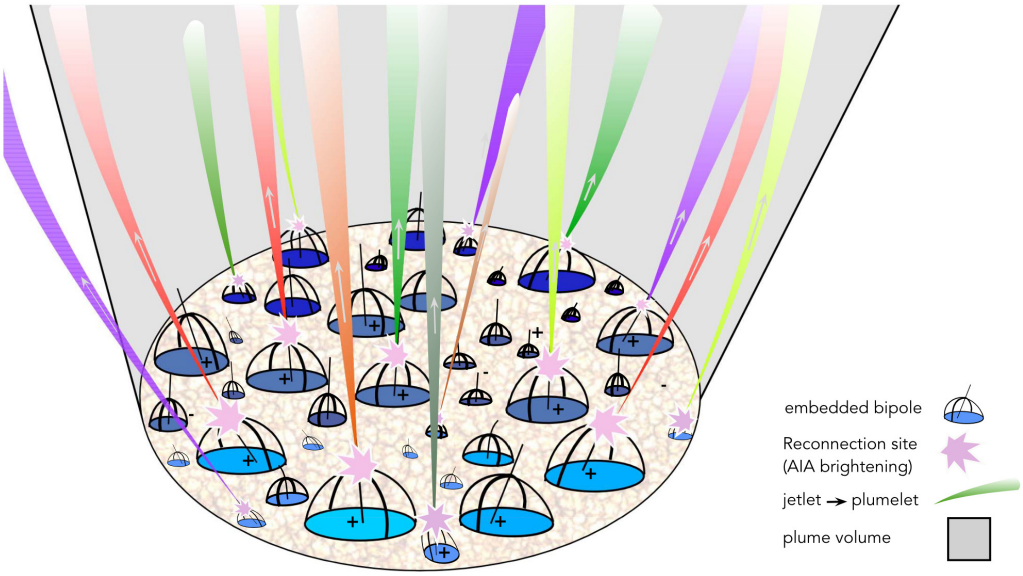


Figure 5.1: Diagram showing how embedded bipoles in a coronal plume (shaded grey volume) could create the switchbacks at PSP through the launch of jetlets via interchange reconnection (reproduced from Kumar et al. 2022).

by interchange reconnection of an embedded bipole in the otherwise unipolar coronal hole, as depicted in Fig. 5.1.

As a result, Kumar et al. (2022) argue that the base of plumes are filled with many bright points that undergo repeated magnetic reconnection, launching kinks in the magnetic field that would be seen as switchbacks by PSP. This kinked magnetic field line is similar to those created in the interchange reconnection (Fisk and Kasper 2020; Zank et al. 2020) and coronal jet ideas (Sterling and Moore 2020; Neugebauer and Sterling 2021). However, Kumar et al. (2022) now suggest that each bright point relates to a switchback patch (Bale et al. 2021; Fargette et al. 2021), with the repeated reconnection creating a series of switchbacks.

Remote sensing observations show that these bright points undergo quasi-periodic reconnection, at a frequency of around 3 → 5 minutes (Uritsky et al. 2021). This matches the long-standing 5-minute oscillations (p-modes, see Section 2.2.2) on the Sun, implying that this photospheric oscillation could repeatedly trigger reconnection at the bright points (Uritsky et al. 2021; Kumar et al. 2022). Therefore, much like the interchange reconnection idea (Fisk and Kasper 2020; Zank et al. 2020), this scenario should create groups of switchbacks that have a similar orientation,

which relates back to the configuration of the magnetic field at the bright point. Additionally, there is now the extra prediction that the switchback in the solar wind should reflect the 3 → 5 minute oscillations on the Sun. While preferential deflection directions have been observed for switchbacks over an entire encounter (Section 4.5), this signal should be visible on a more local scale, especially with PSP so close to the Sun.

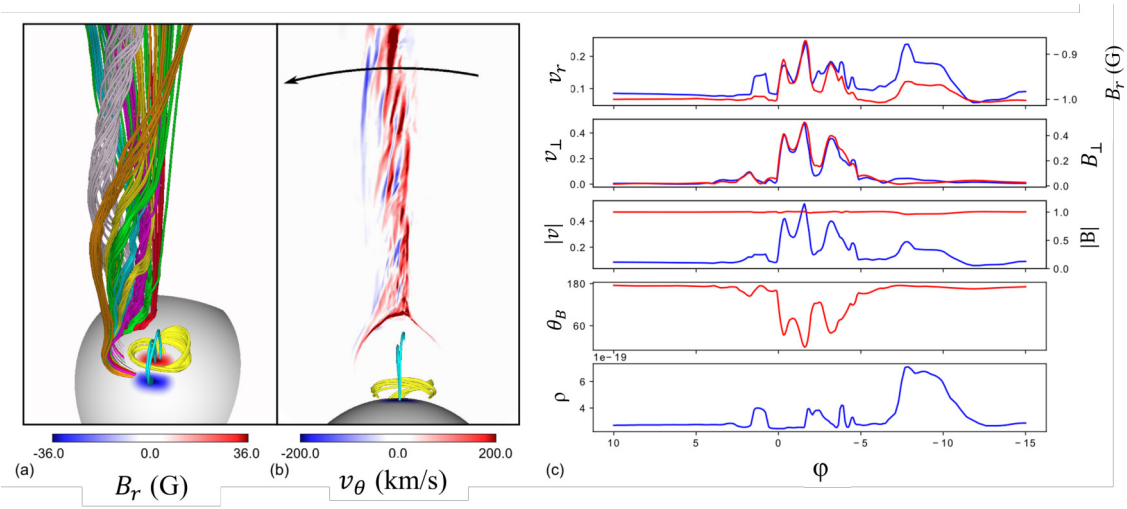


Figure 5.2: Interchange reconnection simulation from Wyper et al. (2022). Quasi-periodic reconnection at the loop creates torsional Alfvén waves (left panel). As the spacecraft moves through a 2D slice (right panel) it will see a periodic pattern of deflections in velocity (blue) and magnetic field (red) (reproduced from Wyper et al. 2022).

There is still some debate on whether kinks in the magnetic field will survive into the solar wind, with Wyper et al. (2022) arguing that kinks would relax due to magnetic tension in the low plasma-β corona. Instead, the authors followed on from the work of Drake et al. (2021) who investigated the release of flux ropes with a 2.5D simulation of interchange reconnection. However, by treating the plasma in 3D in this newer study, the intermittent reconnection of a magnetic null-point was seen to create a continuous source of torsional Alfvén waves.

Consequently, from the same magnetic topology as the bright points in Fig. 5.1, Wyper et al. (2022) has shown that a continuous flow of Alfvén waves would be produced. This would be more stable than the kinked magnetic field usually envisaged in an interchange reconnection scenario (Fisk and Kasper 2020; Kumar

et al. 2022).

As shown to the right of Fig. 5.2, a spacecraft moving through this outflow would experience a series of alternating tangential deflections with a constant $|\vec{B}|$. According to Wyper et al. (2022), there will be a consistent sense of rotation for the waves inside a 'patch' of deflections, i.e. from a single source of reconnection as in Fig. 5.2.

While this simulation was performed on a large-scale, Wyper et al. (2022) expect the process to be scale-invariant. Therefore, such results could represent an underlying feature of any switchback mechanism that invokes interchange reconnection. If this is true, then the signature of alternating tangential deflections should be prevalent throughout the solar wind. However, switchbacks are currently only considered to be isolated deflections in the magnetic field.

One major difference between this simulation and the observed switchbacks is the amplitude of the deflections, which were $<30°$ in the former. Wyper et al. (2022) solved this by suggesting that the pattern of small deflections could act as a seed for the expanding wave theories of in situ switchback generation (Squire et al. 2020; Shoda et al. 2021; Mallet et al. 2021).

Further evidence for interchange reconnection has come from the presence of a high energy tail to the proton core and alpha populations, as reported by Bale et al. (2022). These non-thermal tails had spectral indices consistent with simulations of exhausts from interchange reconnection closer to the Sun. The authors also showed that interchange reconnection could supply sufficient energy to drive the fast wind, as well as produce a continuous outflow of material. They concluded that faster material would be created on one side of the reconnecting loop, as seen in Fig. 5.3, creating an asymmetric pattern in the solar wind speed that is measured by PSP. While this geometry can explain the large-scale speed variations in a patch, there should also be systematic deflections on a smaller scale within the patch according to the work of Wyper et al. (2022) above.

In summary, there seems to be mounting evidence for interchange reconnection as

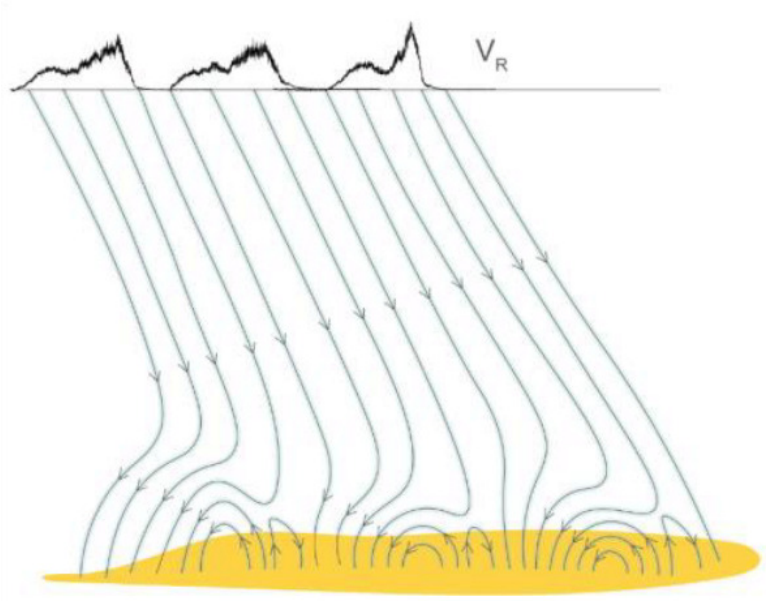


Figure 5.3: Asymmetric radial velocity profile (top) created by interchange reconnection at several coronal loops. Faster solar wind is created by the newly reconnected field lines that occur on one side of each magnetic field loop (reproduced from Bale et al. 2022).

the source for switchbacks. Remote sensing observations from Kumar et al. (2022) show that periodic reconnection is occurring on the Sun, while simulations have shown that interchange reconnection could provide a continuous outflow of material with a sufficient heating rate for the fast solar wind. In situ evidence includes both the high energy ion tails and the asymmetric modulation of the solar wind speed on a large scale. However, there is no evidence yet of the local magnetic field patterns predicted by both Kumar et al. (2022) and Wyper et al. (2022).

Therefore, this chapter will also aim to answer the following questions:

1. Do switchbacks show a consistent pattern of orientation on the local scale?

2. If so, then what is this scale? How does this relate to the solar features?

3. As well as the high energy tail from Bale et al. (2022), is there any proton core heating inside switchbacks?

5.2 Systematic deflections

Up to now, there have been some suggestions that neighbouring switchbacks may be related. For example, Dudok de Wit et al. (2020) used waiting time statistics to deduce that switchbacks had some 'memory'. There were also reports of switchback clusters, where several longer switchbacks would deflect in the same direction. However, there has been no evidence for a consistent pattern in the switchbacks, as predicted by several mechanisms in the previous section.

As PSP moved closer to the Sun in E11, a systematic pattern in the magnetic field emerged, an example of which is shown in Fig. 5.4. The top panel shows the typical dips in B_R that would normally be identified as several switchbacks, using a threshold on the magnetic field angle. More striking, however, was the periodic pattern in the B_T and B_N components, which appeared to be anti-correlated. The corresponding hodograms in the lower panels demonstrate that the magnetic field was still arc polarised, as found for switchbacks in Section 4.3.2. However, unlike previous observations, successive switchbacks are now consistently deflecting back and forth along the same arc. This created a series of alternating tangential deflections, remarkably similar to the predicted spacecraft signal for interchange reconnection in Fig. 5.2 (Wyper et al. 2022). Such a signal is seen throughout the E11 data, providing further evidence that this is due to some underlying process closer to the Sun. Consequently, these in situ observations could represent the imprint of interchange reconnection on the solar wind.

These observations also imply that switchbacks, as they are currently known, are merely a sub-sample of this more fundamental pattern in B_T and B_N. To demonstrate this point, Fig. 5.5a depicts the current definition of a switchback, where the magnetic field deflects away from the background direction and then back again. Taking into consideration that there is now a series of deflections along the same arc, one 'unit' of the new pattern would be represented by Fig. 5.5b. So, these results suggest that more emphasis should be placed on finding times when the magnetic field is consistently deflecting back and forth along the same arc.

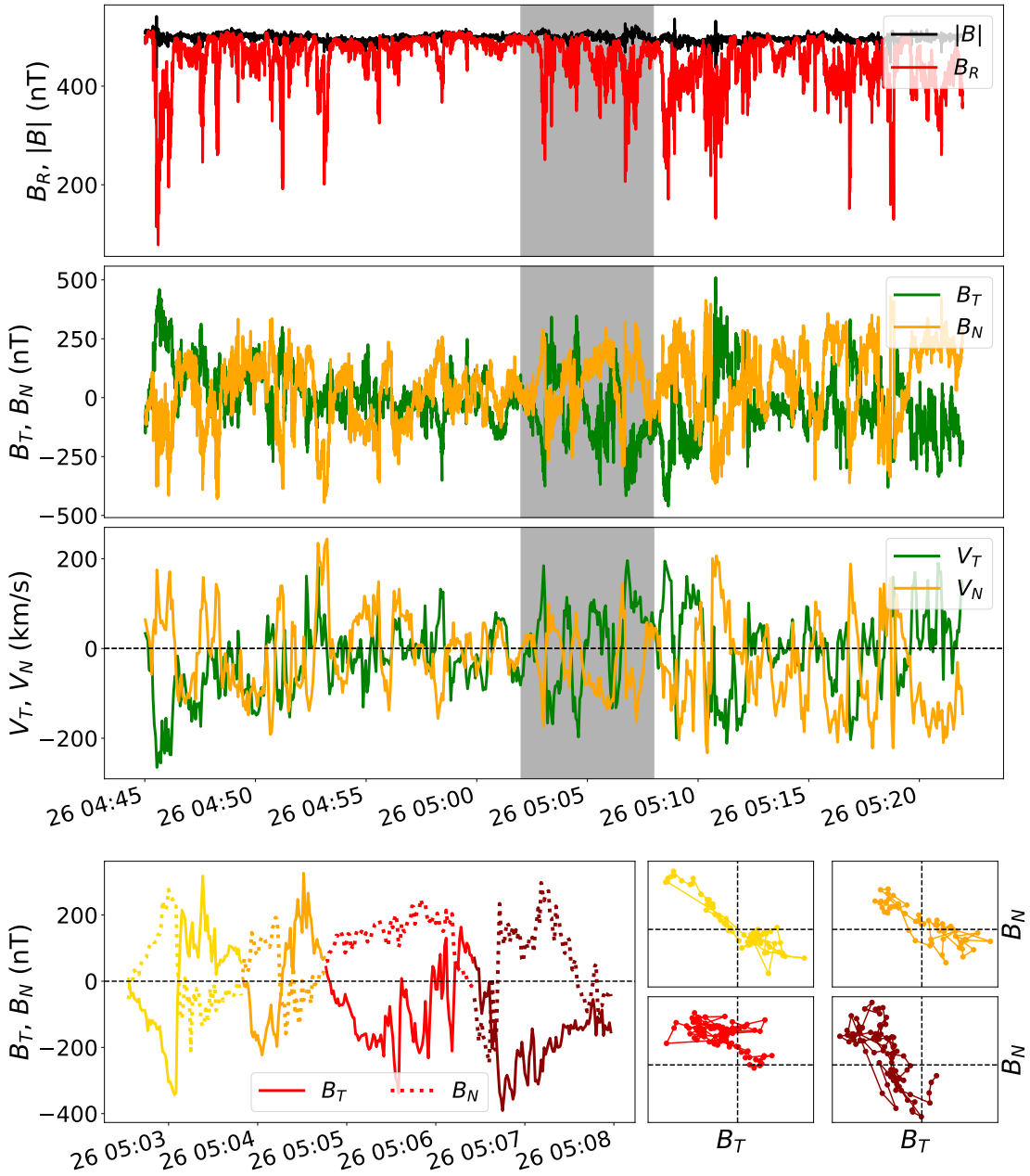


Figure 5.4: Example patch of anti-correlated deflections in B_T (green) and B_N (orange). These are still Alfvénic fluctuations, as shown by a similar pattern in the velocity fluctuations (third panel). The hodograms for the highlighted region are shown in the lower panels, where several successive deflections, split by colour, all travel along the same arc.

This new criterion is applied to the data in the lower panels of Fig. 5.4, where individual units of deflections are distinguished by colour. While this is not as clear as the theoretical depiction in Fig. 5.5b, it demonstrates that the physical shape of switchbacks is more like a continuous train of Alfvén waves than an isolated S-shaped

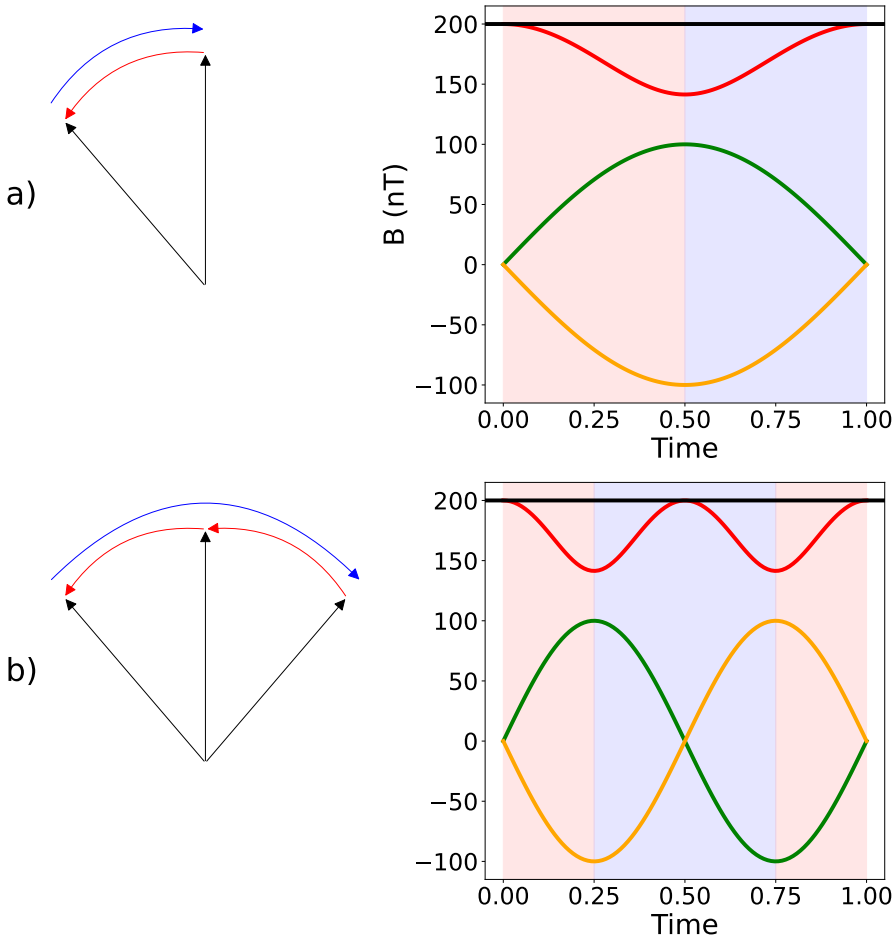


Figure 5.5: Demonstration of how the magnetic field deflections vary for the current (a) and proposed (b) definition of switchbacks. The magnetic field components that would be measured by the spacecraft are shown in the lower panels, following the same colour scheme as previous figures. The current switchback definition (a) has one dip in B_R representing a single deflection away from $\vec{R}$ and back. The proposed definition (b) has two dips in B_R, resulting in the magnetic field deflecting away from $\vec{R}$ twice, while staying arc polarised.

structure.

The PSP data also shows that this rotation of the magnetic field is not always smooth, but has several sharp changes in direction, known as rotational discontinuities (RDs). This makes the switchbacks appear more like the observations of phase steepened Alfvén waves, commonly observed with Ulysses (Vasquez and Hollweg 1996; Riley 1996; Tsurutani et al. 2005; Tsurutani and Ho 1999). This comparison

is further strengthened by reports of $|B|$ dips at the sharp edges of phase steepened Alfvén waves (Tsurutani et al. 2005), which has also been shown for switchbacks (Farrell et al. 2020).

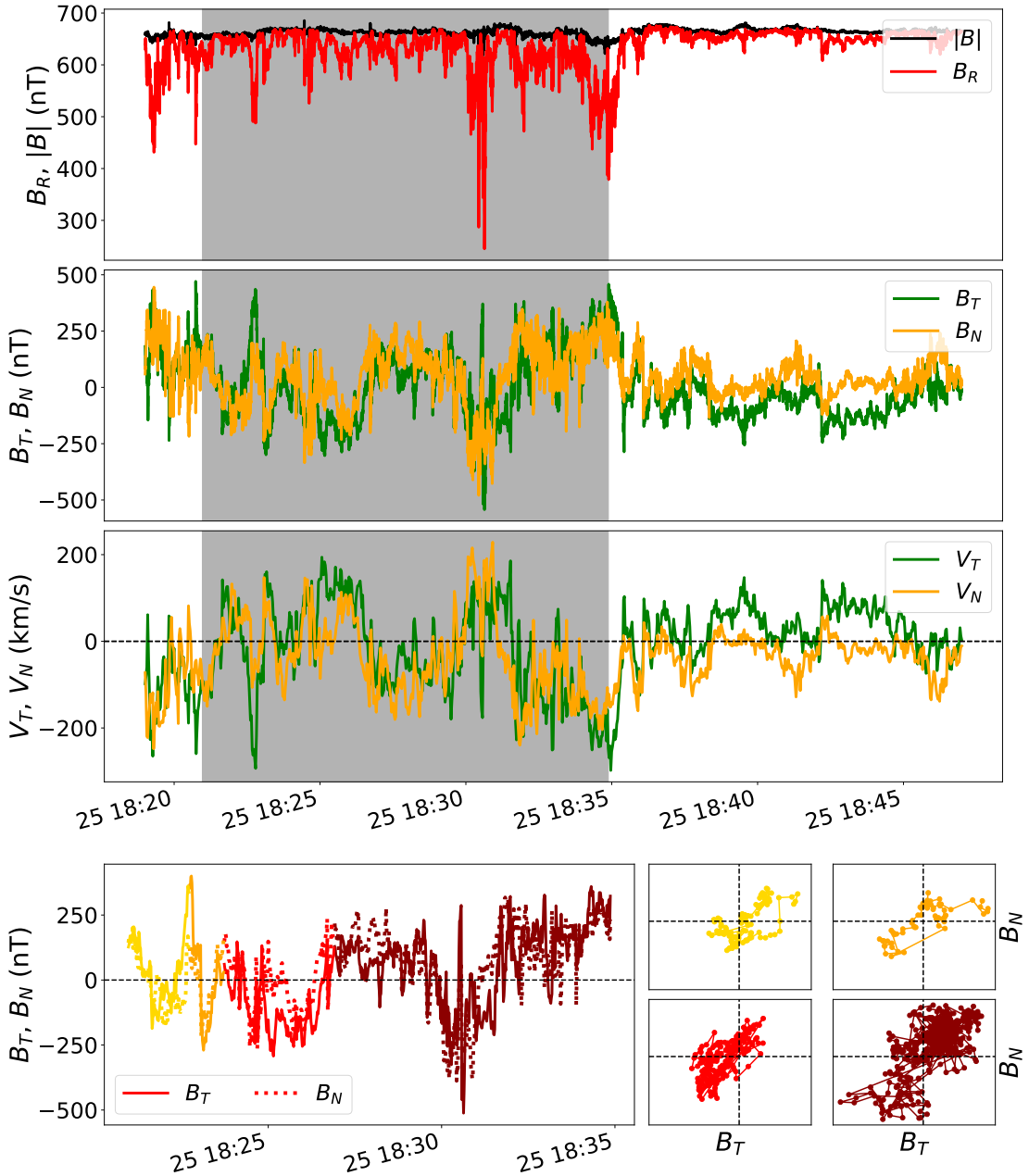


Figure 5.6: Example patch of correlated deflections in B_T (green) and B_N (orange). The hodograms for the highlighted grey region are shown below, where several successive deflections, split by colour, all travel along the same arc.

While the majority of oscillations in B_T and B_N were anti-correlated, there were also times with a correlated pattern in the magnetic field. An example of this can

be seen in Fig. 5.6, with accompanying hodograms in the lower panels.

To compare to the results of the previous chapter (Section 4.5), these two cases can be converted into clock angle and would correspond to:

- 135° → 315° CA for anti-correlation of B_T and B_N (Fig. 5.4)
- 45° → 225° CA for correlation between B_T and B_N (Fig. 5.6)

This is demonstrated further in Fig. 5.7, where the magnetic field is seen to quasi-periodically flip between two different clock angles. When plotted in a similar fashion to the polar histograms from the previous chapter (Fig. 4.19), it is clear that these correspond to the same preferential deflection directions seen over an entire encounter (using several days of data). However, these new results show that the same preferential directions exist on a much smaller timescale (tens of minutes). Therefore, in answer to the first question from Section 5.1.2, a series of switchbacks can have a consistent orientation on the scale of a few minutes, similar to the predictions of Kumar et al. (2022) and Wyper et al. (2022).

It is still not known why the magnetic field deflects in these particular directions, i.e. correlation or anti-correlation of B_T and B_N rather than just oscillations in $\pm B_T$. The scenario proposed by Kumar et al. (2022) relates each switchback patch with a bright point on the Sun, with repeated reconnection creating the switchbacks. This implies that all the switchbacks from the same bright point should have a consistent orientation. However, this was not the case for the switchback patches observed by PSP, with both correlated and anti-correlated deflections existing within the same patch. Wyper et al. (2022) also noted that switchbacks from the same reconnection source would have the same 'sense of rotation', but did not specify a scale at which this reconnection should occur. This point will be returned to after a discussion of the typical deflection scales in Section 5.3.

An alternative explanation can be provided if the switchbacks are assumed to be phase-steepened Alfvén waves, as suggested earlier. Vasquez and Hollweg (1996) demonstrated that initially small-amplitude linearly polarised waves could grow into

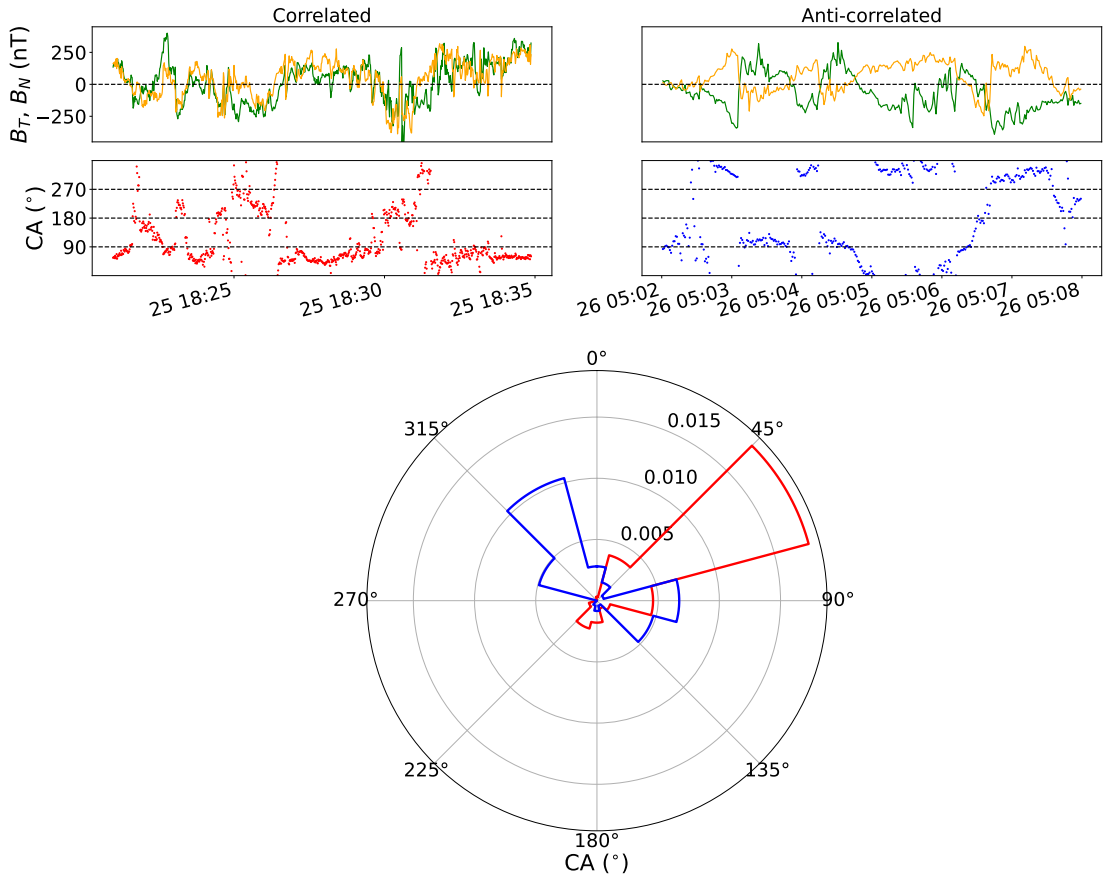


Figure 5.7: Hodograms for the two periods of correlated (red) and anti-correlated (blue) deflections in B_T and B_N. The polar histogram below shows that these correspond to clock angles of 45° → 225° for correlated deflections, and 135° → 315° for anti-correlated deflections.

arc-polarised waves with embedded RDs, which strongly resemble the wave train of Alfvén fluctuations in Fig. 5.4. However, if the amplitude of the waves were strongly modulated in one direction closer to the Sun, then this would encourage the waves to steepen in the same direction. Therefore, the orientation of the deflections at PSP could reflect the magnetic field conditions closer to the Sun.

On visual inspection, it is clear that this new pattern of tangential deflections was present in all the previous PSP encounters, such as the period shown for E2 in Fig. 5.8. As well as being responsible for the preferential deflection directions from Section 4.5, the new pattern of deflections can also explain the existence of the previously observed switchback clusters (Horbury et al. 2020b; Laker et al. 2021b; Laker et al. 2022). For example, looking at the magnetic field in Fig. 5.8, there are a

series of correlated deflections in B_T and B_N. However, due to B_N having a non-zero mean, the deflection angle becomes $>45°$ predominantly for $-B_N$ deflections. So, after applying the normal switchback criteria, a greater number of switchbacks (red in the top panel) are found with $-B_N$, which would then be identified as a 'cluster'.

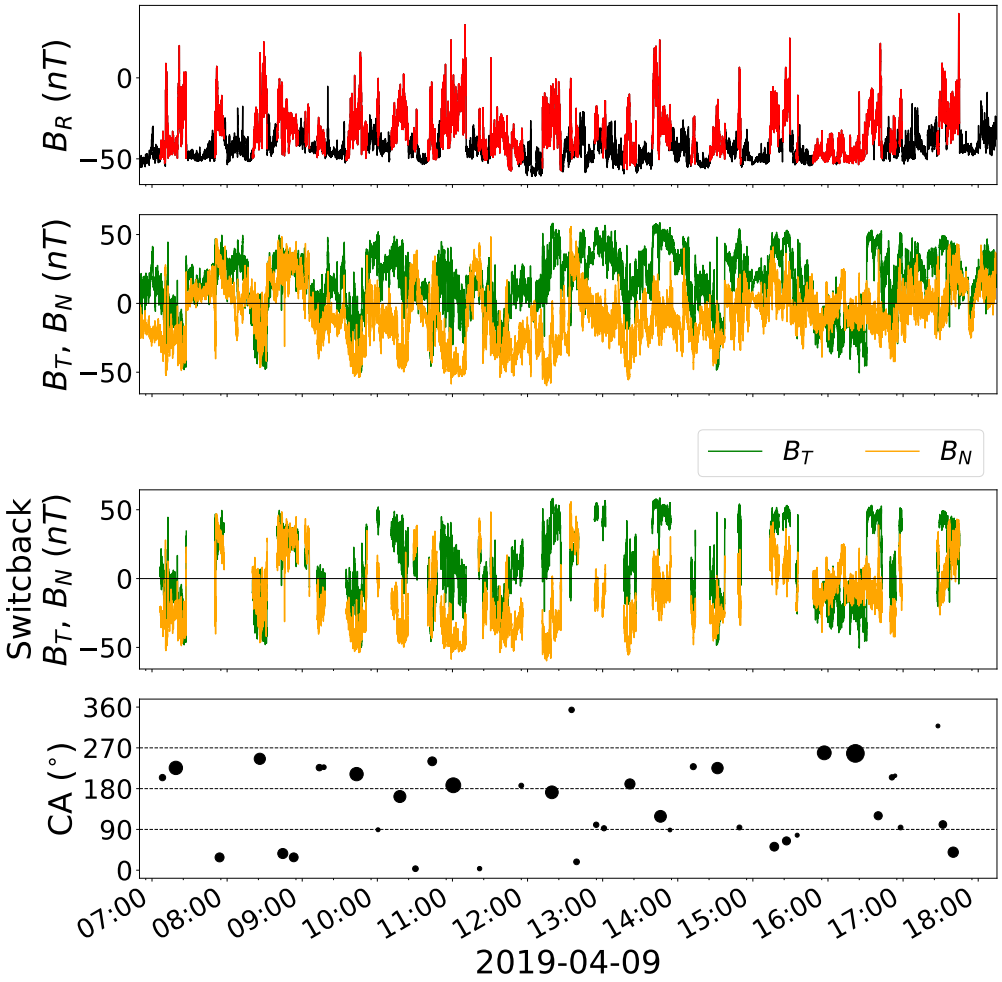


Figure 5.8: Example of a cluster of switchbacks in E2, identified as red in the upper panel. There is a consistent pattern of deflections in B_T and B_N (second panel), with only the components sampled by the switchbacks shown in the third panel. The clock angle of the switchbacks in the lower panel shows that longest ones (largest scatter size) deflect in roughly the same direction.

In summary, with the benefit of closer spacecraft measurements, a new pattern has been identified in the local magnetic field, potentially representing the imprint of interchange reconnection on the solar wind. With this new perspective, the same pattern can be identified throughout the previous PSP encounters. Therefore, it is proposed that the switchback definition should focus on structures where the

magnetic field is deflecting along an arc, rather than the absolute angle from the background.

5.3 Scale of the deflections

If these deflections are the imprint of a process near the Sun, then their scale at the spacecraft could help determine whether they are related to a particular solar feature. From a visual inspection, the magnetic field had a coherent pattern on the order of minutes in both Figs. 5.4 and 5.6. For a more quantitative estimate of the scale, the time series of magnetic field angles (ϕ_B, θ_B) were transformed into the frequency domain with the Fourier transform. Using the angles instead of magnetic field components meant that the results would not depend on $|\vec{B}|$.

An example period during E10 is shown in Fig 5.9, along with the Fourier transform of ϕ_B and θ_B in the lower left, and the cross-spectral density in the lower right. These were estimated using Welch's method for averaging periodograms, with a 30-minute Hann window (Nuttall 1981). During this time, both magnetic field angles had enhanced power at $\sim$2 and 10 minutes. The same scales also had an increased cross-spectral density, indicating that the two angles were co-moving during this period.

Therefore, in addition to having a coherent pattern in the magnetic field, the periods at the spacecraft are remarkably similar to the $3 \rightarrow 5$ minutes oscillations observed at the base of plumes (Uritsky et al. 2021). If this connection is true, then switchbacks would be a direct signature of long studied p-mode oscillations on the Sun's surface. It is important to note, however, that the solar wind measurements are only made by a single spacecraft, meaning that temporal and spatial changes cannot be distinguished. Usually Taylor's hypothesis is invoked, which assumes that the flow of the solar wind past the spacecraft is much quicker than the timescales of plasma evolution (Taylor 1938). Under this assumption, the spacecraft is essentially measuring a spatial cut through the solar wind, and would not be able to measure how the solar wind varies in time. While some authors have questioned the validity

of Taylor's hypothesis when PSP is so close to the Sun (Perez et al. 2021), it is still difficult to disentangle spatial and temporal variations.

Instead of being related to a timescale at the Sun, these deflections in the spacecraft could relate to a longitudinal structure in the solar wind that the spacecraft cuts through. In order to investigate this possibility, the time at the spacecraft was

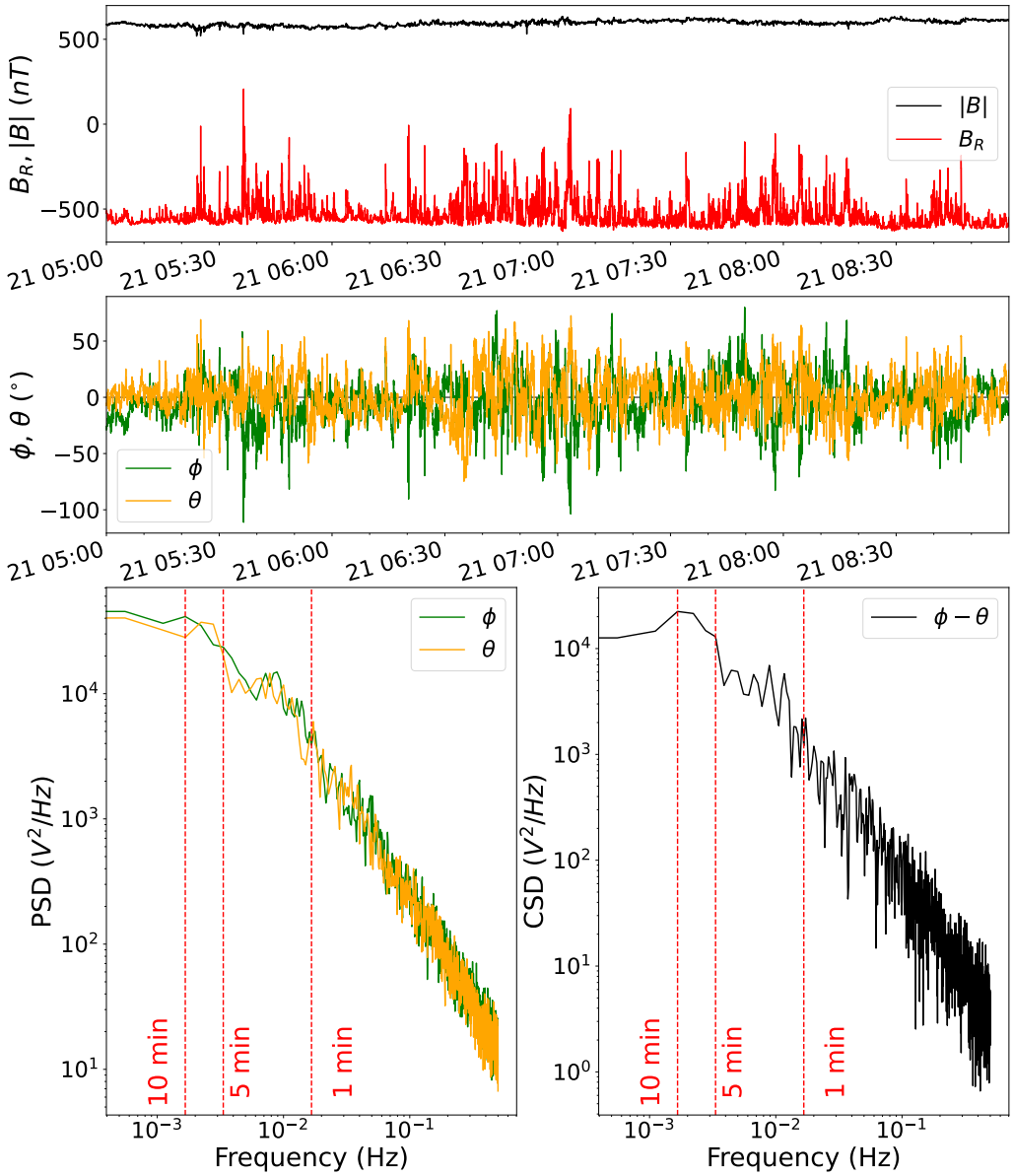


Figure 5.9: Example power and cross-spectral density for a period in E10. There is enhanced power in both ϕ_B and θ_B around 2 and 10 minutes in the lower left panel. Both these scales also had an increased cross-spectral density (lower right panel), indicating that they were co-moving.

converted into spatial coordinates. Similar to Fargette et al. (2021), the angular displacement of the spacecraft, S, was calculated by integrating the trajectory in longitude and latitude:

$$S(t) = \int_0^t dS \tag{5.1}$$

$$dS = \sqrt{\cos^2(\Theta)\, d\Phi^2 + d\Theta^2}. \tag{5.2}$$

Welch's method was then applied using a 2° Hann window, giving the results in Fig. 5.10. Again, there were two peaks in the cross-spectral density, which now appear at 0.5° and 0.1°. To compare this to scales at the Sun's surface, the expansion of the magnetic field must be accounted for.

The magnetic field often expands faster than spherical expansion (r^{-2}) by a factor of:

$$f = \frac{B_\odot}{B} \left(\frac{R_\odot}{r} \right)^2, \tag{5.3}$$

where $B_\odot$ is the magnetic field strength at the Sun's surface (Wang et al. 1997; Riley et al. 2015). Therefore, a spatial scale at the spacecraft, l_{SC}, will correspond to a scale at the Sun of:

$$l_\odot = \frac{l_{SC}}{\sqrt{f}} \frac{R_\odot}{r_{SC}}. \tag{5.4}$$

From Fig. 5.10, measured at $\sim 13\, R_\odot$, the length scales are between $16 \rightarrow 80\,\mathrm{Mm}$, which corresponds to $0.6 \rightarrow 3\,\mathrm{Mm}$ on the Sun's surface using a typical expansion factor of ∼4 (Fargette et al. 2021; Uritsky et al. 2021).

These scales are similar to:

- Granule scale of $\sim 1\,\mathrm{Mm}$ (Nordlund et al. 2009)
- Size of the bright points, $1.4 \rightarrow 2.1\,\mathrm{Mm}$ (2"-3"), in coronal plumes as observed by Kumar et al. (2022)

On larger scales, switchbacks are observed to come in patches, whose size (∼3° → 10° at PSP) has been related to the supergranular network on the Sun (Bale et al. 2021; Fargette et al. 2021). However, it is important to note that coronal plumes

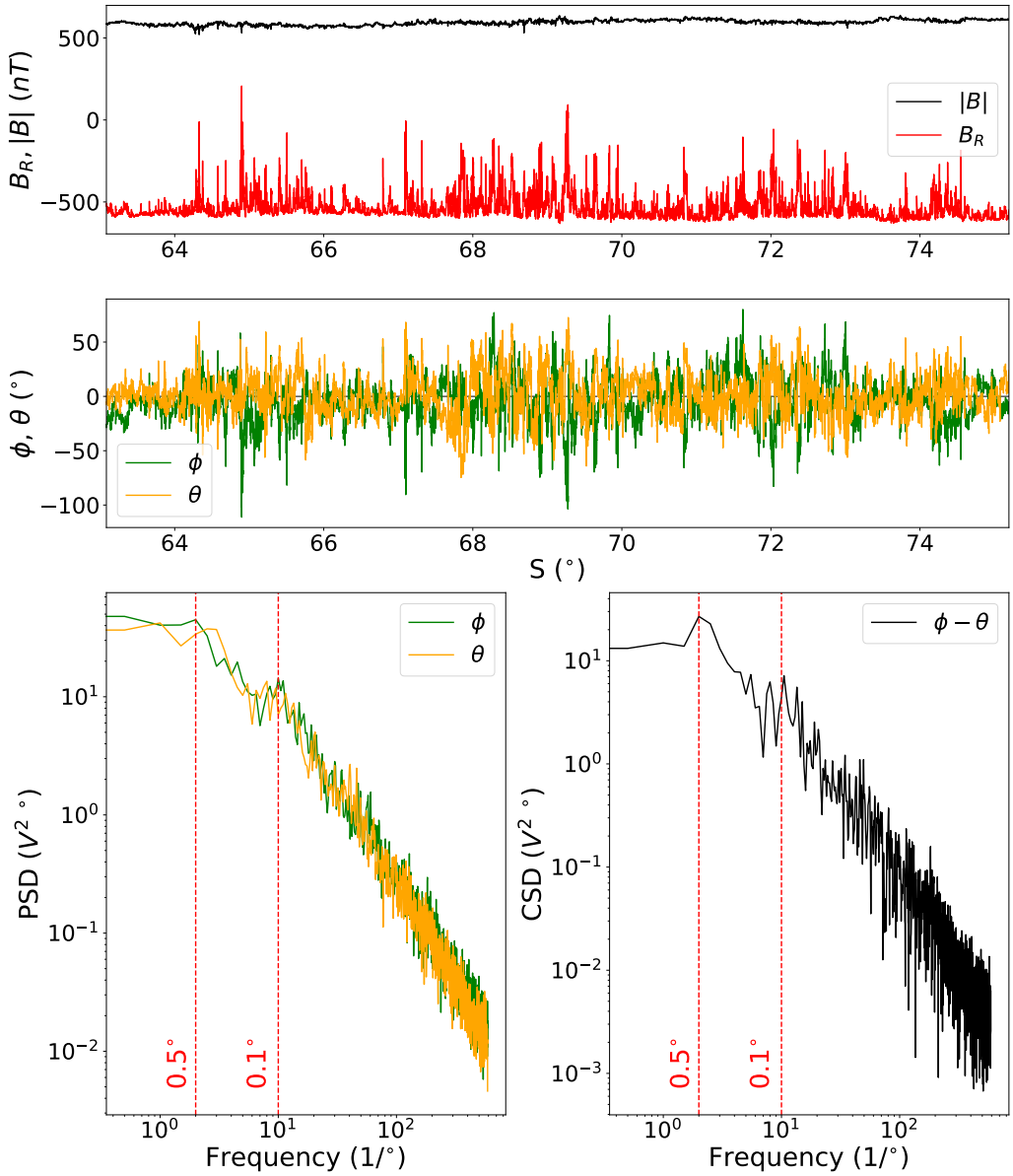


Figure 5.10: Power and cross-spectral density for the same period as Fig. 5.9, but now with respect to the angular displacement. Again, there are two scales of enhanced power in both ϕ_B and θ_B, which are now around 0.5° and 0.1°.

have similar spatial scales to supergranules (Bale et al. 2021). Therefore, switchback patches could be the signature of coronal plumes in the solar wind, with switchbacks being linked to the bright points spread around the plume base. This is a slight deviation on the suggestion from Kumar et al. (2022), who related the temporal scale of patches (hours) to the lifetime of bright points. However, as discussed above, it is easier to compare spatial rather than temporal scales between the spacecraft

and the Sun.

Interestingly, Fargette et al. (2021) also noted that the magnetic field angle varied on a smaller scale than switchback patches, around $0.3° \rightarrow 1.6°$, which they also associated with the granular scale on the Sun. Nonetheless, this chapter provides evidence of a coherent pattern in B_T and B_N at these scales, further strengthening the argument for interchange reconnection as the source of switchbacks.

5.4 Temperature enhancements inside switchbacks

So far, the increased proximity to the Sun has revealed a more systematic pattern in the solar wind during E11, but is there a distinct plasma signature inside switchbacks? Fortunately, the observations from E11 also benefit from a higher orbital speed, resulting in the proton core being more visible in SPAN's FOV. Fig. 5.11 shows an example switchback, with a clear enhancement in both $T_{p,\perp}$ and $T_{p,\parallel}$. The greater increase in $T_{p,\parallel}$ led to the proton core becoming isotropic ($T_{p,\perp}/T_{p,\parallel} \sim 1$) inside the switchback.

It should be noted that the restricted FOV of SPAN can sometimes introduce non-physical results. To prove that this was not the case in this example, the individual VDFs for outside (a) and inside (b) the switchback are shown in Fig. 5.12.

The initial VDF, Fig. 5.12(a), shows an anisotropic proton core (wider perpendicular to the magnetic field), with a proton beam along the magnetic field direction (black arrow). The proton core was fitted with a bi-Maxwellian distribution (see Woodham et al. 2021a), whose derived velocity is depicted by the red dot. Unlike the velocity from the moments (blue dot) the fits show that the centre of the proton core was blocked by the heat shield. The proton core then moved into the SPAN FOV as it rotated with the Alfvénic fluctuation (see Section 2.4.2), and the proton beam was cut off. Consequently, Fig. 5.12(b) shows that the proton core was more isotropic inside the switchback, validating the time series data from Fig. 5.11.

Of course, this one example does not yet prove a consistent plasma signature

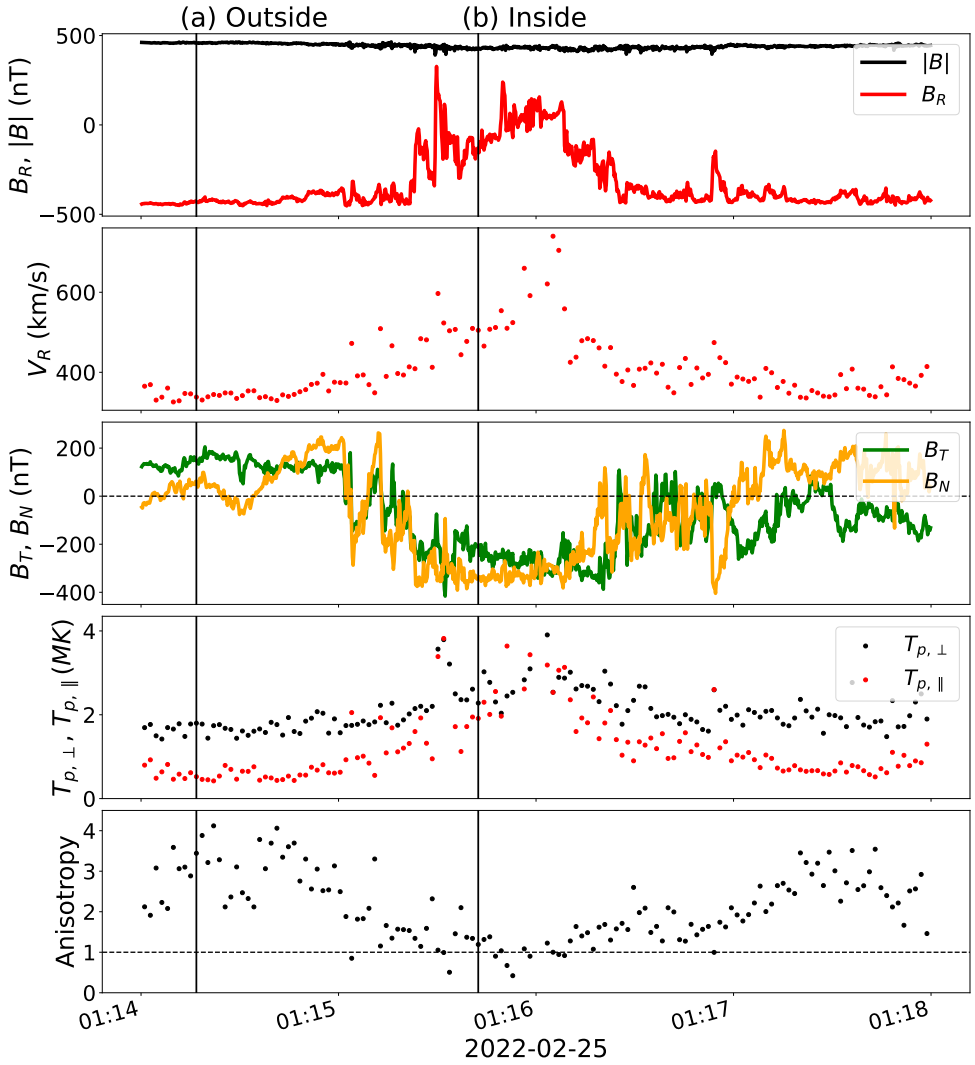


Figure 5.11: Example deflection from E11, demonstrating that both $T_{p,\parallel}$ and $T_{p,\perp}$ are enhanced inside, which reduces the anisotropy ($T_{p,\perp}/T_{p,\parallel}$) of the core to ∼1. Individual VDFs for inside and outside the deflection are shown in Fig. 5.12.

across all switchbacks. To plot the proton temperature across a larger period, it was important to ensure that the proton core was not completely out of the SPAN FOV. This was achieved by calculating the angle of the solar wind from radial in the spacecraft frame, using:

$$\tan^{-1}\left(\frac{V_{sw,T} - V_{SC,T}}{V_{sw,R}}\right), \tag{5.5}$$

where V_{sw} is the solar wind velocity moment of the distribution (blue dot), and V_{SC} is the spacecraft velocity with respect to the Sun in an inertial frame. In order for the

proton core to avoid being blocked by the spacecraft's heat shield, this angle must be sufficiently negative, i.e. not have a strong positive $+V_T$ deflection. Accordingly, in this study, only those times with an angle $<-5°$ were retained.

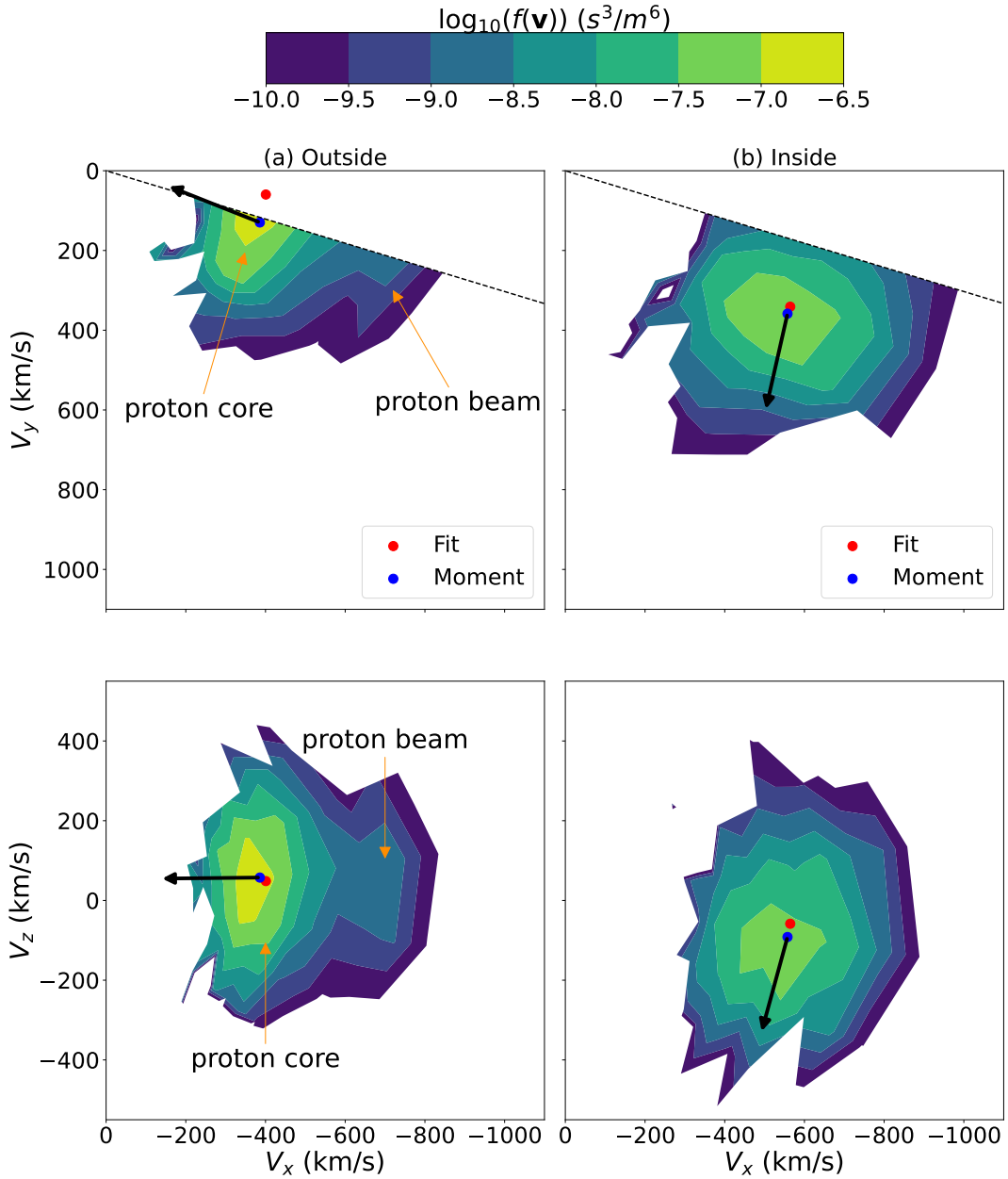


Figure 5.12: VDFs from the example deflection in Fig. 5.11 in the instrument frame, with the proton core and beam labelled. The SPAN FOV is cut off at the dashed line, but as the magnetic field (black arrow) rotates in the deflection, the proton core is moved into the FOV. This is associated with an increased $T_{p,\perp}$ and $T_{p,\parallel}$. The velocity from the moment of the VDF is shown in blue, with the fitted velocity in red.

The resulting data are shown for an extended period in Fig. 5.13, where there was an increased temperature inside each deflection of the quasi-periodic pattern from the previous section. These results are similar to the enhanced $T_{p,\parallel}$ reported for $-B_T$ deflections by Woodham et al. (2021a) in E2, which has been re-plotted in Fig. 5.14. At the time, the authors concluded that 'switchbacks [were] embedded within a larger-scale structure identified by distinct plasma signatures'. However, given the new knowledge of a coherent deflection pattern, the enhancements in temperature should now be classified as the switchbacks themselves, rather than some 'larger-scale structure'. Therefore, by using the proton temperature to define

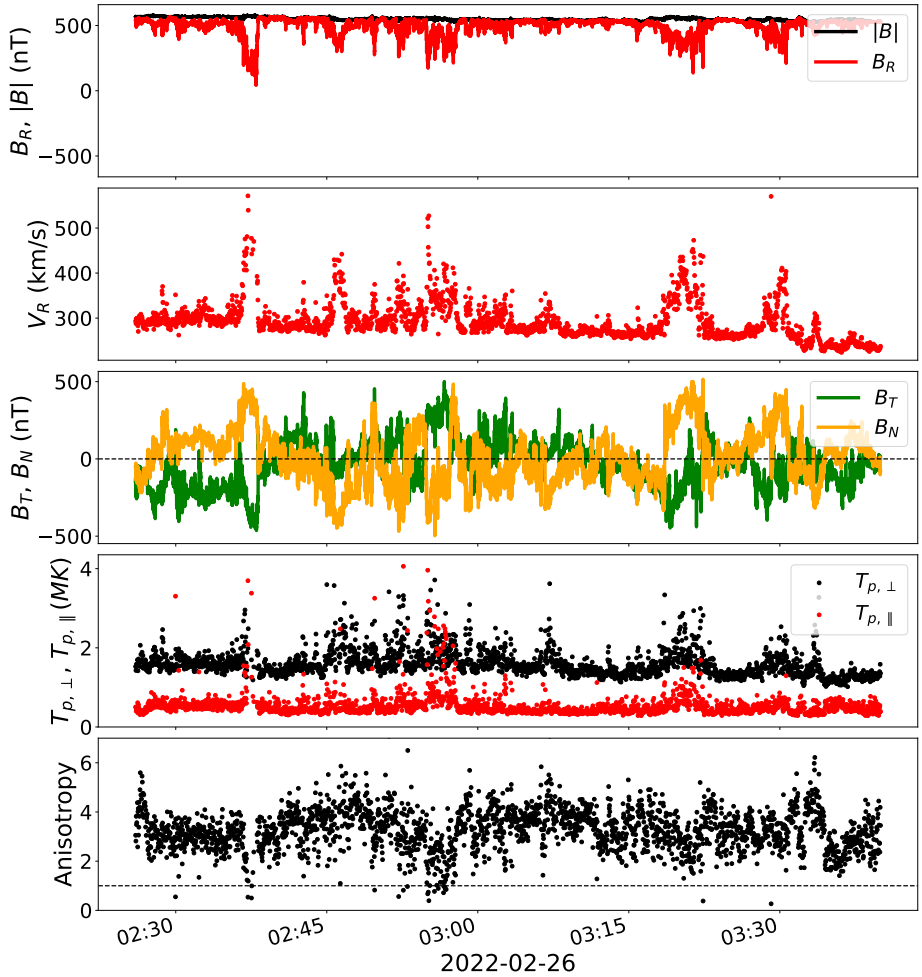


Figure 5.13: Example patch of switchbacks in E11 each associated with an increase in temperature, which also reduced the proton core anisotropy. The heating rates will be studied across switchbacks in Fig. 5.15.

a switchback, the individual dips in B_R, seen in Fig. 5.14, would now be deemed as internal sub-structure, rather than switchbacks in their own right.

Finally, it is also interesting to note that Woodham et al. (2021a) did not see a significant increase in $T_{p,\perp}$. This may imply that the heating mechanism behind $T_{p,\perp}$ becomes less important farther from the Sun.

So, while an earlier study associated temperature increases with a 'larger structure', the new PSP measurements have shown that each switchback is unambiguously associated with an increase in both $T_{p,\perp}$ and $T_{p,\parallel}$.

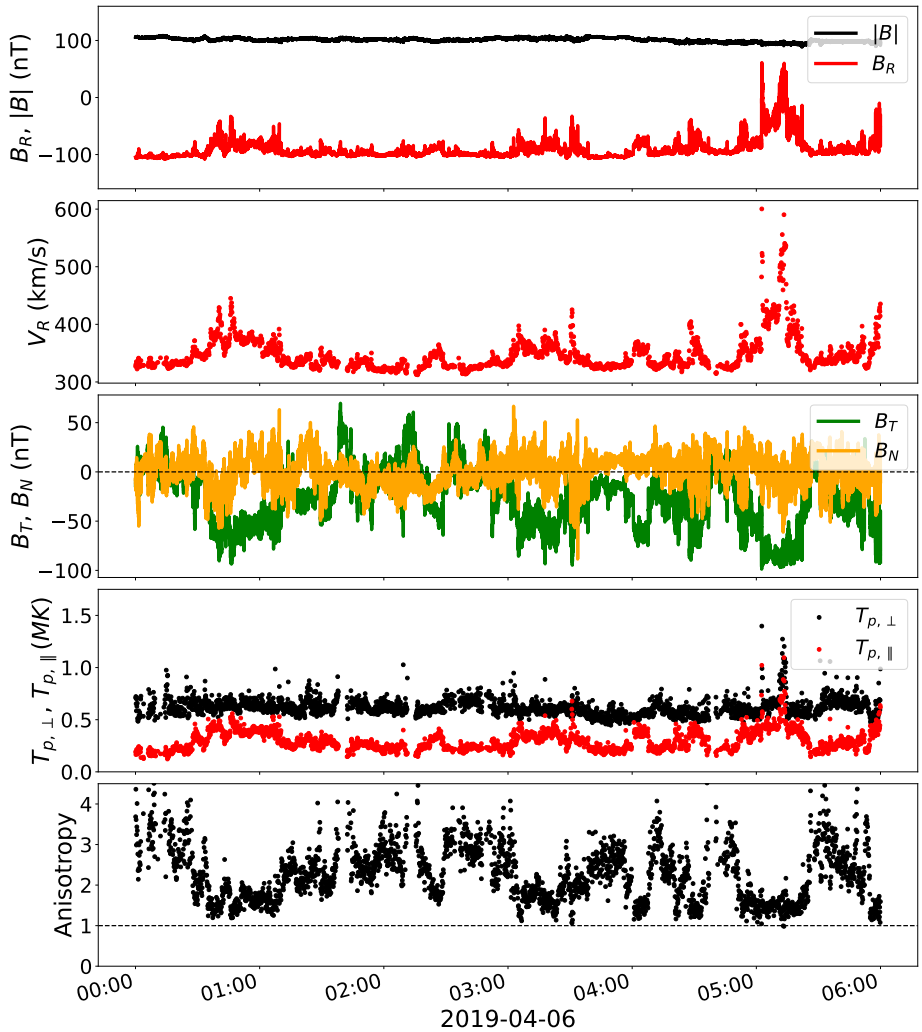


Figure 5.14: Temperature enhancements replotted for the period used by Woodham et al. (2021a) during E2. Deflections in $-B_T$ were associated with enhanced $T_{p,\parallel}$ and a lower anisotropy. This is similar to the results presented in this chapter, but now there is also heating in $T_{p,\perp}$ and a more frequent pattern in B_T and B_N.

5.4.1 Heating inside switchbacks

To further characterise the behaviour of the temperature inside switchbacks, the larger-scale T-V relationship (Section 2.4.5) was first removed. This method is described later in Section 5.5, as part of a more detailed study of the larger-scale T-V relationship with PSP.

For now, only the difference in temperature from the background, $\delta T_{p,\perp}$ and $\delta T_{p,\parallel}$, will be considered inside the switchbacks. While other studies have assessed the change in δT_p against δv (Horbury et al. 2018), this was not considered in this study due to the large changes in v_A across the encounters. Instead, $\delta T_{p,\perp}$, $\delta T_{p,\parallel}$ and temperature anisotropy were plotted against θ_{RB} in Fig. 5.15. This shows a consistent heating signature in the switchbacks, even when compared across different encounters. The higher rate of heating in the parallel direction drove the proton core anisotropy below 1 at ∼75°, before reaching around ∼0.8 past 90°.

Interestingly, both $\delta T_{p,\perp}$ and $\delta T_{p,\parallel}$ appear to flatten out past ∼90°. To extract a heating rate, the change in temperatures were fitted with the following model:

$$\delta T(\theta_{RB}) = \begin{cases} m(\theta_{RB} - \theta_S) + \delta T_S & \text{if } \theta_{RB} < \theta_S \\ \delta T_S & \text{if } \theta_{RB} >= \theta_S \end{cases} \tag{5.6}$$

where m is the gradient (K/°) and δT_S is the saturated temperature increase that begins at the saturation angle, θ_S.

The results of this fitting are shown in Table 5.1 where the average heating rate for $\delta T_{p,\parallel}$, ∼16,000±4,000 K/°, was around twice as high than that for $\delta T_{p,\perp}$, ∼7,000±4,000 K/°. A similar relationship was seen for δT_S, which was ∼1.36±0.47 MK and ∼0.72±0.56 MK for $\delta T_{p,\parallel}$ and $\delta T_{p,\perp}$, respectively. Both the perpendicular and parallel temperatures saturated around $\theta_S = 90°$, implying that switchbacks have a maximum temperature at the centre.

To further demonstrate this point, Fig. 5.16 presents a model switchback cross-section, where the deflection angle increases towards the centre of the physical struc-

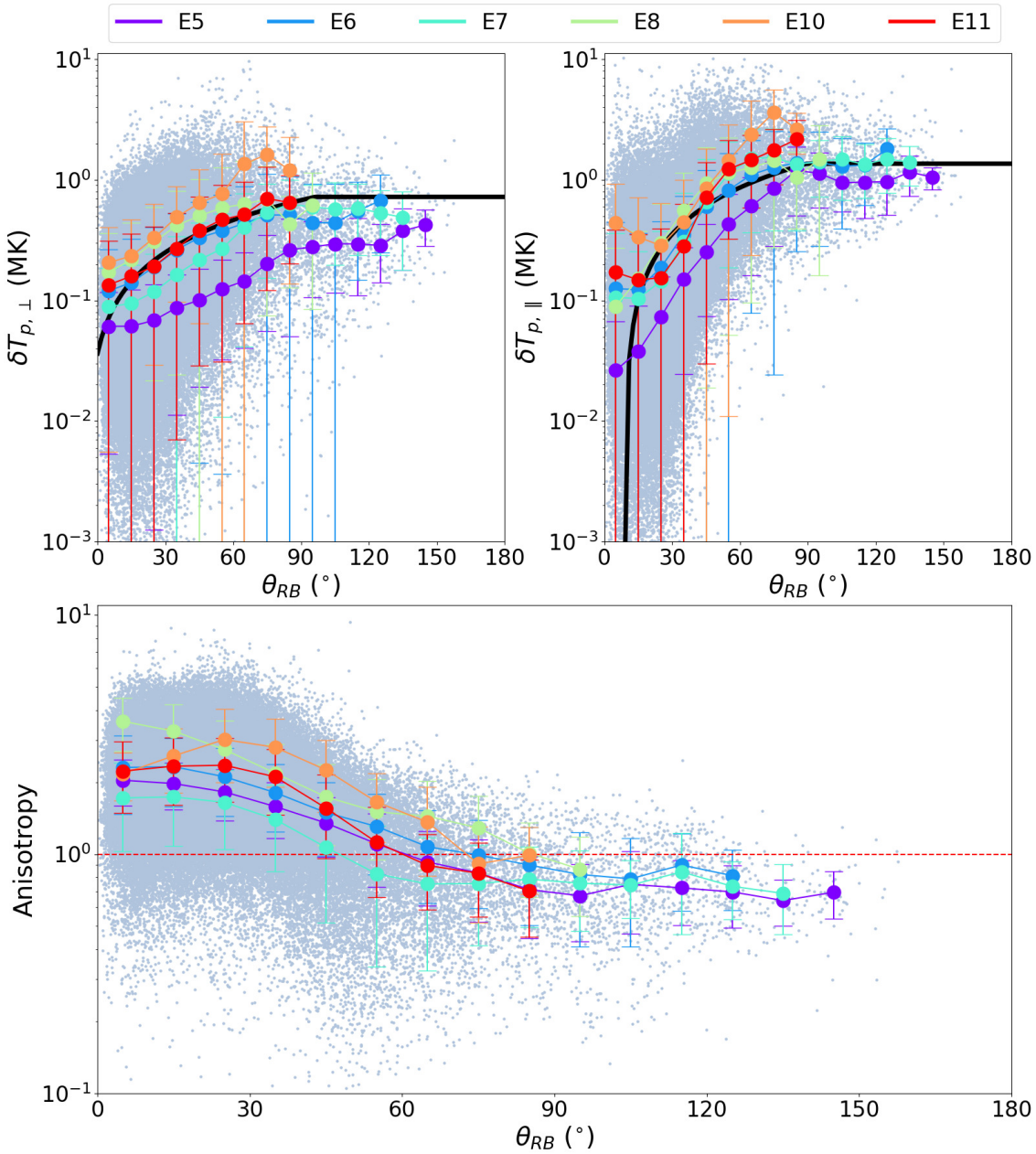


Figure 5.15: Relationship between $\delta T_{p,\perp}$, $\delta T_{p,\parallel}$ and anisotropy with θ_{RB} after the removal of the background T-V relationship. Mean average and standard deviation are shown for 10° bins of θ_{RB}. It appears that $\delta T_{p,\parallel}$ plateaus above 90°. Each encounter was fitted with equation 5.6, with the average results shown by the black line, which is summarised in Table 5.1.

ture. Fig. 5.16(b) shows a sinusoidal temperature profile, initially proposed by Woodham et al. (2021a). This was used to explain how SPAN could see an increase in temperature up to 90°, while SPC measured a similar temperature at both 0° and 180°. However, the new result from Fig. 5.15 suggests that the heating saturates inside switchbacks, as depicted in Fig. 5.16(a).

	$\delta T_{p,\perp}$			$\delta T_{p,\parallel}$		
	m (K/°)	T_S (MK)	θ_S (°)	m (K/°)	T_S (MK)	θ_S (°)
E5	$2,127 \pm 33$	0.366 ± 0.004	161.5 ± 0.0	$10,935 \pm 98$	0.99 ± 0.015	105.4 ± 1.5
E6	$5,816 \pm 92$	0.506 ± 0.008	76.7 ± 1.7	$15,900 \pm 149$	1.437 ± 0.022	97.6 ± 1.6
E7	$3,972 \pm 72$	0.332 ± 0.004	73.6 ± 1.4	$15,239 \pm 222$	0.867 ± 0.011	65.1 ± 1.0
E8	$9,361 \pm 240$	0.619 ± 0.017	57.1 ± 2.0	$22,521 \pm 325$	1.316 ± 0.036	66.6 ± 1.7
E10	$14,807 \pm 268$	1.957 ± 0.029	133.0 ± 0.0	$20,115 \pm 414$	2.307 ± 0.039	119.6 ± 0.0
E11	$6,700 \pm 121$	0.553 ± 0.015	75.1 ± 2.4	$16,995 \pm 189$	1.246 ± 0.026	82.9 ± 1.7
Average	$7,130 \pm 4100$	0.722 ± 0.561	96.2 ± 37.6	$16,952 \pm 3680$	1.361 ± 0.465	89.3 ± 20.2

Table 5.1: Resulting of fitting equation 5.6 to all the data points in each encounter (Fig. 5.15).

Magnetic reconnection at the source could create a structure that was hotter in the centre, while also explaining the preferential heating along the magnetic field direction. Recent results from Bale et al. (2022) have shown that the energetic particles in E10 are likely the high energy tail of the proton core, accelerated by interchange reconnection closer to the Sun. This same period of study also displayed the consistent magnetic deflections discussed in this chapter, which had a consistent heating of the proton core. Therefore, it is possible that the observations from Fig. 5.15 and Bale et al. (2022) are generated by the same underlying reconnection at the Sun. In future, it would be interesting to see if the high energy proton tails are confined within switchbacks, which would provide compelling evidence that switchbacks are created by interchange reconnection.

While the energised particles and associated Alfvén wave both travel on the order of the Alfvén speed shortly after reconnection, the increased Alfvén speed in the corona means that the reconnection outflow will move much slower than the Alfvén waves. This means that the heating signature at the spacecraft should not appear at the same time as the Alfvén wave. Consequently, the reconnection scenario would only work with a continuous outflow inside flux tubes, creating a hotter centre. While simulations have shown a continuous outflow from interchange reconnection (Wyper et al. 2022; Bale et al. 2022), it is not yet known whether this would also lead to a consistent heating inside switchbacks.

Alternatively, the heating inside the switchbacks could also be caused by an in situ plasma instability. The saturation of the heating could be explained by the

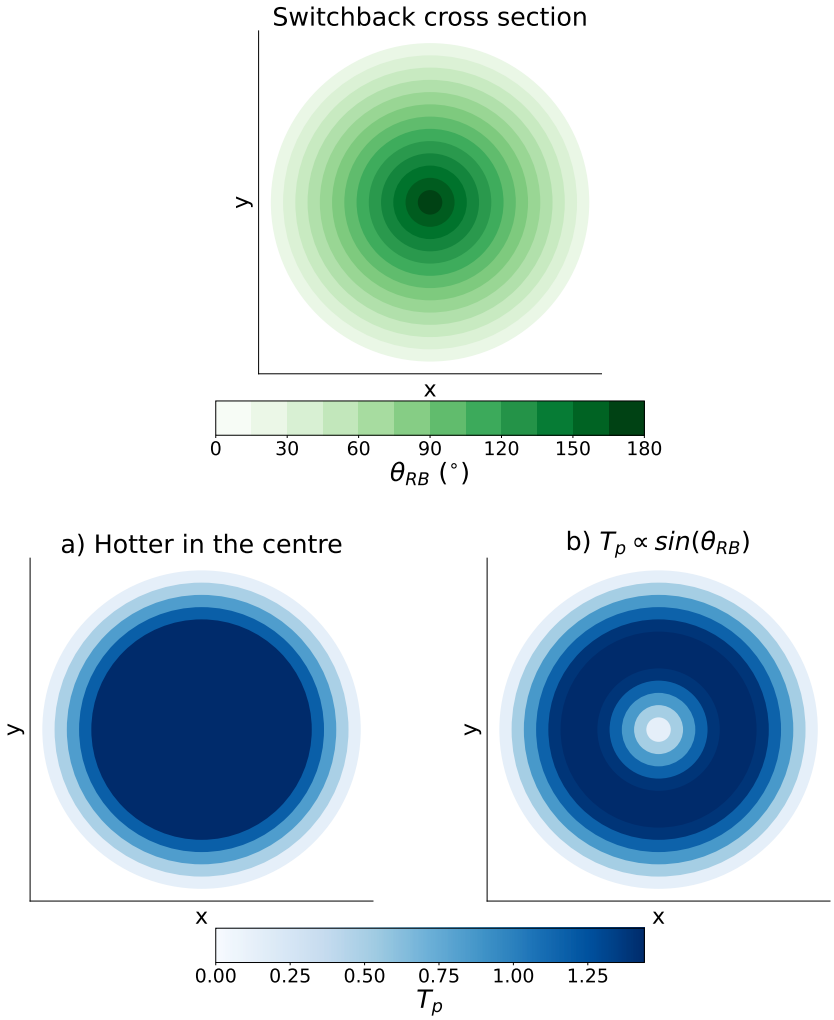


Figure 5.16: Diagram to visualise the two different heating scenarios for a deflection. For demonstration purposes, a cross-section through the deflection is assumed to have increasing θ_{RB} towards the centre (top panel). The temperature could either be hotter towards the centre (a) or related to θ_{RB} in such a way that the temperature at 0° and 180° are the same (b).

plasma properties being different inside switchbacks, removing the necessary driving conditions.

For example, when simulating the evolution of phase-steepened Alfvén waves, Vasquez and Hollweg (1998) noted that ions could be heated parallel to the magnetic field. They explain that the steepening of the waves creates large increases in density, which would then lead to heating of the plasma along the magnetic field direction through Landau damping. Since switchbacks are not associated with density enhancements, this mechanism would have to happen before the switchbacks

are measured by PSP. This would suggest that the heating rate would decrease as the spacecraft moved farther from the Sun.

While this was not a general trend seen across the encounters in Table 5.1 with PSP, it does agree with the lack of $T_{p,\parallel}$ increase observed in other spacecraft at a greater distance. Both Horbury et al. (2018) and D'Amicis et al. (2019) showed that there was no temperature increase inside switchbacks when measured by Helios ($\sim$0.3 AU). However, D'Amicis et al. (2019) noted that the time resolution on Helios was only every 40.5 seconds, which may have led to blurring of the VDF as it was measured.

Using Wind observations, D'Amicis et al. (2019) found that $\delta T_{p,\perp}$ was positively correlated with θ_{RB}, but found no such trend for $\delta T_{p,\parallel}$. The authors suggested that the well-known ion-cyclotron resonance could lead to the increase in $T_{p,\perp}$, which may also be the cause of the perpendicular heating at PSP.

Another explanation was offered by Woodham et al. (2021b), who studied 15 years of Wind observations. They found that the heating of the protons was caused by turbulent dissipation that depended on both θ_{VB} and the plasma β. Enhancements in $T_{p,\perp}$ were associated with a higher Alfvén ion-cyclotron wave activity, and increased $T_{p,\parallel}$ with higher kinetic Alfvén wave[1] activity. Again, a change in θ_{VB} or β inside the switchback could halt the plasma instability, and lead to the heating saturation seen in Fig. 5.15.

5.4.2 Temperature inside a full reversal switchback

While the results from the previous section suggest that there was continued heating inside switchbacks, an earlier report from SPC showed that $T_{p,\parallel}$ was equal at $\theta_{RB} = 0°$ and 180° (Woolley et al. 2020). Therefore, this section examines the SPAN VDFs within a full reversal switchback, which has not been attempted previously.

While it would be preferable to study the same switchbacks as Woolley et al. (2020), the orbital speed of PSP was too low for SPAN to operate in the first

[1]Short wavelength extension to the Alfvén wave where the parallel wavelength is much greater than the perpendicular one

encounter. Instead, several full reversal switchbacks were identified for encounters 5, 6 and 7. Although the orbital speed was higher in the later encounters, $\delta\vec{B}/\vec{B}$ was lower, meaning that the magnetic field rarely rotated to 180°.

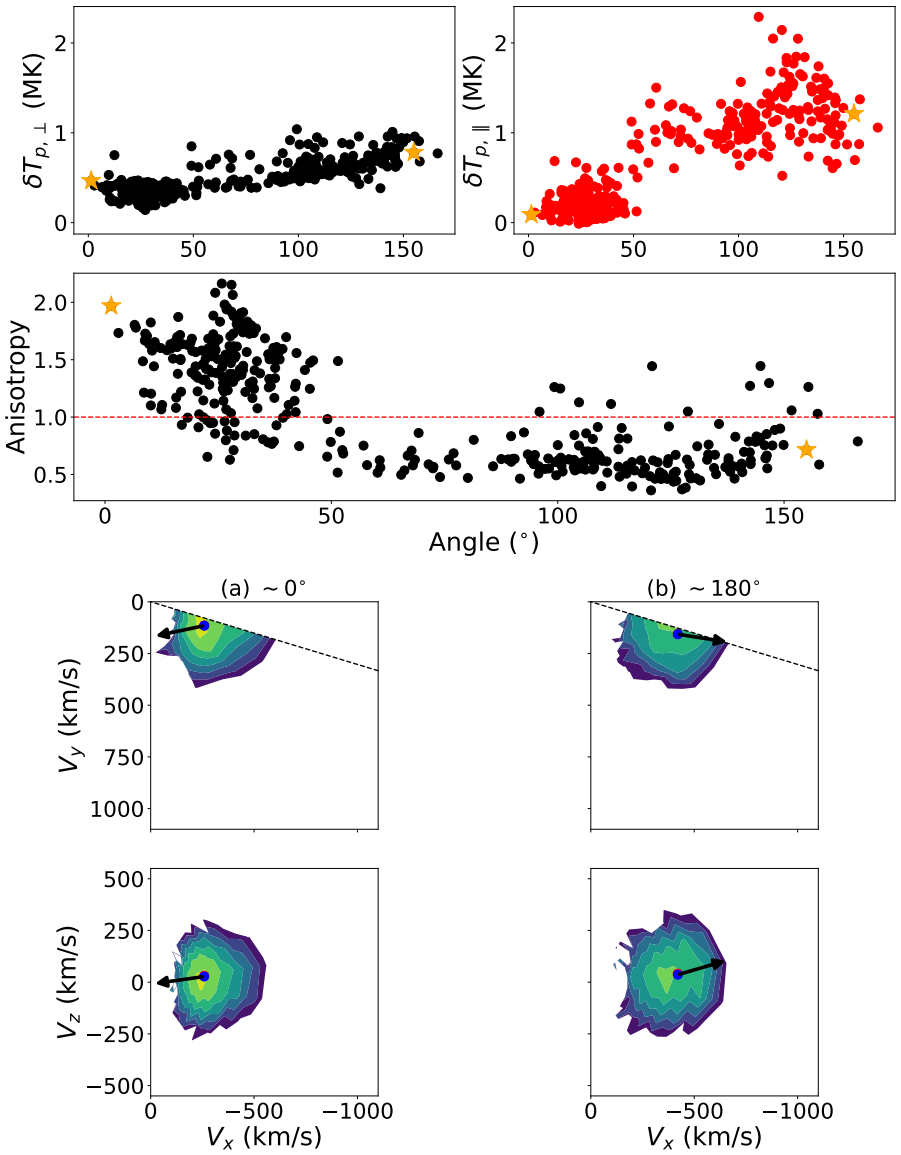


Figure 5.17: Relationship between proton temperatures and anisotropy with θ_{RB} for an example full reversal switchback found in E5. This suggests that the temperatures continue to increase up to 180°. VDFs for the two starred points are displayed in the lower panels to prove this is not an instrumental effect.

An example of the plasma properties observed in a full reversal switchback during E5 is shown in Fig. 5.17. Similar to the results over an entire encounter in Fig. 5.15, $T_{p,\parallel}$ increased with angle at a faster rate than $T_{p,\perp}$. However, now it is clearer that

neither temperature returns to the background value at 180°.

The VDFs in the lower panels of Fig. 5.17 also confirm this behaviour, and show that this was not due to an instrumental effect. Both temperatures varied more linearly than the saturated heating observed over the whole encounter in the previous section. However, another full reversal during E7, in Fig. 5.18, showed the same behaviour as in Fig. 5.15. This could suggest that the saturation effect varies between switchbacks, but can in general be modelled by equation 5.6. These examples, along with others not shown, disagree with the findings from Woolley et al. (2020), who saw no $T_{p,\parallel}$ increase within a switchback using SPC.

To address this disparity, the SPC temperatures are plotted against SPAN for the full reversal in Fig. 5.18. Since these instruments were designed to work when the other one cannot, this was the only example where data was available for both instruments.

As mentioned in Section 2.6.2, SPC can only measure a radial temperature according to equation 2.39. To better compare the results from these instruments, equation 2.39 was used to convert the SPAN temperatures into the same format as SPC. Even with this conversion in Fig. 5.18, the SPAN T_R (dark blue) still did not match SPC temperature (light blue).

Interestingly, SPC did still show that the temperature was roughly equal at both $\theta_{RB} = 0°$ and 180° as reported by Woolley et al. (2020). However, the SPAN VDFs clearly showed an increased temperature, suggesting that SPC cannot reliably measure the proton temperature at large magnetic field angles.

Therefore, in answer to the questions posed at the end of Section 5.1.1:

1. Is there a consistent plasma signature inside switchbacks?

    - Yes, there is an increase in both $T_{p,\perp}$ and $T_{p,\parallel}$ with a consistent heating rate of $\sim$7,000$\pm$4,000 K/° and $\sim$16,000$\pm$4,000 K/°, respectively.
    - This makes the proton core more isotropic inside the switchbacks.
    - The increase may be related to the heating of higher energy particles from Bale et al. (2022).

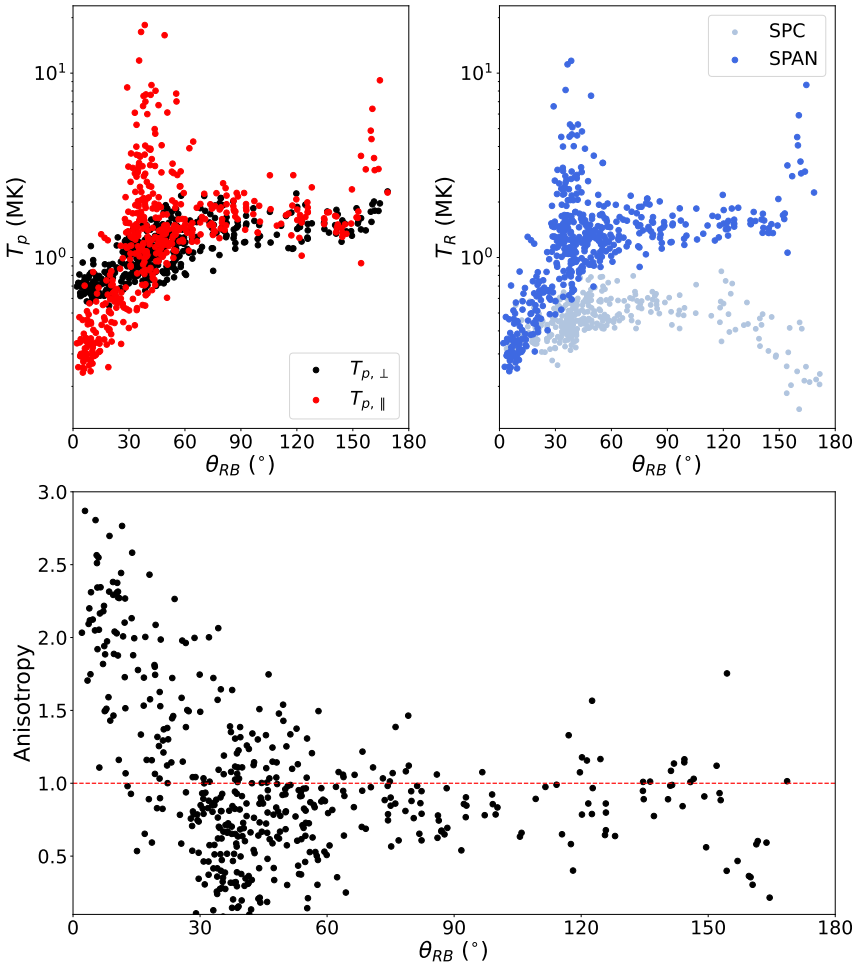


Figure 5.18: Example full reversal deflection, where both SPAN (dark blue) and SPC (light blue) measured the temperature. The SPAN measurements of $T_{p,\perp}$ and $T_{p,\parallel}$ are shown in the upper left panel, along with the anisotropy in the lower panel. The exact cause of the spikes at 30° and 150° is unknown, but is possibly due to the presence of a proton beam. The radial temperature, T_R, in the upper right panel was severely underestimated with SPC compared with SPAN.

2. How do the larger-scale enhancements in $T_{p,\parallel}$ from Woodham et al. (2021a) relate to switchbacks?

   - It is now suggested that the enhancements in $T_{p,\parallel}$ are the switchbacks themselves, and any magnetic field deflections inside are now considered sub-structure.

3. What is the behaviour of the proton core temperature inside switchbacks past 90°?

- The proton temperatures stay elevated as θ_{RB} deflects past 90° and appears to plateau, suggesting that the heating saturates inside switchbacks.

4. Can plasma properties be used to help define a switchback?

   - Yes, along with the expectation that several successive switchbacks will now deflect along the same arc.

5.5 T-V relationship on the large scale

As well as the heating inside switchbacks, the near Sun solar wind also exhibits a strong T-V relationship (see Section 2.4.5). While this was subtracted to reveal the change in temperature within switchbacks, the larger-scale T-V relationship can itself help reveal how the solar wind is heated and accelerated.

To capture the variation in temperature with velocity, a 30-minute rolling window was moved across the data in 10-minute time steps. Within each window the 0.1 quantile of the speed, $T_{p,\perp}$ and $T_{p,\parallel}$ was taken. This method was chosen to represent the baseline temperature and speed, without being affected by the enhancements from the switchbacks. Such an approach worked better than taking the mean average or minimum, where the latter was easily skewed by non-physical outliers.

The final baselines can be seen in Fig. 5.19, which match the large-scale behaviour of the speed and temperature. This method was then applied to Alfvénic periods, with reliable SPAN data, for the latest encounters. Each T-V relationship is plotted in Fig. 5.20, where there was a clear positive correlation for both $T_{p,\perp}$ and $T_{p,\parallel}$ across the encounters.

$T_{p,\perp}$ had a much steeper gradient than $T_{p,\parallel}$, which has been reported in earlier studies (Horbury et al. 2018; Perrone et al. 2019). However, PSP has now travelled close enough to the Sun to see that these temperatures overlap at $\sim$200 km/s.

As discussed in Section 2.4.5, Démoulin (2009) has suggested that the T-V relationship may be related to a heating mechanism acting to both accelerate and heat the solar wind, i.e. slower, cooler wind has not been heated as much. Since $T_{p,\perp}$ has

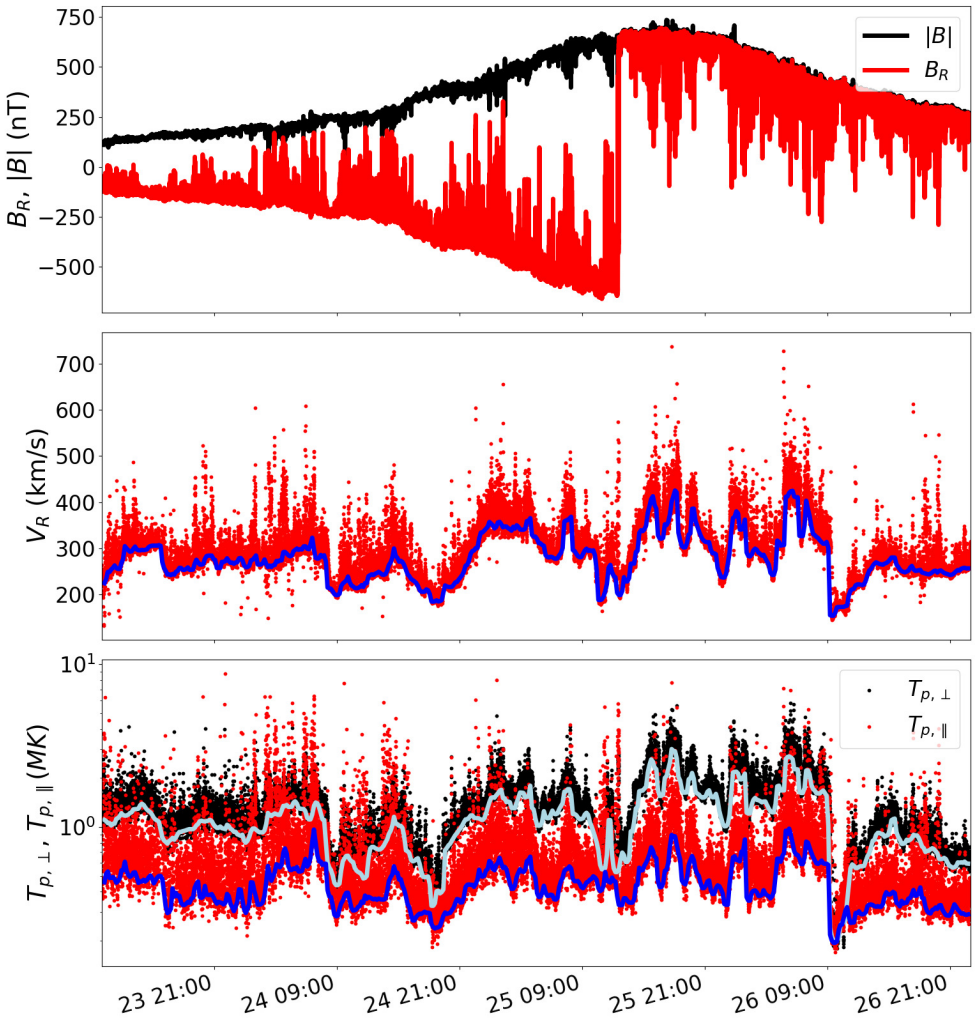


Figure 5.19: Plasma parameters for a period of E11 where the light blue ($T_{p,\perp}$) and dark blue ($T_{p,\parallel}$) lines show the 30-minute rolling averaging used to get the baseline variations in temperature and speed. These are then used to investigate the relationship between temperature and speed on the large scale in Fig. 5.20.

a much steeper gradient, this implies that the heating mechanism acts preferentially in the perpendicular direction to the magnetic field (Perrone et al. 2019).

Since the previous section showed that switchbacks have a greater heating rate for $T_{p,\parallel}$ than $T_{p,\perp}$, it therefore seems unlikely that switchbacks are the source of the solar wind's acceleration and heating, at least not close to the Sun.

Fig. 5.20 also demonstrates that the T-V relationship changed between the encounters. Elliott et al. (2012) also saw that the gradient of the T-V relationship could change, and suggested that this could be due to the interaction of solar wind

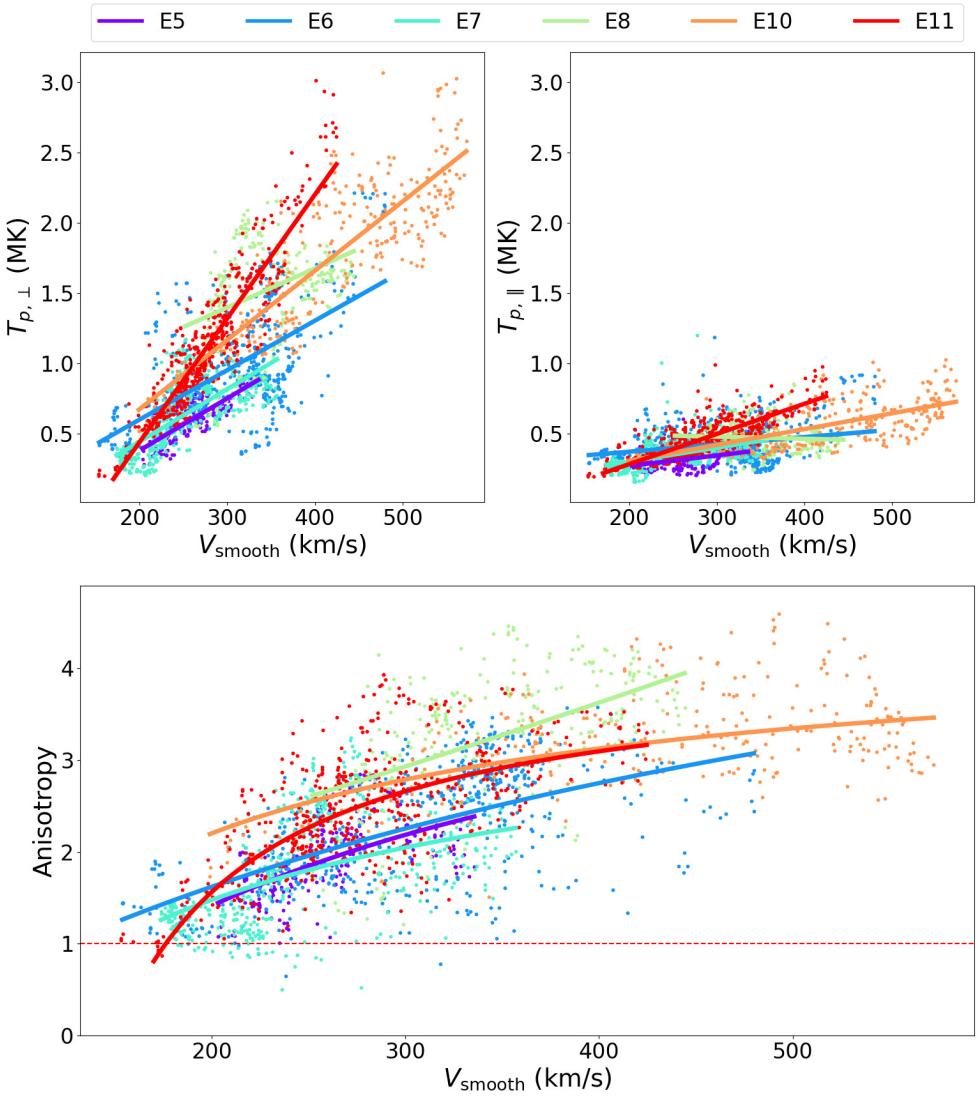


Figure 5.20: T-V relationship for Alfvénic periods in several PSP encounters, each showing a clear positive correlation. Individual fits to the two temperatures were performed for each encounter, which are then used to plot the trend for the anistropy in the lower panel. The overall pattern of anisotropy shows that the proton core becomes isotropic at around 200 km/s.

streams or a change in the source conditions. However, Perrone et al. (2019) showed that the T-V relationship flattens as the solar wind expands into the heliosphere. Those authors explained that the slow solar wind has more time to interact with an in situ heating mechanism, leading to a higher temperature increase with distance compared to the faster wind. To model this behaviour, Perrone et al. (2019) assumed

that the temperature of the solar wind varied as:

$$T \propto r^{-\epsilon}, \tag{5.7}$$

where ϵ is the empirical cooling rate as a function of speed, as measured with Helios. Consequently, as $T(V)$ is extrapolated towards smaller distances with equation 5.7, the gradient of the T-V relationship will increase.

The extrapolations are shown in Fig. 5.21, where there was a generally good agreement with the PSP measurements. This provides further evidence that the 'convective age'[2] of the plasma parcel is the reason behind the evolving T-V relationship (Matthaeus et al. 2006; Perrone et al. 2019).

So perhaps the initial T-V relationship is controlled by conditions at the source region (e.g. flux tube expansion) or some heating mechanism that also accelerates the wind (e.g. Démoulin 2009). Then, as the solar wind moves into the heliosphere, the effect of convective age becomes more important and acts to flatten the T-V relationship.

5.6 Solar wind types

So far in this chapter, only Alfvénic wind with clear switchback signatures, which will be referred to as 'patchy' solar wind, has been studied. There were periods, however, when the solar wind appeared noticeably different. Fig. 5.22 shows an example of a time when the solar wind transitioned from patchy (left of dashed line) to a more 'quiet' solar wind (right of dashed line). As well as fewer switchbacks, this type of solar wind had a temperature anisotropy < 1, marked by a sharp transition in $T_{p,\perp}$.

Similar solar wind was found in several PSP encounters, with Fig. 5.23 summarising the plasma properties of these times. Despite being selected only when the temperature anisotropy was < 1, these periods had consistently slow solar wind

[2] the duration of time the parcel has been in transit from the Sun to the spacecraft

speed (<250 km/s), low alpha particle drift and a high Alfvénicity. These characteristics are similar to the slow Alfvénic solar wind (Section 2.4.3) observed farther from the Sun, which typically has the following properties:

- Slow solar wind speeds (Stansby et al. 2019a)
- More isotropic core than the fast solar wind ($T_\perp/T_\parallel < 1.7$) (Stansby et al. 2019a)
- Lower amplitude fluctuations (D'Amicis and Bruno 2015)
- Similar charge state ratios to fast solar wind (D'Amicis et al. 2019)

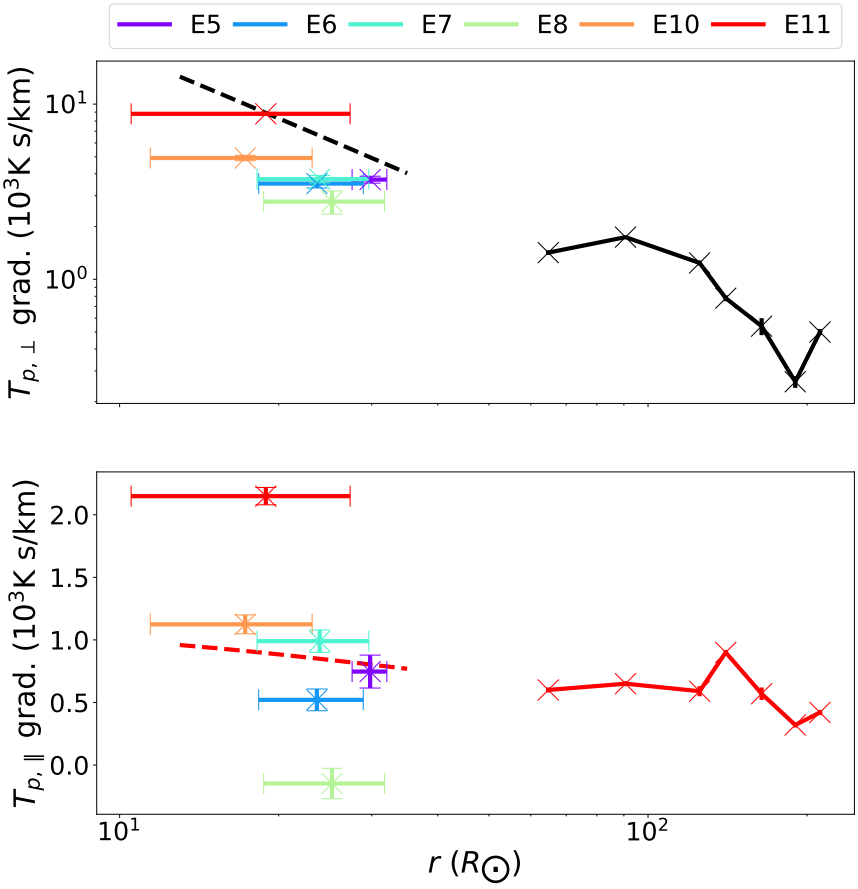


Figure 5.21: Gradients of $T_{p,\perp}$ (top) and $T_{p,\parallel}$ (bottom) with speed taken from Perrone et al. (2019) (solid line), which are extrapolated to smaller distances (dashed line). The predictions of $T_{p,\perp}$ agree well with the measured T-V relationship for the different PSP encounters (coloured scatter), where the horizontal error bars show the range of distances from the Sun. However, there is a larger spread in the gradient of $T_{p,\parallel}$.

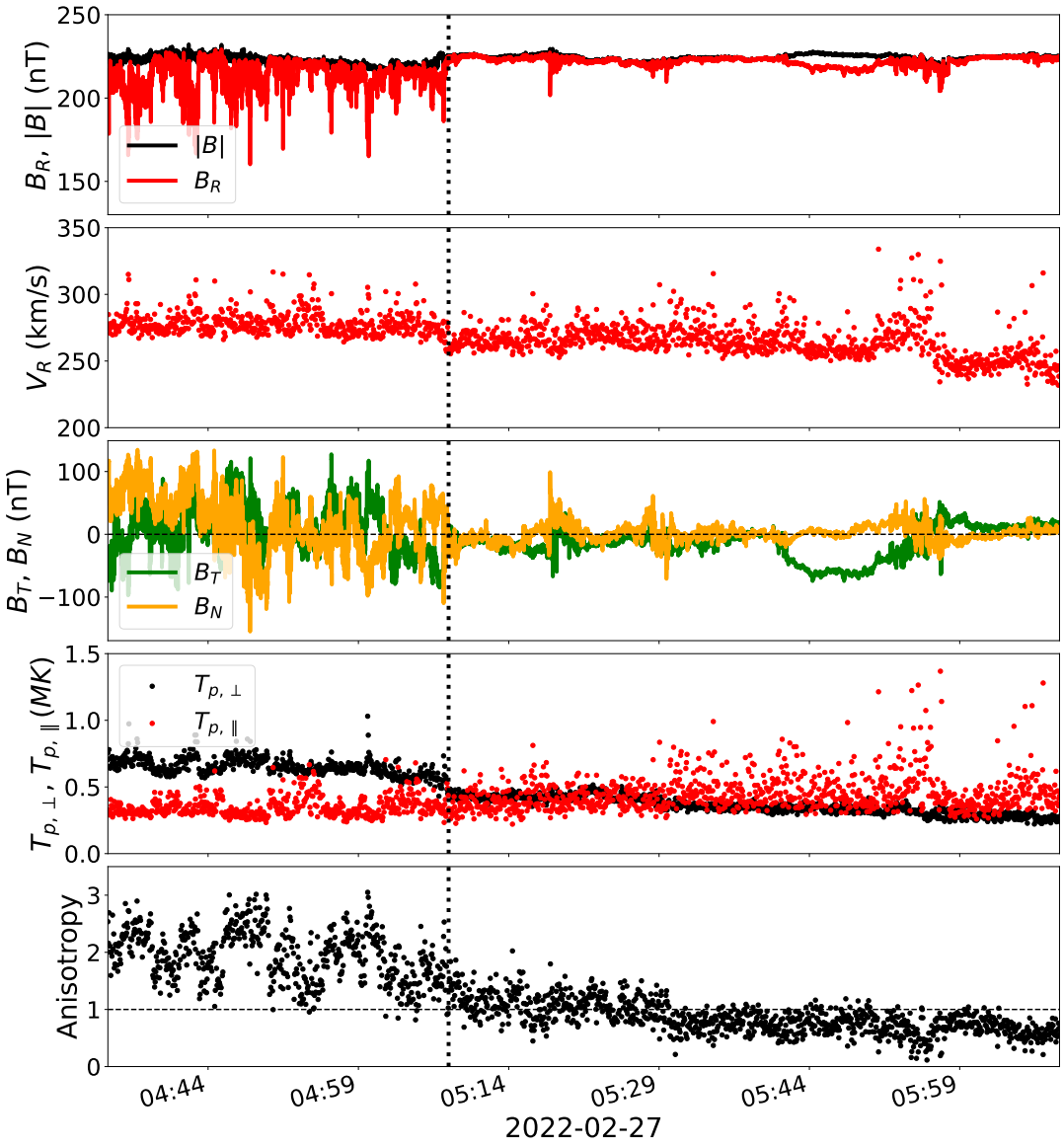


Figure 5.22: Transition from 'patchy' to 'quiet' solar wind in E11, separated by the dashed vertical line. The top panel shows how the magnetic field fluctuations were significantly reduced for the quiet wind, which was also associated with a striking change in temperature anisotropy (lower panel).

While the charge state ratios cannot be investigated by PSP, these similarities mean that the quiet wind is likely the slow Alfvénic wind observed closer to the Sun.

When classified at Helios ($0.3 \rightarrow 0.4$ AU), Stansby et al. (2019b) used a threshold of $T_\perp/T_\parallel < 1.7$ to split the slow and fast Alfvénic wind. However, Fig. 5.23 shows that the 'saddle point' between the two distributions now lies at $T_\perp/T_\parallel = 1.3$, with quiet and fast wind having peaks at 0.7 and 2, respectively. Again, this was lower

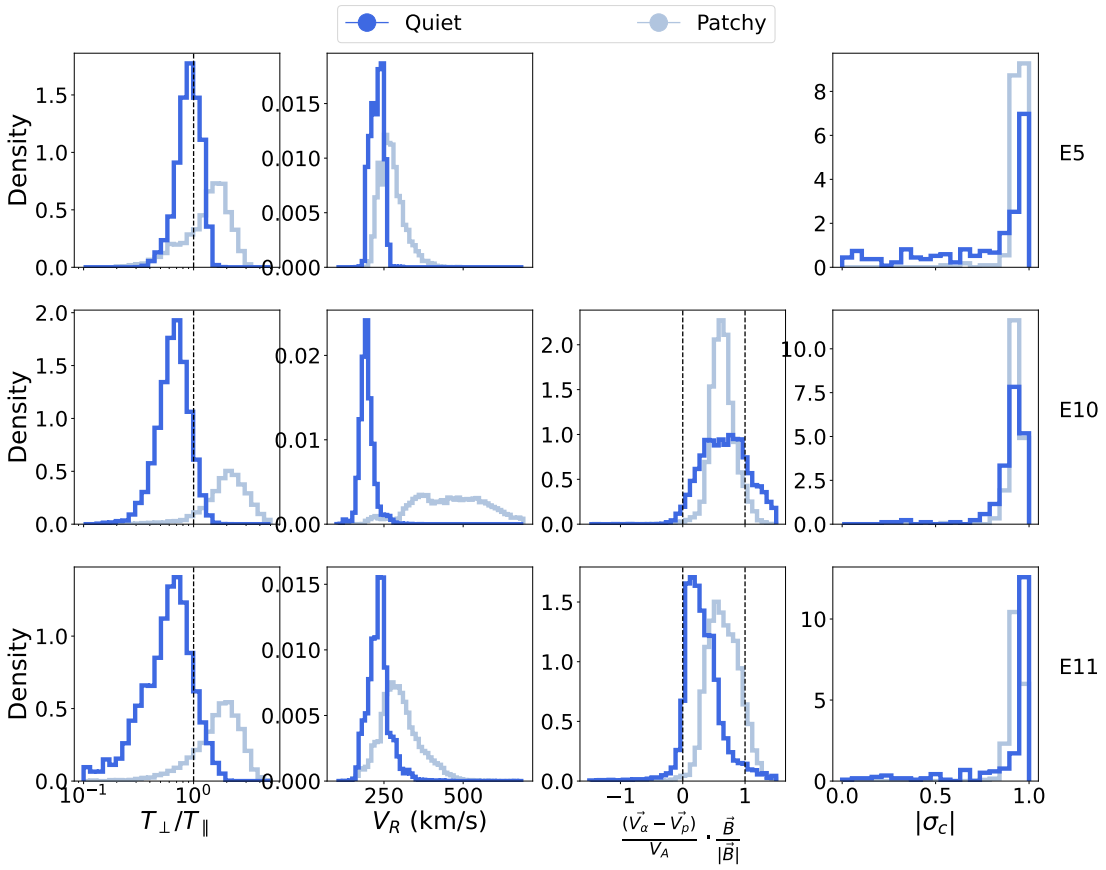


Figure 5.23: Plasma properties of the patchy and quiet wind, which were selected based on the temperature anisotropy (left panels). Right column shows the cross helicity, $|\sigma_c|$, as defined in Section 3.2.4. Despite this, these regions had consistently slower speed and lower alpha drift, but were still Alfvénic.

than the respective values of 1 and 3 at Helios, demonstrating that the proton core anisotropy is still increasing from $<20\,R_\odot$ to $\sim 65\,R_\odot$. Past the intermediate measurements from Helios, the temperature anisotropy is known to reduce with distance as the collisional age of the plasma increases (Kasper et al. 2008; Bale et al. 2009). This implies that there is some heating mechanism increasing the anisotropy closer to the Sun ($<65\,R_\odot$).

A similar heating signature has been observed in the heavy ions (Kohl et al. 1998; Tracy et al. 2016; Kasper et al. 2017), with a strong preferential heating up to $20 \rightarrow 40\,\mathrm{Rs}$ from the Sun. If this same heating mechanism could also increase the anisotropy of the proton core, then PSP would be close enough to see this effect. Ultimately, a more detailed future study looking into the evolution of temperature anisotropy is needed.

As shown in Fig. 5.24, the quiet solar wind does not have a strong correlation between speed and temperature, but was seen to exist at the slower end of the T-V relationship for the patchy wind. This supports the idea that the slow Alfvénic wind has the same release mechanism as the faster solar wind (D'Amicis et al. 2018; Stansby et al. 2020a). In the previous section, it was concluded that the higher gradient for $T_{p,\perp}$ was a consequence of a heating mechanism closer to the Sun. Therefore, the quiet solar wind, with anisotropy ∼1, may represent solar wind that has not been injected with any additional energy.

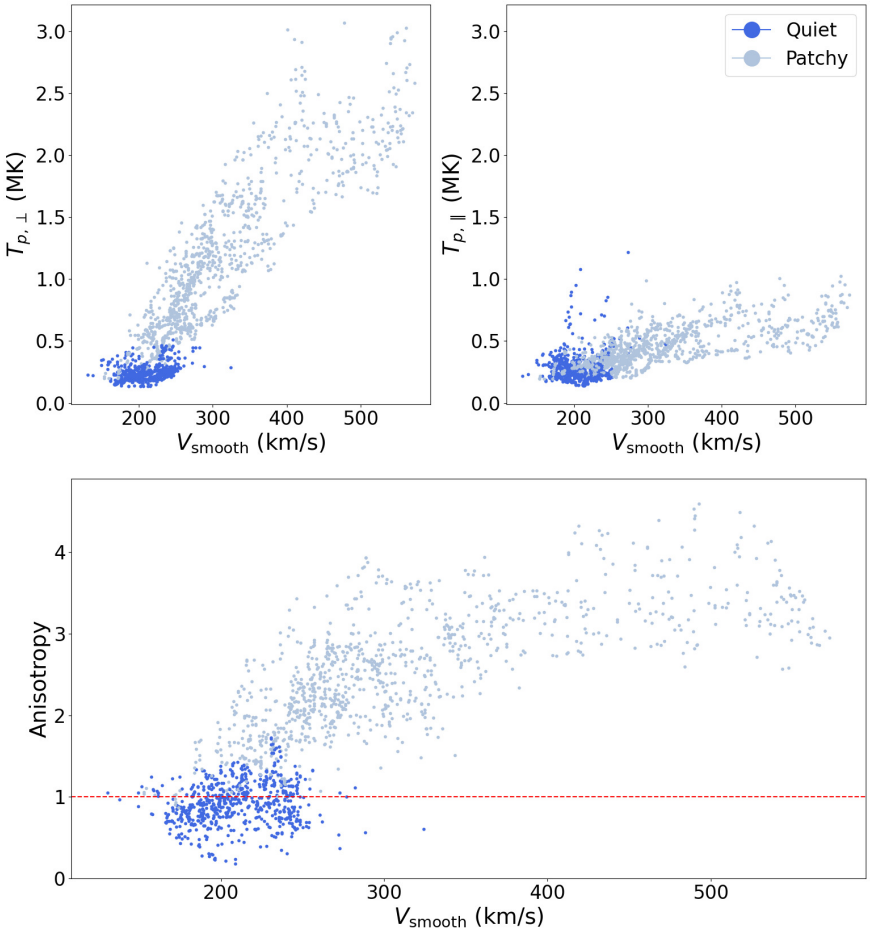


Figure 5.24: The quiet regions (dark blue) do not display a T-V relationship themselves, but appear at the bottom of that for the patchy regions. This suggests that they are a similar type of wind with a slower speed that made them appear different in Fig. 5.22.

A similar conclusion was reached by Halekas et al. (2022), who found that an exospheric model could explain the slow solar wind (<300 km/s) with no additional

heating mechanism required. While the previous section ruled out switchbacks as the driver of the perpendicular heating, these structures could still act as a tracer for the heating mechanism closer to the Sun. This would agree with the theory that switchbacks are the imprint of interchange reconnection on the solar wind. Consequently, the reduced switchback presence in the quiet regions may represent a lack of heating closer to the Sun.

It is important to note, however, that this is not the only way in which a quieter magnetic field could be created. Since the alpha drift is lower in these quiet times, the alphas will rotate with the Alfvénic fluctuations (see Section 2.4.2). This added mass contribution from the alphas could mean that the magnetic field will deflect less for the same energy input, making the field appear smoother.

In summary, there are times when the solar wind appears noticeably different, with a smoother magnetic field and a temperature anisotropy below 1. This was linked to the slow Alfvénic solar wind, which may represent a pristine solar wind lacking any additional heating. Therefore, the reduced switchback signatures in this type of solar wind imply that switchbacks are tracers of the heating process closer to the Sun.

5.7 Conclusions

Following the predictions of some new switchback theories, this chapter looked for signatures of solar processes in the near Sun solar wind. Using data only $13\,R_{\odot}$ from the Sun, switchbacks were found to have a local pattern of deflections, which could represent the imprint of interchange reconnection on the solar wind. These deflections had a scale corresponding to $0.6 \rightarrow 3\,\mathrm{Mm}$ on the Sun's surface, which is similar to that of granules and bright points. It was therefore concluded that these new observations were consistent with interchange reconnection at bright points embedded in a coronal plume.

Furthermore, it was shown that switchbacks were unambiguously associated with temperature enhancements, which has not been clear prior to this study. The pro-

ton core parallel temperature had a heating rate of $\sim$16,000$\pm$4,000 K/°, which was almost twice as high the perpendicular heating of $\sim$7,000$\pm$4,000 K/°. Such a behaviour led to the proton core becoming more isotropic inside the switchback, which was seen across the encounters. Therefore, a new switchback definition was proposed, where a switchback has:

- a consistent magnetic field deflection along the arc of a sphere
- proton core heating inside, where $T_{p,\parallel}$ increases faster than $T_{p,\perp}$
- the proton core temperature anisotropy decreasing to ~ 1

Unlike the standard switchback definition used in Chapter 4, there is now no condition imposed on the absolute angle of the magnetic field. This means that the internal magnetic structure of a switchback can be more easily investigated, as it is no longer linked to the definition.

In addition, switchback temperatures were observed to stay elevated as the magnetic field deflected to 180°. Interestingly, the temperature was observed to reach a maximum at around 90°, implying that the heating saturates inside switchbacks. While it is still unclear how the switchbacks are heated, this could potentially be explained by interchange reconnection. Since Bale et al. (2022) has already linked high energy particles to heating from interchange reconnection, it would be interesting to see if this signature coincides with the proton core heating inside switchbacks.

However, it is important to note that plasma instabilities, such as ion-cyclotron resonance, could also explain the elevated temperatures. The conditions driving the instabilities may change inside switchbacks, leading to the saturated heating signature. Therefore, a future study could investigate the presence of such instabilities and waves inside switchbacks.

On a larger-scale, the solar wind was seen to exhibit a strong T-V relationship, which matched predictions made farther from the Sun. Since there was a stronger T-V relationship for the perpendicular temperature, it was concluded that switchbacks were not the cause of the solar wind's acceleration. Instead, it was suggested

that switchbacks could be a tracer of the heating mechanisms closer to the Sun. Therefore, the quiet solar wind, which had fewer switchbacks, could represent solar wind without any additional heating. A future study could further strengthen this claim by determining if the rate of switchbacks is correlated with the speed of the solar wind.

While there was a consistent heating signature inside the switchbacks at PSP, this has not been observed with other spacecraft. Consequently, it is still not known how the switchbacks merge and contribute to the solar wind. Solar Orbiter could help provide the answer to this question, since it was radially aligned with PSP for a period in E11. In addition to measuring any heating inside switchbacks, Solar Orbiter could measure the composition of minor ions as well as take high-resolution images of any small-scale solar features. This would help link switchbacks to a solar source, and could provide a 'smoking gun' observation for interchange reconnection.

Chapter 6

Conclusions

The work in this thesis was carried out at the start of an exciting new era for solar wind physics, following the launch of two flagship missions. Parker Solar Probe has continued to break the record as the closest spacecraft to orbit around the Sun, exploring a new part of the solar system each time. This novel data set, along with data from several other spacecraft, were used to investigate structure in the solar wind from new perspectives. This chapter summarises the work performed in the thesis and offers suggestions for how future studies could help to improve the understanding of the acceleration and structure of the solar wind.

Chapter 3 presented research completed with the newly formed spacecraft constellation in the inner heliosphere. Multiple spacecraft have been routinely used to study the evolution of the solar wind at different distances from the Sun. However, in Chapter 3, a different approach was taken, and the solar wind structure was studied in latitude. After introducing the different spacecraft and available data products, the ballistic mapping process was explained. This allowed the different spacecraft to be mapped back to the source surface of the Sun, where they could be compared to each other and a coronal magnetic field model. The theory and application of this model were discussed, followed by a description of the methods for estimating the magnetic polarity and local sector boundary orientation.

The results were then presented for two solar rotations at solar minimum, where

the global structure of the solar wind was mapped using only in situ measurements within $\pm 10°$. It was shown that the heliospheric current sheet (HCS) was remarkably flat during these periods, meaning that a small change in latitude could drastically change the solar wind conditions. These results demonstrate that care must be taken when comparing spacecraft at different latitudes, which could be important in the future for the prediction of space weather effects at Earth.

This type of solar wind mapping could also prove useful for the validation of solar wind models, which is usually achieved by flying a virtual spacecraft through the simulation. However, there is now a wide coverage of the solar wind, and the spacecraft data can be used to build up a spatial representation of the solar wind, which can be compared directly to the simulation.

As well as providing a clearer picture of the global solar wind structure, the spacecraft constellation was also used to study large-scale structures in more detail than could be achieved by a single spacecraft. First, a spread in latitude was used to reveal a fine-scale ripple in the HCS of the order of $\sim 15°$ in longitude and $\sim 5°$ latitude. In addition to showing that such a fine-scale ripple could not be captured by the PFSS model, this structure was also used to identify the signature of a comet tail crossing in Solar Orbiter (Matteini et al. 2021). This, along with two other case studies, showed how the data from other spacecraft can be used to provide contextual information. Therefore, even though these spacecraft were designed to fulfil their own aims, Chapter 3 demonstrated that they can be used together to expand the range of research opportunities in the solar wind. It is hoped that these examples can provide inspiration for future studies to investigate the solar wind from new perspectives.

The remainder of this thesis then focused on the properties and generation of switchbacks in the solar wind. These structures became one of the major results from PSP following their dominance of the early data in November 2018. Since then, the understanding of switchbacks has continued to evolve as new data was returned in each PSP encounter. This progression of knowledge is reflected in each of the

three switchback investigations presented in Chapters 4 and 5.

Chapter 4 first summarises the observed switchback properties, followed by a discussion of the different generation mechanisms. Since switchbacks are essentially folds in the magnetic field, they can feasibly be created by many different mechanisms. Therefore, the aim of this chapter was to gather observable evidence that could be used to uncover the true source of switchbacks in the solar wind.

After describing how switchbacks were identified, Section 4.4 attempted to find the average switchback size using data from the first two PSP encounters from November 2018 to April 2019. This work was based on the idea that the switchback duration could depend on the way in which the spacecraft cut through the structure. Following the work of Horbury et al. (2020b), the true switchback shape was assumed to be a long, thin structure. Consequently, it was argued that a longer duration switchback did not necessarily represent a physically larger structure in the solar wind. Instead, the longer duration would be caused by the spacecraft cutting down the length of the switchback.

A model was developed to describe how the switchback duration should vary with deflection direction. This was then fitted to the data from 16 different solar wind streams, giving an average switchback shape and alignment direction for six streams. It was found that the studied switchbacks were around 50,000 km wide, consistent with other estimates (Horbury et al. 2020b; Krasnoselskikh et al. 2020; Larosa et al. 2021; Bandyopadhyay et al. 2021). However, the analysis also showed that switchbacks had an aspect ratio of the order of 10 and were aligned towards the local Parker spiral direction. These results helped form the initial understanding of the physical switchback shape, which has since been compared to the output from several switchback generation mechanisms (reviewed by Raouafi et al. 2023a).

During the first two encounters, there were several reports that switchbacks tended to deflect in the same sense as the Sun's rotation (Kasper et al. 2019; Horbury et al. 2020b). Such behaviour was used as supporting evidence for several proposed generation mechanisms, which predicted the formation of systematic de-

flections (Fisk and Kasper 2020; Schwadron and McComas 2021). However, this characteristic was not expected to be present if switchbacks were created by the expansion of random fluctuations in the solar wind (Squire et al. 2020; Shoda et al. 2021). Therefore, to help distinguish between generation methods, Section 4.5 attempted to find evidence for preferential deflection directions.

After identifying switchbacks across the first eight PSP encounters, it was concluded that the deflection directions were not isotropic. Switchbacks tended to have tangential deflections, but this was found to be in both $\pm\vec{T}$, rather than having a single preferred direction as predicted (Fisk and Kasper 2020; Schwadron and McComas 2021; Johnston et al. 2022). While there was not an exact match to a particular theory, the results indicated that there was some systematic effect in the switchbacks that needed to be explained. These observations could be evidence for a consistent magnetic configuration closer to the Sun, such as repeated magnetic reconnection (Fisk and Kasper 2020; Zank et al. 2020) or the existence of magnetic funnels (Bale et al. 2021). It was originally thought that expanded fluctuations could not generate such an asymmetric distribution of deflection directions. However, the results in Chapter 4 prompted Johnston et al. (2022) and Squire et al. (2022a) to show how an initially random set of fluctuations could be influenced by the Parker spiral to create this effect.

Chapter 4 has therefore helped build a picture of the typical switchback size and internal structure, which has subsequently been used to constrain switchback generation methods. In future, multi spacecraft observations could provide conclusive observations, although, this will most likely need a dedicated mission due to the small-scale size of the switchbacks.

As reviewed by Raouafi et al. (2023a), there has been a tremendous amount of work regarding switchbacks and their formation. However, there has not yet been a conclusive piece of evidence directly linking switchbacks to a source mechanism. This has been made more difficult by seemingly conflicting results about the plasma properties inside switchbacks (Woolley et al. 2020; Woodham et al. 2021a). There-

fore, Chapter 5 aimed to find direct signatures of interchange reconnection, as PSP moved to only 13 $R_\odot$ in February 2022.

A more consistent pattern in the magnetic field was identified, where several successive switchbacks were seen to deflect along the same arc. Since this was remarkably similar to the magnetic field signatures predicted by simulations, it was argued that this could represent the imprint of interchange reconnection on the solar wind. This was further strengthened by the observation that this pattern would have a scale of $\sim 0.6 \rightarrow 3$ Mm on the solar surface, similar to the size of bright points (Kumar et al. 2022). Therefore, it was concluded that coronal plumes modulate the switchbacks into patches, with the bright points at their base creating switchbacks via interchange reconnection.

Due to the increased proximity to the Sun, it was also shown that switchbacks were unambiguously associated with an increased temperature. It was found that switchbacks had a consistent heating rate of $\sim$16,000$\pm$4,000 K/$^\circ$ for $T_{p,\parallel}$ and $\sim$7,000$\pm$4,000 K/$^\circ$ for $T_{p,\perp}$. The difference in heating rates also led to the proton core becoming more isotropic inside the switchbacks. Such a result, along with the new systematic pattern in the magnetic field, were used to propose a new switchback definition. This provides a more robust way to identify switchbacks, which does not rely solely on the absolute magnetic field angle. This will not only help with future switchback studies, but could also represent a paradigm shift in switchback research.

By observing the larger-scale behaviour of temperature, it was also concluded that switchbacks are not directly responsible for the heating of the solar wind. Instead, they may represent tracers of interchange reconnection on the Sun.

The results of this thesis have improved our understanding of structures in the solar wind, particularly the size, shape and deflections patterns of switchbacks. However, there are still many open questions to be answered as the Parker Solar Probe and Solar Orbiter missions continue to return data from previously unmeasured regions.

While Chapter 5 conclusively revealed that switchbacks were associated with

higher temperatures, the exact mechanism remains unclear. Due to physical limitations of the Parker solar probe instrumentation, only the temperature behaviour of the protons could be studied. To make further progress, and more detailed investigation of a wider range of plasma data is needed, particularly of the electron and alpha particles. In combination with the empirical temperature relationship measured in Chapter 5, this extra knowledge can hopefully reveal the underlying mechanism in these complex structures.

Discerning how switchbacks are heated could also impact our understanding of how the solar wind itself is heated and accelerated. As was demonstrated in Chapter 3, the constellation of spacecraft within the solar wind can be combined to create a wider range of potential studies. In this case, Solar Orbiter and Wind were both aligned with PSP for E11, allowing for the heating rate inside switchbacks to be compared with the Chapter 5 results at $\sim$0.5 AU and 1 AU, respectively. Not only can this help interpreting the flow of energy from the Sun out into the heliosphere, but could also be used to constrain solar wind or switchbacks models. In addition, the advanced instrumentation aboard Solar Orbiter could also be used to investigate the abundance and heating of minor ion populations, which is not possible with PSP.

Finally, Chapter 5 revealed a promising link between jetting activity on the Sun and coherent deflection patterns in the solar wind. While the deflections were believed to have similar deflection properties and scale size, definitive proof will only come by tracing individual structures in the solar wind back to impulsive events on the Sun. Such an ambitious task will require a coordinated effort from detailed remote sensing observations, such as Solar Orbiter and DKIST (Rimmele et al. 2020), as well as sophisticated modelling to connect with the spacecraft measurements. Therefore, the future of solar wind physics will likely rely on an unprecedented collaboration between in situ measurements, remote sensing images and computational simulations.

Appendix A

Papers

List of papers produced during my PhD.

First author

1. Coherent deflection pattern and associated temperature enhancements in the near-Sun solar wind (Laker et al. 2023)
2. Switchback deflections beyond the early Parker solar probe encounters (Laker et al. 2022)
3. Multi-spacecraft study of the solar wind at solar minimum: Dependence on latitude and transient outflows (Laker et al. 2021a)
4. Statistical analysis of orientation, shape, and size of solar wind switchbacks (Laker et al. 2021b)

Co-author

1. Parker Solar Probe: Four Years of Discoveries at Solar Cycle Minimum (Raouafi et al. 2023a)
2. Observation and Modelling of the Solar Wind Turbulence Evolution in the Sub-Mercury Inner Heliosphere (Telloni et al. 2022)

3. Evolution of coronal hole solar wind in the inner heliosphere: Combined observations by Solar Orbiter and Parker Solar Probe (Perrone et al. 2022)

4. Flux rope and dynamics of the heliospheric current sheet: Study of the Parker Solar Probe and Solar Orbiter conjunction of June 2020 (Réville et al. 2022)

5. Plasma properties, switchback patches, and low α-particle abundance in slow Alfvénic coronal hole wind at 0.13 au (Woolley et al. 2021)

6. Enhanced proton parallel temperature inside patches of switchbacks in the inner heliosphere (Woodham et al. 2021a)

7. Evolution of Solar Wind Turbulence from 0.1 to 1 au during the First Parker Solar Probe-Solar Orbiter Radial Alignment (Telloni et al. 2021b)

8. Study of two interacting interplanetary coronal mass ejections encountered by Solar Orbiter during its first perihelion passage - Observations and modeling (Telloni et al. 2021a)

9. Solar Orbiter's encounter with the tail of comet C/2019 Y4 (ATLAS): Magnetic field draping and cometary pick-up ion waves (Matteini et al. 2021)

10. Magnetic reconnection as a mechanism to produce multiple thermal proton populations and beams locally in the solar wind (Lavraud et al. 2021)

11. Solar Orbiter observations of an ion-scale flux rope confined to a bifurcated solar wind current sheet (Eastwood et al. 2021)

12. A Solar Source of Alfvénic Magnetic Field Switchbacks: In Situ Remnants of Magnetic Funnels on Supergranulation Scales (Bale et al. 2021)

13. Proton core behaviour inside magnetic field switchbacks (Woolley et al. 2020)

14. Sharp Alfvénic Impulses in the Near-Sun Solar Wind (Horbury et al. 2020b)

15. Highly structured slow solar wind emerging from an equatorial coronal hole (Bale et al. 2019)

Appendix B

Symbols

$R_\odot$	Solar radius
$M_\odot$	Solar mass
$\vec{B}$	Magnetic field
$\vec{E}$	Electric field
$\vec{F}$	Lorentz force
$\vec{v}$	Velocity
$\vec{u}$	Bulk velocity
$\vec{x}$	Position
$\vec{J}$	Current density
t	Time
e	Electron charge
m	Mass
λ_D	Debye length
ϵ_0	Vacuum permittivity
μ_0	Permeability of free space
k_B	Boltzmann constant
T	Temperature
$T_{p,\perp}$	Proton core temperature perpendicular to the magnetic field
$T_{p,\parallel}$	Proton core temperature parallel to the magnetic field
n	Number density
ω_p	Plasma frequency
q	Charge
f_c	Cyclotron frequency
r_L	Larmor Radius (gyroradius)

$f_j(\vec{x}, \vec{v}, t)$	Particle velocity distribution
j	Particle species
ρ_c	Charge density
ρ	Bulk mass density
P	Thermal pressure
β	Plasma beta
σ	Conductivity
v_A	Alfvén speed
r	Distance from the Sun's centre
G	Gravitational constant
c_s	Sound speed
r_c	Critical radius
Ω	Solar rotation rate
ϕ_{ps}	Parker spiral angle
$\phi_{ps,T}$, $\phi_{ps,A}$	Parker spiral angle for Towards and Away magnetic polarity
ϕ_B, θ_B	Magnetic field angles in spherical coordinates
Φ, Θ	Longitude and latitude
Φ_{SS}	Longitude at the source surface
R_{SS}	Source surface height
R_{SC}	Spacecraft distance from the Sun
V_{sw}	Solar wind speed
$\varepsilon_{\text{high}}$, ε_{low}	High and Low Voltage in Faraday Cups
θ_{RB}	Angle between the magnetic field and $\vec{R}$
Ψ	Magnetic scalar potential
σ_c	cross helicity
$\vec{A}$	Average switchback alignment direction
ϕ_A, θ_A	Average switchback alignment direction angles
α_C	Spacecraft cutting angle
W, L	Width and length of a switchback
α_H	Hypotenuse angle of the model switchback
D	Duration of a switchback
V_{SC}	Spacecraft velocity
V_{rel}	Velocity of the switchback relative to the spacecraft
f	Magnetic expansion factor
δT_S	Saturated increase in temperature for a switchback
θ_S	Angle of saturated temperature in a switchback

Appendix C

Abbreviations

ADAPT	Air Force Data Assimilative Photospheric Flux Transport
AIA	Atmospheric Imaging Assembly
AU	Astronomical Unit
CA	Clock Angle
CIR	Co-rotating Interaction Region
CME	Coronal Mass Ejection
DKIST	Daniel K. Inouye Solar Telescope
E1	Encounter 1
ESA	Electrostatic Analyser
FIELDS	Electromagnetic Fields Investigation
FOV	Field of View
GONG	Global Oscillation Network Group
HCS	Heliospheric Current Sheet
ICME	Interplanetary Coronal Mass Ejection
IMPACT	In-situ Measurements of Particles and CME Transients
IS$\odot$IS	Integrated Science Investigation of the Sun
MAG	Solar Orbiter Magnetometer
MPO	Mercury Planetary Orbiter
MFI	Magnetic Field Investigation
MHD	Magnetohydrodynamics
MVA	Minimum Variance Analysis
NASA	National Aeronautics and Space Administration
PAD	Pitch Angle Distribution
PAS	Proton Alpha Sensor

PMS	Planar Magnetic Structure
PLASTIC	PLAsma and SupraThermal Ion Composition
PSP	Parker Solar Probe
RD	Rotational Discontinuity
SDO	Solar Dynamics Observatory
SIR	Stream Interaction Region
SPAN	Solar Probe Analyzer
SPC	Solar Probe Cup
SWEAP	Solar Wind Electrons Alphas and Protons Investigation
SWE	Solar Wind Experiment
VDF	Velocity Distribution Function
WISPR	Wide-field Imager for Parker Solar Probe

Appendix D

Software

I have used the following software in my research:

- Python - https://www.python.org/
- NumPy - https://numpy.org/
- Matplotlib - https://matplotlib.org/
- SciPy - https://scipy.org/
- Pandas - https://pandas.pydata.org/
- pfsspy - https://pfsspy.readthedocs.io/en/stable/index.html
- HelioPy - https://github.com/heliopython/heliopy
- astrospice - https://github.com/astrospice/astrospice
- SpiceyPy - https://spiceypy.readthedocs.io/en/main/
- SPICE - https://naif.jpl.nasa.gov/naif/index.html
- Astropy - https://www.astropy.org/
- SunPy - https://sunpy.org/

Appendix E

Data

The following data used for this thesis is publicly available:

- Parker Solar Probe data - https://cdaweb.gsfc.nasa.gov/pub/data/psp/
- Solar Orbiter data - https://soar.esac.esa.int/soar/
- Wind data - https://cdaweb.gsfc.nasa.gov/pub/data/wind/
- STEREO-A data - https://cdaweb.gsfc.nasa.gov/pub/data/stereo/ahead/

Appendix F

Permissions

Fig. No.	Publisher	Citation	Permission Status
2.3	NASA	Helioviewer	None Required
2.4	Springer	Hathaway (2015)	None Required
2.5	Springer	Hathaway (2015)	None Required
2.6	Springer	Wiegelmann et al. (2014)	None Required
2.7	Springer	Echim et al. (2010)	None Required
2.9	GRL	McComas et al. (2003)	Granted
2.10	Spinger Nature	Marsch (2012)	Granted
2.11	Arxiv	Salem et al. (2021)	Granted
2.12	ApJ	Matteini et al. (2015)	Granted
2.13	NASA	Heil (1980)	None Required
2.14a	Space Physics	Pizzo (1978)	Granted
2.14b	Space Physics	Pizzo (1991)	Granted
2.15	GRL	Gosling et al. (1993)	Granted
2.16	GI	Miles et al. (2017)	None Required
2.18	Living Reviews	Verscharen et al. (2019)	None Required
2.21	Space Sci. Rev.	Kasper et al. (2016)	None Required
Tab. 3.1	A&A	Laker et al. (2021a)	Granted
3.5	JGR	Owens et al. (2013)	Granted
3.10	A&A	Laker et al. (2021a)	Granted
Tab. 3.2	A&A	Laker et al. (2021a)	Granted
3.12	A&A	Matteini et al. (2021)	Granted
3.13	A&A	Laker et al. (2021a)	Granted
3.15	A&A	Laker et al. (2021a)	Granted

4.2	NASA	NASA et al. (2021)	None Required
4.6	MNRAS	Laker et al. (2022)	None Required
4.7	MNRAS	Laker et al. (2022)	None Required
4.12	A&A	Laker et al. (2021b)	Granted
4.13	A&A	Laker et al. (2021b)	Granted
4.17	A&A	Laker et al. (2021b)	Granted
Tab. 4.1	A&A	Laker et al. (2021b)	Granted
4.19	MNRAS	Laker et al. (2022)	None Required
4.20	ApJL	Fisk and Kasper (2020)	None Required
4.22	ApJ	Bale et al. (2021)	Granted
5.1	ApJ	Kumar et al. (2022)	None Required
5.2	ApJ	Wyper et al. (2022)	None Required
5.3	Arxiv	Bale et al. (2022)	Granted

Bibliography

Abbo, L., L. Ofman, S. K. Antiochos, V. H. Hansteen, L. Harra, Y. K. Ko, G. Lapenta, B. Li, P. Riley, L. Strachan, R. von Steiger, and Y. M. Wang (2016). "Slow Solar Wind: Observations and Modeling". In: *Space Science Reviews* 201.1-4, pp. 55–108. ISSN: 15729672. DOI: 10.1007/s11214-016-0264-1.

Acton, Charles, Nathaniel Bachman, Boris Semenov, and Edward Wright (2018). "A Look towards the Future in the Handling of Space Science Mission Geometry". In: *Planetary and Space Science* 150, pp. 9–12. ISSN: 00320633. DOI: 10.1016/j.pss.2017.02.013.

Acton, Charles H. (1996). "Ancillary Data Services of NASA's Navigation and Ancillary Information Facility". In: *Planetary and Space Science* 44.1, pp. 65–70. DOI: 10.1016/0032-0633(95)00107-7.

Acuña, M H, D Curtis, J L Scheifele, C T Russell, P Schroeder, A Szabo, and J G Luhmann (2008). "The STEREO/IMPACT Magnetic Field Experiment". In: *Space Science Reviews* 136.1, pp. 203–226. ISSN: 1572-9672. DOI: 10.1007/s11214-007-9259-2.

Agapitov, O. V. et al. (2020). "Sunward-Propagating Whistler Waves Collocated with Localized Magnetic Field Holes in the Solar Wind: Parker Solar Probe Observations at 35.7 R ⊙ Radii". In: *The Astrophysical Journal* 891.L20. DOI: 10.3847/2041-8213/ab799c.

Akhavan-Tafti, M., J. Kasper, J. Huang, and S. Bale (2021). "Discontinuity Analysis of the Leading Switchback Transition Regions". In: *Astronomy & Astrophysics* 650, A4. ISSN: 0004-6361, 1432-0746. DOI: 10.1051/0004-6361/202039508.

Alberti, Tommaso, Anna Milillo, Daniel Heyner, Lina Z. Hadid, Hans-Ulrich Auster, Ingo Richter, and Yasuhito Narita (2022). "The "Singular" Behavior of the Solar Wind Scaling Features during Parker Solar Probe–BepiColombo Radial Alignment". In: *The Astrophysical Journal* 926.2, p. 174. ISSN: 0004-637X. DOI: 10.3847/1538-4357/ac478d.

Alfvén, Hannes (1942). "Existence of Electromagnetic-Hydrodynamic Waves". In: *Nature* 150.3805, pp. 405–406. ISSN: 0028-0836. DOI: 10.1038/150405d0.

— (1977). "Electric Currents in Cosmic Plasmas". In: *Reviews of Geophysics* 15.3, pp. 271–284. ISSN: 19449208. DOI: 10.1029/RG015i003p00271.

Alipour, N. and H. Safari (2015). "STATISTICAL PROPERTIES OF SOLAR CORONAL BRIGHT POINTS". In: *The Astrophysical Journal* 807.2, p. 175. ISSN: 0004-637X. DOI: 10.1088/0004-637X/807/2/175.

Allen, R C et al. (2021). "Radial Evolution of a CIR: Observations From a Nearly Radially Aligned Event Between Parker Solar Probe and STEREO-A". In: *Geophysical Research Letters* 48.3, e2020GL091376. DOI: 10.1029/2020GL091376.

Altschuler, Martin D. and Gordon Newkirk (1969). "Magnetic Fields and the Structure of the Solar Corona". In: *Solar Physics* 9.1, pp. 131–149. ISSN: 0038-0938. DOI: 10.1007/BF00145734.

Annex, Andrew, Ben Pearson, Benoît Seignovert, Brian T. Carcich, Helge Eichhorn, Jesse A. Mapel, Johan L. Freiherr von Forstner, Jonathan McAuliffe, Jorge Diaz del Rio, Kristin L. Berry, K.-Michael Aye, Marcel Stefko, Miguel de Val-Borro, Shankar Kulumani, Shin-ya Murakami, Kyle Niemeyer, Gavin Medley, and Jean-Luc Margot (2021). *AndrewAnnex/SpiceyPy: SpiceyPy 4.0.1*. Zenodo. DOI: 10.5281/zenodo.4883901.

Antiochos, S. K., C. R. DeVore, and J. A. Klimchuk (1999). "A Model for Solar Coronal Mass Ejections". In: *The Astrophysical Journal* 510, pp. 485–493. ISSN: 0004-637X. DOI: 10.1086/306563.

Antiochos, S. K., Z. Mikić, V. S. Titov, R. Lionello, and J. A. Linker (2011). "A MODEL FOR THE SOURCES OF THE SLOW SOLAR WIND". In: *The As-*

trophysical Journal 731.2, p. 112. ISSN: 0004-637X. DOI: 10.1088/0004-637X/731/2/112.

Archinal, B A, M F A'Hearn, E Bowell, A Conrad, G J Consolmagno, R Courtin, T Fukushima, D Hestroffer, J L Hilton, G A Krasinsky, G Neumann, J Oberst, P K Seidelmann, P Stooke, D J Tholen, P C Thomas, and I P Williams (2011). "Report of the IAU Working Group on Cartographic Coordinates and Rotational Elements: 2009". In: *Celestial Mechanics and Dynamical Astronomy* 109.2, pp. 101–135. ISSN: 1572-9478. DOI: 10.1007/s10569-010-9320-4.

Arden, W. M., A. A. Norton, and X. Sun (2014). "A "Breathing" Source Surface for Cycles 23 and 24". In: *Journal of Geophysical Research: Space Physics* 119.3, pp. 1476–1485. ISSN: 21699380. DOI: 10.1002/2013JA019464.

Axford, W. I. and J. F. McKenzie (1992). *The Origin of High Speed Solar Wind Streams*. https://ui.adsabs.harvard.edu/abs/1992sws..coll....1A/abstract, pp. 1–5.

Babcock, H. W. (1961). "The Topology of the Sun's Magnetic Field and the 22-YEAR Cycle." In: *The Astrophysical Journal* 133, p. 572. ISSN: 0004-637X. DOI: 10.1086/147060.

Badman, Samuel T. et al. (2020). "Magnetic Connectivity of the Ecliptic Plane within 0.5 Au: Potential Field Source Surface Modeling of the First Parker Solar Probe Encounter". In: *The Astrophysical Journal Supplement Series* 246.2, p. 23. ISSN: 0067-0049. DOI: 10.3847/1538-4365/ab4da7.

Bale, S D, T S Horbury, M Velli, M I Desai, J S Halekas, M D McManus, O Panasenco, S T Badman, T A Bowen, B D G Chandran, J F Drake, J C Kasper, R Laker, A Mallet, L Matteini, T D Phan, N E Raouafi, J Squire, L D Woodham, and T Woolley (2021). "A Solar Source of Alfvénic Magnetic Field Switchbacks: In Situ Remnants of Magnetic Funnels on Supergranulation Scales". In: *The Astrophysical Journal* 923.2, p. 174. DOI: 10.3847/1538-4357/ac2d8c.

Bale, S D et al. (2019). "Highly Structured Slow Solar Wind Emerging from an Equatorial Coronal Hole". In: *Nature* 576.7786, pp. 237–242. ISSN: 14764687. DOI: 10.1038/s41586-019-1818-7.

Bale, S. D., J. F. Drake, M. D. McManus, M. I. Desai, S. T. Badman, D. E. Larson, M. Swisdak, N. E. Raouafi, T. Phan, M. Velli, D. J. McComas, C. M. S. Cohen, D. Mitchell, O. Panasenco, and J. C. Kasper (2022). *Interchange Reconnection within Coronal Holes Powers the Fast Solar Wind*. DOI: 10.48550/arXiv.2208.07932.

Bale, S. D., J. C. Kasper, G. G. Howes, E. Quataert, C. Salem, and D. Sundkvist (2009). "Magnetic Fluctuation Power Near Proton Temperature Anisotropy Instability Thresholds in the Solar Wind". In: *Physical Review Letters* 103.21, pp. 1–4. ISSN: 00319007. DOI: 10.1103/PhysRevLett.103.211101.

Bale, S. D. et al. (2016). "The FIELDS Instrument Suite for Solar Probe Plus: Measuring the Coronal Plasma and Magnetic Field, Plasma Waves and Turbulence, and Radio Signatures of Solar Transients". In: *Space Science Reviews* 204, pp. 49–82. ISSN: 15729672. DOI: 10.1007/s11214-016-0244-5.

Balogh, A., R. J. Forsyth, E. A. Lucek, T. S. Horbury, and E. J. Smith (1999). "Heliospheric Magnetic Field Polarity Inversions at High Heliographic Latitudes". In: *Geophysical Research Letters* 26.6, pp. 631–634. ISSN: 00948276. DOI: 10.1029/1999GL900061.

Bandyopadhyay, R. et al. (2021). "Energetic Particle Behavior in Near-Sun Magnetic Field Switchbacks from PSP". In: *Astronomy & Astrophysics* 650, p. L4. ISSN: 0004-6361, 1432-0746. DOI: 10.1051/0004-6361/202039800.

Barnes, Aaron and Joseph V. Hollweg (1974). "Large-Amplitude Hydromagnetic Waves". In: *Journal of Geophysical Research* 79, p. 2302. ISSN: 0148-0227. DOI: 10.1029/JA079i016p02302.

Baumjohann, W. and Rudolf A. Treumann (2022). *Basic Space Plasma Physics*. Third edition. New Jersey: World Scientific. ISBN: 9789811254055.

Belcher, J W and Leverett Davis Jr. (1971). "Large-Amplitude Alfvén Waves in the Interplanetary Medium, 2". In: *Journal of Geophysical Research (1896-1977)* 76.16, pp. 3534–3563. ISSN: 0148-0227. DOI: 10.1029/JA076i016p03534.

Benkhoff, Johannes, Jan van Casteren, Hajime Hayakawa, Masaki Fujimoto, Harri Laakso, Mauro Novara, Paolo Ferri, Helen R. Middleton, and Ruth Ziethe (2010). "BepiColombo-Comprehensive Exploration of Mercury: Mission Overview and Science Goals". In: *Planetary and Space Science* 58.1-2, pp. 2–20. ISSN: 00320633. DOI: 10.1016/j.pss.2009.09.020.

Biermann, L. (1951). "Kometenschweife Und Solare Korpuskularstrahlung". In: *Zeitschrift für Astrophysik* 29. http://adsabs.harvard.edu/abs/1951ZA.....29..274B, p. 274.

— (1957). "Solar Corpuscular Radiation and the Interplanetary Gas". In: *The Observatory* 77. http://adsabs.harvard.edu/abs/1957Obs....77..109B, pp. 109–110.

Birkeland, Kr (1908). *The Norwegian Aurora Polaris Expedition 1902-1903: On the Cause of Magnetic Storms and the Origin of Terrestrial Magnetism: First Section.*

Biskamp, D. (2000). *Magnetic Reconnection in Plasmas*. Cambridge University Press. ISBN: 0-521-58288-1.

Blanco, J J, M A Hidalgo, J Rodriguez-Pacheco, and J Medina (2011). "Interaction between Magnetic Clouds and the Heliospheric Current Sheet at 1AU as It Is Observed by One Single Observation Point". In: *Journal of Atmospheric and Solar-Terrestrial Physics* 73.11, pp. 1339–1347. ISSN: 1364-6826. DOI: 10.1016/j.jastp.2010.10.014.

Bochsler, Peter (2000). "Abundances and Charge States of Particles in the Solar Wind". In: *Reviews of Geophysics* 38.2, pp. 247–266. ISSN: 87551209. DOI: 10.1029/1999RG000063.

Bohlin, J. D. (1977). "Extreme-Ultraviolet Observations of Coronal Holes". In: *Solar Physics* 51.2, pp. 377–398. ISSN: 1573-093X. DOI: 10.1007/BF00216373.

Borrini, G., J. T. Gosling, S. J. Bame, W. C. Feldman, and J. M. Wilcox (1981). "Solar Wind Helium and Hydrogen Structure near the Heliospheric Current Sheet: A Signal of Coronal Streamers at 1 AU". In: *Journal of Geophysical Research: Space Physics* 86.A6, pp. 4565–4573. DOI: 10.1029/ja086ia06p04565.

Broiles, T. W., M. I. Desai, and D. J. McComas (2012). "Formation, Shape, and Evolution of Magnetic Structures in CIRs at 1 AU". In: *Journal of Geophysical Research: Space Physics* 117.3, pp. 1–21. ISSN: 21699402. DOI: 10.1029/2011JA017288.

Bruno, R., V. Carbone, L. Primavera, F. Malara, L. Sorriso-Valvo, B. Bavassano, and P. Veltri (2004). "On the Probability Distribution Function of Small-Scale Interplanetary Magnetic Field Fluctuations". In: *Annales Geophysicae* 22, pp. 3751–3769. DOI: 10.5194/angeo-22-3751-2004.

Bruno, Roberto and Vincenzo Carbone (2013). "The Solar Wind as a Turbulence Laboratory". In: *Living Reviews in Solar Physics* 10.1, p. 2. ISSN: 1614-4961. DOI: 10.12942/lrsp-2013-2.

Burlaga, L F (1983). "Corotating Pressure Waves without Fast Streams in the Solar Wind". In: *Journal of Geophysical Research: Space Physics* 88.A8, pp. 6085–6094. DOI: 10.1029/JA088iA08p06085.

Burlaga, L. F. and K. W. Ogilvie (1970). "Heating of the Solar Wind". In: *The Astrophysical Journal* 159, p. 659. ISSN: 0004-637X. DOI: 10.1086/150340.

Burton, M. E., N. U. Crooker, G. L. Siscoe, and E. J. Smith (1994). "A Test of Source-Surface Model Predictions of Heliospheric Current Sheet Inclination". In: *Journal of Geophysical Research* 99.A1, p. 1. ISSN: 0148-0227. DOI: 10.1029/93ja02100.

Butterworth, Stephen et al. (1930). "On the Theory of Filter Amplifiers". In: *Wireless Engineer* 7.6. https://www.changpuak.ch/electronics/downloads/On_the_Theory_of_Filter_Amplifiers.pdf, pp. 536–541.

Cannon, P (2013). *Extreme Space Weather : Impacts on Engineered Systems and Infrastructure*. Tech. rep. http://eprints.lancs.ac.uk/64443/. Royal Academy of Engineering.

Carrington, R. C. (1853). *Observations of the Spots on the Sun from November 9, 1853, to March 24, 1861, Made at Redhill*. https://archive.org/details/observationsofsp00carr/page/n4.

— (1858). "On the Distribution of the Solar Spots in Latitudes since the Beginning of the Year 1854, with a Map". In: *Monthly Notices of the Royal Astronomical Society* 19, pp. 1–3. ISSN: 0035-8711. DOI: 10.1093/mnras/19.1.1.

— (1859). "Description of a Singular Appearance Seen in the Sun on September 1, 1859". In: *Monthly Notices of the Royal Astronomical Society* 20.1, pp. 13–15. DOI: 10.1093/mnras/20.1.13.

Case, A W et al. (2020). "The Solar Probe Cup on the Parker Solar Probe". In: *The Astrophysical Journal Supplement Series* 246.2, p. 43. DOI: 10.3847/1538-4365/ab5a7b.

Chapman, S (1917). "On the Times of Sudden Commencement of Magnetic Storms". In: *Proceedings of the Physical Society of London* 30.1, p. 205. ISSN: 1478-7814. DOI: 10.1088/1478-7814/30/1/317.

Charbonneau, Paul (2010). "Dynamo Models of the Solar Cycle". In: *Living Reviews in Solar Physics* 7.1, p. 3. DOI: 10.12942/lrsp-2010-3.

Chew, G. F., M. L. Goldberger, F. E. Low, and Subrahmanyan Chandrasekhar (1956). "The Boltzmann Equation and the One-Fluid Hydromagnetic Equations in the Absence of Particle Collisions". In: *Proceedings of the Royal Society of London. Series A. Mathematical and Physical Sciences* 236.1204, pp. 112–118. DOI: 10.1098/rspa.1956.0116.

Chhiber, Rohit, Arcadi V. Usmanov, William H. Matthaeus, and Melvyn L. Goldstein (2018). "Contextual Predictions for Parker Solar Probe I: Critical Surfaces and Regions". http://arxiv.org/abs/1806.00570.

Christensen-Dalsgaard, J., D. O. Gough, and M. J. Thompson (1991). "The Depth of the Solar Convection Zone". In: *The Astrophysical Journal* 378, p. 413. ISSN: 0004-637X. DOI: 10.1086/170441.

Cloutman, L. D. (1979). "A Physical Model of the Solar Granulation." In: *The Astrophysical Journal* 227, pp. 614–628. ISSN: 0004-637X. DOI: 10.1086/156772.

Coleman Jr., Paul J. (1968). "Turbulence, Viscosity, and Dissipation in the Solar-Wind Plasma". In: *The Astrophysical Journal* 153, p. 371. ISSN: 0004-637X. DOI: 10.1086/149674.

Cranmer, Steven R (2009). "Coronal Holes". In: *Living Reviews in Solar Physics* 6. http://adsabs.harvard.edu/abs/2009LRSP....6....3C, p. 66.

Cranmer, Steven R, Adriaan A van Ballegooijen, and Richard J Edgar (2007). "SELF-CONSISTENT CORONAL HEATING AND SOLAR WIND ACCELERATION FROM ANISOTROPIC MAGNETOHYDRODYNAMIC TURBULENCE". In: *The Astrophysical Journal Supplement Series* 171, pp. 520–551. DOI: 10.1086/518001.

Cranmer, Steven R. (2010). "AN EFFICIENT APPROXIMATION OF THE CORONAL HEATING RATE FOR USE IN GLOBAL SUN–HELIOSPHERE SIMULATIONS". In: *The Astrophysical Journal* 710.1, p. 676. ISSN: 0004-637X. DOI: 10.1088/0004-637X/710/1/676.

Crooker, N. U. and D. S. Intriligator (1996). "A Magnetic Cloud as a Distended Flux Rope Occlusion in the Heliospheric Current Sheet". In: *Journal of Geophysical Research: Space Physics* 101.A11, pp. 24343–24348. DOI: 10.1029/96ja02129.

Crooker, N. U., S. W. Kahler, D. E. Larson, and R. P. Lin (2004). "Large-Scale Magnetic Field Inversions at Sector Boundaries". In: *Journal of Geophysical Research: Space Physics* 109.A3, pp. 1–7. ISSN: 21699402. DOI: 10.1029/2003JA010278.

Crooker, N. U., A. H. McAllister, R. J. Fitzenreiter, J. A. Linker, D. E. Larson, R. P. Lepping, A. Szabo, J. T. Steinberg, A. J. Lazarus, Z. Mikic, and R. P. Lin (1998). "Sector Boundary Transformation by an Open Magnetic Cloud". In:

Journal of Geophysical Research: Space Physics 103.A11, pp. 26859–26868. ISSN: 0148-0227. DOI: 10.1029/98ja02391.

D'Amicis, R. and R. Bruno (2015). "ON THE ORIGIN OF HIGHLY ALFVÉNIC SLOW SOLAR WIND". In: *The Astrophysical Journal* 805.1, p. 84. ISSN: 1538-4357. DOI: 10.1088/0004-637X/805/1/84.

D'Amicis, R., D. Perrone, R. Bruno, and M. Velli (2021). "On Alfvénic Slow Wind: A Journey From the Earth Back to the Sun". In: *Journal of Geophysical Research: Space Physics* 126.4, e2020JA028996. ISSN: 2169-9402. DOI: 10.1029/2020JA028996.

D'Amicis, Raffaella, Lorenzo Matteini, and Roberto Bruno (2018). "On Slow Solar Wind with High Alfvénicity: From Composition and Microphysics to Spectral Properties". In: *Monthly Notices of the Royal Astronomical Society* 483.4, pp. 4665–4677. ISSN: 0035-8711. DOI: 10.1093/mnras/sty3329.

— (2019). "On the Slow Solar Wind with High Alfvénicity: From Composition and Microphysics to Spectral Properties". In: *Monthly Notices of the Royal Astronomical Society* 483.4, pp. 4665–4677. ISSN: 0035-8711. DOI: 10.1093/mnras/sty3329.

Davies, E. E. et al. (2021). "In Situ Multi-Spacecraft and Remote Imaging Observations of the First CME Detected by Solar Orbiter and BepiColombo". In: *Astronomy & Astrophysics* 656, A2. ISSN: 0004-6361, 1432-0746. DOI: 10.1051/0004-6361/202040113.

De Hoffmann, F. and E. Teller (1950). "Magneto-Hydrodynamic Shocks". In: *Physical Review* 80.4, pp. 692–703. DOI: 10.1103/PhysRev.80.692.

De Koning, Curt A, V J Pizzo, and D A Biesecker (2009). "Geometric Localization of CMEs in 3D Space Using STEREO Beacon Data: First Results". In: *Solar Phys* 256, pp. 167–181. DOI: 10.1007/s11207-009-9344-7.

DeForest, C. E., J. T. Hoeksema, J. B. Gurman, B. J. Thompson, S. P. Plunkett, R. Howard, R. C. Harrison, and D. M. Hasslerz (1997). "Polar Plume Anatomy:

Results of a Coordinated Observation". In: *Solar Physics* 175.2, pp. 393–410. ISSN: 1573-093X. DOI: 10.1023/A:1004955223306.

DeForest, C. E., P. L. Lamy, and A. Llebaria (2001). "Solar Polar Plume Lifetime and Coronal Hole Expansion: Determination from Long-Term Observations". In: *The Astrophysical Journal* 560.1, p. 490. ISSN: 0004-637X. DOI: 10.1086/322497.

Demarque, P and D B Guenther (1999). "Helioseismology: Probing the Interior of a Star". In: *Proceedings of the National Academy of Sciences of the United States of America* 96.10, pp. 5356–5359. ISSN: 0027-8424. DOI: 10.1073/pnas.96.10.5356.

Démoulin, P. (2009). "Why Do Temperature and Velocity Have Different Relationships in the Solar Wind and in Interplanetary Coronal Mass Ejections?" In: *Solar Physics* 257.1, pp. 169–184. ISSN: 1573-093X. DOI: 10.1007/s11207-009-9338-5.

Desai, Ravindra T., Han Zhang, Emma E. Davies, Julia E. Stawarz, Joan Mico-Gomez, and Pilar Iváñez-Ballesteros (2020). "Three-Dimensional Simulations of Solar Wind Preconditioning and the 23 July 2012 Interplanetary Coronal Mass Ejection". In: *Solar Physics* 295.9, p. 130. ISSN: 1573-093X. DOI: 10.1007/s11207-020-01700-5.

Drake, J. F., A. Agapitov, M. Swisdak, S. T. Badman, S. D. Bale, T. S. Horbury, Justin C. Kasper, R. J. MacDowall, F. S. Mozer, T. D. Phan, M. Pulupa, A. Szabo, and M. Velli (2021). "Switchbacks as Signatures of Magnetic Flux Ropes Generated by Interchange Reconnection in the Corona". In: *Astronomy & Astrophysics*. DOI: 10.1051/0004-6361/202039432.

Dudok de Wit, Thierry, Vladimir V Krasnoselskikh, Stuart D Bale, John W Bonnell, Trevor A Bowen, Christopher H K Chen, Clara Froment, Keith Goetz, Peter R Harvey, Vamsee Krishna Jagarlamudi, Andrea Larosa, Robert J MacDowall, David M Malaspina, William H Matthaeus, Marc Pulupa, Marco Velli, and Phyllis L Whittlesey (2020). "Switchbacks in the Near-Sun Magnetic Field: Long Memory and Impact on the Turbulence Cascade". In: *The Astrophysical*

Journal Supplement Series 246.2, p. 39. ISSN: 1538-4365. DOI: 10.3847/1538-4365/ab5853.

Dunbar, B (2012). *Layers of the Sun*. https://www.nasa.gov/mission_pages/iris/multimedia/layerzoo.html.

Dunn, Richard B. and Jack B. Zirker (1973). "The Solar Filigree". In: *Solar Physics* 33.2, pp. 281–304. ISSN: 1573-093X. DOI: 10.1007/BF00152419.

Durney, B. R. (1972). "Solar-Wind Properties at the Earth as Predicted by One-Fluid Models". In: *Journal of Geophysical Research (1896-1977)* 77.22, pp. 4042–4051. ISSN: 2156-2202. DOI: 10.1029/JA077i022p04042.

Eastwood, J. P., E. Biffis, M. A. Hapgood, L. Green, M. M. Bisi, R. D. Bentley, R. Wicks, L. A. McKinnell, M. Gibbs, and C. Burnett (2017). "The Economic Impact of Space Weather: Where Do We Stand?" In: *Risk Analysis* 37.2. ISSN: 15396924. DOI: 10.1111/risa.12765.

Eastwood, J. P., J. E. Stawarz, T. D. Phan, R. Laker, S. Robertson, L.-L. Zhao, G. P. Zank, B. Lavraud, M. A. Shay, V. Evans, V. Angelini, H. O'Brien, and T. S. Horbury (2021). "Solar Orbiter Observations of an Ion-Scale Flux Rope Confined to a Bifurcated Solar Wind Current Sheet". In: *Astronomy & Astrophysics* 656, A27. ISSN: 0004-6361, 1432-0746. DOI: 10.1051/0004-6361/202140949.

Echim, M., Joseph Lemaire, and Øystein Lie-Svendsen (2010). "A Review on Solar Wind Modeling: Kinetic and Fluid Aspects". In: *Surveys in Geophysics* 32, pp. 1–70. DOI: 10.1007/s10712-010-9106-y.

Edlén, Bengt (1943). "Die Deutung Der Emissionslinien Im Spektrum Der Sonnenkorona. Mit 6 Abbildungen." In: *Zeitschrift fur Astrophysik* 22. https://ui.adsabs.harvard.edu/abs/1943ZA.....22...30E, p. 30. ISSN: 0372-8331.

Elliott, H. A., C. J. Henney, D. J. McComas, C. W. Smith, and B. J. Vasquez (2012). "Temporal and Radial Variation of the Solar Wind Temperature-Speed Relationship". In: *Journal of Geophysical Research: Space Physics* 117.A9. ISSN: 2156-2202. DOI: 10.1029/2011JA017125.

ESA (2023a). *BepiColombo Fact Sheet*. https://sci.esa.int/web/bepicolombo/-/47346-fact-sheet.

— (2023b). *Giuseppe 'Bepi' Colombo: Grandfather of the Fly-By*. https://www.esa.int/About_Us/ESA_history/Giuseppe_Bepi_Colombo_Grandfather_of_the_fly-by.

Fargette, Naïs, Benoit Lavraud, Alexis P Rouillard, Victor Réville, Thierry Dudok De Wit, Clara Froment, Jasper S Halekas, Tai D Phan, David M Malaspina, Stuart D Bale, Justin C Kasper, Philippe Louarn, Anthony W Case, Kelly E Korreck, Davin E Larson, Marc Pulupa, Michael L Stevens, Phyllis L Whittlesey, and Matthieu Berthomier (2021). "Characteristic Scales of Magnetic Switchback Patches Near the Sun and Their Possible Association With Solar Supergranulation and Granulation". In: *The Astrophysical Journal* 919.2, p. 96. DOI: 10.3847/1538-4357/ac1112.

Fargette, Naïs, Benoit Lavraud, Alexis P. Rouillard, Victor Réville, Stuart D. Bale, and Justin Kasper (2022). "The Preferential Orientation of Magnetic Switchbacks, Implications for Solar Magnetic Flux Transport". In: *arXiv:2203.14591 [astro-ph, physics:physics]*. http://arxiv.org/abs/2203.14591.

Farrell, W M, R J MacDowall, J R Gruesbeck, S D Bale, and J C Kasper (2020). "Magnetic Field Dropouts at Near-Sun Switchback Boundaries: A Superposed Epoch Analysis". In: *The Astrophysical Journal Supplement Series* 249.2, p. 28. ISSN: 1538-4365. DOI: 10.3847/1538-4365/ab9eba.

Farrell, W. M., A. P. Rasca, R. J. MacDowall, J. R. Gruesbeck, S. D. Bale, and J. C. Kasper (2021). "Switchback Boundary Dissipation and Relative Age". In: *The Astrophysical Journal* 915.1, p. 68. ISSN: 0004-637X. DOI: 10.3847/1538-4357/ac005b.

Feldman, W C, J R Asbridge, S J Bame, M D Montgomery, and S P Gary (1975). "Solar Wind Electrons". In: *Journal of Geophysical Research (1896-1977)* 80.31, pp. 4181–4196. DOI: 10.1029/JA080i031p04181.

Fisk, L A and J C Kasper (2020). "Global Circulation of the Open Magnetic Flux of the Sun". In: *The Astrophysical Journal* 894.1, p. L4. ISSN: 2041-8213. DOI: 10.3847/2041-8213/ab8acd.

Fisk, L. A. (1996). "Motion of the Footpoints of Heliospheric Magnetic Field Lines at the Sun: Implications for Recurrent Energetic Particle Events at High Heliographic Latitudes". In: *Journal of Geophysical Research: Space Physics* 101.A7, pp. 15547–15553. ISSN: 2156-2202. DOI: 10.1029/96JA01005.

— (2003). "Acceleration of the Solar Wind as a Result of the Reconnection of Open Magnetic Flux with Coronal Loops". In: *Journal of Geophysical Research* 108.A4, p. 1157. ISSN: 0148-0227. DOI: 10.1029/2002JA009284.

Fisk, L. A. and N. A. Schwadron (2001). "The Behavior of the Open Magnetic Field of the Sun". In: *The Astrophysical Journal* 560.1, pp. 425–438. ISSN: 0004-637X. DOI: 10.1086/322503.

Fisk, L. A., T. H. Zurbuchen, and N. A. Schwadron (1999). "On the Coronal Magnetic Field: Consequences of Large-Scale Motions". In: *The Astrophysical Journal* 521.2, pp. 868–877. ISSN: 0004-637X. DOI: 10.1086/307556.

Forsyth, R J, A Balogh, E J Smith, and J T Gosling (1997). "Ulysses Observations of the Northward Extension of the Heliospheric Current Sheet". In: *Geophysical Research Letters* 24.23, pp. 3101–3104. ISSN: 0094-8276. DOI: 10.1029/97GL03099.

Fox, N J, M C Velli, S D Bale, R Decker, A Driesman, R A Howard, J C Kasper, J Kinnison, M Kusterer, D Lario, M K Lockwood, D J McComas, N E Raouafi, and A Szabo (2016). "The Solar Probe Plus Mission: Humanity's First Visit to Our Star". In: *Space Science Reviews* 204.1, pp. 7–48. ISSN: 1572-9672. DOI: 10.1007/s11214-015-0211-6.

Froment, C. et al. (2021). "Direct Evidence for Magnetic Reconnection at the Boundaries of Magnetic Switchbacks with Parker Solar Probe". In: *Astronomy & Astrophysics* 650, A5. ISSN: 0004-6361, 1432-0746. DOI: 10.1051/0004-6361/202039806.

Fu, Hui, Maria S. Madjarska, LiDong Xia, Bo Li, ZhengHua Huang, and Zhipeng Wangguan (2017). "Charge States and FIP Bias of the Solar Wind from Coronal Holes, Active Regions, and Quiet Sun". In: *The Astrophysical Journal* 836, p. 169. ISSN: 0004-637X. DOI: 10.3847/1538-4357/aa5cba.

Galvin, A B et al. (2008). "The Plasma and Suprathermal Ion Composition (PLASTIC) Investigation on the STEREO Observatories". In: *Space Science Reviews* 136.1, pp. 437–486. ISSN: 1572-9672. DOI: 10.1007/s11214-007-9296-x.

Geiss, J., G. Gloeckler, and R. Von Steiger (1995). "Origin of the Solar Wind from Composition Data". In: *Space Science Reviews* 72.1-2, pp. 49–60. ISSN: 00386308. DOI: 10.1007/BF00768753.

Glassmeier, K. -H. et al. (2010). "The Fluxgate Magnetometer of the BepiColombo Mercury Planetary Orbiter". In: *Planetary and Space Science*. Comprehensive Science Investigations of Mercury: The Scientific Goals of the Joint ESA/JAXA Mission BepiColombo 58.1, pp. 287–299. ISSN: 0032-0633. DOI: 10.1016/j.pss.2008.06.018.

Gloeckler, George and Johannes Geiss (2007). "The Composition of the Solar Wind in Polar Coronal Holes". In: *The Composition of Matter*. Springer, New York, pp. 139–152. DOI: 10.1007/978-0-387-74184-0_15.

Gosling, J T, S J Bame, D J Mccomas, J L Phillips, B E Goldstein, and M. Neugebauer (1993). "Latitudinal Variation of Solar Wind Coratating Stream Interaction Regions: Ulysses". In: *Geophysical Research Letters* 20.24, pp. 2789–2792. DOI: 10.1029/93GL03116.

Gosling, J. T., G. Borrini, J. R. Asbridge, S. J. Bame, W. C. Feldman, and R. T. Hansen (1981). "Coronal Streamers in the Solar Wind at 1 AU". In: *Journal of Geophysical Research* 86.A7, p. 5438. ISSN: 0148-0227. DOI: 10.1029/JA086iA07p05438.

Gosling, J. T., A. J. Hundhausen, V. Pizzo, and J. R. Asbridge (1972). "Compressions and Rarefactions in the Solar Wind: Vela 3". In: *Journal of Geophysical Research* 77, p. 5442. ISSN: 0148-0227. DOI: 10.1029/JA077i028p05442.

Gosling, J. T., D. J. McComas, D. A. Roberts, and R. M. Skoug (2009). "A ONE-SIDED ASPECT OF ALFVENIC FLUCTUATIONS IN THE SOLAR WIND". In: *The Astrophysical Journal* 695.2, p. L213. ISSN: 0004-637X. DOI: 10.1088/0004-637X/695/2/L213.

Gosling, J. T., R. M. Skoug, D. J. McComas, and C. W. Smith (2005). "Direct Evidence for Magnetic Reconnection in the Solar Wind near 1 AU". In: *Journal of Geophysical Research: Space Physics* 110.A1. ISSN: 21699402. DOI: 10.1029/2004JA010809.

Gringauz, K. I., V. V. Bezrokikh, V. D. Ozerov, and R. E. Rybchinskii (1960). "A Study of the Interplanetary Ionized Gas, High-Energy Electrons and Corpuscular Radiation from the Sun by Means of the Three-Electrode Trap for Charged Particles on the Second Soviet Cosmic Rocket". In: *Soviet Physics Doklady* 5. http://adsabs.harvard.edu/abs/1960SPhD....5..361G, p. 361.

Grotian, W. (1939). "Zur Frage Der Deutung Der Linien Im Spektrum Der Sonnenkorona". In: *Die Naturwissenschaften* 27.13, p. 214. ISSN: 00281042. DOI: 10.1007/BF01488890.

Grotrian, W. (1939). "Zur Frage der Deutung der Linien im Spektrum der Sonnenkorona". In: *Naturwiss.* 27, p. 214. ISSN: 0028-1042. DOI: 10.1007/BF01488890.

Haberreiter, M., W. Schmutz, and A. G. Kosovichev (2008). "Solving the Discrepancy between the Seismic and Photospheric Solar Radius". In: *The Astrophysical Journal* 675.1, p. L53. ISSN: 0004-637X. DOI: 10.1086/529492.

Hale, George E., Ferdinand Ellerman, S. B. Nicholson, and A. H. Joy (1919). "The Magnetic Polarity of Sun-Spots". In: *The Astrophysical Journal* 49, p. 153. ISSN: 0004-637X. DOI: 10.1086/142452.

Hale, George E. and Seth B. Nicholson (1925). "The Law of Sun-Spot Polarity". In: *The Astrophysical Journal* 62, p. 270. ISSN: 0004-637X. DOI: 10.1086/142933.

Halekas, J. S., P. Whittlesey, D. E. Larson, M. Maksimovic, R. Livi, M. Berthomier, J. C. Kasper, A. W. Case, M. L. Stevens, S. D. Bale, R. J. MacDowall, and M. P. Pulupa (2022). "The Radial Evolution of the Solar Wind as Organized by

Electron Distribution Parameters". In: *The Astrophysical Journal* 936.1, p. 53. ISSN: 0004-637X. DOI: 10.3847/1538-4357/ac85b8.

Hansteen, Viggo H. and Marco Velli (2012). "Solar Wind Models from the Chromosphere to 1 AU". In: *Space Science Reviews* 172.1, pp. 89–121. ISSN: 1572-9672. DOI: 10.1007/s11214-012-9887-z.

Harvey, J. W., F. Hill, R. P. Hubbard, J. R. Kennedy, J. W. Leibacher, J. A. Pintar, P. A. Gilman, R. W. Noyes, A. M. Title, J. Toomre, R. K. Ulrich, A. Bhatnagar, J. A. Kennewell, W. Marquette, J. Patrón, O. Saá, and E. Yasukawa (1996). "The Global Oscillation Network Group (GONG) Project". In: *Science* 272.5266, pp. 1284–1286. DOI: 10.1126/science.272.5266.1284.

Hathaway, David H. (2015). "The Solar Cycle". In: *Living Reviews in Solar Physics* 12.1, p. 4. ISSN: 2367-3648. DOI: 10.1007/lrsp-2015-4.

Heil, Werner (1980). *Heliospheric Current Sheet*. http://wso.stanford.edu/gifs/HCS.html.

Hellinger, Petr, Lorenzo Matteini, Stepan Stverak, Pavel M. Travnicek, and Eckart Marsch (2011). "Heating and Cooling of Protons in the Fast Solar Wind between 0.3 and 1 AU: Helios Revisited". In: *Journal of Geophysical Research: Space Physics* 116.A09105. DOI: 10.1029/2011JA016674.

Heyner, D, I. Richter, F Plaschke, D Fischer, J Mieth, H.-U. Auster, and K.-H. Glassmeier (2020). "Solar Wind Measurements from the Planetary Magnetometer Onboard the BepiColombo Spacecraft". In: *EGU General Assembly 2020*. DOI: 10.5194/egusphere-egu2020-10707.

Heyvaerts, J and E. R. Priest (1982). "Coronal Heating by Phase-Mixed Shear Alfven Waves". In: *Astronomy & Astrophysics* 117. https://ui.adsabs.harvard.edu/abs/1983A&A...117..220H, pp. 220–234.

Hickmann, Kyle S, Humberto C Godinez, Carl J Henney, and C Nick Arge (2015). "Data Assimilation in the ADAPT Photospheric Flux Transport Model". In: *Solar Physics* 290.4, pp. 1105–1118. ISSN: 1573-093X. DOI: 10.1007/s11207-015-0666-3.

Hill, Frank (2018). "The Global Oscillation Network Group Facility—An Example of Research to Operations in Space Weather". In: *Space Weather* 16.10, pp. 1488–1497. ISSN: 1542-7390, 1542-7390. DOI: 10.1029/2018SW002001.

Hoeksema, J. Todd, John M. Wilcox, and Philip H. Scherrer (1983). "Structure of the Heliospheric Current Sheet: 1978-1982." In: *Journal of Geophysical Research* 88.A12, pp. 9910–9918. ISSN: 01480227. DOI: 10.1029/JA088iA12p09910.

Hollweg, Joseph V (2008). *The Solar Wind: Our Current Understanding and How We Got Here*. Tech. rep. https://www.ias.ac.in/article/fulltext/joaa/029/01-02/0217-0237, pp. 217–237.

— (1974). "Transverse Alfvén Waves in the Solar Wind: Arbitrary k, v0, B0, and |δB|". In: *Journal of Geophysical Research (1896-1977)* 79.10, pp. 1539–1541. ISSN: 2156-2202. DOI: 10.1029/JA079i010p01539.

Horbury, T. S., L. Matteini, and D. Stansby (2018). "Short, Large-Amplitude Speed Enhancements in the near-Sun Fast Solar Wind". In: *Monthly Notices of the Royal Astronomical Society* 478.2, pp. 1980–1986. ISSN: 13652966. DOI: 10.1093/mnras/sty953.

Horbury, T. S. et al. (2020a). "The Solar Orbiter Magnetometer". In: *A&A* 642, A9. ISSN: 0004-6361, 1432-0746. DOI: 10.1051/0004-6361/201937257.

Horbury, Timothy S et al. (2020b). "Sharp Alfvénic Impulses in the Near-Sun Solar Wind". In: *The Astrophysical Journal Supplement Series* 246.2, p. 45. DOI: 10.3847/1538-4365/ab5b15.

Hundhausen, A. J. (1993). "Sizes and Locations of Coronal Mass Ejections: SMM Observations from 1980 and 1984-1989". In: *Journal of Geophysical Research: Space Physics* 98.A8, pp. 13177–13200. ISSN: 2156-2202. DOI: 10.1029/93JA00157.

Hundhausen, A. J., H. E. Gilbert, and S. J. Bame (1968). "The State of Ionization of Oxygen in the Solar Wind". In: *The Astrophysical Journal* 152, p. L3. ISSN: 0004-637X. DOI: 10.1086/180165.

Hundhausen, A. J. and J. T. Gosling (1976). "Solar Wind Structure at Large Heliocentric Distances: An Interpretation of Pioneer 10 Observations". In: *Journal of Geophysical Research* 81, p. 1436. ISSN: 0148-0227. DOI: 10.1029/JA081i007p01436.

Ionson, J. A. (1978). "Resonant Absorption of Alfvénic Surface Waves and the Heating of Solar Coronal Loops." In: *The Astrophysical Journal* 226, pp. 650–673. ISSN: 0004-637X. DOI: 10.1086/156648.

Isenberg, Philip A. (2001). "Heating of Coronal Holes and Generation of the Solar Wind by Ion-Cyclotron Resonance". In: *Space Science Reviews* 95.1/2, pp. 119–131. ISSN: 00386308. DOI: 10.1023/A:1005287225222.

— (2004). "The Kinetic Shell Model of Coronal Heating and Acceleration by Ion Cyclotron Waves: 3. The Proton Halo and Dispersive Waves". In: *Journal of Geophysical Research (Space Physics)* 109, A03101. ISSN: 0148-0227. DOI: 10.1029/2002JA009449.

Jian, L K, P J MacNeice, A Taktakishvili, D Odstrcil, B Jackson, H.-S. Yu, P Riley, I V Sokolov, and R M Evans (2015). "Validation for Solar Wind Prediction at Earth: Comparison of Coronal and Heliospheric Models Installed at the CCMC". In: *Space Weather* 13.5, pp. 316–338. DOI: 10.1002/2015SW001174.

Jian, L., C. T. Russell, J. G. Luhmann, and R. M. Skoug (2006). "Properties of Stream Interactions at One AU During 1995 – 2004". In: *Solar Physics* 239.1-2, pp. 337–392. ISSN: 0038-0938. DOI: 10.1007/s11207-006-0132-3.

Johnston, Zade, Jonathan Squire, Alfred Mallet, and Romain Meyrand (2022). "On the Properties of Alfvénic Switchbacks in the Expanding Solar Wind: Three-dimensional Numerical Simulations". In: *Physics of Plasmas* 29.7, p. 072902. ISSN: 1070-664X. DOI: 10.1063/5.0097983.

Jones, G. H. and A. Balogh (2000). "Context and Heliographic Dependence of Heliospheric Planar Magnetic Structures". In: *Journal of Geophysical Research: Space Physics* 105.A6, pp. 12713–12724. ISSN: 2156-2202. DOI: 10.1029/2000JA900003.

Jones, Geraint H, Qasim Afghan, and Oliver Price (2020). "Prospects for the In Situ Detection of Comet C/2019 Y4 ATLAS by Solar Orbiter". In: *Research Notes of the AAS* 4.5, p. 62. DOI: 10.3847/2515-5172/ab8fa6.

Kahler, S. W., N. U. Crocker, and J. T. Gosling (1996). "The Topology of Intra-sector Reversals of the Interplanetary Magnetic Field". In: *Journal of Geophysical Research: Space Physics* 101.A11, pp. 24373–24382. ISSN: 2156-2202. DOI: 10.1029/96JA02232.

Kaiser, M. L., T. A. Kucera, J. M. Davila, O. C. St. Cyr, M. Guhathakurta, and E. Christian (2008). "The STEREO Mission: An Introduction". In: *Space Science Reviews* 136.1-4, pp. 5–16. ISSN: 0038-6308, 1572-9672. DOI: 10.1007/s11214-007-9277-0.

Karpen, J. T., C. R. DeVore, S. K. Antiochos, and E. Pariat (2017). "RECONNECTION-DRIVEN CORONAL-HOLE JETS WITH GRAVITY AND SOLAR WIND". In: *The Astrophysical Journal* 834.1, p. 62. ISSN: 0004-637X. DOI: 10.3847/1538-4357/834/1/62.

Kasper, J. C., K. G. Klein, T. Weber, M. Maksimovic, A. Zaslavsky, S. D. Bale, B. A. Maruca, M. L. Stevens, and A. W. Case (2017). "A Zone of Preferential Ion Heating Extends Tens of Solar Radii from the Sun". In: *The Astrophysical Journal* 849.2, p. 126. ISSN: 0004-637X. DOI: 10.3847/1538-4357/aa84b1.

Kasper, J. C., A. J. Lazarus, and S. P. Gary (2008). "Hot Solar-Wind Helium: Direct Evidence for Local Heating by Alfvén-Cyclotron Dissipation". In: *Physical Review Letters* 101.26, p. 261103. ISSN: 0031-9007. DOI: 10.1103/PhysRevLett.101.261103.

Kasper, J. C., M. L. Stevens, K. E. Korreck, B. A. Maruca, K. K. Kiefer, N. A. Schwadron, and S. T. Lepri (2012). "EVOLUTION OF THE RELATIONSHIPS BETWEEN HELIUM ABUNDANCE, MINOR ION CHARGE STATE, AND SOLAR WIND SPEED OVER THE SOLAR CYCLE". In: *The Astrophysical Journal* 745.2, p. 162. ISSN: 0004-637X. DOI: 10.1088/0004-637X/745/2/162.

Kasper, J. C. et al. (2019). "Alfvénic Velocity Spikes and Rotational Flows in the Near-Sun Solar Wind". In: *Nature* 576.7786, pp. 228–231. ISSN: 14764687. DOI: 10.1038/s41586-019-1813-z.

Kasper, J. C. et al. (2021). "Parker Solar Probe Enters the Magnetically Dominated Solar Corona". In: *Physical Review Letters* 127.25, p. 255101. DOI: 10.1103/PhysRevLett.127.255101.

Kasper, Justin C., Michael L. Stevens, Alan J. Lazarus, John T. Steinberg, and Keith W. Ogilvie (2007). "Solar Wind Helium Abundance as a Function of Speed and Heliographic Latitude: Variation through a Solar Cycle". In: *The Astrophysical Journal* 660.1, p. 901. ISSN: 0004-637X. DOI: 10.1086/510842.

Kasper, Justin C. et al. (2016). "Solar Wind Electrons Alphas and Protons (SWEAP) Investigation: Design of the Solar Wind and Coronal Plasma Instrument Suite for Solar Probe Plus". In: *Space Science Reviews* 204, pp. 131–186. ISSN: 15729672. DOI: 10.1007/s11214-015-0206-3.

Khrabrov, A. V. and B. U. Ö. Sonnerup (1998). "DeHoffmann-Teller Analysis". In: *ISSI Scientific Reports Series* 1. https://www.issibern.ch/forads/sr-001-09.pdf, pp. 221–248.

Kilpua, Emilia, Hannu E. J. Koskinen, and Tuija I. Pulkkinen (2017). "Coronal Mass Ejections and Their Sheath Regions in Interplanetary Space". In: *Living Reviews in Solar Physics* 14.1, p. 5. ISSN: 1614-4961. DOI: 10.1007/s41116-017-0009-6.

Kivelson, M. G. and C. T. Russell, eds. (1995). *Introduction to Space Physics*. Cambridge ; New York: Cambridge University Press. ISBN: 978-0-521-45104-8.

Klein, L and L.F. Burlaga (1980). "Interplanetary Sector Boundaries 1971-1973". In: *Journal of Geophysical Research* 85.A5, pp. 2269–2276. DOI: 10.1029/JA085iA05p02269.

Klimchuk, James A. (2006). "On Solving the Coronal Heating Problem". In: *Solar Physics* 234.1, pp. 41–77. ISSN: 1573-093X. DOI: 10.1007/s11207-006-0055-z.

Kohl, J. L. et al. (1998). "UVCS/SOHO Empirical Determinations of Anisotropic Velocity Distributions in the Solar Corona". In: *The Astrophysical Journal* 501, pp. L127–L131. ISSN: 0004-637X. DOI: 10.1086/311434.

Kopp, R. A. and G. W. Pneuman (1976). "Magnetic Reconnection in the Corona and the Loop Prominence Phenomenon". In: *Solar Physics* 50.1, pp. 85–98. ISSN: 00380938. DOI: 10.1007/BF00206193.

Koutchmy, Serge and Moissei Livshits (1992). "Coronal Streamers". In: *Space Science Reviews* 61.3, pp. 393–417. ISSN: 1572-9672. DOI: 10.1007/BF00222313.

Kraft, S., J. P. Luntama, and K. G. Puschmann (2017). "Remote Sensing Optical Instrumentation for Enhanced Space Weather Monitoring from the L1 and L5 Lagrange Points". In: *International Conference on Space Optics — ICSO 2016*. Ed. by Nikos Karafolas, Bruno Cugny, and Zoran Sodnik. Biarritz, France: SPIE, p. 81. ISBN: 978-1-5106-1613-4. DOI: 10.1117/12.2296100.

Krasnoselskikh, V. et al. (2020). "Localized Magnetic-field Structures and Their Boundaries in the Near-Sun Solar Wind from Parker Solar Probe Measurements". In: *The Astrophysical Journal* 893, p. 93. ISSN: 1538-4357. DOI: 10.3847/1538-4357/ab7f2d.

Krieger, A. S., A. F. Timothy, and E. C. Roelof (1973). "A Coronal Hole and Its Identification as the Source of a High Velocity Solar Wind Stream". In: *Solar Physics* 29.2, pp. 505–525. ISSN: 00380938. DOI: 10.1007/BF00150828.

Kumar, Pankaj, Judith T. Karpen, Spiro K. Antiochos, Peter F. Wyper, C. Richard DeVore, and Craig E. DeForest (2019). "Multiwavelength Study of Equatorial Coronal-hole Jets". In: *The Astrophysical Journal* 873.1, p. 93. ISSN: 0004-637X. DOI: 10.3847/1538-4357/ab04af.

Kumar, Pankaj, Judith T. Karpen, Vadim M. Uritsky, Craig E. Deforest, Nour E. Raouafi, and C. Richard DeVore (2022). "Quasi-Periodic Energy Release and Jets at the Base of Solar Coronal Plumes". In: *The Astrophysical Journal* 933.1, p. 21. ISSN: 0004-637X. DOI: 10.3847/1538-4357/ac6c24.

Kutzer, A. (1977). "Helios". In: *13th Annual Meeting and Technical Display Incorporating the Forum on the Future of Air Transportation*. Washington, DC: American Institute of Aeronautics and Astronautics. DOI: 10.2514/6.1977-266.

Laker, R, T S Horbury, S D Bale, L Matteini, T Woolley, L D Woodham, J E Stawarz, E E Davies, J P Eastwood, M J Owens, H O'Brien, V Evans, V Angelini, I Richter, D Heyner, C J Owen, P Louarn, and A Fedorov (2021a). "Multi-Spacecraft Study of the Solar Wind at Solar Minimum: Dependence on Latitude and Transient Outflows". In: *A&A* 652. DOI: 10.1051/0004-6361/202140679.

Laker, R, T S Horbury, L Matteini, S D Bale, J E Stawarz, L D Woodham, and T Woolley (2022). "Switchback Deflections beyond the Early Parker Solar Probe Encounters". In: *Monthly Notices of the Royal Astronomical Society*, stac2477. ISSN: 0035-8711, 1365-2966. DOI: 10.1093/mnras/stac2477.

Laker, R., T. S. Horbury, S. D. Bale, L. Matteini, T. Woolley, L. D. Woodham, S. T. Badman, M. Pulupa, J. C. Kasper, M. Stevens, A. W. Case, and K. E. Korreck (2021b). "Statistical Analysis of Orientation, Shape, and Size of Solar Wind Switchbacks". In: *Astronomy & Astrophysics* 650, A1. DOI: 10.1051/0004-6361/202039354.

Laker, Ronan, T S Horbury, L D Woodham, S D Bale, and L Matteini (2023). "Coherent Deflection Pattern and Associated Temperature Enhancements in the Near-Sun Solar Wind". In: *Monthly Notices of the Royal Astronomical Society*, stad3351. ISSN: 0035-8711. DOI: 10.1093/mnras/stad3351.

Landi, S., P. Hellinger, and M. Velli (2005). "On the Origin of the Heliospheric Magnetic Field Polarity Inversion at High Latitudes". In: 592. https://ui.adsabs.harvard.edu/abs/2005ESASP.592..785L, p. 785.

Larosa, A., V. Krasnoselskikh, T. Dudok de Wit, O. Agapitov, C. Froment, V. K. Jagarlamudi, M. Velli, S. D. Bale, A. W. Case, K. Goetz, P. Harvey, J. C. Kasper, K. E. Korreck, D. E. Larson, R. J. MacDowall, D. Malaspina, M. Pulupa, C. Revillet, and M. L. Stevens (2021). "Switchbacks: Statistical Properties and Devia-

tions from Alfvénicity". In: *Astronomy & Astrophysics* 650, A3. ISSN: 0004-6361, 1432-0746. DOI: 10.1051/0004-6361/202039442.

Lavraud, B. et al. (2021). "Magnetic Reconnection as a Mechanism to Produce Multiple Thermal Proton Populations and Beams Locally in the Solar Wind". In: *Astronomy & Astrophysics* 656, A37. ISSN: 0004-6361, 1432-0746. DOI: 10.1051/0004-6361/202141149.

Leighton, Robert B., Robert W. Noyes, and George W. Simon (1962). "Velocity Fields in the Solar Atmosphere. I. Preliminary Report." In: *The Astrophysical Journal* 135, p. 474. ISSN: 0004-637X. DOI: 10.1086/147285.

Lemen, James R et al. (2012). "The Atmospheric Imaging Assembly (AIA) on the Solar Dynamics Observatory (SDO)". In: *Solar Phys* 275, pp. 17–40. DOI: 10.1007/s11207-011-9776-8.

Lepping, R P, M H Acũna, L F Burlaga, W M Farrell, J A Slavin, K H Schatten, F Mariani, N F Ness, F M Neubauer, Y C Whang, J B Byrnes, R S Kennon, P V Panetta, J Scheifele, and E M Worley (1995). "The WIND Magnetic Field Investigation". In: *Space Science Reviews* 71.1, pp. 207–229. ISSN: 1572-9672. DOI: 10.1007/BF00751330.

Liang, H, G P Zank, M Nakanotani, and L.-L. Zhao (2021). "Assessing the Role of Interchange Reconnection in Forming Switchbacks". In: *The Astrophysical Journal* 917.2, p. 110. ISSN: 0004-637X. DOI: 10.3847/1538-4357/ac0a73.

Liewer, P. C., E. M. De Jong, J. R. Hall, R. A. Howard, W. T. Thompson, J. L. Culhane, L. Bone, and L. Van Driel-Gesztelyi (2009). "Stereoscopic Analysis of the 19 May 2007 Erupting Filament". In: *Solar Physics* 256.1-2, pp. 57–72. ISSN: 00380938. DOI: 10.1007/s11207-009-9363-4.

Lin, Naiguo, P. J. Kellogg, R. J. MacDowall, A. Balogh, R. J. Forsyth, J. L. Phillips, A. Buttighoffer, and M. Pick (1995a). "Observations of Plasma Waves in Magnetic Holes". In: *Geophysical Research Letters* 22.23, pp. 3417–3420. ISSN: 19448007. DOI: 10.1029/95GL03266.

Lin, R P, K A Anderson, S Ashford, C Carlson, D Curtis, R Ergun, D Larson, J McFadden, M McCarthy, G K Parks, H Rème, J M Bosqued, J Coutelier, F Cotin, C D'Uston, K -P. Wenzel, T R Sanderson, J Henrion, J C Ronnet, and G Paschmann (1995b). "A Three-Dimensional Plasma and Energetic Particle Investigation for the Wind Spacecraft". In: *Space Science Reviews* 71.1, pp. 125–153. ISSN: 1572-9672. DOI: 10.1007/BF00751328.

Lin, R. P., R. A. Schwartz, S. R. Kane, R. M. Pelling, and K. C. Hurley (1984). "Solar Hard X-ray Microflares". In: *The Astrophysical Journal* 283, pp. 421–425. ISSN: 0004-637X. DOI: 10.1086/162321.

Liou, Kan and Chin-Chun Wu (2021). "Characteristics of the Heliospheric Current Sheets at the Sector Boundaries: Wind Observations from 1995–2020". In: *The Astrophysical Journal* 920.1, p. 39. ISSN: 0004-637X. DOI: 10.3847/1538-4357/ac1586.

Liu, Y., J. T. Hoeksema, P. H. Scherrer, J. Schou, S. Couvidat, R. I. Bush, T. L. Duvall, K. Hayashi, X. Sun, and X. Zhao (2012). "Comparison of Line-of-Sight Magnetograms Taken by the Solar Dynamics Observatory/Helioseismic and Magnetic Imager and Solar and Heliospheric Observatory/Michelson Doppler Imager". In: *Solar Physics* 279, pp. 295–316. ISSN: 0038-0938. DOI: 10.1007/s11207-012-9976-x.

Lopez, R. E., J. W. Freeman, and E. C. Roelof (1986). "The Relationship between Proton Temperature and Momentum Flux Density in the Solar Wind". In: *Geophysical Research Letters* 13, pp. 640–643. ISSN: 0094-8276. DOI: 10.1029/GL013i007p00640.

Mackay, Duncan and Anthony Yeates (2012). "The Sun's Global Photospheric and Coronal Magnetic Fields: Observations and Models". In: *Living Reviews in Solar Physics* 9.1, p. 6. ISSN: 1614-4961. DOI: 10.12942/lrsp-2012-6.

Macneil, Allan R, Mathew J Owens, Robert T Wicks, Mike Lockwood, Sarah N Bentley, and Matthew Lang (2020). "The Evolution of Inverted Magnetic Fields

through the Inner Heliosphere". In: *Monthly Notices of the Royal Astronomical Society* 494.3, pp. 3642–3655. ISSN: 0035-8711. DOI: 10.1093/mnras/staa951.

Madjarska, Maria S. (2019). "Coronal Bright Points". In: *Living Reviews in Solar Physics* 16.1, p. 2. ISSN: 1614-4961. DOI: 10.1007/s41116-019-0018-8.

Magyar, Norbert, Dominik Utz, Robertus Erdélyi, and Valery M Nakariakov (2021). *Could Switchbacks Originate in the Lower Solar Atmosphere? II. Propagation of Switchbacks in the Solar Corona*.

Mallet, Alfred, Jonathan Squire, Benjamin D G Chandran, Trevor Bowen, and Stuart D Bale (2021). *Evolution of Large-Amplitude Alfvén Waves and Generation of Switchbacks in the Expanding Solar Wind*. DOI: 10.3847/1538-4357/ac0c12.

Malyshkin, Leonid M. (2008). "Model of Hall Reconnection". In: *Physical Review Letters* 101.22, p. 225001. DOI: 10.1103/PhysRevLett.101.225001.

Marsch, E., K.-H. Mühlhäuser, H. Rosenbauer, R. Schwenn, and F. M. Neubauer (1982a). "Solar Wind Helium Ions: Observations of the Helios Solar Probes between 0.3 and 1 AU". In: *Journal of Geophysical Research* 87.A1, p. 35. ISSN: 0148-0227. DOI: 10.1029/JA087iA01p00035.

Marsch, E., K.-H. Mühlhäuser, R. Schwenn, H. Rosenbauer, W. Pilipp, and F. M. Neubauer (1982b). "Solar Wind Protons: Three-dimensional Velocity Distributions and Derived Plasma Parameters Measured between 0.3 and 1 AU". In: *Journal of Geophysical Research* 87.A1, p. 52. ISSN: 0148-0227. DOI: 10.1029/ja087ia01p00052.

Marsch, Eckart (2012). "Helios: Evolution of Distribution Functions 0.3–1 AU". In: *Space Science Reviews* 172.1, pp. 23–39. ISSN: 1572-9672. DOI: 10.1007/s11214-010-9734-z.

Matteini, L., T. S. Horbury, F. Pantellini, M. Velli, and S. J. Schwartz (2015). "Ion Kinetic Energy Conservation and Magnetic Field Strength Constancy in Multi-Fluid Solar Wind Alfvénic Turbulence". In: *Astrophysical Journal* 802.1, p. 11. ISSN: 15384357. DOI: 10.1088/0004-637X/802/1/11.

Matteini, L. et al. (2021). "Solar Orbiter's Encounter with the Tail of Comet C/2019 Y4 (ATLAS): Magnetic Field Draping and Cometary Pick-up Ion Waves". In: *Astronomy & Astrophysics* 656, A39. ISSN: 0004-6361, 1432-0746. DOI: 10.1051/0004-6361/202141229.

Matteini, Lorenzo, Timothy S. Horbury, Marcia Neugebauer, and Bruce E. Goldstein (2014). "Dependence of Solar Wind Speed on the Local Magnetic Field Orientation: Role of Alfvénic Fluctuations". In: *Geophysical Research Letters* 41.2, pp. 259–265. ISSN: 00948276. DOI: 10.1002/2013GL058482.

Matthaeus, W. H., H. A. Elliott, and D. J. McComas (2006). "Correlation of Speed and Temperature in the Solar Wind". In: *Journal of Geophysical Research: Space Physics* 111.A10. ISSN: 2156-2202. DOI: 10.1029/2006JA011636.

Matthaeus, W. H., G. P. Zank, S. Oughton, D. J. Mullan, and P. Dmitruk (1999). "Coronal Heating by Magnetohydrodynamic Turbulence Driven by Reflected Low-Frequency Waves". In: *The Astrophysical Journal* 523.1, pp. L93–L96. ISSN: 0004637X. DOI: 10.1086/312259.

McComas, D. J., S. J. Bame, B. L. Barraclough, W. C. Feldman, H. O. Funsten, J. T. Gosling, P. Riley, R. Skoug, A. Balogh, R. Forsyth, B. E. Goldstein, and M. Neugebauer (1998). "Ulysses' Return to the Slow Solar Wind". In: *Geophysical Research Letters* 25.1, pp. 1–4. ISSN: 00948276. DOI: 10.1029/97GL03444.

McComas, D. J., H. A. Elliott, N. A. Schwadron, J. T. Gosling, R. M. Skoug, and B. E. Goldstein (2003). "The Three-Dimensional Solar Wind around Solar Maximum". In: *Geophysical Research Letters* 30.10. ISSN: 00948276. DOI: 10.1029/2003GL017136.

McComas, D. J., M. Velli, W. S. Lewis, L. W. Acton, M. Balat-Pichelin, V. Bothmer, Jr B. Dirling, W. C. Feldman, G. Gloeckler, S. R. Habbal, D. M. Hassler, I. Mann, W. H. Matthaeus, Jr L. McNutt, R. A. Mewaldt, N. Murphy, L. Ofman, Jr C. Sittler, C. W. Smith, and T. H. Zurbuchen (2007). "Understanding Coronal Heating and Solar Wind Acceleration: Case for in Situ near-Sun

Measurements". In: *Reviews of Geophysics* 45.1, pp. 1–26. ISSN: 87551209. DOI: 10.1029/2006RG000195.

McComas, D. J. et al. (2016). "Integrated Science Investigation of the Sun (ISIS): Design of the Energetic Particle Investigation". In: *Space Science Reviews* 204.1, pp. 187–256. ISSN: 1572-9672. DOI: 10.1007/s11214-014-0059-1.

McIntosh, Scott W., Bart De Pontieu, Mats Carlsson, Viggo Hansteen, Paul Boerner, and Marcel Goossens (2011). "Alfvénic Waves with Sufficient Energy to Power the Quiet Solar Corona and Fast Solar Wind". In: *Nature* 475.7357, pp. 477–480. ISSN: 1476-4687. DOI: 10.1038/nature10235.

McManus, Michael D, Trevor A Bowen, Alfred Mallet, Christopher H K Chen, Benjamin D G Chandran, Stuart D Bale, Davin E Larson, Thierry Dudok De Wit, J C Kasper, Michael Stevens, Phyllis Whittlesey, Roberto Livi, Kelly E Korreck, Keith Goetz, Peter R Harvey, Marc Pulupa, Robert J Macdowall, David M Malaspina, Anthony W Case, and J W Bonnell (2020). "Cross Helicity Reversals in Magnetic Switchbacks". In: *The Astrophysical Journal Supplement Series* 246.2, p. 67. DOI: 10.3847/1538-4365/ab6dce.

McManus, Michael D., Jaye Verniero, Stuart D. Bale, Trevor A. Bowen, Davin E. Larson, Justin C. Kasper, Roberto Livi, Lorenzo Matteini, Ali Rahmati, Orlando Romeo, Phyllis Whittlesey, and Thomas Woolley (2022). "Density and Velocity Fluctuations of Alpha Particles in Magnetic Switchbacks". In: *The Astrophysical Journal* 933.1, p. 43. ISSN: 0004-637X. DOI: 10.3847/1538-4357/ac6ba3.

Meng, Ming-Ming, Ying D. Liu, Chong Chen, and Rui Wang (2022). "Analysis of the Distribution, Rotation and Scale Characteristics of Solar Wind Switchbacks: Comparison between the First and Second Encounters of Parker Solar Probe". In: *Research in Astronomy and Astrophysics* 22.3, p. 035018. ISSN: 1674-4527. DOI: 10.1088/1674-4527/ac49e4.

Meyer-Vernet, Nicole (2007). *Basics of the Solar Wind*. Cambridge Atmospheric and Space Science Series. Cambridge: Cambridge University Press. ISBN: 978-0-521-81420-1. DOI: 10.1017/CBO9780511535765.

Mikić, Zoran, Jon A. Linker, Dalton D. Schnack, Roberto Lionello, and Alfonso Tarditi (1999). "Magnetohydrodynamic Modeling of the Global Solar Corona". In: *Physics of Plasmas* 6.5, pp. 2217–2224. ISSN: 1070-664X. DOI: 10.1063/1.873474.

Miles, David, Ian Mann, Andy Kale, David Milling, Barry Narod, John Bennest, David Barona, and Martyn Unsworth (2017). "The Effect of Construction Material on the Thermal Gain Dependence of a Fluxgate Magnetometer Sensor". In: *Geoscientific Instrumentation, Methods and Data Systems Discussions*, pp. 1–34. DOI: 10.5194/gi-2017-32.

Miralles, M.P., S.R. Cranmer, and J.L. Kohl (2004). "Low-Latitude Coronal Holes during Solar Maximum". In: *Advances in Space Research* 33.5, pp. 696–700. ISSN: 0273-1177. DOI: 10.1016/S0273-1177(03)00239-4.

Moore, Ronald L., Jonathan W. Cirtain, Alphonse C. Sterling, and David A. Falconer (2010). "DICHOTOMY OF SOLAR CORONAL JETS: STANDARD JETS AND BLOWOUT JETS". In: *The Astrophysical Journal* 720.1, p. 757. ISSN: 0004-637X. DOI: 10.1088/0004-637X/720/1/757.

Mozer, F. S., S. D. Bale, J. W. Bonnell, J. F. Drake, E. L. M. Hanson, and M. C. Mozer (2021). "On the Origin of Switchbacks Observed in the Solar Wind". In: *The Astrophysical Journal* 919.1, p. 60. ISSN: 0004-637X. DOI: 10.3847/1538-4357/ac110d.

Mozer, F. S. et al. (2020). "Switchbacks in the Solar Magnetic Field: Their Evolution, Their Content, and Their Effects on the Plasma". In: *The Astrophysical Journal Supplement Series* 246.2, p. 68. ISSN: 0067-0049. DOI: 10.3847/1538-4365/ab7196.

Muller, R. and Th. Roudier (1992). "Formation of Network Bright Points by Granule Compression". In: *Solar Physics* 141.1, pp. 27–33. ISSN: 1573-093X. DOI: 10.1007/BF00155901.

Müller, D., R. G. Marsden, O. C. St. Cyr, and H. R. Gilbert (2013). "Solar Orbiter: Exploring the Sun-Heliosphere Connection". In: *Solar Physics* 285.1-2, pp. 25–70. DOI: 10.1007/s11207-012-0085-7.

Müller, D. et al. (2020). "The Solar Orbiter Mission - Science Overview". In: *Astronomy & Astrophysics* 642, A1. ISSN: 0004-6361, 1432-0746. DOI: 10.1051/0004-6361/202038467.

Nakagawa, T., A. Nishida, and T. Saito (1989). "Planar Magnetic Structures in the Solar Wind". In: *Journal of Geophysical Research* 94.A9, p. 11761. ISSN: 0148-0227. DOI: 10.1029/JA094iA09p11761.

Nandy, Dibyendu (2021). "Progress in Solar Cycle Predictions: Sunspot Cycles 24–25 in Perspective". In: *Solar Physics* 296.3, p. 54. ISSN: 1573-093X. DOI: 10.1007/s11207-021-01797-2.

Narita, Yasuhito (2017). "Review Article: Wave Analysis Methods for Space Plasma Experiment". In: *Nonlinear Processes in Geophysics* 24.2, pp. 203–214. ISSN: 1023-5809. DOI: 10.5194/npg-24-203-2017.

NASA (2023). *WIND SPACECRAFT*. https://wind.nasa.gov/.

NASA, NASA's Goddard Space Flight Center, Miles Hatfield, Lina Tran, and Mary-Pat Hrybyk Keith (2021). *Switchbacks Science: Explaining Parker Solar Probe's Magnetic Puzzle*. http://www.nasa.gov/feature/goddard/2021/switchbacks-science-explaining-parker-solar-probe-s-magnetic-puzzle.

Ness, N. F. (1970). "Magnetometers for Space Research". In: *Space Science Reviews* 11.4, pp. 459–554. DOI: 10.1007/BF00183028.

Neugebauer, M., B. E. Goldstein, D. J. McComas, S. T. Suess, and A. Balogh (1995). "Ulysses Observations of Microstreams in the Solar Wind from Coronal Holes". In: *Journal of Geophysical Research: Space Physics* 100.A12, pp. 23389–23395. ISSN: 2156-2202. DOI: 10.1029/95JA02723.

Neugebauer, M., P. C. Liewer, E. J Smith, R. M. Skoug, and T. H. Zurbuchen (2002). "Sources of the Solar Wind at Solar Activity Maximum". In: *Journal*

of Geophysical Research: Space Physics 107.A12, SSH 13–1–SSH 13–15. ISSN: 01480227. DOI: 10.1029/2001JA000306.

Neugebauer, M., J. T. Steinberg, R. L. Tokar, B. L. Barraclough, E. E. Dors, R. C. Wiens, D. E. Gingerich, D. Luckey, and D. B. Whiteaker (2003). "Genesis On-Board Determination of the Solar Wind Flow Regime". In: *Space Science Reviews* 105, pp. 661–679. ISSN: 0038-6308. DOI: 10.1023/A:1024478129261.

Neugebauer, Marcia (2012). "EVIDENCE FOR POLAR X-RAY JETS AS SOURCES OF MICROSTREAM PEAKS IN THE SOLAR WIND". In: *The Astrophysical Journal* 750.1, p. 50. ISSN: 0004-637X. DOI: 10.1088/0004-637X/750/1/50.

Neugebauer, Marcia and Bruce E. Goldstein (2013). "Double-Proton Beams and Magnetic Switchbacks in the Solar Wind". In: *AIP Conference Proceedings*. Vol. 1539. American Institute of PhysicsAIP, pp. 46–49. DOI: 10.1063/1.4810986.

Neugebauer, Marcia and Conway W. Snyder (1966). "Mariner 2 Observations of the Solar Wind: 1. Average Properties". In: *Journal of Geophysical Research* 71.19, pp. 4469–4484. ISSN: 01480227. DOI: 10.1029/JZ071i019p04469.

Neugebauer, Marcia and Alphonse C. Sterling (2021). "Relation of Microstreams in the Polar Solar Wind to Switchbacks and Coronal X-Ray Jets". In: *The Astrophysical Journal Letters* 920.2, p. L31. ISSN: 2041-8205. DOI: 10.3847/2041-8213/ac2945.

Nieves-Chinchilla, Teresa et al. (2020). "Analysis of the Internal Structure of the Streamer Blowout Observed by the Parker Solar Probe During the First Solar Encounter". In: *The Astrophysical Journal Supplement Series* 246.2, p. 63. ISSN: 0067-0049. DOI: 10.3847/1538-4365/ab61f5.

Nikolić, L (2019). "On Solutions of the PFSS Model With GONG Synoptic Maps for 2006–2018". In: *Space Weather* 17.8, pp. 1293–1311. DOI: 10.1029/2019SW002205.

Nolte, J. T., A. S. Krieger, A. F. Timothy, R. E. Gold, E. C. Roelof, G. Vaiana, A. J. Lazarus, J. D. Sullivan, and P. S. McIntosh (1976). "Coronal Holes as Sources of Solar Wind". In: *Solar Physics* 46.2, pp. 303–322. ISSN: 00380938. DOI: 10.1007/BF00149859.

Nordlund, Åke, Robert F. Stein, and Martin Asplund (2009). "Solar Surface Convection". In: *Living Reviews in Solar Physics* 6.1, p. 2. ISSN: 1614-4961. DOI: 10.12942/lrsp-2009-2.

Norton, A. A., J. Pietarila Graham, R. K. Ulrich, J. Schou, S. Tomczyk, Y. Liu, B. W. Lites, A. López Ariste, R. I. Bush, H. Socas-Navarro, and P. H. Scherrer (2006). "Spectral Line Selection for HMI: A Comparison of Fe I 6173 Å and Ni I 6768 Å". In: *Solar Physics* 239.1, pp. 69–91. ISSN: 1573-093X. DOI: 10.1007/s11207-006-0279-y.

Nuttall, Albert H. (1981). "Some Windows With Very Good Side-lobe Behavior". In: DOI: 10.1109/tassp.1981.1163506.

Odstrcil, D. (2003). "Modeling 3-D Solar Wind Structure". In: *Advances in Space Research*. Heliosphere at Solar Maximum 32.4, pp. 497–506. ISSN: 0273-1177. DOI: 10.1016/S0273-1177(03)00332-6.

Ogilvie, K W, D J Chornay, R J Fritzenreiter, F Hunsaker, J Keller, J Lobell, G Miller, J D Scudder, E C Sittler, R B Torbert, D Bodet, G Needell, A J Lazarus, J T Steinberg, J H Tappan, A Mavretic, and E Gergin (1995). "SWE, a Comprehensive Plasma Instrument for the WIND Spacecraft". In: *Space Science Reviews* 71.1, pp. 55–77. ISSN: 1572-9672. DOI: 10.1007/BF00751326.

Ogilvie, K W and M D Desch (1997). "The WIND Spacecraft and Its Early Scientific Results". In: *Advances in Space Research* 20.4, pp. 559–568. ISSN: 0273-1177. DOI: 10.1016/S0273-1177(97)00439-0.

Owen, C. J. et al. (2020). "The Solar Orbiter Solar Wind Analyser (SWA) Suite". In: *A&A* 642, A16. DOI: 10.1051/0004-6361/201937259.

Owens, M J, N U Crooker, and M Lockwood (2013). "Solar Origin of Heliospheric Magnetic Field Inversions: Evidence for Coronal Loop Opening within Pseudostreamers". In: *Journal of Geophysical Research: Space Physics* 118.5, pp. 1868–1879. DOI: 10.1002/jgra.50259.

Owens, M. J., M. Lockwood, and L. A. Barnard (2020a). "The Value of CME Arrival Time Forecasts for Space Weather Mitigation". In: *Space Weather* 18.9, e2020SW002507. ISSN: 1542-7390. DOI: 10.1029/2020SW002507.

Owens, M. J., H. E. Spence, S. McGregor, W. J. Hughes, J. M. Quinn, C. N. Arge, P. Riley, J. Linker, and D. Odstrcil (2008). "Metrics for Solar Wind Prediction Models: Comparison of Empirical, Hybrid, and Physics-Based Schemes with 8 Years of L1 Observations". In: *Space Weather* 6. ISSN: 15427390. DOI: 10.1029/2007SW000380.

Owens, Mathew J., Matthew Lang, Pete Riley, Mike Lockwood, and Amos S. Lawless (2020b). "Quantifying the Latitudinal Representivity of in Situ Solar Wind Observations". In: *Journal of Space Weather and Space Climate* 10, p. 8. ISSN: 2115-7251. DOI: 10.1051/SWSC/2020009.

Owocki, S. P., T. E. Holzer, and A. J. Hundhausen (1983). "The Solar Wind Ionization State as a Coronal Temperature Diagnostic". In: *The Astrophysical Journal* 275, pp. 354–366. ISSN: 0004-637X. DOI: 10.1086/161538.

Palmerio, Erika, Emilia K. J. Kilpua, and Neel P. Savani (2016). "Planar Magnetic Structures in Coronal Mass Ejection-Driven Sheath Regions". In: *Annales Geophysicae* 34.2, pp. 313–322. ISSN: 0992-7689. DOI: 10.5194/angeo-34-313-2016.

Panasenco, Olga et al. (2020). "Exploring Solar Wind Origins and Connecting Plasma Flows from the *Parker Solar Probe* to 1 Au: Nonspherical Source Surface and Alfvénic Fluctuations". In: *The Astrophysical Journal Supplement Series* 246.2, p. 54. ISSN: 1538-4365. DOI: 10.3847/1538-4365/ab61f4.

Parker, E. N. (1957). "Sweet's Mechanism for Merging Magnetic Fields in Conducting Fluids". In: *Journal of Geophysical Research* 62.4, pp. 509–520. DOI: 10.1029/jz062i004p00509.

— (1958a). "Cosmic-Ray Modulation by Solar Wind". In: *Physical Review* 110.6, pp. 1445–1449. ISSN: 0031-899X. DOI: 10.1103/PhysRev.110.1445.

— (1958b). "Dynamics of the Interplanetary Gas and Magnetic Fields". In: *The Astrophysical Journal* 128, p. 664. DOI: 10.1086/146579.

Parker, E. N. (1965). "Dynamical Theory of the Solar Wind". In: *Space Science Reviews* 4.5-6, pp. 666–708. DOI: 10.1007/BF00216273.

— (1988). "Nanoflares and the Solar X-ray Corona". In: *The Astrophysical Journal* 330, pp. 474–479. DOI: 10.1086/166485.

Parnell, C.E. (2001). "A Model of the Solar Magnetic Carpet". In: *Solar Physics* 200.1, pp. 23–45. ISSN: 1573-093X. DOI: 10.1023/A:1010312014999.

Parnell, Clare E. and Ineke De Moortel (2012). "A Contemporary View of Coronal Heating". In: *Philosophical Transactions of the Royal Society A: Mathematical, Physical and Engineering Sciences* 370.1970, pp. 3217–3240. ISSN: 1364503X. DOI: 10.1098/rsta.2012.0113.

Paschmann, Götz, Patrick W Daly, O Sonnerup, and Maureen Scheible (1998). "Reprinted from Analysis Methods for Multi-Spacecraft Data Minimum and Maximum Variance Analysis". In: http://www.issibern.ch/forads/sr-001-08.pdf.

Peng, Jun, Yong C.-M. Liu, Jia Huang, Hui Li, Berndt Klecker, Antoinette B Galvin, Kristin Simunac, Charles Farrugia, L K Jian, Yang Liu, and Jie Zhang (2017). "In Situ Analysis of Heliospheric Current Sheet Propagation". In: *Journal of Geophysical Research: Space Physics* 122.10, pp. 9803–9814. DOI: 10.1002/2017JA024194.

Perez, Jean C., Sofiane Bourouaine, Christopher H. K. Chen, and Nour E. Raouafi (2021). "Applicability of Taylor's Hypothesis during Parker Solar Probe Perihelia". In: *Astronomy & Astrophysics* 650, A22. ISSN: 0004-6361, 1432-0746. DOI: 10.1051/0004-6361/202039879.

Perrone, D. et al. (2022). "Evolution of Coronal Hole Solar Wind in the Inner Heliosphere: Combined Observations by Solar Orbiter and Parker Solar Probe". In: *Astronomy & Astrophysics* 668, A189. ISSN: 0004-6361, 1432-0746. DOI: 10.1051/0004-6361/202243989.

Perrone, Denise, D Stansby, T S Horbury, and L Matteini (2019). "Thermodynamics of Pure Fast Solar Wind: Radial Evolution of the Temperature–Speed Relation-

ship in the Inner Heliosphere". In: *Monthly Notices of the Royal Astronomical Society* 488.2, pp. 2380–2386. ISSN: 0035-8711. DOI: 10.1093/mnras/stz1877.

Petschek, H. E. (1964). "Magnetic Field Annihilation". In: *The Physics of Solar Flares*. Ed. by Wilmot N Hess. Vol. 50. http://adsabs.harvard.edu/full/1964NASSP..50..425P. Washington DC, p. 425.

Pilipp, W G, H Miggenrieder, K Muehlhaueser, H Rosenbauer, R Schwenn, and F M Neubauer (1987). "Variations of Electron Distribution Functions in the Solar Wind". In: *Journal of Geophysical Research* 92.A2, pp. 1103–1118. DOI: 10.1029/JA092iA02p01103.

Pizzo, V. (1978). "A Three-Dimensional Model of Corotating Streams in the Solar Wind, 1. Theoretical Foundations". In: *Journal of Geophysical Research: Space Physics* 83.A12, pp. 5563–5572. ISSN: 2156-2202. DOI: 10.1029/JA083iA12p05563.

Pizzo, V. J. (1991). "The Evolution of Corotating Stream Fronts near the Ecliptic Plane in the Inner Solar System: 2. Three-dimensional Tilted-Dipole Fronts". In: *Journal of Geophysical Research: Space Physics* 96.A4, pp. 5405–5420. DOI: 10.1029/91JA00155.

— (1994a). "Global, Quasi-Steady Dynamics of the Distant Solar Wind, 1. Origin of North-South Flows in the Outer Heliosphere". In: *Journal of Geophysical Research: Space Physics* 99.3, pp. 4173–4183. ISSN: 21699402. DOI: 10.1029/93JA03239.

— (1994b). "Global, Quasi-Steady Dynamics of the Distant Solar Wind: 2. Deformation of the Heliospheric Current Sheet". In: *Journal of Geophysical Research* 99.A3, p. 4185. ISSN: 0148-0227. DOI: 10.1029/93JA03474.

Poedts, Stefaan and Jens Pomoell (2017). "EUHFORIA: A Solar Wind and CME Evolution Model". In: https://ui.adsabs.harvard.edu/abs/2017EGUGA..19.7396P, p. 7396.

Pokhotelov, D., S. von Alfthan, Y. Kempf, R. Vainio, H. E. J. Koskinen, and M. Palmroth (2013). "Ion Distributions Upstream and Downstream of the Earth's

Bow Shock: First Results from Vlasiator". In: *Annales Geophysicae* 31.12, pp. 2207–2212. ISSN: 0992-7689. DOI: 10.5194/angeo-31-2207-2013.

Poletto, Giannina (2015). "Solar Coronal Plumes". In: *Living Rev. Solar Phys* 12, p. 7. DOI: 10.1007/lrsp-2015-7.

Priest, E. R. (1998). "Heating the Solar Corona by Magnetic Reconnection". In: *Astrophysics and Space Science* 264.1-4, pp. 77–100. ISSN: 0004640X. DOI: 10.1023/A:1002440524834.

Priest, E. R. and T. G. Forbes (1986). "New Models for Fast Steady State Magnetic Reconnection". In: *Journal of Geophysical Research: Space Physics* 91.A5, pp. 5579–5588. ISSN: 2156-2202. DOI: 10.1029/JA091iA05p05579.

Priest, Eric and Terry Forbes (2007). *Magnetic Reconnection: MHD Theory and Applications*. Cambridge University Press. ISBN: 978-0-521-03394-7.

Raouafi, N E, · S Patsourakos, · E Pariat, · P R Young, · A C Sterling, and B N E Raouafi (2016). "Solar Coronal Jets: Observations, Theory, and Modeling". In: *Space Sci Rev* 201, pp. 1–53. DOI: 10.1007/s11214-016-0260-5.

Raouafi, N. E. et al. (2023a). "Parker Solar Probe: Four Years of Discoveries at Solar Cycle Minimum". In: *Space Science Reviews* 219.1, p. 8. ISSN: 1572-9672. DOI: 10.1007/s11214-023-00952-4.

Raouafi, N.-E., G. J. D. Petrie, A. A. Norton, C. J. Henney, and S. K. Solanki (2008). "Evidence for Polar Jets as Precursors of Polar Plume Formation". In: *The Astrophysical Journal* 682.2, pp. L137–L140. ISSN: 0004-637X. DOI: 10.1086/591125.

Raouafi, N.-E. and G. Stenborg (2014). "ROLE OF TRANSIENTS IN THE SUSTAINABILITY OF SOLAR CORONAL PLUMES". In: *The Astrophysical Journal* 787.2, p. 118. ISSN: 0004-637X. DOI: 10.1088/0004-637X/787/2/118.

Raouafi, Nour E., G. Stenborg, D. B. Seaton, H. Wang, J. Wang, C. E. DeForest, S. D. Bale, J. F. Drake, V. M. Uritsky, J. T. Karpen, C. R. DeVore, A. C. Sterling, T. S. Horbury, L. K. Harra, S. Bourouaine, J. C. Kasper, P. Kumar, T. D. Phan, and M. Velli (2023b). "Magnetic Reconnection as the Driver of the

Solar Wind". In: *The Astrophysical Journal* 945.1, p. 28. ISSN: 0004-637X. DOI: 10.3847/1538-4357/acaf6c.

Rast, Mark Peter (2003). "The Scales of Granulation, Mesogranulation, and Supergranulation". In: *The Astrophysical Journal* 597.2, pp. 1200–1210. ISSN: 0004-637X. DOI: 10.1086/381221.

Réville, V. et al. (2022). "Flux Rope and Dynamics of the Heliospheric Current Sheet: Study of the Parker Solar Probe and Solar Orbiter Conjunction of June 2020". In: *Astronomy & Astrophysics* 659, A110. ISSN: 0004-6361, 1432-0746. DOI: 10.1051/0004-6361/202142381.

Réville, Victor, Marco Velli, Alexis P. Rouillard, Benoit Lavraud, Anna Tenerani, Chen Shi, and Antoine Strugarek (2020). "Tearing Instability and Periodic Density Perturbations in the Slow Solar Wind". In: *The Astrophysical Journal* 895.1, p. L20. ISSN: 20418213. DOI: 10.3847/2041-8213/ab911d.

Richardson, I. G. and H. V. Cane (2010). "Near-Earth Interplanetary Coronal Mass Ejections During Solar Cycle 23 (1996 – 2009): Catalog and Summary of Properties". In: *Solar Physics* 264.1, pp. 189–237. ISSN: 0038-0938. DOI: 10.1007/s11207-010-9568-6.

Richardson, I. G., E. W. Cliver, and H. V. Cane (2001). "Sources of Geomagnetic Storms for Solar Minimum and Maximum Conditions during 1972–2000". In: *Geophysical Research Letters* 28.13, pp. 2569–2572. ISSN: 0094-8276. DOI: 10.1029/2001GL013052.

Richardson, Ian G. (2018). "Solar Wind Stream Interaction Regions throughout the Heliosphere". In: *Living Reviews in Solar Physics* 15.1, pp. 1–95. ISSN: 16144961. DOI: 10.1007/s41116-017-0011-z.

Richardson, John D and Karolen I Paularena (1997). "Streamer Belt Structure at Solar Minima". In: *Geophysical Research Letters* 24.11, pp. 1435–1438. DOI: 10.1029/97GL01251.

Rieutord, Michel and François Rincon (2010). "The Sun's Supergranulation". In: *Living Reviews in Solar Physics* 7.1, p. 2. ISSN: 1614-4961. DOI: 10.12942/lrsp-2010-2.

Riley, P. and R. Lionello (2011). "Mapping Solar Wind Streams from the Sun to 1 AU: A Comparison of Techniques". In: *Solar Physics* 270.2, pp. 575–592. ISSN: 1573-093X. DOI: 10.1007/s11207-011-9766-x.

Riley, Pete (1996). "Properties of Arc-Polarized Alfvén Waves in the Ecliptic Plane: Ulysses Observations". In: *Journal of Geophysical Research: Space Physics* 101.A9, pp. 19987–19993. ISSN: 2156-2202. DOI: 10.1029/96JA01743.

Riley, Pete, J. A. Linker, and Z. Mikić (2002). "Modeling the Heliospheric Current Sheet: Solar Cycle Variations". In: *Journal of Geophysical Research: Space Physics* 107.A7, pp. 1–7. ISSN: 21699402. DOI: 10.1029/2001JA000299.

Riley, Pete, J. A. Linker, Z. Mikić, R. Lionello, S. A. Ledvina, and J. G. Luhmann (2006). "A Comparison between Global Solar Magnetohydrodynamic and Potential Field Source Surface Model Results". In: *The Astrophysical Journal* 653.2, pp. 1510–1516. ISSN: 0004-637X. DOI: 10.1086/508565.

Riley, Pete, Jon A. Linker, and C. Nick Arge (2015). "On the Role Played by Magnetic Expansion Factor in the Prediction of Solar Wind Speed". In: *Space Weather* 13.3, pp. 154–169. ISSN: 15427390. DOI: 10.1002/2014SW001144.

Rimmele, Thomas R. et al. (2020). "The Daniel K. Inouye Solar Telescope – Observatory Overview". In: *Solar Physics* 295.12, p. 172. ISSN: 1573-093X. DOI: 10.1007/s11207-020-01736-7.

Roberts, D. Aaron (2010). "DEMONSTRATIONS THAT THE SOLAR WIND IS NOT ACCELERATED BY WAVES OR TURBULENCE". In: *The Astrophysical Journal* 711.2, p. 1044. ISSN: 0004-637X. DOI: 10.1088/0004-637X/711/2/1044.

Rosenbauer, H, R Schwenn, E Marsch, B Meyer, H Miggenrieder, M. D. Montgomery, K. H. Muehlhaeuser, W Pilipp, W Voges, and S. M. Zink (1977). "A Survey on Initial Results of the HELIOS Plasma Experiment". In: *Journal of Geophysics*

Zeitschrift Geophysik 42.6. https://ntrs.nasa.gov/citations/19780026418, pp. 561–580.

Rosenberg, Ronald L. and Paul J. Coleman (1969). "Heliographic Latitude Dependence of the Dominant Polarity of the Interplanetary Magnetic Field". In: *Journal of Geophysical Research* 74.24, pp. 5611–5622. ISSN: 01480227. DOI: 10.1029/JA074i024p05611.

Rosenthal, C S, T J Bogdan, M Carlsson, S B F Dorch, V Hansteen, S W Mcintosh, A Mcmurry, Stein5, R. F, and A Nordlund (2002). "WAVES IN THE MAGNETIZED SOLAR ATMOSPHERE. I. BASIC PROCESSES AND INTERNETWORK OSCILLATIONS". In: *THE ASTROPHYSICAL JOURNAL* 564, pp. 508–524. DOI: 10.1086/324214.

Roudier, Th. and R. Muller (1986). "Structure of the Solar Granulation." In: *Solar Physics* 107, pp. 11–26. ISSN: 0038-0938. DOI: 10.1007/BF00155337.

Rouillard, A. P., J. A. Davies, B. Lavraud, R. J. Forsyth, N. P. Savani, D. Bewsher, D. S. Brown, N. R. Sheeley, C. J. Davis, R. A. Harrison, R. A. Howard, A. Vourlidas, M. Lockwood, S. R. Crothers, and C. J. Eyles (2010). "Intermittent Release of Transients in the Slow Solar Wind: 1. Remote Sensing Observations". In: *Journal of Geophysical Research: Space Physics* 115.A4103. ISSN: 01480227. DOI: 10.1029/2009JA014471.

Rouillard, Alexis P et al. (2020). "Relating Streamer Flows to Density and Magnetic Structures at the Parker Solar Probe". In: *The Astrophysical Journal Supplement Series* 246.2. DOI: 10.3847/1538-4365/ab579a.

Ruffolo, D, W H Matthaeus, R Chhiber, A V Usmanov, Y Yang, R Bandyopadhyay, T N Parashar, M L Goldstein, C E DeForest, and M Wan (2020). "Shear-Driven Transition to Isotropically Turbulent Solar Wind Outside the Alfvén Critical Zone". In: *The Astrophysical Journal* 902.2, p. 94. ISSN: 1538-4357. DOI: 10.3847/1538-4357/abb594.

Saito, K. (1958). "Polar Rays of the Solar Corona". In: *Publications of the Astronomical Society of Japan* 10. https://ui.adsabs.harvard.edu/abs/1958PASJ...10...49S, p. 49. ISSN: 0004-6264.

Salem, Chadi S., Marc Pulupa, Stuart D. Bale, and Daniel Verscharen (2021). *Precision Electron Measurements in the Solar Wind at 1 Au from NASA's Wind Spacecraft*. DOI: 10.48550/arXiv.2107.08125.

Samson, J. C. and K. L. Yeung (1986). "Some Generalizations on the Method of Superposed Epoch Analysis". In: *Planetary and Space Science* 34.11, pp. 1133–1142. ISSN: 0032-0633. DOI: 10.1016/0032-0633(86)90025-5.

Sanchez-Diaz, E, A P Rouillard, B Lavraud, E Kilpua, and J A Davies (2019). "In Situ Measurements of the Variable Slow Solar Wind near Sector Boundaries". In: *The Astrophysical Journal* 882.1, p. 51. ISSN: 1538-4357. DOI: 10.3847/1538-4357/ab341c.

Sanchez-Diaz, E., A. P. Rouillard, J. A. Davies, B. Lavraud, R. F. Pinto, and E. Kilpua (2017). "The Temporal and Spatial Scales of Density Structures Released in the Slow Solar Wind During Solar Activity Maximum". In: *The Astrophysical Journal* 851.1, p. 32. ISSN: 1538-4357. DOI: 10.3847/1538-4357/aa98e2.

Savcheva, Antonia, Jonathan Cirtain, Edward E. DeLuca, Loraine L. Lundquist, Leon Golub, Mark Weber, Masumi Shimojo, Kiyoto Shibasaki, Taro Sakao, Noriyuki Narukage, Saku Tsuneta, and Ryouhei Kano (2007). "A Study of Polar Jet Parameters Based on Hinode XRT Observations". In: *Publications of the Astronomical Society of Japan* 59.sp3, S771–S778. ISSN: 0004-6264. DOI: 10.1093/pasj/59.sp3.S771.

Schatten, Kenneth H., John M. Wilcox, and Norman F. Ness (1969). "A Model of Interplanetary and Coronal Magnetic Fields". In: *Solar Physics* 6.3, pp. 442–455. ISSN: 0038-0938. DOI: 10.1007/BF00146478.

Schwabe, Heinrich (1844). "Sonnen — Beobachtungen Im Jahre 1843". In: *Astronomische Nachrichten* 21.15, pp. 233–235. DOI: 10.1002/asna.18440211505.

Schwadron, N A and D J McComas (2021). "Switchbacks Explained: Super-Parker Fields—The Other Side of the Sub-Parker Spiral". In: *The Astrophysical Journal* 909.1, p. 95. ISSN: 0004-637X. DOI: 10.3847/1538-4357/abd4e6.

Schwenn, R, M D Montgomery, H Rosenbauer, H Miggenrieder, K H Mühlhäuser, S J Bame, W C Feldman, and R T Hansen (1978). "Direct Observation of the Latitudinal Extent of a High-Speed Stream in the Solar Wind". In: *Journal of Geophysical Research: Space Physics* 83.A3, pp. 1011–1017. DOI: 10.1029/JA083iA03p01011.

Schwenn, R. (1983). "The Average Solar Wind in the Inner Heliosphere: Structures and Slow Variations". In: *JPL Solar Wind Five*. https://ntrs.nasa.gov/archive/nasa/casi.ntrs.nasa.gov/19840005037.pdf, pp. 489–507.

Schwenn, Rainer (1990). "Large-Scale Structure of the Interplanetary Medium". In: *Physics of the Inner Heliosphere I: Large-Scale Phenomena*. Ed. by Rainer Schwenn and Eckart Marsch. Berlin, Heidelberg: Springer Berlin Heidelberg, pp. 99–181. ISBN: 978-3-642-75361-9. DOI: 10.1007/978-3-642-75361-9_3.

Schwenn, Rainer and Eckart Marsch, eds. (1990). *Physics of the Inner Heliosphere I*. Berlin, Heidelberg: Springer Berlin Heidelberg. ISBN: 978-3-642-75363-3. DOI: 10.1007/978-3-642-75361-9.

Shibata, Kazunari, Yoshinori Ishido, Loren W. Acton, Keith T. Strong, Tadashi Hirayama, Yutaka Uchida, Alan H. McAllister, Ryoji Matsumoto, Saku Tsuneta, Toshifumi Shimizu, Hirohisa Hara, Takashi Sakurai, Kiyoshi Ichimoto, Yohei Nishino, and Yoshiaki Ogawara (1992). "Observations of X-Ray Jets with the YOHKOH Soft X-Ray Telescope". In: *Publications of the Astronomical Society of Japan* 44. https://ui.adsabs.harvard.edu/abs/1992PASJ...44L.173S, pp. L173–L179. ISSN: 0004-6264.

Shimojo, Masumi, Shizuyo Hashimoto, Kazunari Shibata, Tadashi Hirayama, Hugh S. Hudson, and Loren W. Acton (1996). "Statistical Study of Solar X-Ray Jets Observed with the YOHKOH Soft X-Ray Telescope". In: *Publications of the*

Astronomical Society of Japan 48, pp. 123–136. ISSN: 0004-6264. DOI: 10.1093/pasj/48.1.123.

Shoda, Munehito, Benjamin D G Chandran, and Steven R Cranmer (2021). "Turbulent Generation of Magnetic Switchbacks in the Alfvénic Solar Wind". In: *The Astrophysical Journal* 915.1, p. 52. ISSN: 0004-637X. DOI: 10.3847/1538-4357/abfdbc.

Simon, G. W. and R. B. Leighton (1964). "Velocity Fields in the Solar Atmosphere. III. Large-Scale Motions, the Chromospheric Network, and Magnetic Fields." In: *The Astrophysical Journal* 140, p. 1120. ISSN: 0004-637X. DOI: 10.1086/148010.

Siscoe, G L and L T Finley (1969). "Meridional (North-South) Motions of the Solar Wind". In: *Solar Physics* 9.2, pp. 452–466. ISSN: 1573-093X. DOI: 10.1007/BF02391671.

Siscoe, G. L., B Goldstein, and A. J. Lazarus (1969). "East-West Asymmetry in the Solar Wind Velocity". In: *Journal of Geophysical Research: Space Physics* 74.7. DOI: http://dx.doi.org/10.1029/JA074i007p0175.

Smith, E. J., A. Balogh, M. Neugebauer, and D. McComas (1995). "Ulysses Observations of Alfvén Waves in the Southern and Northern Solar Hemispheres". In: *Geophysical Research Letters* 22, pp. 3381–3384. ISSN: 0094-8276. DOI: 10.1029/95GL03268.

Smith, Edward J and John H Wolfe (1976). "Observations of Interaction Regions and Corotating Shocks between One and Five AU: Pioneers 10 and 11". In: *Geophysical Research Letters* 3.3, pp. 137–140. DOI: 10.1029/GL003i003p00137.

Solanki, Sami K., Bernd Inhester, and Manfred Schüssler (2006). "The Solar Magnetic Field". In: *Reports on Progress in Physics* 69.3, p. 563. ISSN: 0034-4885. DOI: 10.1088/0034-4885/69/3/R02.

Sonnerup, B. U. Ö., G. Paschmann, I. Papamastorakis, N. Sckopke, G. Haerendel, S. J. Bame, J. R. Asbridge, J. T. Gosling, and C. T. Russell (1981). "Evidence for Magnetic Field Reconnection at the Earth's Magnetopause". In: *Jour-*

nal of Geophysical Research 86.A12, p. 10049. ISSN: 0148-0227. DOI: 10.1029/ja086ia12p10049.

Squire, J, B D G Chandran, and R Meyrand (2020). "In-Situ Switchback Formation in the Expanding Solar Wind". In: *The Astrophysical Journal* 891.1, p. L2. ISSN: 2041-8213. DOI: 10.3847/2041-8213/ab74e1.

Squire, Jonathan, Zade Johnston, Alfred Mallet, and Romain Meyrand (2022a). "On the Properties of Alfvénic Switchbacks in the Expanding Solar Wind: The Influence of the Parker Spiral". In: *Physics of Plasmas* 29.11, p. 112903. ISSN: 1070-664X. DOI: 10.1063/5.0099924.

Squire, Jonathan, Romain Meyrand, Matthew W. Kunz, Lev Arzamasskiy, Alexander A. Schekochihin, and Eliot Quataert (2022b). "High-Frequency Heating of the Solar Wind Triggered by Low-Frequency Turbulence". In: *Nature Astronomy*, pp. 1–9. ISSN: 2397-3366. DOI: 10.1038/s41550-022-01624-z.

Stansby, D, L Matteini, T S Horbury, D Perrone, R D'Amicis, and L Berčič (2020a). "The Origin of Slow Alfvénic Solar Wind at Solar Minimum". In: *Monthly Notices of the Royal Astronomical Society* 492.1, pp. 39–44. ISSN: 0035-8711. DOI: 10.1093/mnras/stz3422.

Stansby, D., T. S. Horbury, and L. Matteini (2019a). "Diagnosing Solar Wind Origins Using In-Situ Measurements in the Inner Heliosphere". In: *Monthly Notices of the Royal Astronomical Society* 482.2, pp. 1706–1714. DOI: 10.1093/mnras/sty2814.

Stansby, D., C. S. Salem, L. Matteini, and T. S. Horbury (2018). "A New Inner Heliosphere Proton Parameter Data Set from the Helios Mission". http://arxiv.org/abs/1807.04376.

Stansby, David, Lucie M. Green, Lidia van Driel-Gesztelyi, and Timothy S. Horbury (2021). "Active Region Contributions to the Solar Wind over Multiple Solar Cycles". In: *Solar Physics* 296.8, p. 116. ISSN: 1573-093X. DOI: 10.1007/s11207-021-01861-x.

Stansby, David, Timothy S. Horbury, Samantha Wallace, and C. Nick Arge (2019b). "Predicting Large-scale Coronal Structure for Parker Solar Probe Using Open Source Software". In: *Research Notes of the AAS* 3.3, p. 57. ISSN: 2515-5172. DOI: 10.3847/2515-5172/AB13B7.

Stansby, David, Anthony Yeates, and Samuel T Badman (2020b). "Pfsspy: A Python Package for Potential Field Source Surface Modelling". In: *Journal of Open Source Software* 5.54, p. 2732. DOI: 10.21105/joss.02732.

Sterling, Alphonse C. and Ronald L. Moore (2020). "Coronal-Jet-Producing Minifilament Eruptions as a Possible Source of Parker Solar Probe (PSP) Switchbacks". In: *The Astrophysical Journal Letters* 896.L18. DOI: 10.3847/2041-8213/ab96be.

Suess, S. T., D. J. McComas, and J. T. Hoeksema (1993). "Prediction of the Heliospheric Current Sheet Tilt: 1992-1996". In: *Geophysical Research Letters* 20.3, pp. 161–164. DOI: 10.1029/93GL00078.

Sunny, Jibin V., Archana Giri Nair, Megha Babu, and Rajkumar Hajra (2023). "A Comparative Study on Geoeffective and Non-Geoeffective Corotating Interaction Regions". In: *Advances in Space Research* 71.1, pp. 268–274. ISSN: 0273-1177. DOI: 10.1016/j.asr.2022.09.051.

Suzuki, Takeru K and Shu-ichiro Inutsuka (2005). "Making the Corona and the Fast Solar Wind: A Self-consistent Simulation for the Low-Frequency Alfvén Waves from the Photosphere to 0.3 AU". In: *The Astrophysical Journal* 632.1, pp. L49–L52. ISSN: 0004-637X. DOI: 10.1086/497536.

Szabo, Adam et al. (2020). "The Heliospheric Current Sheet in the Inner Heliosphere Observed by the Parker Solar Probe". In: *The Astrophysical Journal Supplement Series* 246.2, p. 47. DOI: 10.3847/1538-4365/ab5dac.

Taylor, G. I. (1938). "The Spectrum of Turbulence". In: *Proceedings of the Royal Society of London. Series A - Mathematical and Physical Sciences* 164.919, pp. 476–490. DOI: 10.1098/rspa.1938.0032.

Telloni, D. et al. (2021a). "Study of Two Interacting Interplanetary Coronal Mass Ejections Encountered by Solar Orbiter during Its First Perihelion Passage - Observations and Modeling". In: *Astronomy & Astrophysics* 656, A5. ISSN: 0004-6361, 1432-0746. DOI: 10.1051/0004-6361/202140648.

Telloni, Daniele et al. (2021b). "Evolution of Solar Wind Turbulence from 0.1 to 1 Au during the First Parker Solar Probe-Solar Orbiter Radial Alignment". In: *The Astrophysical Journal Letters* 912.2, p. L21. ISSN: 2041-8205. DOI: 10.3847/2041-8213/abf7d1.

Telloni, Daniele et al. (2022). "Observation and Modeling of the Solar Wind Turbulence Evolution in the Sub-Mercury Inner Heliosphere". In: *The Astrophysical Journal Letters* 938.2, p. L8. ISSN: 2041-8205. DOI: 10.3847/2041-8213/ac9624.

Temmer, M, M A Reiss, L Nikolic, S J Hofmeister, and A M Veronig (2017). "Preconditioning of Interplanetary Space Due to Transient CME Disturbances". In: *The Astrophysical Journal* 835.2, p. 141. DOI: 10.3847/1538-4357/835/2/141.

Tenerani, Anna, Nikos Sioulas, Lorenzo Matteini, Olga Panasenco, Chen Shi, and Marco Velli (2021). "Evolution of Switchbacks in the Inner Heliosphere". In: *The Astrophysical Journal Letters* 919.2, p. L31. ISSN: 2041-8205, 2041-8213. DOI: 10.3847/2041-8213/ac2606.

Tenerani, Anna et al. (2020). "Magnetic Field Kinks and Folds in the Solar Wind". In: *The Astrophysical Journal Supplement Series* 246.2, p. 32. DOI: 10.3847/1538-4365/ab53e1.

Thieme, K. M., E. Marsch, and R. Schwenn (1990). "Spatial Structures in High-Speed Streams as Signatures of Fine Structures in Coronal Holes." In: *Annales Geophysicae* 8. https://ui.adsabs.harvard.edu/abs/1990AnGeo...8..713T, pp. 713–723. ISSN: 0992-76891432-0576 Annales Geophysicae.

Thomas, Barry T. and Edward J. Smith (1981). "The Structure and Dynamics of the Heliospheric Current Sheet". In: *Journal of Geophysical Research* 86.A13, p. 11105. ISSN: 0148-0227. DOI: 10.1029/ja086ia13p11105.

Thompson, W. T. (2006). "Coordinate Systems for Solar Image Data". In: *Astronomy & Astrophysics* 449.2, pp. 791–803. ISSN: 0004-6361. DOI: 10.1051/0004-6361:20054262.

Tian, H. et al. (2014). "Prevalence of Small-Scale Jets from the Networks of the Solar Transition Region and Chromosphere". In: *Science* 346.6207, p. 1255711. DOI: 10.1126/science.1255711.

Titov, V. S., Z. Mikić, J. A. Linker, R. Lionello, and S. K. Antiochos (2011). "MAGNETIC TOPOLOGY OF CORONAL HOLE LINKAGES". In: *The Astrophysical Journal* 731.2, p. 111. ISSN: 0004-637X. DOI: 10.1088/0004-637X/731/2/111.

Tomczyk, S., S. W. McIntosh, S. L. Keil, P. G. Judge, T. Schad, D. H. Seeley, and J. Edmondson (2007). "Alfvén Waves in the Solar Corona". In: *Science* 317.5842, pp. 1192–1196. ISSN: 00368075. DOI: 10.1126/science.1143304.

Torok, T, G Aulanier, B Schmieder, K K Reeves, and L Golub (2009). "FAN-SPINE TOPOLOGY FORMATION THROUGH TWO-STEP RECONNECTION DRIVEN BY TWISTED FLUX EMERGENCE". In: *The Astrophysical Journal* 704, pp. 485–495. DOI: 10.1088/0004-637X/704/1/485.

Tracy, Patrick J., Justin C. Kasper, Jim M. Raines, Paul Shearer, Jason A. Gilbert, and Thomas H. Zurbuchen (2016). "Constraining Solar Wind Heating Processes by Kinetic Properties of Heavy Ions". In: *Physical Review Letters* 116, p. 255101. ISSN: 0031-9007. DOI: 10.1103/PhysRevLett.116.255101.

Tsurutani, B T, G S Lakhina, J S Pickett, F L Guarnieri, N Lin, and B E Goldstein (2005). "Nonlinear Alfvén Waves, Discontinuities, Proton Perpendicular Acceleration, and Magnetic Holes/Decreases in Interplanetary Space and the Magnetosphere: Intermediate Shocks?" In: *Nonlinear Processes in Geophysics* 12.3. https://hal.archives-ouvertes.fr/hal-00302560, pp. 321–336.

Tsurutani, B. T., C. M. Ho, E. J. Smith, M. Neugebauer, B. E. Goldstein, J. S. Mok, J. K. Arballo, A. Balogh, D. J. Southwood, and W. C. Feldman (1994). "The Relationship between Interplanetary Discontinuities and Alfvén Waves:

Ulysses Observations". In: *Geophysical Research Letters* 21.21, pp. 2267–2270. ISSN: 00948276. DOI: 10.1029/94GL02194.

Tsurutani, Bruce T and Christian M Ho (1999). "A Review of Discontinuities and Alfvén Waves in Interplanetary Space: Ulysses Results". In: *Reviews of Geophysics* 37.4, pp. 517–541. ISSN: 8755-1209. DOI: 10.1029/1999RG900010.

Tu, C. -Y. and E. Marsch (1995). "MHD Structures, Waves and Turbulence in the Solar Wind: Observations and Theories". In: *Space Science Reviews* 73.1, pp. 1–210. ISSN: 1572-9672. DOI: 10.1007/BF00748891.

— (2001). "On Cyclotron Wave Heating and Acceleration of Solar Wind Ions in the Outer Corona". In: *Journal of Geophysical Research* 106, pp. 8233–8252. ISSN: 0148-0227. DOI: 10.1029/2000JA000024.

Ulrich, Roger K and John E Boyden (2006). "CARRINGTON COORDINATES AND SOLAR MAPS". In: *Solar Physics* 235, pp. 17–29. DOI: 10.1007/s11207-006-0041-5.

Uritsky, V M, C E DeForest, J T Karpen, C R DeVore, P Kumar, N E Raouafi, and P F Wyper (2021). "Plumelets: Dynamic Filamentary Structures in Solar Coronal Plumes". In: *The Astrophysical Journal* 907.1, p. 1. ISSN: 1538-4357. DOI: 10.3847/1538-4357/abd186.

van Driel-Gesztelyi, Lidia and Lucie May Green (2015). "Evolution of Active Regions". In: *Living Reviews in Solar Physics* 12.1, p. 1. ISSN: 2367-3648. DOI: 10.1007/lrsp-2015-1.

Vasquez, Bernard J. and Joseph V. Hollweg (1996). "Formation of Arc-Shaped Alfvén Waves and Rotational Discontinuities from Oblique Linearly Polarized Wave Trains". In: *Journal of Geophysical Research* 101, pp. 13527–13540. ISSN: 0148-0227. DOI: 10.1029/96JA00612.

— (1998). "Formation of Imbedded Rotational Discontinuities with Nearly Field Aligned Normals". In: *Journal of Geophysical Research: Space Physics* 103.A1, pp. 349–365. ISSN: 2169-9402. DOI: 10.1029/97ja02993.

Velli, M. (1993). "On the Propagation of Ideal, Linear Alfven Waves in Radially Stratified Stellar Atmospheres and Winds". In: *Astronomy and Astrophysics* 270. https://ui.adsabs.harvard.edu/abs/1993A&A...270..304V, pp. 304–314. ISSN: 0004-6361.

Velli, M. et al. (2020). "Understanding the Origins of the Heliosphere: Integrating Observations and Measurements from Parker Solar Probe, Solar Orbiter, and Other Space- and Ground-Based Observatories". In: *Astronomy & Astrophysics* 642, A4. ISSN: 0004-6361, 1432-0746. DOI: 10.1051/0004-6361/202038245.

Verdini, A., M. Velli, W. H. Matthaeus, S. Oughton, and P. Dmitruk (2010). "A Turbulence-Driven Model for Heating and Acceleration of the Fast Wind in Coronal Holes". In: *The Astrophysical Journal* 708, pp. L116–L120. ISSN: 0004-637X. DOI: 10.1088/2041-8205/708/2/L116.

Verdini, Andrea and Marco Velli (2007). "Alfven Waves and Turbulence in the Solar Atmosphere and Solar Wind". In: *The Astrophysical Journal* 662.1, pp. 669–676. ISSN: 0004-637X. DOI: 10.1086/510710.

Verscharen, Daniel, Kristopher G Klein, and Bennett A Maruca (2019). "The Multi-Scale Nature of the Solar Wind". In: *Living Reviews in Solar Physics* 16.1, p. 5. ISSN: 1614-4961. DOI: 10.1007/s41116-019-0021-0.

Viall, N. M., L. Kepko, and H. E. Spence (2008). "Inherent Length-Scales of Periodic Solar Wind Number Density Structures". In: *Journal of Geophysical Research: Space Physics* 113.A7. ISSN: 01480227. DOI: 10.1029/2007JA012881.

Viall, Nicholeen M. and Angelos Vourlidas (2015). "PERIODIC DENSITY STRUCTURES and the ORIGIN of the SLOW SOLAR WIND". In: *Astrophysical Journal* 807.2. ISSN: 15384357. DOI: 10.1088/0004-637X/807/2/176.

Villante, U, R Bruno, F Mariani, L F Burlaga, and N F Ness (1979). "The Shape and Location of the Sector Boundary Surface in the Inner Solar System". In: *Journal of Geophysical Research: Space Physics* 84.A11, pp. 6641–6648. DOI: 10.1029/JA084iA11p06641.

von Steiger, R, J Geiss, G Gloeckler, and A B Galvin (1995). "Kinetic Properties of Heavy Ions in the Solar Wind from SWICS/Ulysses". In: *Space Science Reviews* 72.1, pp. 71–76. ISSN: 1572-9672. DOI: 10.1007/BF00768756.

Vourlidas, Angelos and Russell A. Howard (2006). "The Proper Treatment of Coronal Mass Ejection Brightness: A New Methodology and Implications for Observations". In: *The Astrophysical Journal* 642.2, p. 1216. ISSN: 0004-637X. DOI: 10.1086/501122.

Vourlidas, Angelos et al. (2016). "The Wide-Field Imager for Solar Probe Plus (WISPR)". In: *Space Science Reviews* 204.1, pp. 83–130. ISSN: 1572-9672. DOI: 10.1007/s11214-014-0114-y.

Wang, Yi-Ming, Scott H. Hawley, and Neil R. Sheeley (1996). "The Magnetic Nature of Coronal Holes". In: *Science* 271.5248, pp. 464–469. DOI: 10.1126/science.271.5248.464.

Wang, Y. -M., N. R. Sheeley Jr., J. L. Phillips, and B. E. Goldstein (1997). "Solar Wind Stream Interactions and the Wind Speed-Expansion Factor Relationship." In: *The Astrophysical Journal* 488, pp. L51–L54. ISSN: 0004-637X. DOI: 10.1086/310918.

Wang, Y. M. (2000). "The Dynamical Nature of the Coronal Streamer Belt". In: *Advances in Space Research* 105. ISSN: 02731177. DOI: 10.1016/S0273-1177(02)00323-X.

Wang, Y.-M and N. R. Sheeley (1990). "SOLAR WIND SPEED AND CORONAL FLUX-TUBE EXPANSION". In: *The Astrophysical Journal* 355, pp. 726–732. DOI: 10.1086/168805.

Wang, Y.-M., Jr. N. R. Sheeley, and N. B. Rich (2007). "Coronal Pseudostreamers". In: *The Astrophysical Journal* 658.2, p. 1340. ISSN: 0004-637X. DOI: 10.1086/511416.

Wang, Y.-M., M. Pick, and G. M. Mason (2006). "Coronal Holes, Jets, and the Origin of 3He-rich Particle Events". In: *The Astrophysical Journal* 639.1, p. 495. ISSN: 0004-637X. DOI: 10.1086/499355.

Wang, Y.-M., N. R. Sheeley Jr., J. H. Walters, G. E. Brueckner, R. A. Howard, D. J. Michels, P. L. Lamy, R. Schwenn, and G. M. Simnett (1998). "Origin of Streamer Material in the Outer Corona". In: *The Astrophysical Journal* 498.2, pp. L165–L168. ISSN: 0004637X. DOI: 10.1086/311321.

Webb, David F. and Timothy A. Howard (2012). "Coronal Mass Ejections: Observations". In: *Living Reviews in Solar Physics* 9, p. 3. ISSN: 1614-4961. DOI: 10.12942/lrsp-2012-3.

Whittlesey, Phyllis L et al. (2020). "The Solar Probe ANalyzers-Electrons on the Parker Solar Probe". In: *The Astrophysical Journal Supplement Series* 246.2, p. 74. DOI: 10.3847/1538-4365/ab7370.

Wiegelmann, Thomas, Julia K. Thalmann, and Sami K. Solanki (2014). "The Magnetic Field in the Solar Atmosphere". In: *The Astronomy and Astrophysics Review* 22.1, p. 78. ISSN: 1432-0754. DOI: 10.1007/s00159-014-0078-7.

Wilcox, John M. (1968). "The Interplanetary Magnetic Field, Solar Origin and Terrestrial Effects". In: *Space Science Reviews* 8, pp. 258–328. DOI: 10.1007/BF00227565.

Wilson, Lynn B., Michael L. Stevens, Justin C. Kasper, Kristopher G. Klein, Bennett A. Maruca, Stuart D. Bale, Trevor A. Bowen, Marc P. Pulupa, and Chadi S. Salem (2018). "The Statistical Properties of Solar Wind Temperature Parameters Near 1 Au". In: *The Astrophysical Journal Supplement Series* 236.2, p. 41. ISSN: 0067-0049. DOI: 10.3847/1538-4365/aab71c.

Winterhalter, D, E J Smith, M E Burton, N Murphy, and D J McComas (1994). "The Heliospheric Plasma Sheet". In: *Journal of Geophysical Research: Space Physics* 99.A4, pp. 6667–6680. ISSN: 0148-0227. DOI: 10.1029/93JA03481.

Woodham, L D, T S Horbury, L Matteini, T Woolley, R Laker, S D Bale, G Nicolaou, J E Stawarz, D Stansby, H Hietala, D E Larson, R Livi, J L Verniero, M McManus, J C Kasper, K E Korreck, N Raouafi, M Moncuquet, and M P Pulupa (2021a). "Enhanced Proton Parallel Temperature inside Patches of Switchbacks in the Inner Heliosphere". In: *A&A* 650. DOI: 10.1051/0004-6361/202039415.

Woodham, L. D., R. T. Wicks, D. Verscharen, J. M. TenBarge, and G. G. Howes (2021b). "Dependence of Solar Wind Proton Temperature on the Polarization Properties of Alfvénic Fluctuations at Ion-kinetic Scales". In: *The Astrophysical Journal* 912.2, p. 101. ISSN: 0004-637X. DOI: 10.3847/1538-4357/abed51.

Woolley, Thomas, Lorenzo Matteini, Timothy S Horbury, Stuart D Bale, Lloyd D Woodham, Ronan Laker, Benjamin L Alterman, John W Bonnell, Anthony W Case, Justin C Kasper, Kristopher G Klein, Mihailo M Martinović, and Michael Stevens (2020). "Proton Core Behaviour inside Magnetic Field Switchbacks". In: *Monthly Notices of the Royal Astronomical Society* 498.4, pp. 5524–5531. ISSN: 0035-8711. DOI: 10.1093/mnras/staa2770.

Woolley, Thomas, Lorenzo Matteini, Michael D McManus, Laura Berčič, Samuel T Badman, Lloyd D Woodham, Timothy S Horbury, Stuart D Bale, Ronan Laker, Julia E Stawarz, and Davin E Larson (2021). "Plasma Properties, Switchback Patches, and Low α -Particle Abundance in Slow Alfvénic Coronal Hole Wind at 0.13 Au". In: *Monthly Notices of the Royal Astronomical Society* 508.1, pp. 236–244. ISSN: 0035-8711, 1365-2966. DOI: 10.1093/mnras/stab2281.

Wyper, Peter F., C. R. DeVore, S. K. Antiochos, D. I. Pontin, Aleida K. Higginson, Roger Scott, Sophie Masson, and Theo Pelegrin-Frachon (2022). "The Imprint of Intermittent Interchange Reconnection on the Solar Wind". In: *The Astrophysical Journal Letters* 941.2, p. L29. ISSN: 2041-8205. DOI: 10.3847/2041-8213/aca8ae.

Yamauchi, Yohei, Steven T Suess, John T Steinberg, and Takashi Sakurai (2004). "Differential Velocity between Solar Wind Protons and Alpha Particles in Pressure Balance Structures". In: *Journal of Geophysical Research: Space Physics* 109.A3. ISSN: 0148-0227. DOI: 10.1029/2003JA010274.

Yeates, Anthony (2018). "Antyeates1983/Pfss: First Release of Pfss Code." In: DOI: 10.5281/ZENODO.1472183.

Yokoyama, Takaaki and Kazunari Shibata (1995). "Magnetic Reconnection as the Origin of X-ray Jets and Hα Surges on the Sun". In: *Nature* 375.6526, pp. 42–44. ISSN: 00280836. DOI: 10.1038/375042a0.

Yu, H.-S., B. V. Jackson, A. Buffington, P. P. Hick, M. Shimojo, and N. Sako (2014). "THE THREE-DIMENSIONAL ANALYSIS OF HINODE POLAR JETS USING IMAGES FROM LASCO C2, THE STEREO COR2 CORONAGRAPHS, AND SMEI". In: *The Astrophysical Journal* 784.2, p. 166. ISSN: 0004-637X. DOI: 10.1088/0004-637X/784/2/166.

Zank, G P, M Nakanotani, L.-L. Zhao, L Adhikari, and J Kasper (2020). "The Origin of Switchbacks in the Solar Corona: Linear Theory". In: *The Astrophysical Journal* 903.1, p. 1. ISSN: 1538-4357. DOI: 10.3847/1538-4357/abb828.

Zhao, L., T. H. Zurbuchen, and L. A. Fisk (2009). "Global Distribution of the Solar Wind during Solar Cycle 23: ACE Observations". In: *Geophysical Research Letters* 36.14. ISSN: 1944-8007. DOI: 10.1029/2009GL039181.

Zhao, Xuepu and J. Todd Hoeksema (1996). "Effect of Coronal Mass Ejections on the Structure of the Heliospheric Current Sheet". In: *Journal of Geophysical Research: Space Physics* 101.A3, pp. 4825–4834. ISSN: 2156-2202. DOI: 10.1029/95ja03568.

Zurbuchen, Thomas H and Ian G Richardson (2006). "In-Situ Solar Wind and Magnetic Field Signatures of Interplanetary Coronal Mass Ejections". In: *Coronal Mass Ejections*. New York, NY: Springer New York, pp. 31–43. ISBN: 978-0-387-45088-9. DOI: 10.1007/978-0-387-45088-9_3.